

University of Alberta

Surface Plasmon Enhanced Random Lasing

by

Graeme Dice



A thesis submitted to the Faculty of Graduate Studies and Research
in partial fulfillment of the requirements for the degree of

Master of Science

Department of Electrical and Computer Engineering

Edmonton, Alberta

Fall 2006



Library and
Archives Canada

Bibliothèque et
Archives Canada

Published Heritage
Branch

Direction du
Patrimoine de l'édition

395 Wellington Street
Ottawa ON K1A 0N4
Canada

395, rue Wellington
Ottawa ON K1A 0N4
Canada

Your file *Votre référence*
ISBN: 978-0-494-22250-8
Our file *Notre référence*
ISBN: 978-0-494-22250-8

NOTICE:

The author has granted a non-exclusive license allowing Library and Archives Canada to reproduce, publish, archive, preserve, conserve, communicate to the public by telecommunication or on the Internet, loan, distribute and sell theses worldwide, for commercial or non-commercial purposes, in microform, paper, electronic and/or any other formats.

The author retains copyright ownership and moral rights in this thesis. Neither the thesis nor substantial extracts from it may be printed or otherwise reproduced without the author's permission.

AVIS:

L'auteur a accordé une licence non exclusive permettant à la Bibliothèque et Archives Canada de reproduire, publier, archiver, sauvegarder, conserver, transmettre au public par télécommunication ou par l'Internet, prêter, distribuer et vendre des thèses partout dans le monde, à des fins commerciales ou autres, sur support microforme, papier, électronique et/ou autres formats.

L'auteur conserve la propriété du droit d'auteur et des droits moraux qui protègent cette thèse. Ni la thèse ni des extraits substantiels de celle-ci ne doivent être imprimés ou autrement reproduits sans son autorisation.

In compliance with the Canadian Privacy Act some supporting forms may have been removed from this thesis.

Conformément à la loi canadienne sur la protection de la vie privée, quelques formulaires secondaires ont été enlevés de cette thèse.

While these forms may be included in the document page count, their removal does not represent any loss of content from the thesis.

Bien que ces formulaires aient inclus dans la pagination, il n'y aura aucun contenu manquant.


Canada

Abstract

This thesis presents the results of experimental and theoretical investigation of the effects of surface plasmon resonance on random laser systems. A numerical model is developed using the Finite Difference Time Domain algorithm to investigate the role of scattering from novel particles in a random laser system. Simulated results support the case for optical gain enhancement caused by surface plasmon resonance in silver nanoparticles. Several random laser devices are constructed and tested from the suspension of both silver and alumina nanoparticles in a laser dye. The use of silver scattering particles reduces the minimum spectral emission linewidth the input energy fluence threshold for lasing when compared to a random laser with alumina scattering particles. Random lasers are also constructed from the solid suspension of silver and alumina scattering nanoparticles in a solid photoresist. It is determined that the use of surface plasmon enhancement of local optical gain enables the construction of random lasers with superior performance to conventional random lasers with dielectric scatterers.

Acknowledgements

I would like to thank my parents, whose unwavering support has kept me on the path to finishing this thesis. I would also like to thank my fellow lab mates Ken, Vik, Scott, Sushil, and my supervisor Dr. Elezzabi for helping me over the course of the past two years, and for assisting me in bringing this thesis to its successful completion.

Table of Contents

Chapter 1 – Thesis Outline	1
1.1 <i>Thesis Motivation</i>	1
1.2 <i>Thesis Goal</i>	2
1.3 <i>Thesis Organization</i>	2
1.4 <i>References</i>	3
Chapter 2 – Introduction	5
2.1 Light Scattering	5
2.1.1 <i>Single Scattering</i>	5
2.1.2 <i>Rayleigh Scattering</i>	7
2.1.3 <i>Mie Scattering Theory</i>	8
2.1.4 <i>Multiple Scattering</i>	10
2.2 Random Lasers	11
2.2.1 <i>Single Material Random Lasers</i>	12
2.2.2 <i>Random Lasers with Scatterers Suspended in Laser Dye</i>	14
2.2.3 <i>Coherent and Incoherent Random Lasing</i>	15
2.2.4 <i>Scattering Effects in Random Lasers</i>	17
2.3 Surface Plasmon Resonance	19
2.3.1 <i>Metallic Particles in Random Lasers</i>	21
2.3.2 <i>Surface Enhanced Raman Scattering</i>	21
2.4 References	25
Chapter 3 – Random Laser Modeling	30
3.1 Modeling of Random Lasers	30
3.2 The Finite-Difference Time-Domain Algorithm	31
3.2.1 <i>Solution of Maxwell’s Equations</i>	31
3.2.2 <i>Numerical Stability of Solution</i>	36
3.2.3 <i>FDTD Boundary Condition</i>	37
3.2.4 <i>Radiation Source</i>	39
3.2.5 <i>Dispersive Metals</i>	43
3.2.6 <i>Dispersive Dielectrics</i>	46
3.2.7 <i>Optical Gain Material</i>	48
3.2.8 <i>FDTD Simulation Suite</i>	54
3.3 FDTD Light Scattering Simulations	55
3.3.1 <i>Single Scattering Intensity Profile</i>	55
3.3.2 <i>Spatial Electric Field Distribution Surrounding Al₂O₃ Nanoparticles</i>	58
3.3.3 <i>Spatial Distribution of Electric Field Surrounding Ag Nanoparticles</i>	61
3.4 FDTD Gain Model Simulations	68
3.4.1 <i>FDTD Simulation</i>	68
3.4.2 <i>Simulation of a Resonant Optical Cavity</i>	68
3.4.3 <i>Simulation of a Random Gain Media</i>	82
3.5 References	94

Chapter 4 - Random Lasers from Scattering Particles Suspended in Laser Dye	96
4.1 Dye-Scatterer Based Random Lasers	96
4.1.1 <i>Absorption Spectrum of Rhodamine 6G Laser Dye</i>	96
4.1.2 <i>Light Emission from Rhodamine 6G</i>	98
4.1.3 <i>Dielectric Scattering Particles</i>	102
4.1.4 <i>Metallic Scattering Particles</i>	105
4.2 Dielectric Scatterer Based Random Laser Construction	112
4.3 Spectral Features in Random Laser Emission	115
4.3.1 <i>Spectral Features from Al₂O₃ Scatterer Based Random Lasers</i>	115
4.3.2 <i>Linewidth Variation for Al₂O₃ Scatterer Based Random Lasers</i>	126
4.3.3 <i>Intensity Variation for Al₂O₃ Scatterer Based Random Lasers</i>	128
4.4 Silver Scatterer Based Random Lasers	128
4.4.1 <i>Spectral features from Ag scatterer Based Random Lasers</i>	130
4.4.2 <i>Linewidth Variation in Ag Scatterer Based Random Lasers</i>	139
4.4.3 <i>Intensity Variation in Ag Scatterer Based Random Lasers</i>	141
4.4.4 <i>Input Pump Energy Fluence Threshold for Lasing</i>	143
4.5 Hybrid Ag/Al₂O₃ Scatterer Based Random Lasers	145
4.5.1 <i>Hybrid Random Lasers</i>	146
4.5.2 <i>Spectral Behaviour of Hybrid Random Lasers</i>	147
4.5.3 <i>Linewidth Variation from Hybrid Random Lasers</i>	150
4.5.4 <i>Intensity Variation from Random Lasers</i>	152
4.6 References	155
Chapter 5 – Solid Random Laser	157
5.1 SU-8 Based Random Laser	157
5.2 Solid Suspension of Scattering Particles	157
5.3 SU-8 Based Random Laser Construction	158
5.3.1 <i>Scattering Particles in SU-8</i>	159
5.3.2 <i>Spincoating of SU-8 and Scattering Particles</i>	160
5.3.3 <i>Optical Arrangement</i>	161
5.4 Rhodamine 6G and SU-8 based Random Lasers	161
5.4.1 <i>Light Emission from Rhodamine 6G dissolved in SU-8</i>	164
5.4.2 <i>Light Emission with Al₂O₃ Scattering Particles</i>	164
5.4.3 <i>Light Emission with Ag Scattering Particles</i>	168
5.4.4 <i>Linewidth Variation for SU-8 Based Random Lasers</i>	172
5.4.5 <i>Intensity Variation for Al₂O₃ Scatterer Based Random Lasers</i>	174
5.5 Line Excitation of SU-8 Based Random Lasers	176
5.5.1 <i>Line Excitation of Rhodamine 6G dissolved in SU-8</i>	176

5.5.2	<i>Light Emission with Al₂O₃ Scattering Particles</i>	178
5.5.3	<i>Light Emission with Ag Scattering Particles</i>	180
5.5.4	<i>Lasing Energy Fluence Threshold for SU-8 Based Solid State Random Lasers</i>	182
5.5.5	<i>Intensity Variation for Al₂O₃ Scatterer Based Random Lasers</i>	185
5.6	References	188
Chapter 6 – Conclusions		189
6.1	Conclusion	189
6.2	Future Possibilities	191
Appendix A – Finite-Difference Time-Domain Software Source Code		192

List of Tables

Table 4.1	98
Table 4.2	119
Table 4.3	121
Table 4.4	124
Table 4.5	126
Table 4.6	128
Table 4.7	134
Table 4.8	134
Table 4.9	136
Table 4.10	139
Table 4.11	141
Table 5.1	159
Table 5.2	159
Table 5.3	160
Table 5.4	164
Table 5.5	166
Table 5.6	170
Table 5.7	172
Table 5.8	174
Table 5.9	174
Table 5.10	176
Table 5.11	178
Table 5.12	182
Table 5.13	182
Table 5.14	185
Table 5.15	186

List of Figures

- Figure 2.1 – Scattering (σ_{sca}) and absorption (σ_{abs}) cross-sections calculated from Rayleigh theory for a spherical silver nanoparticle with a 5 nm diameter. 9
- Figure 2.2 – (a) Schematic depiction of random laser operation for a collection of scattering particles that provide optical gain. All optical amplification occurs inside the scattering particles. (b) Schematic depiction of random laser operation for separate scattering particles surrounded by the gain media. Optical amplification occurs outside the scattering particles. For both, the pump radiation enters from the left, and observed emitted radiation exits to the left. 13
- Figure 2.3 – Comparison of Q_{sca} for a 100 nm diameter Ag sphere (solid line) to a 100 nm diameter Al_2O_3 sphere (dot-dashed line). 24
- Figure 3.1 – The Yee-grid unit cell. The magnetic and electric fields are separated by a half space step, $\Delta x/2$. 32
- Figure 3.2 – Magnetic and Electric loss terms in the Berenger Perfectly Matched Layer (PML). 40
- Figure 3.3 – Relative permittivity of silver as a function of wavelength. 44
- Figure 3.4 – Relative electric permittivity of Alumina (Al_2O_3) assuming no absorption as a function of wavelength in the visible range. 47
- Figure 3.5 – Energy level diagram for the simulated gain medium. P_r is the pumping rate, and τ_{32} , τ_{32} , τ_{32} are the energy level lifetimes. 50
- Figure 3.6 – (a) The total electric field for $\lambda = 600$ nm radiation incident on the bottom of a 300 nm diameter glass cylinder. (b) The electric field scattered from the cylinder. 56
- Figure 3.7 – (solid line) Scattered intensity profile calculated via the FDTD simulation for $\lambda = 600$ nm radiation incident on the bottom of a 300 nm diameter glass cylinder. (dashed line) Scattered intensity profile as calculated by Mie theory. 57
- Figure 3.8 – Simulated electric field distribution surrounding 25 nm (a, b), 50 nm (c, d) and 100 nm (e, f) diameter Al_2O_3 particles suspended in methanol. The electric field is calculated for both $\lambda_{pump} = 532$ nm and $\lambda_{laser} = 564$ nm which are incident from the left side. 59

Figure 3.9 – Simulated average electric field distribution $\lambda_{pump} = 532$ nm (incident from the left side) in ensembles composed 25 nm (a), 50 nm (b) and 100 nm (c) diameter Al_2O_3 particles suspended in methanol. Each image is $1.25 \mu\text{m} \times 1.25 \mu\text{m}$. 60

Figure 3.10 – Simulated average electric field distribution surrounding 25 nm (a, b), 50 nm (c, d) and 100 nm (e, f) diameter Ag particles suspended in methanol. The electric field is calculated for both $\lambda_{pump} = 532$ nm and $\lambda_{laser} = 564$ nm which are incident from the left side. Large electric field enhancement (~ 30) near the surface of each nanoparticle is evident at both wavelengths. 62

Figure 3.11 – Normalized peak intensity at $\lambda_{pump} = 532$ nm (solid line) and $\lambda_{laser} = 564$ nm (dashed-dotted line) as a function of the distance to the center of 25 nm (a), 50 nm (b), and 100 nm (c) Ag nanoparticles suspended in methanol. A near-field interaction region of large electromagnetic field enhancement is present within ~ 10 nm of the surface of each particle. 63

Figure 3.12 – Simulated average electric field distribution surrounding Ag squares having 50 nm long sides (a, b) and Ag triangles with 50 nm long bases (c-j) pointing in all cardinal directions. For the displayed particle shapes, the $\lambda_{pump} = 532$ nm and $\lambda_{laser} = 564$ nm radiation are incident from the left side. 65

Figure 3.13 – Simulated average electric field distribution surrounding an ensemble of Ag nanoparticles with diameters of 25 nm (a), 50 nm (b), and 100 nm (c). The $\lambda_{pump} = 532$ nm incident (from the left side) radiation is scattered throughout the simulation space. Large electric field enhancement is evident at the surface of each particle and within regions between adjacent particles. Each image is $1.25 \mu\text{m} \times 1.25 \mu\text{m}$. 66

Figure 3.14 – Simulated average electric field distribution of an ensemble consisting of 57% 50 nm diameter Ag and 43% 100 nm diameter Al_2O_3 nanoparticles. The $\lambda_{pump} = 532$ nm radiation is incident from the left side. The image is $1.25 \mu\text{m} \times 1.25 \mu\text{m}$. 67

Figure 3.15 – Calculated atomic population levels for a four-level gain media (Levels N_0 and N_3 not shown) with a pumping rate of $1 \times 10^7 \text{ s}^{-1}$. The development of the population inversion for the gain media without a resonant cavity can be seen. 69

Figure 3.16 – Illustration of the $25 \mu\text{m} \times 25 \mu\text{m}$ simulated laser cavity. (a) The cavity geometry is colour coded according to the material at each grid point. Black represents free space, blue represents the gain material, and yellow represents the silver mirrors. 71

- Figure 3.16 – (b) The electric field magnitude of the pump beam at time $t = 2$ ps. The pump beam is incident from the bottom at $\lambda = 500$ nm. The image size is $25 \mu\text{m} \times 25 \mu\text{m}$. 72
- Figure 3.16 – (c) The spontaneously emitted electric field magnitude at $t = 2$ ps. The image size is $25 \mu\text{m} \times 25 \mu\text{m}$. 73
- Figure 3.16 – (d) Electric field magnitude at $t = 80$ ps illustrating the amplification of radiation propagating along the optical axis of the resonator. The image size is $25 \mu\text{m} \times 25 \mu\text{m}$. 74
- Figure 3.17 – Population levels N_2 and N_1 as calculated by the FDTD simulation as a function of t at the center of the optical resonator cavity shown in Figure 3.16. 76
- Figure 3.18 – The wavelength distribution of spontaneously emitted radiation for the FDTD simulation. The dashed-dotted line is the expected Lorentzian wavelength distribution with a bandwidth of 60 nm. The solid line is the actual distribution of radiation sources within the simulation space. 77
- Figure 3.19 – The temporal evolution of the spectral components present in the FDTD simulation of the emitted field. Each graph in the figure represents the emitted radiation spectrum over a specific 10 ps long time period. (a) 0-10 ps (b) 10-20 ps (c) 20-30 ps 78
- Figure 3.19 – (d) 30-40 ps (e) 50-60 ps (f) 70-80 ps 79
- Figure 3.19 – (g) 90-100 ps (h) 110-120 ps (i) 140-150 ps. 80
- Figure 3.20 – Total spectral intensity as a function of time for the simulated optical resonator cavity. 81
- Figure 3.21 – Illustrations describing the operation of the simulated random laser. (a) The cavity geometry, which is $5 \mu\text{m} \times 5 \mu\text{m}$ and colour coded according to the material at each grid point. Black represents free space, blue represents the gain material, and yellow represents the silver mirrors. 84
- Figure 3.21 – (b) The electric field magnitude of the pump beam at time $t = 0.25$ ps. The image size is $5 \mu\text{m} \times 5 \mu\text{m}$. 85
- Figure 3.21 – (c) The spontaneously emitted electric field magnitude at $t = 0.25$ ps. The image size is $5 \mu\text{m} \times 5 \mu\text{m}$. 86

- Figure 3.21 – (d) Electric field magnitude at $t = 15$ ps illustrating the intense amplification that occurs due to multiple scattering. The image size is $5 \mu\text{m} \times 5 \mu\text{m}$. 87
- Figure 3.22 – The temporal evolution of the spectral components present in the FDTD simulation of the random laser. Each graph in the figure represents the emitted radiation spectrum over a specific 0.5 ps long time period. (a) 0-0.5 ps (b) 1.5-2.0 ps (c) 3.5-4.0 ps 90
- Figure 3.22 – (d) 5.5-6.0 ps (e) 7.5-8.0 ps (f) 9.5-10.0 ps 91
- Figure 3.22 – (g) 11.5-12.0 ps (h) 13.5-14.0 ps (i) 15.5-16.0 ps. 92
- Figure 3.23 – Peak spectral intensity in the simulated random laser as a function of time. 93
- Figure 4.1 – The measured absorption coefficient as a function of wavelength for Rhodamine 6G dye dissolved in methanol at a concentration of 10^{-3} mol/L. 97
- Figure 4.2 – The emission spectrum of 10^{-3} mol/L Rhodamine 6G dissolved in methanol at input pump energy fluences from $F = 0.2$ mJ/cm² to 10.9 mJ/cm². (a) $F = 0.2$ mJ/cm² (b) $F = 0.6$ mJ/cm² (c) $F = 1.7$ mJ/cm² 99
- Figure 4.2 – (d) $F = 3.4$ mJ/cm² (e) $F = 4.2$ mJ/cm² (f) $F = 5.9$ mJ/cm² 100
- Figure 4.2 – (g) $F = 7.6$ mJ/cm² (h) $F = 9.2$ mJ/cm² (i) $F = 10.9$ mJ/cm². 101
- Figure 4.3 – The theoretically calculated value of Q_{ext} as a function of wavelength for a 100 nm diameter Al₂O₃ particle suspended in methanol. 103
- Figure 4.4 – The mean free path at $\lambda = 564$ nm for 100 nm diameter Al₂O₃ spheres suspended in methanol as a function of particle concentration. 104
- Figure 4.5 – (a) Scattering efficiency (Q_{sca}) (solid line) and absorption efficiency (Q_{abs}) (dashed-dotted line) for 55 nm diameter Ag nanoparticles. (b) Scattering efficiency (Q_{sca}) (solid line) and absorption efficiency (Q_{abs}) (dashed-dotted line) for 130 nm diameter Ag nanoparticles. (c) Scattering efficiency (Q_{sca}) (solid line) and absorption efficiency (Q_{abs}) (dashed-dotted line) for 80 nm diameter Cu nanoparticles. (d) Scattering efficiency (Q_{sca}) (solid line) and absorption efficiency (Q_{abs}) (dashed-dotted line) for 80 nm diameter Au nanoparticles. The normalized emission spectrum in each graph is for 10^{-3} mol/L Rhodamine 6G at a pump energy fluence of 10.9 mJ/cm², which has a peak wavelength of 559 nm. 107

- Figure 4.6 – (a) Measured optical extinction vs. wavelength for Ag nanoparticles suspended in methanol. (b) Q_{ext} calculated by Mie theory for a 55 nm diameter Ag nanosphere in methanol. Both measured and calculated extinctions peak at $\lambda = 411$ nm, and indicate the effective suspended particle size. 109
- Figure 4.7 – (a) SEM Image of Ag particle microclusters before ultrasonic dispersal. (b) SEM image of Ag nanoparticles after dispersal. 110
- Figure 4.8 – Calculated values of (solid line) Q_{ext} , (dashed-dotted line) Q_{scat} , and (dotted line) Q_{abs} in the visible spectrum from $\lambda = 200$ nm to 1000 nm for a 55 nm diameter spherical Ag nanoparticle. 111
- Figure 4.9 – The calculated value of the optical mean free path (ℓ) as a function of the concentration of 55 nm diameter Ag particles suspended in methanol. 113
- Figure 4.10 – The experimental setup used to collect random laser spectra. The pump laser is a green Nd:YAG second harmonic beam at $\lambda_{pump} = 532$ nm. The random laser is the suspended scattering particles in Rhodamine 6G laser dye. Emitted radiation is collected and analyzed by the Ocean Optic Spectrometer. 114
- Figure 4.11 – The emission spectra for an Al_2O_3 scatterer based gain media having $\ell = 85$ μm over input pump energy fluences from $F = 0.2$ mJ/cm^2 to 10.9 mJ/cm^2 . (a) $F = 0.2$ mJ/cm^2 (b) $F = 0.6$ mJ/cm^2 (c) $F = 1.7$ mJ/cm^2 116
- Figure 4.11 – (d) $F = 3.4$ mJ/cm^2 (e) $F = 4.2$ mJ/cm^2 (f) $F = 5.9$ mJ/cm^2 117
- Figure 4.11 – (g) $F = 7.6$ mJ/cm^2 (h) $F = 9.2$ mJ/cm^2 (i) $F = 10.9$ mJ/cm^2 . 118
- Figure 4.12 – Light emission spectra from Rhodamine 6G with Al_2O_3 nanoparticles at a mean free path $\ell = 340$ μm . (a) The broadband fluorescence spectrum (linewidth = 35 nm) from the sample pumped at $F = 0.6$ mJ/cm^2 . (b) The narrowband emission spectrum with linewidth = 5.5 nm pumped at $F = 4.2$ mJ/cm^2 . (c) The narrowband emission spectrum with linewidth = 5.5 nm pumped at $F = 10.9$ mJ/cm^2 . 120
- Figure 4.13 – Spectrum of light emission from Rhodamine 6G with Al_2O_3 nanoparticles at a mean free path $\ell = 680$ μm . (a) The broadband fluorescence spectrum (linewidth = 36 nm) from the sample pumped at $F = 0.4$ mJ/cm^2 . (b) The narrowband emission spectrum with linewidth = 5.7 nm pumped at $F = 10.9$ mJ/cm^2 . 122

- Figure 4.14 – Spectrum of light emission from Rhodamine 6G with Al_2O_3 nanoparticles at a mean free path $\ell = 2700 \mu\text{m}$. (a) The broadband fluorescence spectrum pumped at $F = 0.4 \text{ mJ/cm}^2$. (b) The emission spectrum at $F = 10.9 \text{ mJ/cm}^2$ which has a well-defined peak at 564 nm with a relatively wide linewidth of 8 nm. (c) The emission spectrum pumped at $F = 15.4 \text{ mJ/cm}^2$, where the spectral emission linewidth narrows to 6 nm and the emission intensity doubles. 125
- Figure 4.15 – FWHM linewidth variation of random lasers with $\ell = 85 \mu\text{m}$ (■), $340 \mu\text{m}$ (●), $680 \mu\text{m}$ (▲), and $2700 \mu\text{m}$ (▼), as a function of F from 0.2 mJ/cm^2 to 15.4 mJ/cm^2 . 127
- Figure 4.16 – Relative peak emitted intensity vs. input pump fluence F for Al_2O_3 scatterer based random lasers having $\ell = 85 \mu\text{m}$ (■), $\ell = 340 \mu\text{m}$ (●), $\ell = 680 \mu\text{m}$ (▲), and $\ell = 2700 \mu\text{m}$ (▼). 129
- Figure 4.17 – The emission spectra for an Ag scatterer based gain media having $\ell = 78 \mu\text{m}$ over input pump energy fluences from $F = 0.5 \text{ mJ/cm}^2$ to 24.6 mJ/cm^2 . (a) $F = 0.5 \text{ mJ/cm}^2$ (b) $F = 1.4 \text{ mJ/cm}^2$ (c) $F = 3.8 \text{ mJ/cm}^2$ 131
- Figure 4.17 – (d) $F = 7.6 \text{ mJ/cm}^2$ (e) $F = 9.5 \text{ mJ/cm}^2$ (f) $F = 13.2 \text{ mJ/cm}^2$ 132
- Figure 4.17 – (g) $F = 17.0 \text{ mJ/cm}^2$ (h) $F = 20.8 \text{ mJ/cm}^2$ (i) $F = 24.6 \text{ mJ/cm}^2$. 133
- Figure 4.18 – Spectrum of light emission from Rhodamine 6G with suspended Ag nanoparticles at $\ell = 350 \mu\text{m}$. (a) The broadband fluorescence spectrum having a linewidth of 36 nm pumped at $F = 0.95 \text{ mJ/cm}^2$. (b) The narrowband emission spectrum at $F = 3.8 \text{ mJ/cm}^2$ which has a linewidth of 4.5 nm. (c) A 5-fold increase in emission intensity at $F = 9.5 \text{ mJ/cm}^2$ with the same 4.5 nm linewidth. 135
- Figure 4.19 – Spectrum of light emission from Rhodamine 6G with suspended Ag nanoparticles at a mean free path $\ell = 1.05 \text{ mm}$. (a) The broadband fluorescence spectrum (linewidth = 36 nm) pumped at $F = 0.5 \text{ mJ/cm}^2$. (b) The narrowband emission spectrum at $F = 3.8 \text{ mJ/cm}^2$ which has a linewidth of 6.7 nm. (c) A thirty fold increase in emission intensity at $F = 24.6 \text{ mJ/cm}^2$ with a 4.2 nm emission linewidth. 137
- Figure 4.20 – Spectrum of light emission from Rhodamine 6G with Ag nanoparticles at a mean free path $\ell = 3200 \mu\text{m}$. (a) The broadband fluorescence spectrum (linewidth = 36 nm) pumped at $F = 0.95 \text{ mJ/cm}^2$. (b) The narrowband emission spectrum at $F = 3.8 \text{ mJ/cm}^2$. (c) An order of magnitude increase in the emission intensity at $F = 9.5 \text{ mJ/cm}^2$ with a bandwidth of 4.6 nm. 138

Figure 4.21 – Variation in emission linewidth as a function of input pump fluence F for Ag scatterer based random lasers having $\ell = 78 \mu\text{m}$ (■), $\ell = 350 \mu\text{m}$ (●), $\ell = 1.05 \text{ mm}$ (▲), $\ell = 3.2 \text{ mm}$ (downwards triangles), and $\ell = 43 \text{ mm}$ (◆). The Al_2O_3 scatterer based random laser having $\ell = 170 \mu\text{m}$ (□) is shown for comparison purposes. The effects of SP enhanced random lasing are evident, as the threshold energy fluence is $\sim 5 \text{ mJ/cm}^2$ at both $\ell = 3.2 \text{ mm}$ and $\ell = 350 \mu\text{m}$. Additionally, the Ag scatterer based random lasers with $\ell = 350 \mu\text{m}$, 1.05 mm , and 3.2 mm all have a smaller threshold fluence than the Al_2O_3 scatterer based random laser with $\ell = 170 \mu\text{m}$. 140

Figure 4.22 – Relative peak emitted intensity vs. input pump fluence F for Ag scatterer based random lasers having $\ell = 78 \mu\text{m}$ (■), $\ell = 350 \mu\text{m}$ (●), $\ell = 1.05 \text{ mm}$ (▲), $\ell = 3.2 \text{ mm}$ (▼), and $\ell = 43 \text{ mm}$ (◆). 142

Figure 4.23 – Dependence of the input pump energy fluence threshold, F , (Δ) and the bandwidth narrowing factor (\square) on scattering strength, L/ℓ . Random lasing is observed over a wide optimal range of scattering strengths, centred at the crossover between the weak and modestly scattering regimes ($L/\ell = 1$). 144

Figure 4.24 – Effective mean free path (ℓ_{eff}) vs. Ag particle concentration for hybrid Ag/ Al_2O_3 scatterer based random lasers having $\ell_{\text{Al}_2\text{O}_3} = 340 \mu\text{m}$ (◇), $\ell_{\text{Al}_2\text{O}_3} = 680 \mu\text{m}$ (Δ) and $\ell_{\text{Al}_2\text{O}_3} = 2700 \mu\text{m}$ (●). There is little change in ℓ_{eff} for random lasers with $\ell_{\text{Al}_2\text{O}_3} = 340 \mu\text{m}$ and $\ell_{\text{Al}_2\text{O}_3} = 680 \mu\text{m}$, however, the random laser with $\ell_{\text{Al}_2\text{O}_3} = 2700 \mu\text{m}$ experiences significantly more scattering as Ag particles are added. 148

Figure 4.25 – Hybrid random laser spectra having $\ell_{\text{Al}_2\text{O}_3} = 340 \mu\text{m}$ (a), $\ell_{\text{Al}_2\text{O}_3} = 680 \mu\text{m}$ (b), and $\ell_{\text{Al}_2\text{O}_3} = 2700 \mu\text{m}$ (c). The spectra are depicted for cases without Ag particles, and at a Ag particle concentration of $57 \mu\text{g/mL}$. An intensity enhancement of ~ 3.1 is observed for random lasers with both $\ell_{\text{Al}_2\text{O}_3} = 340 \mu\text{m}$ and $\ell_{\text{Al}_2\text{O}_3} = 680 \mu\text{m}$. At $\ell_{\text{Al}_2\text{O}_3} = 2700 \mu\text{m}$ the peak emitted intensity is decreased by a factor of ~ 0.7 . 149

Figure 4.26 – Minimum FWHM emission linewidth vs. Ag particle concentration for hybrid Ag/ Al_2O_3 scatterer based random lasers having $\ell_{\text{Al}_2\text{O}_3} = 340 \mu\text{m}$ (◇), $\ell_{\text{Al}_2\text{O}_3} = 680 \mu\text{m}$ (Δ), and $\ell_{\text{Al}_2\text{O}_3} = 2700 \mu\text{m}$ (●). The minimum FWHM emission linewidth for a silver scatterer based random laser (\circ) is depicted as a function of Ag particle concentration. A small decrease in linewidth with increasing Ag particle concentration

can be seen for $\ell_{Al_2O_3} = 340 \mu\text{m}$, and $\ell_{Al_2O_3} = 680 \mu\text{m}$, while linewidth remains approximately constant for $\ell_{Al_2O_3} = 2700 \mu\text{m}$. 151

Figure 4.27 – Relative peak emitted intensity vs. Ag particle concentration for hybrid random lasers having $\ell_{Al_2O_3} = 340 \mu\text{m}$ (\diamond), $\ell_{Al_2O_3} = 680 \mu\text{m}$ (\triangle), and $\ell_{Al_2O_3} = 2700 \mu\text{m}$ (\bullet). The $\ell_{Al_2O_3} = 340$ and $\ell_{Al_2O_3} = 680 \mu\text{m}$ curves show that a maximum peak intensity enhancement factor of ~ 3.1 occurs at the optimum Ag particle concentration of $57 \mu\text{g/mL}$. 154

Figure 5.1 – Schematic depiction of the experimental apparatus for observation of random lasing using an SU-8 based scattering matrix. Pump light is coupled into the SU-8 + Rhodamine 6G layer. Edge emitted light is coupled into an Ocean Optics fiber spectrometer. 162

Figure 5.2 - The measured absorption coefficient as a function of wavelength for Rhodamine 6G dye dissolved in SU-8 at a concentration of 4.2×10^{-3} mol/L. 163

Figure 5.3 - Emission spectra from Rhodamine 6G dissolved in SU-8 at a concentration of 4.2×10^{-3} mol/L (a) The broadband fluorescence spectrum having a FWHM linewidth of 35 nm obtained from the sample when pumped at $F = 7.6 \text{ mJ/cm}^2$. (b) The emission spectrum for the sample pumped at $F = 114 \text{ mJ/cm}^2$, having a linewidth of 18.3 nm. 165

Figure 5.4 - Emission spectra from Rhodamine 6G dissolved in SU-8 with Al_2O_3 nanoparticles at $\ell = 200 \mu\text{m}$. (a) The broadband fluorescence spectrum having a FWHM linewidth of 32 nm obtained from the sample when pumped at $F = 7.6 \text{ mJ/cm}^2$. (b) The emission spectrum for the sample pumped at $F = 53 \text{ mJ/cm}^2$, having a linewidth of 15 nm. This spectrum indicates the onset of random lasing from the device. (c) The measured emission spectrum at $F = 114 \text{ mJ/cm}^2$, having a linewidth of 6.7 nm, indicating random lasing. 167

Figure 5.5 - Emission spectra from Rhodamine 6G dissolved in SU-8 with Ag nanoparticles at $\ell = 200 \mu\text{m}$. (a) The broadband fluorescence spectrum having a FWHM linewidth of 40 nm from the sample pumped at $F = 15 \text{ mJ/cm}^2$. (b) The emitted spectrum for the sample pumped at $F = 53 \text{ mJ/cm}^2$, having a linewidth of 9.9 nm. (c) The measured emission spectrum at $F = 114 \text{ mJ/cm}^2$, with a linewidth of 6 nm, indicating random lasing. 169

Figure 5.6 – Emission spectra from Rhodamine 6G dissolved in SU-8 with Ag nanoparticles at $\ell = 1000 \mu\text{m}$. (a) The broadband fluorescence spectrum having a FWHM linewidth of 36 nm from the sample pumped at $F = 7.6 \text{ mJ/cm}^2$. (b) The emitted spectrum for the sample pumped at

$F = 53 \text{ mJ/cm}^2$, having a linewidth of 30 nm. This indicates that the random gain media is still below the lasing threshold. (c) The measured emission spectrum at $F = 114 \text{ mJ/cm}^2$, indicating random lasing with a linewidth of 8.8 nm.

171

Figure 5.7 – The FWHM linewidth variation as a function of F from $F = 7.6 \text{ mJ/cm}^2$ to $F = 114 \text{ mJ/cm}^2$ for random gain media in SU-8 without any scatterers (◆), with Al_2O_3 scatterers at $\ell = 200 \text{ }\mu\text{m}$ (■), and with Ag scatterers at $\ell = 200 \text{ }\mu\text{m}$ (●) and $1000 \text{ }\mu\text{m}$ (▲).

173

Figure 5.8 - The relative peak intensity variation as a function of F from 7.6 mJ/cm^2 to 114 mJ/cm^2 for random gain media in SU-8 without any scatterers (◆), with Al_2O_3 scatterers at $\ell = 200 \text{ }\mu\text{m}$ (■), and with Ag scatterers at both $\ell = 200 \text{ }\mu\text{m}$ (●) and $1000 \text{ }\mu\text{m}$ (▲).

175

Figure 5.9 - Emission spectra from Rhodamine 6G dissolved in SU-8 at a concentration of $4.2 \times 10^{-3} \text{ mol/L}$. A cylindrical lens focuses the pump spot to a line 1 mm wide and 8 mm long. (a) The narrowband spectrum having a FWHM linewidth of 7 nm obtained from the sample when pumped at $F = 0.7 \text{ mJ/cm}^2$. (b) The emission spectrum for the sample pumped at $F = 11.1 \text{ mJ/cm}^2$, having a linewidth of 5.3 nm.

177

Figure 5.10 – The emission spectra from Rhodamine 6G dissolved in SU-8 with Al_2O_3 nanoparticles at $\ell = 200 \text{ }\mu\text{m}$. (a) The broadband fluorescence spectrum having a FWHM linewidth of 32 nm obtained from the sample when pumped at $F = 0.7 \text{ mJ/cm}^2$. (b) The emission spectrum for the sample pumped at $F = 6.7 \text{ mJ/cm}^2$. The linewidth at this pump fluence is 8 nm.

179

Figure 5.11 - Emission spectra obtained from Rhodamine 6G dissolved in SU-8 with Ag nanoparticles at $\ell = 200 \text{ }\mu\text{m}$. (a) The narrowband emission spectrum with a FWHM linewidth of 6 nm from the sample pumped at $F = 0.7 \text{ mJ/cm}^2$. (b) The emission spectrum for the sample pumped at $F = 11.1 \text{ mJ/cm}^2$, having a linewidth of 6 nm. Random lasing occurs at all studied input fluences.

181

Figure 5.12 - Emission spectra from Rhodamine 6G dissolved in SU-8 with Ag nanoparticles at $\ell = 1000 \text{ }\mu\text{m}$. (a) The broadband fluorescence spectrum having a FWHM linewidth of 32 nm from the sample pumped at $F = 0.7 \text{ mJ/cm}^2$. (b) The emitted spectrum for the sample pumped at $F = 2.2 \text{ mJ/cm}^2$, having a linewidth of 6 nm.

183

Figure 5.13 – Input pump energy fluence threshold graphed as a function of the length of the excitation line. The width of the excitation line is 1 mm in all cases. Each symbol represents a gain media with Al_2O_3 scatterers at

$\ell = 200 \mu\text{m}$ (■), with Ag scatterers at both $\ell = 200 \mu\text{m}$ (●) and $1000 \mu\text{m}$ (▲), and without any scattering particles (◆). 184

Figure 5.14 – Peak output intensity as a function of the length of the excitation line. The width of the excitation line is 1 mm in all cases. Each symbol represents a gain media with Al_2O_3 scatterers at $\ell = 200 \mu\text{m}$ (■), with Ag scatterers at both $\ell = 200 \mu\text{m}$ (●) and $1000 \mu\text{m}$ (▲), and without any scattering particles (◆). 187

Chapter 1: Thesis Outline

1.1 Thesis Motivation

The propagation of an electromagnetic wave through a disordered medium results in several phenomena such as diffusive light scattering in colloidal suspensions (paint, milk, and blood); ballistic photon transport in infrared biological imaging; and Anderson localization of light in very highly scattering media [1, 2]. The combination of multiple scattering with an optically amplifying media may cause the phenomenon known as random lasing. Unlike a conventional laser, a random laser is an optical device that does not produce a collimated beam of radiation, but instead emits isotropic laser-like light [3]. Such behaviour was first theoretically predicted by Letokhov in 1968, who proposed that the incorporation of strong successive scattering events into an optically amplifying media would result in spectrally narrow, spatially diffuse, intense stimulated laser-like light emission [4]. The fundamental characteristic of a random laser is that while a conventional laser sustains a lasing mode in a precisely aligned resonator cavity, a random laser relies on non-resonant optical feedback from multiple light scattering events to sustain an optical gain above threshold [4-8].

Laser-like light emission was first observed from a disordered gain media in 1986 by Markushev et al., who optically pumped a $\text{Na}_5\text{La}_{1-x}\text{Nd}_x(\text{MoO}_4)_4$ powder [9]. Following this initial work, N. M. Lawandy et al. demonstrated random laser operation from a suspension of 250 nm diameter TiO_2 scattering particles in Rhodamine 640 perchlorate dye [10]. Since these pioneering results, random lasers have been constructed from a variety of materials, such as optically amplifying powder, where scattering centres provide the optical gain [11], and liquid suspensions, where scattering centres are

suspended in a surrounding gain material [10]. Potential applications for these unique lasers include optical displays; biological identification; temperature sensors; inertial confinement fusion; security purposes; and tuneable narrowband coherent light sources [12-16].

1.2 Thesis Goal

The goal of this thesis is to investigate the use of metallic scattering particles in random laser systems. To achieve this goal, several random laser devices are constructed and tested. A numerical model is developed to investigate the role of scattering from novel particles in a random laser system.

1.3 Thesis Organization

This thesis consists of 6 chapters and one appendix to outline the experimental and theoretical work. This chapter, 1, contains an outline of the thesis. Chapter 2 describes the theoretical background necessary for an understanding of random laser devices. Chapter 3 provides a description of the theoretical model for the time-domain simulation of electromagnetic scattering and random lasers. Chapter 4 contains the results of experimental work on random lasers constructed using the suspension of scattering particles in a liquid laser dye. Chapter 5 describes results of experimental work on solid state random laser devices. The conclusions of the thesis are presented in chapter 6. Appendix A contains the program code for the theoretical model described in chapter 3.

1.4 References

- [1] D. Wiersma, and A. Lagendijk, “Laser Action in Very White Paint,” *Physics World*, 33 (Jan. 1997).
- [2] D. Wiersma, P. Bartolini, A. Lagendijk, and R. Righini, “Localization of light in a disordered medium,” *Nature*, **390**, 671 (1997).
- [3] D. Wiersma, “The smallest random laser,” *Nature*, **406**, 132 (2000).
- [4] V. S. Letokhov, “Generation of light by a scattering medium with negative resonance absorption,” *Sov. Phys. JETP*, **26**, 835 (1968).
- [5] D. S. Wiersma and A. Lagendijk, “Light diffusion with gain and random lasers,” *Phys. Rev. E*, **54**, 4256-4265 (1996).
- [6] S. John and G. Pang, “Theory of lasing in a multiple-scattering medium,” *Phys. Rev. A*, **54**, 3642-3652 (1996).
- [7] L. Florescu, and S. John, “Photon Statistics and Coherence in Light Emission from a Random Laser,” *Phys. Rev. Lett.*, **93**, 013602 (2004).
- [8] A. L. Burin, H. Cao, and M. Ratner, “Understanding and control of random lasing,” *Physica B*, **338**, 212 (2003).
- [9] V. M. Markushev, V. F. Zolin, and Ch. M. Briskina, “Luminescence and induced emission from neodymium in powders of double sodium-lanthanum molybdate,” *Sov. J. Quantum Electron.*, **16**, 281-283 (1986)
- [10] N. M. Lawandy, R. M. Balachandran, A. S. L. Gomes, and E. Sauvain, “Laser action in strongly scattering media,” *Nature* **368**, 436-438 (1994).

- [11] H. Cao, Y. G. Zhao, S. T. Ho, E. W. Seelig, Q. H. Wang, and R. P. H. Chang, "Random laser action in semiconductor powder," *Phys. Rev. Lett.*, **82**, 2278-2281 (1999).
- [12] H. Cao, J. Y. Xu, E. W. Seelig, and R. P. H. Chang, "Microlaser made of disordered media," *Appl. Phys. Lett.*, **76**, 2997-2999 (2000).
- [13] D. S. Wiersma, and S. Cavaleri, "Light emission: A temperature-tunable random laser," *Nature*, **414**, 708 (2001).
- [14] D. S. Wiersma, and S. Cavaleri, "Temperature-controlled random laser action in liquid crystal infiltrated systems," *Phys. Rev. E*, **66**, 056612 (2002).
- [15] C. Gouedard, D. Husson, C. Sauteret, F. Auzel, and A. Migus, "Generation of spatially incoherent short pulses in laser-pumped neodymium stoichiometric crystals and powders," *J. Opt. Soc. Am. B*, **10**, 2362 (1993).
- [16] R. M. Balachandran, D. P. Pacheco, N. M. Lawandy, "Photonic Textile Fibers," *Appl. Opt.*, **35**, 1991-1994 (1996).

Chapter 2: Introduction

2.1 Light Scattering

2.1.1 Single Scattering

In a medium, a scattering centre occurs wherever a particle has a refractive index contrast with the surrounding medium. When an incident electromagnetic wave interacts with a scattering centre, conduction band electrons absorb a fraction of the incident radiation, while the re-radiated emission is scattered around the particle [1]. For many scattering particles the cross-sectional area that interacts with incident radiation is not equal to the physical cross-sectional area of the particle. For a metal particle, the electric field lines are curved towards the conducting surface in a region much larger than the physical size of the particle. The factors that determine the scattering cross-section of a scattering particle include the magnitude of the difference in refractive index between the particle and the surrounding medium, as well as the size and shape of the scatterer [2]. For scatterers that are much smaller than the incident light wavelength, having $a \ll 0.05\lambda$, where a is the particle diameter and λ is the incident wavelength, the quasistatic approximation holds. This approximation assumes that the particle is small enough that the phase of electromagnetic radiation is constant across the particle.

The theoretical investigation of single scattering events involves the determination of the optical cross-sections of a scattering particle which is effective the interaction area surrounding the particle, where incident light will be absorbed or scattered by the particle. The three optical cross-sections that characterize light scattering from a single particle are the extinction (σ_{ext}), absorption (σ_{abs}), and scattering cross-sections (σ_{sca}). In the field of light scattering, extinction is defined as the amount of light

prevented from reaching a detector, placed on the opposite side of a scattering particle, by either scattering or absorption [1]. Since light extinction is the combination of scattered and absorbed light, the extinction cross-section of a particle is defined as its interaction area that either absorbs light or scatters it away from a detector:

$$\sigma_{ext} = \sigma_{sca} + \sigma_{abs} . \quad (2.1)$$

The extinction (Q_{ext}), scattering (Q_{sca}) and absorption (Q_{abs}) efficiencies are dimensionless quantities relating the physical cross-sectional area of the scattering particle, A , to the respective optical cross-sectional area through:

$$Q_{ext} = \sigma_{ext} / A , \quad (2.2)$$

$$Q_{sca} = \sigma_{sca} / A , \quad (2.3)$$

and

$$Q_{abs} = \sigma_{abs} / A . \quad (2.4)$$

The relationship between the incident wavelength and the scattering particle size is quantified as the size parameter, x :

$$x = ka = 2\pi na / \lambda , \quad (2.5)$$

where k is the wave number inside the particle, a is the radius of the particle, n is the particle's refractive index, and λ is the incident wavelength outside the particle. Another important parameter in such context is the refractive index contrast, m , between the particle and the surrounding medium which is given by:

$$m = n_1 / n , \quad (2.6)$$

where n_1 is the refractive index of the particle, and n is the refractive index of the surrounding medium.

2.1.2 Rayleigh Scattering

For scattering particles where the particle size is much smaller than the wavelength (size parameter $x \ll 1$), numerical values of Q_{ext} , Q_{sca} , and Q_{abs} are obtained from Rayleigh scattering theory. This theory assumes the scatterer to be a dipole surrounded by a homogeneous medium. For a scattering particle, the relative permittivity describes the ability of the material to store electric charge:

$$\epsilon_r = \epsilon_r' + i\epsilon_r'' , \quad (2.7)$$

where ϵ_r' is the real part of the permittivity, and ϵ_r'' is the imaginary part of the permittivity. For metals, the variability in the permittivity as a function of wavelength, can be particularly large. Silver, for example, has a relative permittivity of $0.2 + i3.2$ at $\lambda = 200$ nm, compared to $-50.9 + i3.9$ at $\lambda = 1000$ nm. Given a spherical metallic particle with a diameter of $a < 0.05\lambda$, the ease with which an incident electromagnetic field will polarize the scattering dipole is the polarizability, α :

$$\alpha = \epsilon_0 3V \frac{\epsilon_r - 1}{\epsilon_r + 2} , \quad (2.8)$$

where V is the volume of the particle and ϵ_r is its relative permittivity. Given α the scattering and absorption cross-sections are calculated via [1]:

$$\sigma_{sca} = \frac{k^4}{6\pi} \left| \frac{\alpha}{\epsilon_0} \right|^2 = \frac{k^4}{6\pi} (3V)^2 \frac{(\epsilon_r' - 1)^2 + \epsilon_r''^2}{(2 + \epsilon_r')^2 + \epsilon_r''^2} , \quad (2.9)$$

and

$$\sigma_{abs} = k \Im \left| \frac{\alpha}{\epsilon_0} \right|^2 = k 3V \frac{3\epsilon_r''}{(2 + \epsilon_r')^2 + \epsilon_r''^2} . \quad (2.10)$$

It should be noted from equations 2.9 and 2.10 that σ_{abs} and σ_{sca} experience a resonant increase whenever $\epsilon'_r = -2$. This occurs when the incident radiation is at the surface plasmon frequency, ω_{sp} , and is known as the particle plasmon resonance. This frequency ω_{sp} is equal to $\omega_{sp} = \omega_p / \sqrt{3}$ for spherical metal particles [1]. Figure 2.1 depicts the values of σ_{sca} and σ_{abs} calculated by Rayleigh theory as a function of wavelength for a spherical silver nanoparticle with a 5 nm diameter. As illustrated, there is a resonant peak in the σ_{sca} and σ_{abs} curves at $\lambda = 355$ nm. Note that the scattering cross-section increases as a function of λ^4 , which is expected for Rayleigh scattering [1].

2.1.3 Mie Scattering Theory

For scattering particles where the size parameter is not much smaller than one, Rayleigh scattering fails to provide an accurate approximation of σ_{sca} and σ_{abs} . For such particles, Maxwell's equations are rigorously solved to calculate the optical cross-sections. Mie theory allows the calculation of σ_{ext} , σ_{sca} and σ_{abs} for a homogeneous spherical particle embedded in an infinitely uniform medium. This theory was first developed in 1908 by Gustav Mie to investigate the colours of light scattered in a colloidal suspension of gold particles in water [1]. The calculation begins with the definition of a plane wave in terms of its vector spherical harmonics, to take advantage of the assumed spherical symmetry of the scattering particle. The scattered field outside and inside of the spherical scatterer are then determined through a solution of the Ricatti-Bessel functions, $\psi_n(\rho)$ and $\xi_n(\rho)$:

$$\psi_n(\rho) = \rho j_n(\rho), \quad (2.11)$$

$$\xi_n(\rho) = \rho h_n^{(1)}(\rho), \quad (2.12)$$

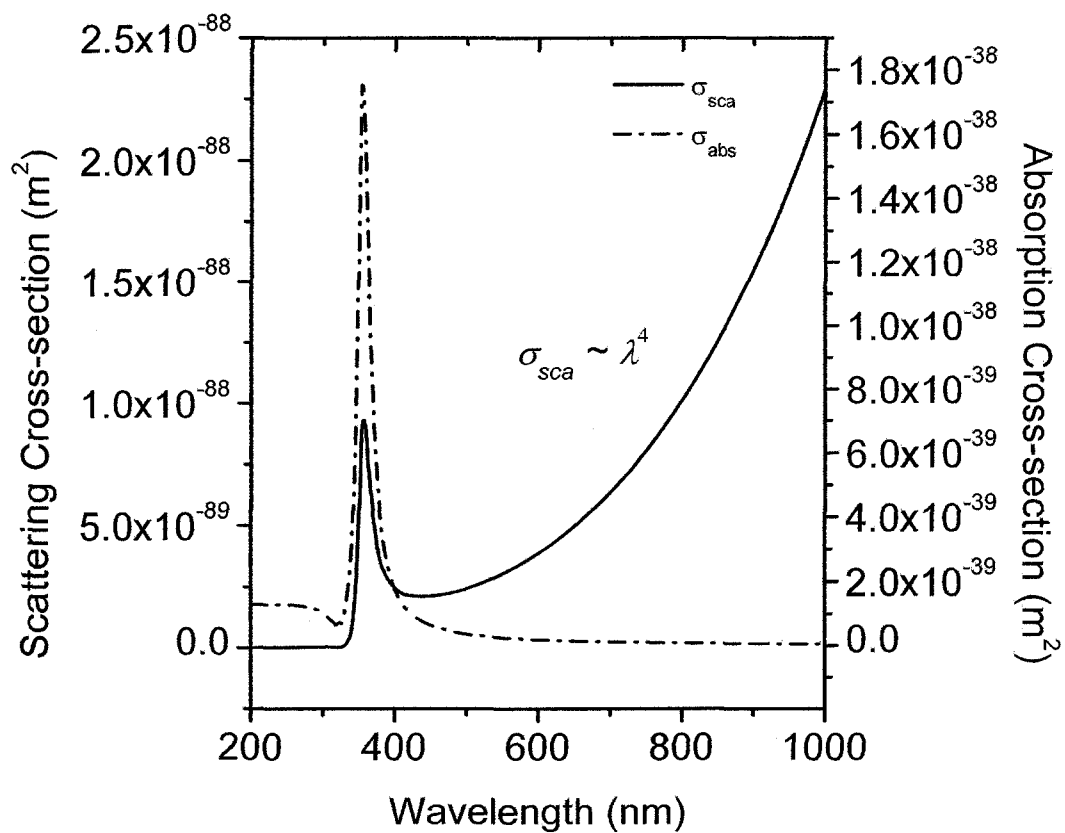


Figure 2.1 – Scattering (σ_{sca}) and absorption (σ_{abs}) cross-sections calculated from Rayleigh theory for a spherical silver nanoparticle with a 5 nm diameter.

where j_n and $h_n^{(1)}$ are spherical Bessel functions of the first kind and third kind, and ρ is a numerical index. The scattering coefficients a_n and b_n are then calculated:

$$a_n = \frac{m\psi_n(mx)\psi_n'(x) - \psi_n(x)\psi_n'(mx)}{m\psi_n(mx)\xi_n'(x) - \xi_n(x)\psi_n'(mx)}, \quad (2.13)$$

$$b_n = \frac{\psi_n(mx)\psi_n'(x) - m\psi_n(x)\psi_n'(mx)}{\psi_n(mx)\xi_n'(x) - m\xi_n(x)\psi_n'(mx)}, \quad (2.14)$$

where x is the particle size parameter and m is the refractive index contrast. The values of a_n and b_n are related to σ_{sca} and σ_{ext} through:

$$\sigma_{sca} = \frac{2\pi}{k^2} \sum_{n=1}^{\infty} (2n+1) (|a_n|^2 + |b_n|^2), \quad (2.15)$$

$$\sigma_{ext} = \frac{2\pi}{k^2} \sum_{n=1}^{\infty} (2n+1) \text{Re}\{a_n + b_n\}, \quad (2.16)$$

for spherical particles of arbitrary size and material composition.

2.1.4 Multiple Scattering

Light that escapes from a highly scattering medium after experiencing multiple scattering events appears as a diffuse glow. This arises because of the randomization of the phase of scattered radiation after several scattering events. A fundamental parameter of a disordered medium is the mean distance that light travels before interacting with a scattering centre. This quantity is the optical mean free path, ℓ . The mean free path is determined by both the volume concentration and the scattering cross-section of particles in the disordered media:

$$\ell = \frac{1}{\sigma_{sca} N}, \quad (2.17)$$

where N is the number density of scattering particles and σ_{scat} is the scattering cross-section of the scattering particles. Assuming no absorption of light within the sample, the characteristic length scale for diffusive transport is the length of the sample L . For a disordered media where $\ell \ll L$ a photon is likely to experience multiple scattering events and be temporarily trapped within the media [3]. In samples where $L/\ell > 10$, numerous scattering events occur, and the use of the diffusion approximation to describe light scattering in such media is adequate [4]. Photon transport through such a multiply scattering media is characterized as a random walk where the incident photon is redirected randomly along a new path through interaction with a scattering centre.

2.2 Random Lasers

A laser device requires both an optical gain material and a method to extract energy from the gain material. An optical gain material provides amplification through the stimulated emission of photons arising from transitions from a metastable energy level N_2 to a lower energy level N_1 . A population inversion is developed between N_2 and N_1 by exciting the laser material with an energy source such as a flashlamp, laser radiation, or an electrical source. Energy is typically extracted from the gain material through the use of a resonant cavity that provides feedback amplification to overcome the total optical losses of the laser. In an optical resonator cavity, scattered light does not propagate in the correct mode, and therefore does not contribute to lasing. Light may also be temporarily trapped in a gain media to maximize the emission [3]. A laser without a resonant cavity relies on sustaining sufficient optical gain such that a single traversal by emitted light results in amplification above the lasing threshold. This can be accomplished through the use of

multiple elastic scattering events to increase the optical path length of emitted light. Such a scattering optical gain media is known as a random laser.

2.2.1 *Single Material Random Lasers*

The use of a material that provides both optical gain and optical scattering allows the construction of a random laser from a single material. A schematic description of this type of random laser is depicted in Figure 2.2 (a), which illustrates a collection of scattering particles that provide optical gain, surrounded by an optically inactive medium. Amplification of the spontaneously emitted radiation at each scattering interaction leads to intense, spectrally narrow light emission from the random gain media. Random lasers of this type are typically constructed from powdered optically active crystals such as Ce^{3+} or Pr^{3+} doped Al_2O_3 [5], doped neodymium powders [6, 7], crushed titanium sapphire [8], or from ZnO [9, 10]. ZnO nano-clusters are particularly attractive, as they are highly scattering, having a refractive index of $n_{\text{ZnO}} \cong 2$ [11], and are also highly amplifying with a gain cross-section of 100 cm^{-1} at ultraviolet wavelengths [10]. Clusters of nanometre sized ZnO crystals are precipitated to form micro-clusters of up to 2×10^4 ZnO particles. Both pump light at $\lambda = 266 \text{ nm}$ and the emitted fluorescence at $\lambda = 380 \text{ nm}$ are scattered throughout the ensemble [12]. Amplification occurs as the emitted light is recurrently scattered throughout the cluster of ZnO nanoparticle cluster. The result is a series of narrowband emission spikes with a full width at half maximum (FWHM) linewidth of $\sim 0.12 \text{ nm}$ [12].

However, in such a random gain media it is difficult to control the scattering strength independently of the optical gain volume, as the scattering strength cannot be

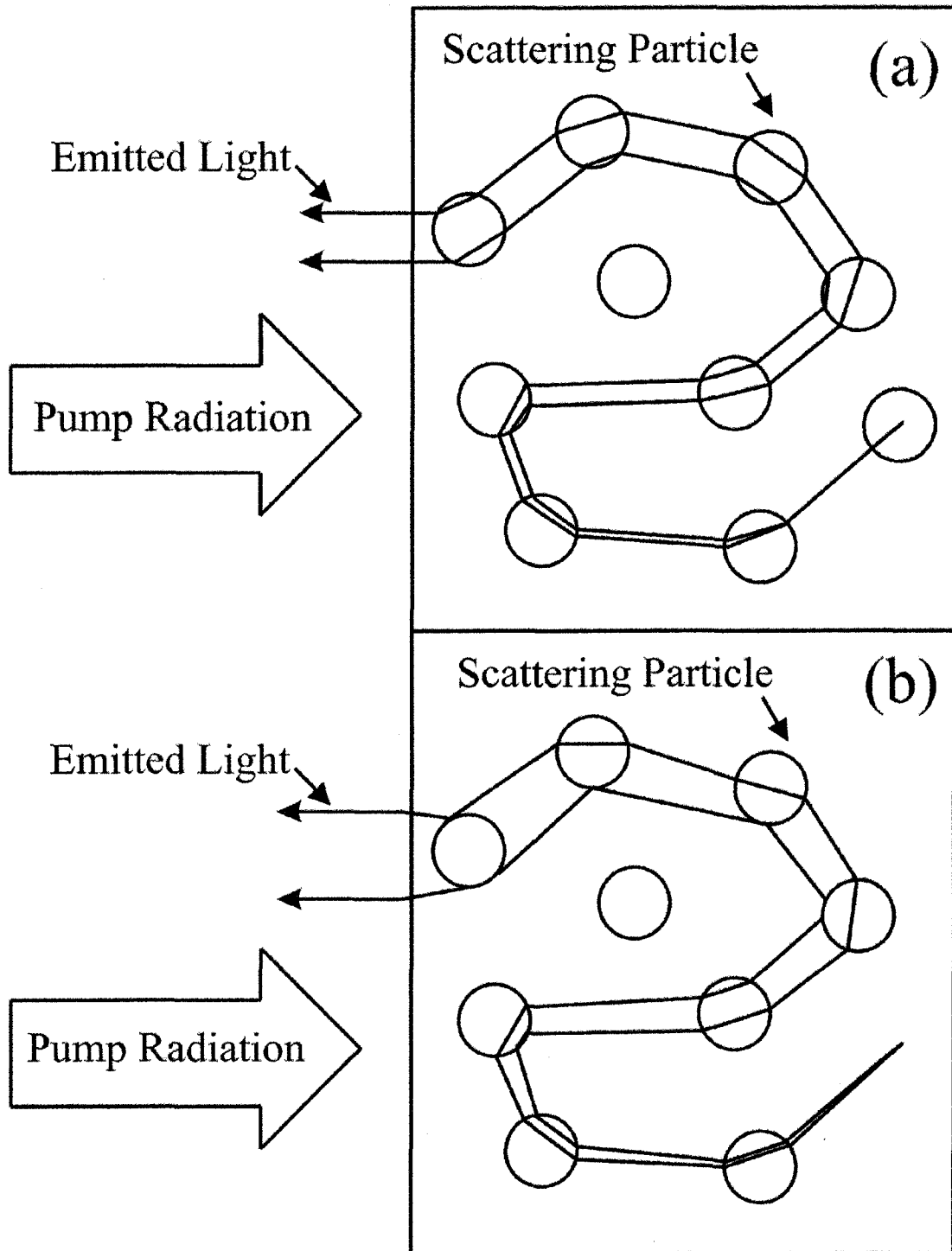


Figure 2.2 – (a) Schematic depiction of random laser operation for a collection of scattering particles that provide optical gain. All optical amplification occurs inside the scattering particles. (b) Schematic depiction of random laser operation for separate scattering particles surrounded by the gain media. Optical amplification occurs outside the scattering particles. For both, the pump radiation enters from the left, and observed emitted radiation exits to the left.

modified without also changing the volume of available gain material. In order to alter ℓ , either the physical size of the particles or the physical separation between particles must be changed, which also alters the volume of the active gain region in turn. However, it is possible to change ℓ by adding a filler material to create the required refractive index contrast with the particles. This allows ℓ to be controlled at a constant gain volume.

2.2.2 *Random Lasers with Scatterers Suspended in Liquid Dyes*

To construct a random laser there must be many scattering particles suspended in an optical gain material. For such a gain media, the active gain volume is the entire spatial volume not occupied by scattering particles. When the gain material and scattering centres are separated, the effects of scattering and gain can be investigated separately, providing greater control over random laser optimization [13]. A schematic description of the random lasing process in a dye-scatterer based random laser is shown in Figure 2.2 (b). Here, spontaneously emitted fluorescence is recurrently scattered throughout the gain media by interaction with optically inactive scatterers. In order for the random gain media to exceed the lasing threshold, the active gain material must provide sufficient gain over the length of the scattered path to overcome total optical losses. The available gain volume, V_g , must thus be greater than the critical volume, V_{cr} :

$$V_{cr} = \left(\frac{\ell \ell_g}{3} \right)^{3/2}, \quad (2.18)$$

where ℓ_g is the path length in the laser dye over which light is amplified by a factor of e^{+1} [14, 15].

Since the first demonstration of a dye-scatterer random laser formed from the suspension of 250 nm diameter TiO_2 scattering particles in Rhodamine 640 perchlorate dye by Lawandy et al. [16], many alternative laser dye infiltrated materials have been investigated. A dye-scatterer based random laser has been developed from the suspension of 100 nm diameter ZnO particles in Rhodamine 640 dye [17], where the semiconductor particles were used solely for their scattering properties. Other dye-scatterer based random lasers with dielectric scattering particles include a colloid comprised of IR-26 laser dye and 300 nm diameter Al_2O_3 particles [18]. An alternative arrangement using a sintered glass powder infiltrated with a solution of Lambdachrome 6500 laser dye dissolved in a liquid crystal (7CB), provided a temperature-dependent scattering gain medium. Here the physical state, either the birefringent nematic phase or the isotropic liquid phase, determined the scattering strength and the lasing threshold as a function of temperature [19, 20].

Random lasing has also been achieved through the use of polymer-dispersed liquid crystals that provide tunability as a function of both temperature and applied electric field [21]. More recently, random lasing has been demonstrated in Rhodamine 6G infiltrated human colon tissue [22]. Each of these material combinations provides the required constituents of a random laser: an ensemble of highly scattering particles surrounded by an optical gain media.

2.2.3 Coherent and Incoherent Random Lasing

For both solid powder and dye-scatterer based random lasers, the emission spectrum can be classified as arising from either coherent or incoherent feedback mechanisms. For a

random laser that operates in a scattering regime where diffusive incoherent non-resonant feedback is prominent, the emission consists of a single spectral line with a bandwidth of a few nanometres [16, 23]. For suspensions of scattering particles in liquid dyes, such incoherent random lasing has been demonstrated from: 250 nm diameter TiO₂ scattering particles in Rhodamine 640 perchlorate dye [16]; a colloid comprised of IR-26 laser dye and 300 nm diameter Al₂O₃ particles [18]; and other dye-scatterer random lasers [16, 23]. In contrast, a scattering regime having sufficient strength for closed optical feedback loops results in coherent feedback that produces a series of spectrally narrow lines with sub-nanometre linewidth [9, 12, 24]. Coherent random lasing has been demonstrated via scattering from 100 nm diameter ZnO particles suspended in Rhodamine 640 dye [17]. More recently, coherent random lasing has been demonstrated in Rhodamine 6G infiltrated human colon tissue, where additional distinct spectral lines are attributed to cancerous tissues [22]. A third feedback mechanism resulting in a similar series of sub-nanometre linewidth spectral lines involves the statistical probability that a single photon will travel an extremely long optical path and thereby experience preferential amplification at a single wavelength. A single photon that travels a sufficiently long random walk will experience an exponential gain, and come to dominate the emission from a random media that is not in the localization regime [25]. Whether the light emission from a random gain media takes the form of the sub-nanometre linewidth spikes of coherent random lasing, or the single ~ 5 nm wide peak of incoherent random lasing is determined by the mean free path, the temporal length of the pump pulse, and the input pump energy fluence. For 100 nm diameter ZnO particles suspended in a solution of 5×10^{-3} mol/L Rhodamine 640 perchlorate dissolved in methanol, the critical mean free path

is found to be $\ell = 3 \mu\text{m}$ with a critical pump energy is $1.0 \mu\text{J}$. For this material combination, incoherent random lasing occurs for pump energies of less than $1.0 \mu\text{J}$ for $\ell = 3 \mu\text{m}$, and at all investigated energies for $\ell = 9 \mu\text{m}$ [17]. Additionally, experiments on either TiO_2 or ZnO particles suspended in either Sulforhodamine B or Rhodamine 640 B dissolved in methanol indicate that sub-nanometre peaks only appear when the random gain media is pumped by a picosecond laser pulse. Nanosecond pump pulses produce a spectrum characteristic of incoherent random lasing. Thus, an incoherent random laser may actually produce coherent sub-nanometre peaks, but these are washed out by averaging over long pump pulses [26].

2.2.4 Scattering Effects in Random Lasers

A typical random laser scatters light at dielectric particle boundaries to create the optical feedback required for laser emission. For the general case of dye dielectric scatterer based random lasers, multiple scattering increases the optical path length, and results in the development of intense quasi-monochromatic light emission. This emission depends on several factors, including the active pump light-induced optical gain volume, the scattering strength of the dielectric particle, and the local optical gain. Ideally, each of these parameters is independently optimized to maximize the random laser output. While random lasers consisting of scattering particles surrounded by a gain medium allow such optimization, the active gain volume depends on a number of factors, such as the scattering strength of the medium and the physical size of the scattering particles. As the scattering strength increases, the probability that light is prematurely backscattered out of the active gain region increases. In order to maximize the gain volume, it is necessary to

find the optimum combination of scattering materials and gain media to provide the greatest optical gain, while minimizing total optical losses [14].

For a gain medium with mean free path ℓ the scattering strength is determined by L/ℓ , where L is the characteristic linear dimension of the random media. A typical gain media will have an absorption length for emitted light ℓ_a that is much greater than the absorption length for pump light. When $\ell_a < \ell$, the absorption length is too small to allow for diffusive scattering of emitted light within the active gain region. Laser photons that are emitted within the active gain region travel a path where they are amplified until they escape the gain region. For an excitation beam with a diameter that is large compared to the absorption length of pump light, and large compared to the absorption length of emitted light, there is a high probability that these escaping photons will revisit the active gain region. These photons are then amplified further before they escape from the gain region as the process repeats. Thus, both the diffusion length of pump photons and the probability of scattering back into the active gain region, influence the photon residence time [27]. When ℓ_a is shorter than both the diameter of the pump laser focal spot and the physical length of the medium, the characteristic dimension L of the random gain media is taken to be equal to ℓ_a . For Rhodamine 6G laser dye at a concentration of 10^{-3} mol/L, emitted light has $\ell_a = 1.6$ mm and 40 μm at $\lambda_{laser} = 564$ nm and $\lambda_{pump} = 532$ nm, respectively. Thus, a photon that is emitted within the active gain volume is likely to escape into the surrounding, non-amplifying random media. For a scattering strength of $L/\ell > 10$ photons emitted within the active gain volume experience multiple scattering events, and can return to the active gain region for further

amplification. For a random gain media in the modestly scattering regime, which is defined as $1 \leq L/\ell \leq 10$, photons emitted within the active gain volume experience multiple scattering events and can return to the active gain region for further amplification [6]. In contrast, when $L \ll \ell$, light scattering events are relatively rare, and there is insufficient non-resonant optical feedback to support random lasing. The lack of optical feedback in such a weakly scattering gain medium necessitates large optical gain accompanying each scattering event to compensate for small sojourn time within the gain medium [28].

2.3 Surface Plasmon Resonance

The phenomena resulting from light interaction and scattering from sub-wavelength size metallic particles are fundamentally distinct from those resulting from similarly sized dielectric particles. For a bulk metal or a thin metal film, a surface plasmon (SP) oscillation can be excited as an evanescent wave that propagates along the surface of the metal as long as the real part of the permittivity is negative [29]. The dispersion equation for a surface plasmon is shown in equation 2.19:

$$k_{sp} = k_0 \sqrt{\frac{\epsilon_1(\omega)\epsilon_2(\omega)}{\epsilon_1(\omega) + \epsilon_2(\omega)}} \quad 2.19$$

Here, the k_{sp} is the wave vector of the surface plasmon, k_0 is the wave vector of incident light, and $\epsilon_1(\omega)$ and $\epsilon_2(\omega)$ are the respective frequency dependent dielectric functions of the metal and the dielectric. For a typical metal k_{sp} is slightly larger k_0 indicating that the momentum of the surface plasmon is greater than the exciting photon in free space [30]. To couple incident radiation into the surface plasmon mode it is necessary to compensate

for the difference in momentum between the surface plasmon and the incident exciting photon. Such coupling is typically accomplished through the use of either prism or Kretschmann coupling, or via a diffraction grating on the metal surface. Additionally, a metallic sub-wavelength sized particle can sustain a collective oscillation of conduction band electrons that is known as a particle surface plasmon without the use of any specialized optical coupling geometries [1, 31]. Due to the resonant SP response, which is greatest for sub-wavelength sized metallic particles, σ_{sca} , σ_{abs} , and σ_{ext} are greatly enhanced near the resonant wavelength [32]. For sub-wavelength sized metal spheres where the quasistatic approximation applies, electromagnetic radiation is resonantly absorbed where the negative real part of the permittivity is $\epsilon_r = -2$ [1, 31, 32]. For particles larger than the incident wavelength, the momentum coupling criteria is not met, and localized surface plasmons are not excited in the particle [33].

The difference between Q_{sca} for a metal particle and Q_{sca} for a dielectric particle of similar dimensions can be seen in Figure 2.3. Note that there are significant differences between Q_{sca} for a 100 nm diameter Ag sphere and for a 100 nm Al₂O₃ sphere. Considering the 100 nm diameter Ag nanosphere at the peak of the plasmon resonance curve, $\lambda = 400$ nm, one calculates that $Q_{sca} = 5.0$, compared to $Q_{sca} = 0.2$ for the 100 nm diameter Al₂O₃ sphere at the same wavelength. Clearly, for the same spherical size in the visible wavelength range, the scattering efficiency of the metal particle is up to 25 times greater than the dielectric particle at the peak of the SP curve. The magnitude and peak wavelength of the plasmon resonance curve of a sub-wavelength sized metallic nanoparticle is highly influenced by the shape of the particle [34]. As an example, a redshift of the SP peak was measured for an 80 nm diameter Ag sphere from

$\lambda = 450 \text{ nm}$ to $\lambda = 650 \text{ nm}$ for a silver triangular prism with 80 nm long sides [34]. In addition to enhanced scattering, SP resonance from radiation coupled into a silver nanoparticle results in the localization of the electromagnetic field near the particle's surface [32].

2.3.1 Metallic Particles in Random Lasers

It is possible to construct a novel random laser utilizing SP enhancement incorporating metal spheres as strong scatterers. When a metallic particle is suspended in a laser dye, field enhancement of the pump's electric field increases the energy fluence in the region surrounding the particle relative to the rest of the medium. Both the spontaneous emission rate and the optical gain are increased in the dye region surrounding the particle. This increased gain is accessed by co-localization of the pump light and laser emission, whose wavelengths fall within the SP resonance bandwidth. A spontaneously emitted photon that is scattered from the particle traverses this gain region and experiences large optical amplification. It is expected that improved performance in terms of a smaller FWHM emission linewidth, and a reduced input energy fluence threshold for lasing is obtained by exploiting this unique property of metal nanoparticles [35].

2.3.2 Surface Enhanced Raman Scattering

Raman scattering is an inelastic scattering process from a molecule that results in scattered photons which have a wavelength shift that corresponds to the vibrational energy levels of the scattering molecule. Typical Raman scattering cross-sections are fourteen orders of magnitude smaller than the absorption cross-section of a dye molecule

[36]. However, near the surface of rough metallic surfaces or metallic nanoparticles, there is an enhancement of the Raman scattering by a factor of $10^6 - 10^9$. This effect is known as surface enhanced Raman scattering (SERS), and arises due to the combination of electromagnetic field enhancement caused by surface plasmon resonances in the metal nanoparticles, and a chemical interaction between the scattering molecule and the particle surface. Typically, the SP enhancement is on the order of $10^6 - 10^7$ for a single gold or silver spheroidal nanoparticle, while the chemical effect further increases the enhancement factor by a factor of $10 - 10^2$. When two spheroidal nanoparticles are very close to each other (~ 1 nm spacing), hotspots develop where the SERS electromagnetic enhancement factor can reach 10^{12} [37]. When the chemical effect is included, total enhancement factors of 10^{14} have been observed. As the SERS enhancement factor from SP resonance increases with the fourth power of the local field surrounding the metallic nanostructure, and decreases with the twelfth power of the distance to the surface, it is much stronger for molecules adsorbed on the particle surface at wavelengths near the particle plasmon resonance [37].

For a fluorescent dye with a quantum efficiency (QE) close to one, such as Rhodamine 6G (QE ~ 0.95), fluorescence quenching occurs for dye molecules within ~ 40 Å of the surface of a silver nanoparticle [38]. At a QE close to one, the enhancement of the QE from the SP enhanced EM field is counteracted by the non-radiative decay channels that arise due to the SP resonance in the nanoparticle [39]. However, as the quenching effect decreases faster with the distance between the dye molecule and the particle surface than the SP field enhancement decreases with distance, overall fluorescence enhancement is observed for thick coatings of Rhodamine 6G [37, 39], or

Rhodamine B [40]. Thus, it is expected that for the case of silver scattering particles suspended in a dye solution, the fluorescence quenching of adsorbed dye molecules will act to reduce the total SP enhancement available from any given silver nanoparticle.

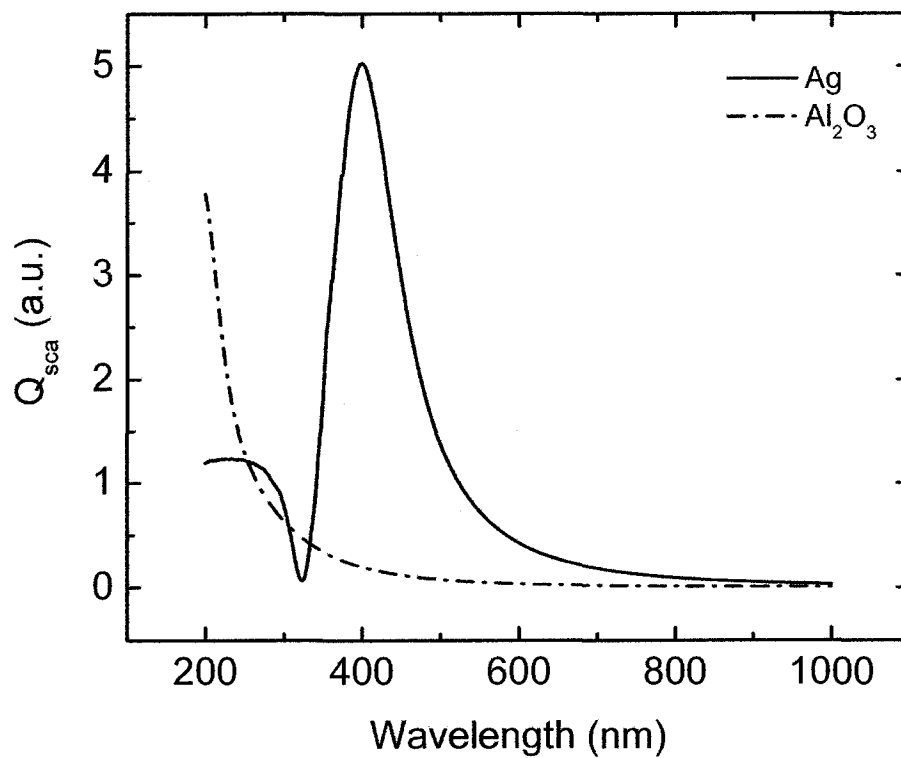


Figure 2.3 – Comparison of Q_{sca} for a 100 nm diameter Ag sphere (solid line) to a 100 nm diameter Al_2O_3 sphere (dot-dashed line).

2.4 References

- [1] C. Bohren and D. Huffman, *Absorption and Scattering of Light by Small Particles*, (Wiley, New York, 1983).
- [2] D. Wiersma, and A. Lagendijk, "Laser Action in Very White Paint," *Physics World*, 33 (Jan. 1997).
- [3] D. Wiersma, "The smallest random laser," *Nature*, **406**, 132 (2000).
- [4] K. M. Yoo, F. Liu, and R. R. Alfano, "When does the diffusion approximation fail to describe photon transport in random media," *Phys. Rev. Lett.*, **64**, 2647-1650 (1990).
- [5] G. R. Williams, S. B. Bayram, and S. C. Rand, "Laser action in strongly scattering rare-earth-metal-doped dielectric nanophosphors," *Phys. Rev. A*, **65**, 013807 (2001).
- [6] M. Bahoura, K. J. Morris, and M. A. Noginov "Threshold and slope efficiency of $\text{Nd}_{0.5}\text{La}_{0.5}\text{Al}_3(\text{BO}_3)_4$ ceramic random laser: effect of the pumped spot size," *Opt. Comm.*, **201**, 405 (2002).
- [7] M. A. Noginov, N. E. Noginova, H. J. Caulfield, P. Venkateswarlu, T. Thompson, M. Mahdi, and V. Ostroumov, "Short-pulsed stimulated emission in the powders of $\text{NdAl}_3(\text{BO}_3)_4$, $\text{NdSc}_3(\text{BO}_3)_4$, and $\text{Nd}:\text{Sr}_5(\text{PO}_4)_3\text{F}$ laser crystals," *J. Opt. Soc. Am. B*, **13**, 2024 (1996).
- [8] M. A. Noginov, N. Noginova, S. U. Egarievwe, H. J. Caulfield, C. Cochrane, J. C. Wang, M. R. Kokta, J. Paitz, "Study of the pumping regimes in Ti-sapphire and $\text{Nd}_{0.5}\text{La}_{0.5}\text{Al}_3(\text{BO}_3)_4$ powders," *Opt. Mater.*, **10**, 297-303 (1998).

- [9] H. Cao, Y. G. Zhao, S. T. Ho, E. W. Seelig, Q. H. Wang, and R. P. H. Chang, "Random laser action in semiconductor powder," *Phys. Rev. Lett.*, **82**, 2278-2281 (1999).
- [10] H. Cao, Y. G. Zhao, H. C. Ong, S. T. Ho, J. Y. Dai, J. Y. Wu, and R. P. H. Chang, "Ultraviolet lasing in resonators formed by scattering in semiconductor polycrystalline films," *Appl. Phys. Lett.*, **73**, 3656-3658 (1998).
- [11] M. J. Weber, *CRC Handbook of Optical Materials*, (Boca Raton, CRC Press, 2003).
- [12] H. Cao, J. Y. Xu, E. W. Seelig, R. P. H. Chang, "Microlaser made of disordered media," *Appl. Phys. Lett.*, **76**, 2997-2999 (2000).
- [13] M. Siddique, R. R. Alfano, G. A. Berger, M. Kempe, and A. Z. Genack, "Time-resolved studies of stimulated emission from colloidal dye solutions," *Opt. Lett.*, **21**, 450-452 (1996).
- [14] D. S. Wiersma and A. Lagendijk, "Light diffusion with gain and random lasers," *Phys. Rev. E*, **54**, 4256-4265 (1996).
- [15] H. Cao, "Lasing in random media," *Waves Random Media*, **13**, R1-R39 (2003).
- [16] N. M. Lawandy, R. M. Balachandran, A. S. L. Gomes, and E. Sauvain, "Laser action in strongly scattering media," *Nature*, **368**, 436-438 (1994).
- [17] H. Cao, J. Y. Xu, S. H. Chang, and S. T. Ho, "Transition from amplified spontaneous emission to laser action in strongly scattering media," *Phys. Rev. E*, **61**, 1985-1989 (2000)
- [18] J. Pinto, L. Esterowitz, and B. Feldman, "Novel optically pumped narrowband emitting polymeric materials," *Proc. SPIE*, **3265**, 130-134 (1998).

- [19] D. S. Wiersma, and S. Cavaliere, "Light emission: A temperature-tunable random laser," *Nature*, **414**, 708 (2001).
- [20] D. S. Wiersma and S. Cavaliere, "Temperature-controlled random laser action in liquid crystal infiltrated systems," *Phys. Rev. E*, **66**, 056612 (2002).
- [21] S. Gottardo, S. Cavaliere, O. Yaroshchuk, and D. S. Wiersma, "Quasi-two-dimensional diffusive random laser action," *Phys. Rev. Lett.*, **93**, 263901 (2004).
- [22] R. C. Polson, and Z. V. Vardeny, "Random lasing in human tissues," *Appl. Phys. Lett.*, **85**, 1289-1291 (2004).
- [23] R. M. Balachandran, D. P. Pacheco, and N. M. Lawandy, "Laser action in polymeric gain media containing scattering particles," *App. Opt.*, **35**, 640-643 (1996).
- [24] R. C. Polson, and Z. V. Vardeny, "Organic random lasers in the weak-scattering regime," *Phys. Rev. B*, **71**, 045205 (2005).
- [25] S. Mujumdar, M. Ricci, R. Torre, D. S. Wiersma, "Amplified Extended Modes in Random Lasers," *Phys. Rev. Lett.*, **93**, 053903 (2004).
- [26] G. van Soest, *Experiments on Random Lasers*, Doctoral Thesis, (Van der Waals-Zeeman Instituut, 2001).
- [27] G. van Soest, M. Tomita, and A. Lagendijk, "Amplifying volume in scattering media," *Opt. Lett.*, **24**, 306-308 (1999).
- [28] B. R. Prasad, H. Ramachandran, A. K. Sood, C. K. Subramanian, N. Kumar, "Lasing in active, sub-mean-free path-sized systems with dense, random, weak scatterers," *Appl. Opt.*, **36**, 7718-7724 (1997).

- [29] W. L. Barnes, A. Dereux, and T. W. Ebbesen, "Surface plasmon subwavelength optics," *Nature*, **424**, 824-830 (2003).
- [30] J. R. Sambles, G. W. Bradbery, and F. Yang, "Optical excitation of surface plasmons: and introduction," *Contemp. Phys.*, **32**, 173-183 (1991).
- [31] J. J. Mock, D. R. Smith, and S. Schultz, "Local refractive index dependence of plasmon resonance spectra from individual nanoparticles," *Nano Letters*, **3**, 485-491 (2003).
- [32] J. P. Kottman and O. J. F. Martin, "Spectral response of plasmon resonant nanoparticles with a non-regular shape," *Opt. Express*, **6**, 213-219 (2000).
- [33] A. D. Boardman, *Electromagnetic Surface Modes*, (Wiley, New York, 1982).
- [34] J. J. Mock, M. Barbic, D. R. Smith, D. A. Schultz, and S. Schultz, "Shape effects in plasmon resonance of individual colloidal nanoparticles," *J. Chem. Phys.*, **116**, 6755-6759 (2002).
- [35] G. D. Dice, S. Mujumdar, and A. Y. Elezzabi, "Plasmonically enhanced diffusive and subdiffusive metal nanoparticle-dye random laser," *Appl. Phys. Lett.*, **86**, 131105 (2005).
- [36] S. Chan, S. Kwon, T. Koo, L. P. Lee, and A. A. Berlin, "Surface-enhanced Raman scattering of small molecules from silver-coated silicon nanopores," *Adv. Mater.*, **15**, 1595-1598 (2003).
- [37] K. Kneipp, H. Kneipp, I. Itzkan, R. R. Dasari, and M. S. Feld, "Surface-enhanced Raman scattering and biophysics," *J. Phys.: Condens. Matter*, **14**, R597-R6224 (2002).

- [38] A. Leitner, M. A. Lippitsch, S. Draxler, M. Riegler, and F. R. Aussenegg, "Fluorescence properties of dyes adsorbed to silver islands, investigated by picosecond techniques," *Appl. Phys. B.*, **36**, 105-109 (1985).
- [39] D. A. Weitz, S. Garoff, J. I. Gersten, and A. Nitzan, "The enhancement of Raman scattering, resonance Raman scattering, and fluorescence from molecules adsorbed on a rough silver surface," *J. Chem. Phys.*, **78**, 5324-5338 (1983).
- [40] A. M. Glass, P. F. Liao, J. G. Bergmann, "Interaction of metal particles with adsorbed dye molecules: absorption and luminescence," *Opt. Lett.*, **5**, 368-370 (1980).

Chapter 3: Random Laser Modeling

3.1 Modeling of Random Lasers

In this chapter a time-domain simulation is developed to calculate the electromagnetic fields inside of an arbitrarily structured scattering gain media and model a random laser. For a random laser, the pump energy fluence threshold, the local optical gain, and the gain saturation are strong functions of the local pump energy fluence. An ideal model of a random laser will calculate the magnitude and phase of the local electric and magnetic fields in the vicinity of many types of materials and geometric structures. Due to the surface plasmon caused electric field enhancement, it is crucial to simulate the electromagnetic field in the spatial region surrounding the metallic scattering particles in a surface plasmon enhanced random laser system. The simulation must be able to couple the pump and emitted electromagnetic fields and simultaneously calculate their spatial overlap. Experimentally, it is challenging to study the electromagnetic field distribution surrounding a scattering particle as this investigation requires non-invasive optical probes with nanometre resolution capable of measuring field quantities deep within the active optical gain volume.

In this chapter, a finite-difference time-domain (FDTD) software suite is developed to model random lasing. Simulation results are presented for light scattering from both dielectric and metallic particles. Results are also presented for ensembles of multiple scattering particles. Random lasing is investigated for a scattering media formed from Ag scattering particles surrounded by an optical gain material.

Several models have been developed previously to study random laser operation, ranging from: Monte Carlo simulations of photon propagation [1]; to theoretical

descriptions based on diffusion transport theory [2, 3]. Unlike the FDTD algorithm, models using diffusion transport theory or Monte Carlo techniques do not allow for the direct simulation of the electric and magnetic fields in the surroundings of each scattering particle, and cannot be used to simulate random lasing from metallic scattering particles.

3.2 The Finite-Difference Time-Domain Algorithm

The FDTD method directly simulates the temporal evolution of electromagnetic fields in an arbitrary material structure instead of experimentally measuring the electromagnetic field distribution in a random gain media. It is a simulation technique that allows the direct evaluation of the electric and magnetic fields at any point in time and space in any arbitrary media. The standard FDTD simulation method is a second order accurate algorithmic solution to Maxwell's equations that was first proposed by Yee in 1966 [4]. This algorithm solves Maxwell's equations over a Cartesian grid applied to the simulation space as shown in Figure 3.1. Here, the electric and magnetic fields are separated by both a half space step, $\Delta x/2$, and a half time step, $\Delta t/2$. In the FDTD calculations, each updating equation is sequentially applied over the entire simulation space for every time step to determine the electromagnetic fields at any given point in time and space [5].

3.2.1 Solution of Maxwell's Equations

The following section presents the FDTD algorithm used to solve the differential form of Maxwell's equations,

$$\nabla \times \mathbf{H} = \sigma \mathbf{E} + \epsilon \frac{\partial \mathbf{E}}{\partial t}, \quad (3.1)$$

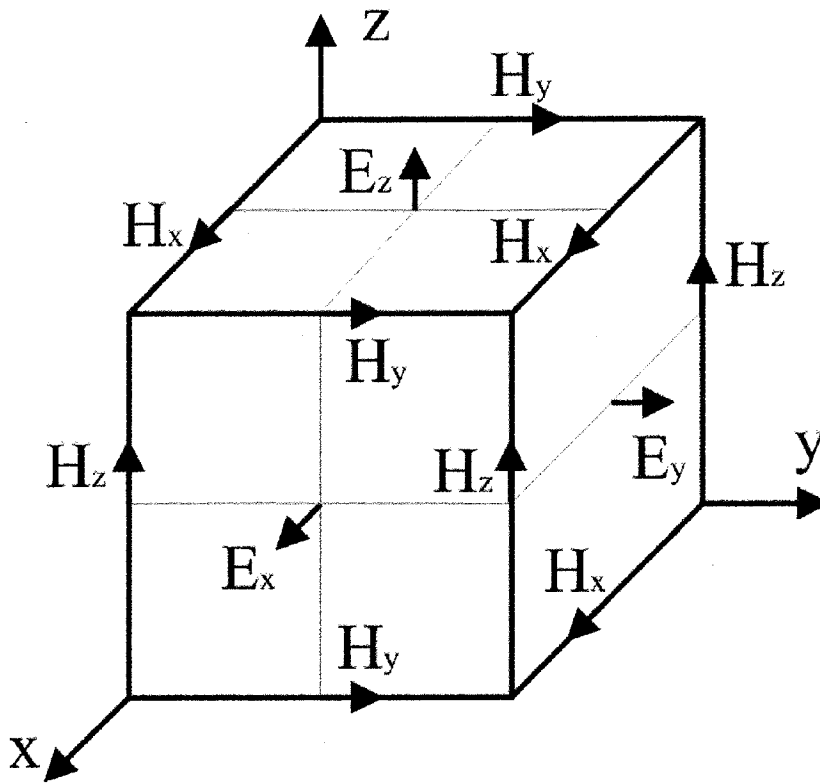


Figure 3.1 – The Yee-grid unit cell. The magnetic and electric fields are separated by a half space step, $\Delta x/2$.

and

$$\nabla \times \mathbf{E} = \rho' \mathbf{H} - \mu \frac{\partial \mathbf{H}}{\partial t}, \quad (3.2)$$

where \mathbf{D} , \mathbf{E} , and \mathbf{H} are the displacement, electric field, and magnetic field vectors, $\varepsilon(\omega)$ is the frequency dependent permittivity, and μ_0 is the permeability of free space. Assuming that $\partial\varepsilon/\partial t \ll \omega\varepsilon$, Maxwell's equations are split into their scalar equivalents over the Cartesian grid used by the FDTD algorithm:

$$\frac{\partial E_x}{\partial t} = \frac{1}{\varepsilon} \left(\frac{\partial H_z}{\partial y} - \frac{\partial H_y}{\partial z} - \sigma E_x \right) \quad (3.3)$$

$$\frac{\partial E_y}{\partial t} = \frac{1}{\varepsilon} \left(\frac{\partial H_x}{\partial z} - \frac{\partial H_z}{\partial x} - \sigma E_y \right) \quad (3.4)$$

$$\frac{\partial E_z}{\partial t} = \frac{1}{\varepsilon} \left(\frac{\partial H_y}{\partial x} - \frac{\partial H_x}{\partial y} - \sigma E_z \right) \quad (3.5)$$

$$\frac{\partial H_x}{\partial t} = \frac{1}{\mu} \left(\frac{\partial E_y}{\partial z} - \frac{\partial E_z}{\partial y} - \rho' H_x \right) \quad (3.6)$$

$$\frac{\partial H_y}{\partial t} = \frac{1}{\mu} \left(\frac{\partial E_z}{\partial x} - \frac{\partial E_x}{\partial z} - \rho' H_y \right) \quad (3.7)$$

$$\frac{\partial H_z}{\partial t} = \frac{1}{\mu} \left(\frac{\partial E_x}{\partial y} - \frac{\partial E_y}{\partial x} - \rho' H_z \right) \quad (3.8)$$

To create forms of these equations that are amenable to numerical calculation, a central difference is applied to each. Assuming that the size of the space step $\Delta s = \Delta x = \Delta y = \Delta z$, and that the temporal step size is Δt , then the first order temporal and spatial derivatives of any function are:

$$\frac{\partial f}{\partial x}(i\Delta x, j\Delta y, k\Delta z, n\Delta t) = \frac{f^n(i+1/2, j, k) - f^n(i-1/2, j, k)}{\Delta x}, \quad (3.9)$$

and

$$\frac{\partial f}{\partial t}(i\Delta x, j\Delta y, k\Delta z, n\Delta t) = \frac{f^{n+1/2}(i, j, k) - f^{n-1/2}(i, j, k)}{\Delta t}, \quad (3.10)$$

where i , j , and k are the Cartesian grid coordinates, and n is the current time step.

Additionally, the second order derivative with respect to time is:

$$\frac{\partial^2 f}{\partial t^2}(i\Delta x, j\Delta y, k\Delta z, n\Delta t) = \frac{f^{n+1}(i, j, k) - 2f^n(i, j, k) + f^{n-1}(i, j, k)}{\Delta t^2}. \quad (3.11)$$

Application of this central difference formalism to Maxwell's equations (3.3 - 3.8) results in the following set of equations that are used for calculating the electric and magnetic fields at alternating half time steps:

$$\begin{aligned} & H_x^{n+1/2}(i, j, k) \\ &= D_a(i, j, k)H_x^{n-1/2}(i, j, k) + \\ & D_b(i, j, k) \left(\begin{array}{l} E_y^n(i, j, k+1/2) - E_y^n(i, j, k-1/2) \\ + E_z^n(i, j-1/2, k) - E_z^n(i, j+1/2, k) \end{array} \right) \end{aligned} \quad (3.12)$$

$$\begin{aligned} & H_y^{n+1/2}(i, j, k) \\ &= D_a(i, j, k)H_y^{n-1/2}(i, j, k) + \\ & D_b(i, j, k) \left(\begin{array}{l} E_z^n(i+1/2, j, k) - E_z^n(i-1/2, j, k) \\ + E_x^n(i, j, k-1/2) - E_x^n(i, j, k+1/2) \end{array} \right) \end{aligned} \quad (3.13)$$

$$\begin{aligned} & H_z^{n+1/2}(i, j, k) \\ &= D_a(i, j, k)H_z^{n-1/2}(i, j, k) + \\ & D_b(i, j, k) \left(\begin{array}{l} E_x^n(i, j+1/2, k) - E_x^n(i, j-1/2, k) \\ + E_y^n(i-1/2, j, k) - E_y^n(i+1/2, j, k) \end{array} \right) \end{aligned} \quad (3.14)$$

$$\begin{aligned} & E_x^{n+1}(i, j, k) \\ &= C_a(i, j, k)E_x^n(i, j, k) + \\ & C_b(i, j, k) \left(\begin{array}{l} H_z^{n+1/2}(i, j+1/2, k) - H_z^{n+1/2}(i, j-1/2, k) \\ + H_y^{n+1/2}(i, j, k-1/2) - H_y^{n+1/2}(i, j, k+1/2) \end{array} \right) \end{aligned} \quad (3.15)$$

$$\begin{aligned}
& E_y^{n+1}(i, j, k) \\
& = C_a(i, j, k) E_y^n(i, j, k) + \\
& C_b(i, j, k) \left(\begin{array}{l} H_x^{n+1/2}(i, j, k+1/2) - H_x^{n+1/2}(i, j, k-1/2) \\ + H_z^{n+1/2}(i-1/2, j, k) - H_z^{n+1/2}(i+1/2, j, k) \end{array} \right)
\end{aligned} \tag{3.16}$$

$$\begin{aligned}
& E_z^{n+1}(i, j, k) \\
& = C_a(i, j, k) E_z^n(i, j, k) + \\
& C_b(i, j, k) \left(\begin{array}{l} H_y^{n+1/2}(i+1/2, j, k) - H_y^{n+1/2}(i-1/2, j, k) \\ + H_x^{n+1/2}(i, j-1/2, j) - H_x^{n+1/2}(i, j+1/2, j) \end{array} \right)
\end{aligned} \tag{3.17}$$

The coefficients C_a , C_b , D_a , and D_b in equations 3.12 - 3.17 are functions of the material at each grid point, as well as the time and space step of the simulation.

$$C_a(i, j, k) = \frac{1 - \frac{\sigma(i, j, k) \Delta t}{2\varepsilon(i, j, k)}}{1 + \frac{\sigma(i, j, k) \Delta t}{2\varepsilon(i, j, k)}} \tag{3.18}$$

$$C_b(i, j, k) = \frac{\frac{\Delta t}{\varepsilon(i, j, k) \Delta s}}{1 + \frac{\sigma(i, j, k) \Delta t}{2\varepsilon(i, j, k)}} \tag{3.19}$$

$$D_a(i, j, k) = \frac{1 - \frac{\rho'(i, j, k) \Delta t}{2\mu(i, j, k)}}{1 + \frac{\rho'(i, j, k) \Delta t}{2\mu(i, j, k)}} \tag{3.20}$$

$$D_b(i, j, k) = \frac{\frac{\Delta t}{\mu(i, j, k) \Delta s}}{1 + \frac{\rho'(i, j, k) \Delta t}{2\mu(i, j, k)}} \tag{3.21}$$

Here, σ is the electric conductivity, ε is the permittivity, ρ' is the magnetic conductivity or loss term, μ is the magnetic permeability, Δt is the time step, and Δs is the space step.

It should be noted that for lossless materials such as free space, where the magnetic and electric conductivities are zero, C_a , C_b , D_a , and D_b reduce to:

$$C_a(i, j, k) = 1 \quad (3.22)$$

$$C_b(i, j, k) = \frac{\Delta t}{\epsilon(i, j, k) \Delta s} \quad (3.23)$$

$$D_a(i, j, k) = 1 \quad (3.24)$$

$$D_b(i, j, k) = \frac{\Delta t}{\mu(i, j, k) \Delta s} \quad (3.25)$$

The six update equations (3.12 – 3.17) form the basis for the calculation of electromagnetic fields using the FDTD method. Using these equations, both the magnetic and the electric fields are updated at every half time step to obtain a complete picture of the combined electromagnetic field inside of the simulation space.

3.2.2 Numerical Stability of Solution

The FDTD algorithm requires that the values of Δt and Δs are carefully chosen to ensure numerical stability. Spatially, it is shown in chapter 5 of reference [5] that Δs must be less than one tenth of the smaller of the wavelength or the minimum feature size. This limitation is necessary due to the fact that a wavefront in the FDTD geometry is defined by scalar field values at several adjacent points in the grid. If Δs is on the order of the wavelength of incident light, the wavelength inside the simulation space becomes uncertain. The feature size limits the maximum value of Δs due to the discretization of smooth curves. On the temporal scale, magnetic and electric field components must

propagate across the half space step offset between the \mathbf{E} and \mathbf{H} fields. This requires that the maximum time step be:

$$\Delta t \leq \frac{\Delta s}{c\sqrt{3}}, \quad (3.26)$$

to ensure wave propagation [5]. An extreme limitation is placed on the maximum feasible geometry size by these conditions. This problem is exacerbated for geometries where features are much smaller than the light wavelength. If the feature size, for example, is $1/10^{\text{th}}$ of the wavelength, then number of time steps increases by a factor of 10 and the amount of memory storage by a factor of 10^3 . An additional limitation is that for conductivity to have a physical meaning the time step should be greater than the relaxation time for an electric field to decay by $1/e$ without any forcing field. The relaxation time is estimated via $\tau_r = \epsilon_0/\sigma$, where τ_r is the relaxation time, ϵ_0 is the permittivity of free space, and σ is the electric conductivity [6]. For silver, which has a conductivity of $\sim 6.1 \times 10^7$ S/m [7], the relaxation time is $\sim 1.4 \times 10^{-19}$ s.

3.2.3 FDTD Boundary Condition

As computational resources are finite, the FDTD geometry cannot be extended to infinity in all directions. At the edge of the simulation space, the electric and magnetic field values are set to a single specific value, and each boundary acts as a perfect reflector of incident radiation. Electromagnetic energy is not allowed to leave the computational window and the simulation becomes unstable. As such, reflections at each border must be eliminated by bounding the geometry with a mathematically constructed artificial media known as a perfectly matched layer (PML) [8]. An ideal PML is a reflectionless absorber that prevents the instability from simulated radiation interacting with the edge of

the computational window. A PML separates the six scalar Maxwell's equations (3.3 - 3.8) into 12 equations (3.27 – 3.38) that deal solely with propagation along a single cardinal direction within the PML:

$$\varepsilon \frac{\partial E_{xy}}{\partial t} + \sigma_y E_{xy} = \frac{\partial (H_{zx} + H_{zy})}{\partial y} \quad (3.27)$$

$$\varepsilon \frac{\partial E_{xz}}{\partial t} + \sigma_z E_{xz} = -\frac{\partial (H_{yz} + H_{yx})}{\partial z} \quad (3.28)$$

$$\varepsilon \frac{\partial E_{yz}}{\partial t} + \sigma_z E_{yz} = \frac{\partial (H_{xy} + H_{xz})}{\partial z} \quad (3.29)$$

$$\varepsilon \frac{\partial E_{yx}}{\partial t} + \sigma_x E_{yx} = -\frac{\partial (H_{zx} + H_{zy})}{\partial x} \quad (3.30)$$

$$\varepsilon \frac{\partial E_{zx}}{\partial t} + \sigma_x E_{zx} = \frac{\partial (H_{yz} + H_{yx})}{\partial x} \quad (3.31)$$

$$\varepsilon \frac{\partial E_{zy}}{\partial t} + \sigma_y E_{zy} = \frac{\partial (H_{xy} + H_{xz})}{\partial y} \quad (3.32)$$

$$\mu \frac{\partial H_{xy}}{\partial t} + \sigma_y^* H_{xy} = -\frac{\partial (E_{zx} + E_{zy})}{\partial y} \quad (3.33)$$

$$\mu \frac{\partial H_{xz}}{\partial t} + \sigma_z^* H_{xz} = \frac{\partial (E_{yz} + E_{yx})}{\partial z} \quad (3.34)$$

$$\mu \frac{\partial H_{yz}}{\partial t} + \sigma_z^* H_{yz} = -\frac{\partial (E_{xy} + E_{xz})}{\partial z} \quad (3.35)$$

$$\mu \frac{\partial H_{yx}}{\partial t} + \sigma_x^* H_{yx} = \frac{\partial (E_{zx} + E_{zy})}{\partial x} \quad (3.36)$$

$$\mu \frac{\partial H_{zx}}{\partial t} + \sigma_x^* H_{zx} = -\frac{\partial (E_{yz} + E_{yx})}{\partial x} \quad (3.37)$$

$$\mu \frac{\partial H_{zy}}{\partial t} + \sigma_y^* H_{zy} = \frac{\partial (E_{xy} + E_{xz})}{\partial y} \quad (3.38)$$

Here, $\sigma = E/J$ and $\sigma^* = B/J$ are the electric and magnetic conductivities in the PML region. The separation of the six scalar equations (3.3 – 3.8) into these 12 component parts (3.27 – 3.38) allows electric and magnetic losses to depend on the direction of radiation propagation in the simulation space. In a PML, radiation that propagates perpendicular to the borders is attenuated, while radiation propagates without losses parallel to each edge and is then absorbed in the corner regions of the PML. To minimize reflections from this artificial media, its impedance is made equal to that of free space by setting:

$$\frac{\sigma}{\epsilon_0} = \frac{\sigma^*}{\mu_0}. \quad (3.39)$$

Additionally, in order to minimize reflections caused by an abrupt transition from free space to the PML, it is necessary to increase the conductivity geometrically:

$$\sigma(p) = \sigma_m \left(\frac{p}{\Delta s} \right)^2, \quad (3.40)$$

where σ_m is the maximum conductivity, and p is the number of grid points into the PML boundary [8]. For a two-dimensional planar geometry, the value of σ_m varies along each edge as illustrated in Figure 3.2.

3.2.4 Radiation Source

The simplest form of a radiation source within the simulation geometry is a single grid point that radiates in all directions, having an electric field equal to:

$$E_z(i, j, k) = E_0 \cos\left(\frac{2\pi c \Delta t n}{\lambda}\right), \quad (3.41)$$

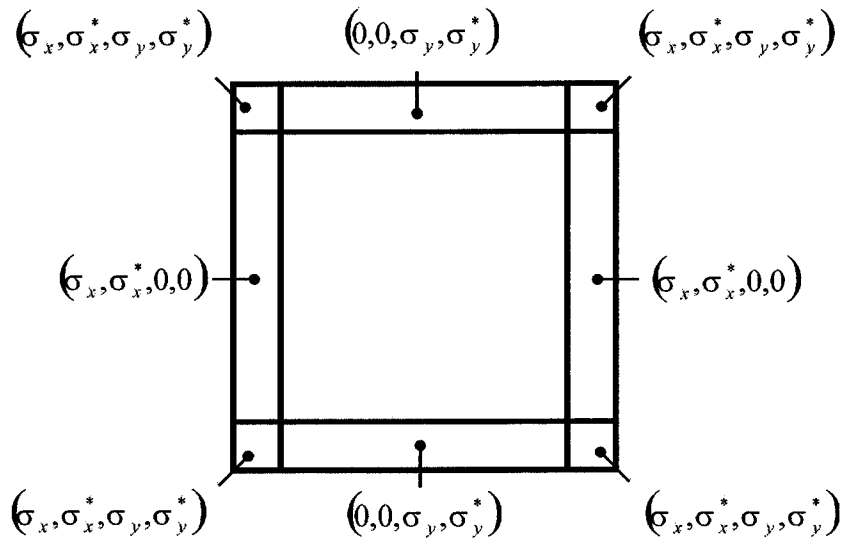


Figure 3.2 – Magnetic and Electric loss terms in the Berenger Perfectly Matched Layer (PML).

where E_0 is the amplitude of the field, n is the current time step, and λ is the desired wavelength. Equation 3.41 represents a hard source, or one that forces the value of the electric field at a specific location to a fixed value. When electromagnetic radiation is incident on a hard source, it behaves in a similar manner to short-circuit termination of a transmission line, as the incident wave is completely reflected. A perfectly reflecting plane is created for a series of hard radiation sources distributed at grid points along a plane in the simulation geometry. To prevent this reflection from the source, the total field/scattered field formulation is applied [5]. This formalism separates the electromagnetic field inside the simulation geometry into two components: the incident field in the absence of any scattering objects, $\mathbf{E}_i(i, j, k, t)$, and the scattered field in the presence of a scattering object, $\mathbf{E}_s(i, j, k, t)$. The total field in the simulation space, $\mathbf{E}_t(i, j, k, t)$, is the sum of these individual components:

$$\mathbf{E}_t(i, j, k, t) = \mathbf{E}_i(i, j, k, t) + \mathbf{E}_s(i, j, k, t). \quad (3.42)$$

For a two dimensional simulation, $E_{z,inc}^n$ and $H_{z,inc}^{n+1/2}$ terms are added directly into the Yee-Grid equations 3.14 and 3.15 respectively:

$$\begin{aligned} & H_z^{n+1/2}(i, j, k) \\ & = D_a(i, j, k) H_z^{n-1/2}(i, j, k) + \\ & D_b(i, j, k) \left(\begin{array}{l} E_x^n(i, j+1/2, k) - E_x^n(i, j-1/2, k) - E_{z,inc}^n \\ + E_y^n(i-1/2, j, k) - E_y^n(i+1/2, j, k) \end{array} \right) \end{aligned} \quad (3.43)$$

$$\begin{aligned} & E_x^{n+1}(i, j, k) \\ & = C_a(i, j, k) E_x^n(i, j, k) + \\ & C_b(i, j, k) \left(\begin{array}{l} H_z^{n+1/2}(i, j+1/2, k) - H_z^{n+1/2}(i, j-1/2, k) - H_{z,inc}^{n+1/2} \\ + H_y^{n+1/2}(i, j, k-1/2) - H_y^{n+1/2}(i, j, k+1/2) \end{array} \right) \end{aligned} \quad (3.44)$$

The numerical values of $E_{z,inc}^n$ and $H_{z,inc}^{n+1/2}$ are calculated to match the first order Hermite-Gaussian mode along a specified focal plane for the simulated incident beam, and are described by:

$$E_z(i, j, k) = A \frac{w_0}{w_z} \exp\left(-\frac{j^2}{w_z^2}\right), \quad (3.45)$$

$$Z_0 = \frac{\pi n w_0^2}{\lambda}, \quad (3.46)$$

and

$$w_z = w_0 \sqrt{1 + \frac{j^2}{w_0^2}}, \quad (3.47)$$

where w_0 is the beam waist, w_z is the beam waist at a distance y from the focal plane, and Z_0 is the Rayleigh range of the beam. In order to create a beam-like directional source in the FDTD simulation space, it is necessary to take into account the one half space step and one half time step offset between the \mathbf{E} and \mathbf{H} components of the electromagnetic field. Along a single dimension, a propagating sinusoidal wave takes the form of the wave equation,

$$E_z(j, t) = E_0 \cos(\omega t - kj), \quad (3.48)$$

where k is the wave number of source radiation. Thus, the radiation source in the FDTD simulation space will propagate in the positive y direction as long as the \mathbf{H} field is one half of a space step behind the \mathbf{E} field. Additionally, the \mathbf{H} field must also lag by one half of a time step behind the \mathbf{E} field. This modification of the source terms, to account for the spatial and temporal offset between the \mathbf{E} and \mathbf{H} fields, creates a directional beam source where radiation leakage in the reverse direction is up to four orders of magnitude smaller than the source radiation in the forward direction.

3.2.5 Dispersive Metals

In the following sections the FDTD simulation of dispersive or non-dispersive dielectrics, metals, and optical gain media is discussed. The simplest case is the propagation of light through non-dispersive materials, such as dielectrics and metals at single wavelength, which are modeled through the ϵ , μ , σ , and ρ' terms in Yee's grid equations (3.12 – 3.17). For the wideband radiation present in the fluorescence spectrum of a gain material, it is essential to create a model that automatically accounts for the incident wavelength. This is especially important for the simulation of SP resonance in metals, where the permittivity depends strongly on frequency as seen in Figure 3.3 for Ag in the visible range. For metals, the dependence of the complex permittivity, $\epsilon(\omega)$, is included via the Drude model [9], which treats the metal as a collection of electrons that behave as a non-interacting gas:

$$\epsilon(\omega) = \epsilon_0 \epsilon_\infty + \frac{\epsilon_0 \omega_p^2}{i\omega\nu - \omega^2}. \quad (3.50)$$

where ω_p is the plasma frequency, ν is the damping frequency, ϵ_∞ is the DC dielectric constant, and ϵ_0 is the permittivity of free space. A typical method of incorporating frequency dependent parameters into the FDTD simulation is the use of the auxiliary differential equation (ADE) method [10]. As $\epsilon(\omega)$ is both variable and frequency dependent, care must be taken to properly incorporate it into the FDTD model. The electric displacement, \mathbf{D} , at any point in the geometry is related to \mathbf{E} through:

$$\mathbf{D} = \epsilon(\omega)\mathbf{E}, \quad (3.51)$$

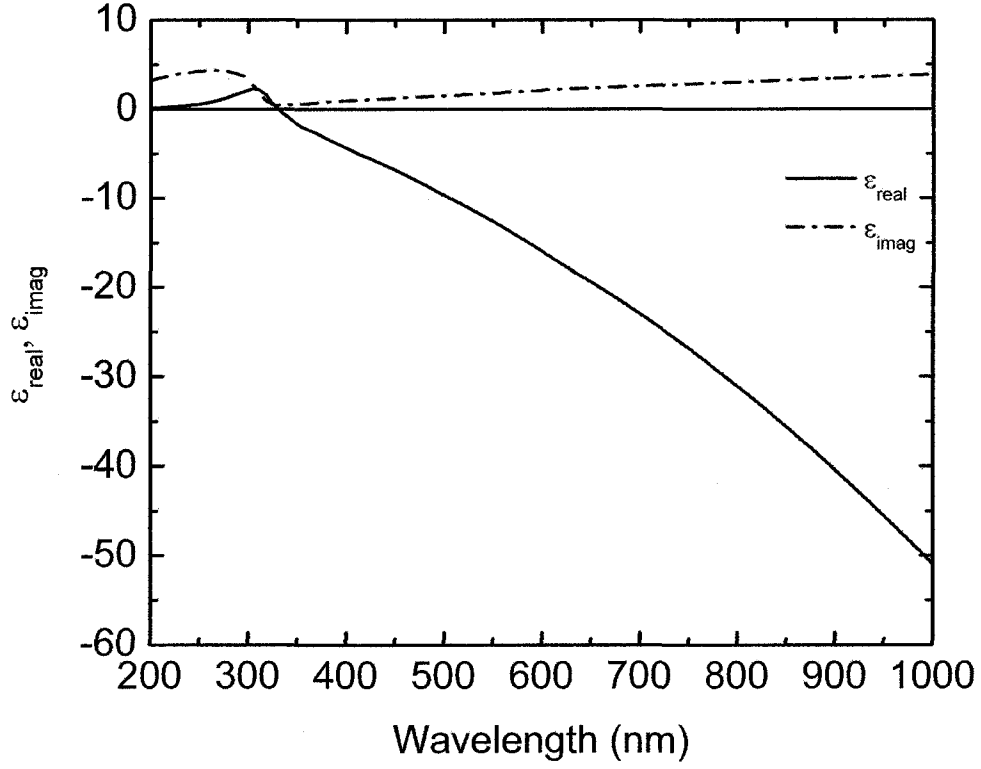


Figure 3.3 – Relative permittivity of silver as a function of wavelength.

which allows the displacement to be calculated during the Yee-grid update cycle by removing the material dependence of ϵ , and μ from equations 3.12 - 3.17. An example is shown below which illustrates the calculation of D_x at an arbitrary update step:

$$\begin{aligned}
& D_x^{n+1}(i, j, k) \\
& = D_x^n(i, j, k) + \\
& \frac{\Delta t}{\Delta s} \left(H_z^{n+1/2}(i, j+1/2, k) - H_z^{n+1/2}(i, j-1/2, k) \right) \\
& \left(+ H_y^{n+1/2}(i, j, k-1/2) - H_y^{n+1/2}(i, j, k+1/2) \right)
\end{aligned} \tag{3.52}$$

Once the value of \mathbf{D} is known, $\epsilon(\omega)$ can be coupled into the time-domain FDTD simulation by applying an inverse Fourier transformation to the combination of equations 3.50 and 3.51 [10]:

$$v \frac{d\mathbf{D}}{dt} + \frac{d^2\mathbf{D}}{dt^2} = \omega_p^2 \epsilon_0 \mathbf{E} + v \epsilon_\infty \epsilon_0 \frac{d\mathbf{E}}{dt} + \epsilon_\infty \epsilon_0 \frac{d^2\mathbf{E}}{dt^2}. \tag{3.53}$$

Next, the standard central differencing schema is applied to obtain an equation relating the calculated value of \mathbf{D} to \mathbf{E} :

$$\begin{aligned}
& E_x^{n+1}(i, j, k) = \\
& \frac{m_1 D_z^{n+1}(i, j, k) - 4D_z^n(i, j, k) + m_2 D_z^{n-1}(i, j, k) + 4\epsilon_0 \epsilon_\infty E_z^n(i, j, k) - m_3 E_z^{n-1}(i, j, k)}{m_4}, \tag{3.54}
\end{aligned}$$

where the constants m_1 , m_2 , m_3 , and m_4 are defined as:

$$m_1 = 2 + v\Delta t \tag{3.55}$$

$$m_2 = 2 - v\Delta t \tag{3.56}$$

$$m_3 = \omega_p^2 \epsilon_0 \Delta t^2 - v \epsilon_0 \epsilon_\infty \Delta t + 2 \epsilon_0 \epsilon_\infty \tag{3.57}$$

$$m_4 = \omega_p^2 \epsilon_0 \Delta t^2 + v \epsilon_0 \epsilon_\infty \Delta t + 2 \epsilon_0 \epsilon_\infty. \tag{3.58}$$

3.2.6 Dispersive Dielectrics

The modeling of a dispersive dielectric material requires a similar approach to the modeling of a dispersive metal. In this section, the refractive index variation is fitted to a Sellmeier type refractive index equation [7]:

$$n^2 = 1 + \frac{B_n \lambda^2}{\lambda^2 - \omega_n}, \quad (3.59)$$

where B_n and ω_n are fitting coefficients. Figure 3.4 depicts the permittivity of Al_2O_3 in the visible wavelength range as calculated from Sellmeier fitting coefficients [7]. This figure illustrates that the variation takes ϵ_{real} from 3.6 to 3.1 from $\lambda = 200$ nm to 1000 nm. While this variation is small compared to the much larger change in ϵ_{real} for silver (0.2 to -51.0) over the same wavelength range, it must still be included when simulating Al_2O_3 scatterers. As in the modeling of a metal, the ADE method couples \mathbf{D} , which does not depend on material parameters to \mathbf{E} . For dielectrics, the coupling is accomplished through the use of the electric polarization, \mathbf{P} , that is associated with the electric field in the dielectric material. Thus, the unknown electric field at the next time step is coupled to the previously known \mathbf{D} and \mathbf{P} through:

$$\mathbf{D} = \epsilon_0 \mathbf{E} + \mathbf{P}. \quad (3.60)$$

Next, the treatment presented in references [11] and [12] is followed, where for a Sellmeier fitting equation with three resonances, ω_n , the following system of differential equations is developed:

$$\frac{d^2 \mathbf{P}_1}{dt^2} + \omega_1^2 (1 + B_1) \mathbf{P}_1 + \omega_1^2 B_1 \mathbf{P}_2 + \omega_1^2 B_1 \mathbf{P}_3 = \omega_1^2 B_1 \mathbf{D}, \quad (3.61)$$

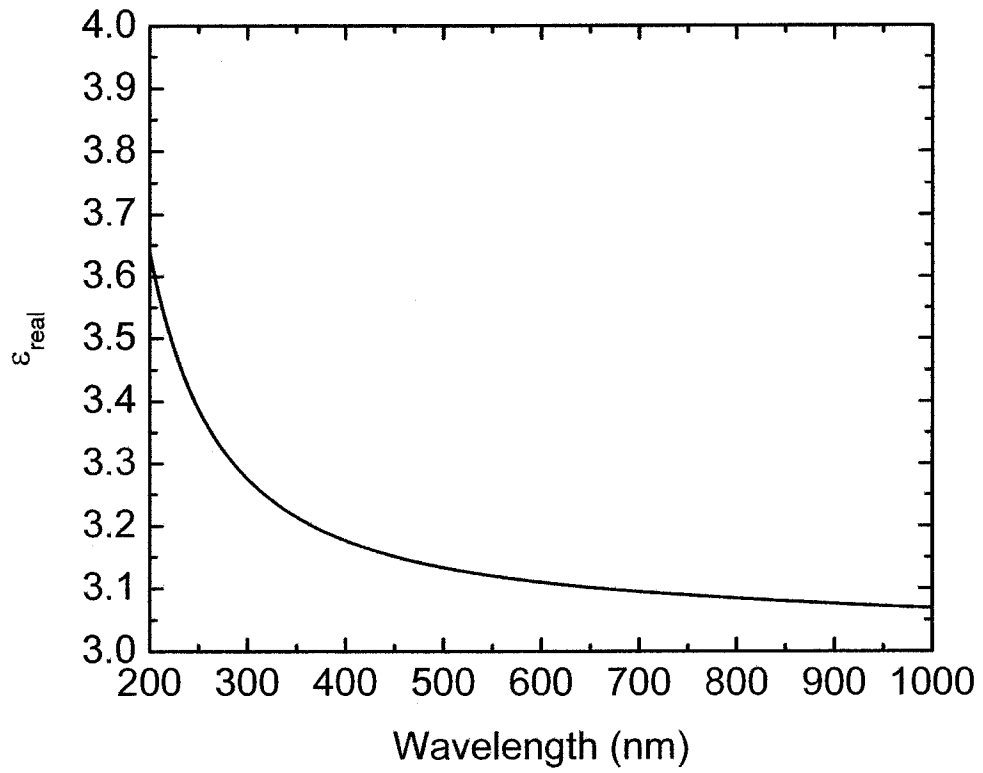


Figure 3.4 – Relative electric permittivity of Alumina (Al_2O_3) assuming no absorption as a function of wavelength in the visible range.

$$\frac{d^2 \mathbf{P}_2}{dt^2} + \omega_2^2 (1 + B_2) \mathbf{P}_2 + \omega_2^2 B_2 \mathbf{P}_1 + \omega_2^2 B_2 \mathbf{P}_3 = \omega_2^2 B_2 \mathbf{D}, \quad (3.62)$$

$$\frac{d^2 \mathbf{P}_3}{dt^2} + \omega_3^2 (1 + B_3) \mathbf{P}_3 + \omega_3^2 B_3 \mathbf{P}_1 + \omega_3^2 B_3 \mathbf{P}_2 = \omega_3^2 B_3 \mathbf{D}. \quad (3.63)$$

Using a semi-implicit central differencing schema, these terms are separated into a system of three discrete equations that, once inverted, allow \mathbf{P} to be updated:

$$a_1 \mathbf{P}_1^{n+1} + c_1 \mathbf{P}_2^{n+1} + c_1 \mathbf{P}_3^{n+1} = c_1 (\mathbf{D}^{n+1} + \mathbf{D}^{n-1}) - c_1 (\mathbf{P}_2^{n-1} + \mathbf{P}_3^{n-1}) + 4\mathbf{P}_1^n + g_1 \mathbf{P}_1^{n-1}, \quad (3.64)$$

$$c_2 \mathbf{P}_1^{n+1} + a_2 \mathbf{P}_2^{n+1} + c_2 \mathbf{P}_3^{n+1} = c_2 (\mathbf{D}^{n+1} + \mathbf{D}^{n-1}) - c_2 (\mathbf{P}_1^{n-1} + \mathbf{P}_3^{n-1}) + 4\mathbf{P}_2^n + g_2 \mathbf{P}_2^{n-1}, \quad (3.65)$$

$$c_3 \mathbf{P}_1^{n+1} + c_3 \mathbf{P}_2^{n+1} + a_3 \mathbf{P}_3^{n+1} = c_3 (\mathbf{D}^{n+1} + \mathbf{D}^{n-1}) - c_3 (\mathbf{P}_1^{n-1} + \mathbf{P}_2^{n-1}) + 4\mathbf{P}_3^n + g_3 \mathbf{P}_3^{n-1}, \quad (3.66)$$

where a_i, b_i, c_i are the constant terms:

$$a_i = 2 + \omega_i^2 \Delta t^2 (1 + B_i), \quad (3.67)$$

$$c_i = \omega_i^2 \Delta t^2 B_i, \quad (3.68)$$

$$g_i = -2 - \omega_i^2 \Delta t^2 (1 + B_i). \quad (3.69)$$

This system of three equations is then solved to obtain \mathbf{P}_i^{n+1} which is used to calculate \mathbf{E}^{n+1} :

$$\mathbf{E}^{n+1} = \frac{1}{\epsilon_0} (\mathbf{D}^{n+1} - \mathbf{P}_1^{n+1} - \mathbf{P}_2^{n+1} - \mathbf{P}_3^{n+1}). \quad (3.70)$$

3.2.7 Optical Gain Material

A material with optical gain presents unique modeling challenges in the FDTD environment. Assigning a negative electrical conductivity is a simple method to simulate a material that provides optical gain. Two problems with negative absorption are that the gain is constant across the entire wavelength range, and that as there is no gain saturation

an unlimited buildup of energy occurs in a simulated cavity. To avoid these two problems, it is necessary to adjust the model so that the gain varies with frequency, and that the amount of energy obtainable from the gain material is finite. In this section, a model is presented that determines the population density matrix by following the formalism presented in reference [13]. Due to computational resource limits, the model is limited to two dimensions. Figure 3.5 depicts a level diagram for the four-level system used in the model. A set of rate equations models the gain media by calculating the population in levels N_0 through N_3 at each point in time and space. In the model, atoms are pumped from the ground state (N_0) to the upper state (N_3), at a pumping rate (P_r) that is determined by the intensity of pump radiation. The population in each level then spontaneously decays to the energy levels N_0 through N_2 at rates controlled by the lifetime of each level τ_{ab} , where a is the source and b is the target level for the spontaneous decay. Atomic transitions between N_2 and N_1 in the model are caused by spontaneous emission at a rate determined by the transition lifetime, τ_{21} , and by stimulated emission from the electric field in the gain media. A population inversion builds up between the lasing levels N_2 and N_1 , as long as $\tau_{32} < \tau_{21}$ and $\tau_{21} > \tau_{10}$. In the atomic gain system, the polarization density, \mathbf{P} , couples the population inversion between levels N_2 and N_1 to the electric field as outlined in reference [14]:

$$\begin{aligned} \frac{d^2 \mathbf{P}(i, j, k, t)}{dt^2} + \Delta \omega_a \frac{d \mathbf{P}(i, j, k, t)}{dt} + \omega_a^2 \mathbf{P}(i, j, k, t) = \\ \frac{\gamma_r e^2}{\gamma_c m_e} \Delta N(i, j, k, t) \mathbf{E}(i, j, k, t) \end{aligned} \quad (3.71)$$

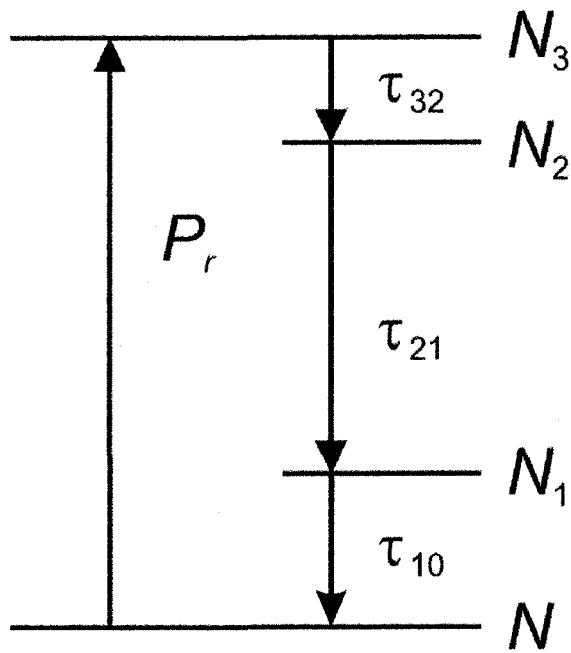


Figure 3.5 – Energy level diagram for the simulated gain medium. P_r is the pumping rate, and τ_{32} , τ_{32} , τ_{32} are the energy level lifetimes.

In equation 3.71, e is the charge on an electron, m_e is the mass of an electron, ω_a is the central frequency of the gain spectrum, and $\Delta\omega_a$ is FWHM linewidth of the atomic transition between N_2 and N_1 :

$$\Delta\omega_a = \frac{1}{\tau_{21}} + \frac{2}{T_2}, \quad (3.72)$$

where T_2 is the mean dephasing time of N_2 . Additionally, $\gamma_r = 1/\tau_{21}$, while γ_c is defined as:

$$\gamma_c = \frac{e^2}{m} \frac{\omega_a^2}{6\pi\epsilon_0 c^3}. \quad (3.73)$$

Finally, the population inversion between levels N_2 and N_1 is represented by

$$\Delta N(i, j, k, t) = N_1(i, j, k, t) - N_2(i, j, k, t). \quad (3.74)$$

A set of four coupled rate equations is constructed to describe the population of each energy level:

$$\frac{dN_3(x, y, t)}{dt} = P_r N_0(x, y, t) - \frac{N_3(x, y, t)}{\tau_{32}}, \quad (3.75)$$

$$\frac{dN_2(x, y, t)}{dt} = \frac{N_3(x, y, t)}{\tau_{32}} + E(x, y, t) \frac{1}{\hbar\omega_a} \frac{dP(x, y, t)}{dt} - \frac{N_2(x, y, t)}{\tau_{21}}, \quad (3.76)$$

$$\frac{dN_1(x, y, t)}{dt} = \frac{N_2(x, y, t)}{\tau_{21}} - E(x, y, t) \frac{1}{\hbar\omega_a} \frac{dP(x, y, t)}{dt} + \frac{N_1(x, y, t)}{\tau_{10}}, \quad (3.77)$$

$$\frac{dN_0(x, y, t)}{dt} = \frac{N_1(x, y, t)}{\tau_{10}} - P_r N_0(x, y, t). \quad (3.78)$$

These rate equations are then incorporated into the FDTD method through the use of a semi-implicit central differencing scheme applied to equation 3.71:

$$\mathbf{P}^{n+1} = \frac{4\mathbf{P}^n + q_1\mathbf{P}^{n-1} + q_2\mathbf{E}^n (N_1^n - N_2^n)}{q_4}, \quad (3.79)$$

which has constant terms:

$$q_1 = -2 + \Delta t \Delta \omega_a - \Delta t^2 \Delta \omega_a^2, \quad (3.80)$$

$$q_2 = \frac{2\Delta t^2 \gamma_r e^2}{\gamma_c m_e}, \quad (3.81)$$

and

$$q_3 = 2 + \Delta t \Delta \omega_a + \Delta t^2 \omega_a^2. \quad (3.82)$$

The rate equations (3.75 - 3.78) are also discretized to:

$$a_1 N_0^{n+1} + d_1 N_3^{n+1} = e_1 N_0^{n-1} + h_1 N_3^{n-1}, \quad (3.83)$$

$$c_2 N_2^{n+1} + d_1 N_3^{n+1} = g_1 N_2^{n-1} + h_2 N_3^{n-1} + i_2 (\mathbf{P}^{n+1} - \mathbf{P}^{n-1}) \mathbf{E}^n, \quad (3.84)$$

$$b_3 N_1^{n+1} + c_3 N_2^{n+1} = f_3 N_1^{n-1} + g_3 N_2^{n-1} + i_3 (\mathbf{P}^{n+1} - \mathbf{P}^{n-1}) \mathbf{E}^n, \quad (3.85)$$

$$a_4 N_0^{n+1} + b_4 N_1^{n+1} = e_4 N_0^{n-1} + f_4 N_1^{n-1}, \quad (3.86)$$

where the constant terms are:

$$a_1 = -\Delta t \tau_{32} P_r, \quad (3.87)$$

$$d_1 = \tau_{32} + \Delta t, \quad (3.88)$$

$$c_2 = \hbar \omega_a \tau_{32} \tau_{21} - \Delta t \hbar \omega_a \tau_{32}, \quad (3.89)$$

$$d_2 = -\Delta t \hbar \omega_a \tau_{21}, \quad (3.90)$$

$$b_3 = \hbar \omega_a \tau_{21} \tau_{10} + \Delta t \hbar \omega_a \tau_{21}, \quad (3.91)$$

$$c_3 = -\Delta t \hbar \omega_a \tau_{10}, \quad (3.92)$$

$$a_4 = \tau_{10} + \Delta t \tau_{10} P_r, \quad (3.93)$$

$$b_4 = -\Delta t, \quad (3.94)$$

$$e_1 = \Delta t \tau_{32} P_r, \quad (3.95)$$

$$h_1 = \tau_{32} - \Delta t, \quad (3.96)$$

$$g_2 = \hbar \omega_a \tau_{32} \tau_{21} - \hbar \Delta t \omega_a \tau_{32}, \quad (3.97)$$

$$h_2 = \hbar \omega_a \Delta t \tau_{21}, \quad (3.98)$$

$$i_2 = \tau_{32} \tau_{21}, \quad (3.99)$$

$$f_3 = \hbar \omega_a \tau_{21} \tau_{10} - \hbar \omega_a \Delta t \tau_{21}, \quad (3.100)$$

$$g_3 = \hbar \Delta t \omega_a \tau_{10}, \quad (3.101)$$

$$i_3 = -\tau_{21} \tau_{10}, \quad (3.102)$$

$$e_4 = \tau_{10} - \Delta t \tau_{10} P_r, \quad (3.103)$$

$$f_4 = \Delta t, \quad (3.104)$$

With the inversion of this system of equations, the value of \mathbf{P} can be found at each time step and used to obtain \mathbf{E} according to equation 3.70. The remaining features to be implemented in the model are spontaneous radiation sources within the media, and the determination of the pumping rate.

For the gain media, the pump radiation and emitted radiation exist in separate simulation spaces with identical material geometries. This allows the pumping rate to be calculated directly from the electric field intensity at each given point in space without including any effects from spontaneously emitted radiation. Here, a pump beam is launched from a total field/scattered field source plane (Section 3.2.4) into the media. A simplifying assumption is made that the gain media does not deplete the pump radiation, as the simulation space has a maximum length of approximately 5 μm , while the

absorption length for pump radiation in the Rhodamine 6G laser dye is approximately 40 μm . The intensity distribution of the pump beam is then used to determine the instantaneous pumping rate throughout the simulation space.

The FDTD simulation of a gain media requires a radiation source for spontaneous emission that will propagate and be amplified in the gain media. Accordingly, each grid point in the simulation space is randomly assigned a frequency, ν , using a Lorentzian distribution:

$$\frac{g(\nu)}{g(\nu_0)} = \frac{\Delta\nu^2}{4\left((\nu-\nu_0)^2 + \left(\frac{\Delta\nu}{2}\right)^2\right)}. \quad (3.105)$$

Where $\Delta\nu$ is FWHM emission bandwidth, and ν_0 is the central frequency of the gain transition between levels N_2 and N_1 . Next, the electric field amplitude, E_s , at each grid point is calculated from:

$$E_s(i, j, k, t) = \sqrt{\frac{\hbar\omega_a N_2}{\pi\tau_{21}\Delta s}}, \quad (3.106)$$

which calculates the amplitude according to the number of atoms that spontaneously fall from N_2 to N_1 during each time step. A simulation space is thus created where every grid square behaves as a point source oscillating at some frequency, ν_s , with an amplitude, E_s , determined by the by the pumping and stimulated emission history of the spatial grid location.

3.2.8 FDTD Simulation Suite

A software suite was constructed through the combination of each of the FDTD methodologies previously presented. The FDTD suite combines the ability to perform

two dimensional time domain electromagnetic simulations with the ability to simulate dispersive dielectrics, metals, and optical gain media. The code is written in C++, and is listed in Appendix A. A selection of simulated results is outlined in the remainder of this chapter.

3.3 FDTD Light Scattering Simulations

3.3.1 Single Scattering Intensity Profile

Using the FDTD model outlined in section 3.2, it is possible to study many phenomena related to the propagation of light in a random media, such as the scattering of light from single dielectric and metallic particles. Both shape and size effects influence the scattering, extinction and absorption cross sections, the location and width of the SP resonance, and the magnitude of the localized SP fields surrounding metallic nanoparticles. To view these effects in the FDTD simulation, the electric and magnetic field scattered by a particle in the simulation geometry is determined through equation 3.42. The instantaneous scattered field at any point on the simulation grid is determined by subtracting the incident field, E_i , from the total field, E_t [15]. Figure 3.6 illustrates the total field, (Figure 3.6 (a)), and the resultant scattered field, (Figure 3.6 (b)), after subtracting the incident field for a continuous wave Gaussian beam at $\lambda = 600$ nm, incident from the bottom on a 300 nm diameter glass cylinder. Radiation is primarily scattered in the forward direction, with a lobe in the reverse direction that is surrounded by regions of lesser intensity centred at 120° measured from the forward direction. Figure 3.7 compares the scattered angular intensity profile from the FDTD simulation to a theoretical profile obtained via Mie theory [16]. In Figure 3.7 (solid line) the scattered

$$\lambda = 600 \text{ nm}$$

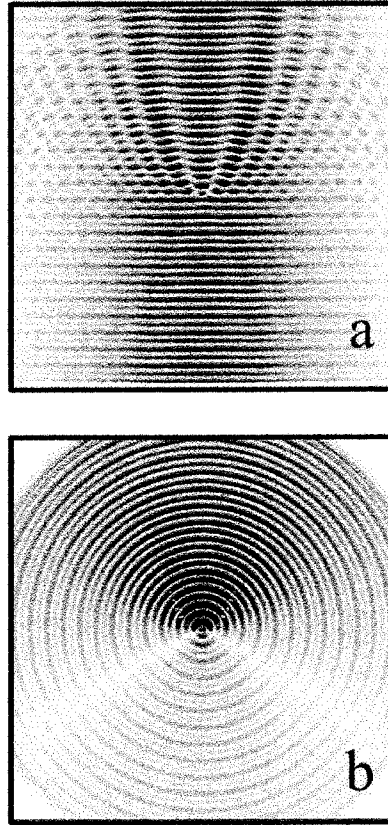


Figure 3.6 – (a) The total electric field for $\lambda = 600 \text{ nm}$ radiation incident on the bottom of a 300 nm diameter glass cylinder. (b) The electric field scattered from the cylinder.

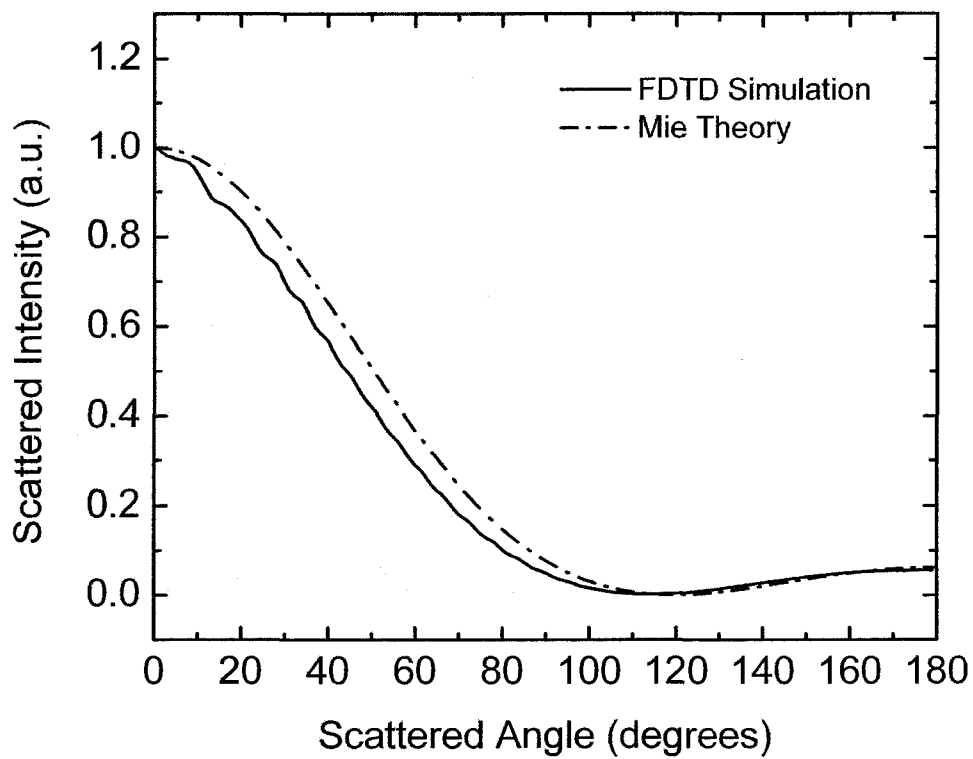


Figure 3.7 – (solid line) Scattered intensity profile calculated via the FDTD simulation for $\lambda = 600$ nm radiation incident on the bottom of a 300 nm diameter glass cylinder. (dashed line) Scattered intensity profile as calculated by Mie theory.

intensity profile is depicted as calculated via the FDTD simulation. Here, the figure confirms that radiation is primarily scattered in the forward direction. The single reverse lobe arises due to the interference between multiple scattered wavelets from the cylinder. Figure 3.7 (dashed line) illustrates the scattered intensity profile of the same particle as calculated by Mie theory. For these two profiles, the maximum error is less than 10%.

3.3.2 *Spatial Electric Field Distribution Surrounding Al₂O₃ Nanoparticles*

While the angular intensity profile can be obtained from FDTD simulations of the scattered electromagnetic field surrounding a particle, this does not show the total distribution of the EM field in two dimensions surrounding the particle. Such information is useful to determine the spatial distribution, and the effective pumping rate in the region surrounding both solitary particles and ensembles of scattering nanoparticles. Figure 3.8 depicts the time-averaged total electric field in the spatial region surrounding solitary 25 nm, 50 nm, and 100 nm diameter Al₂O₃ cylinders suspended in methanol at both the pump wavelength, $\lambda_{pump} = 532$ nm, and the peak emission wavelength, $\lambda_{laser} = 564$ nm. Each scattering particle has a surface roughness of ~ 1 nm. The advantage of averaging the field amplitude over the entire simulation time compared to an instantaneous profile is that the average field picture produces a single image illustrating the overall field profile of the scattered radiation. For a dielectric Al₂O₃ particle, the field distribution at both $\lambda_{pump} = 532$ nm and $\lambda_{laser} = 564$ nm arises purely from scattering. The overall effect is that radiation interacting with an individual Al₂O₃ particle will have its direction of propagation altered by scattering.

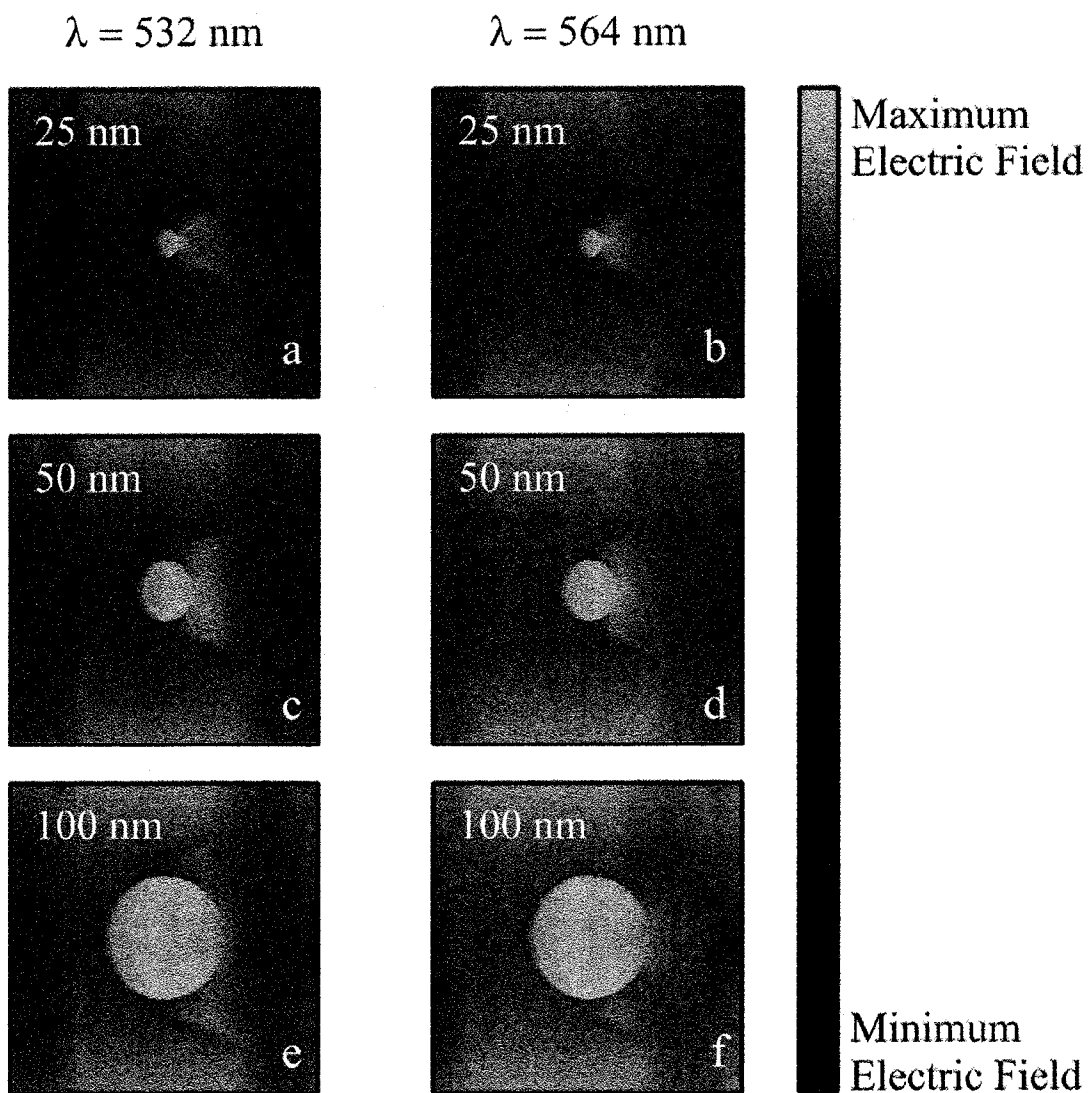


Figure 3.8 – Simulated electric field distribution surrounding 25 nm (a, b), 50 nm (c, d) and 100 nm (e, f) diameter Al_2O_3 particles suspended in methanol. The electric field is calculated for both $\lambda_{\text{pump}} = 532 \text{ nm}$ and $\lambda_{\text{laser}} = 564 \text{ nm}$ which are incident from the left side.

$\lambda = 532 \text{ nm}$

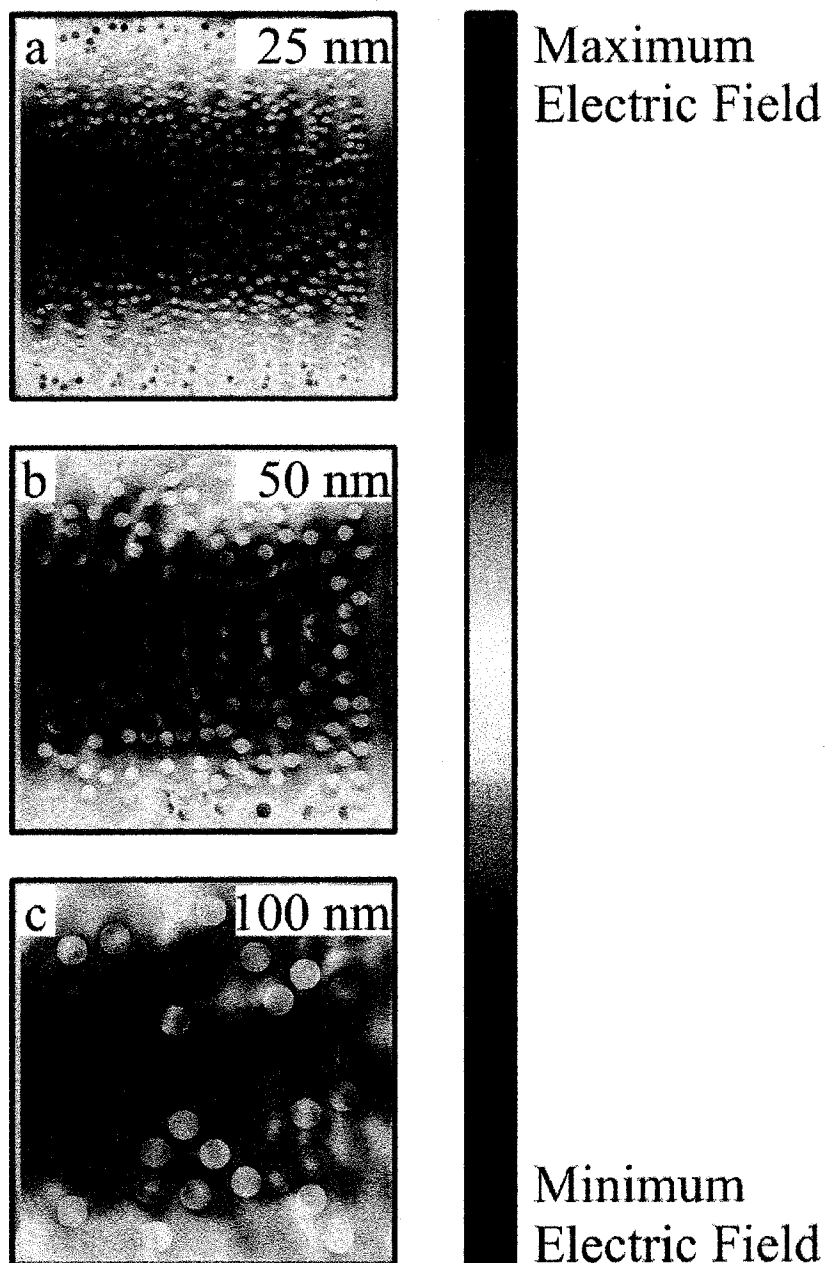


Figure 3.9 – Simulated average electric field distribution $\lambda_{\text{pump}} = 532 \text{ nm}$ (incident from the left side) in ensembles composed 25 nm (a), 50 nm (b) and 100 nm (c) diameter Al_2O_3 particles suspended in methanol. Each image is $1.25 \mu\text{m} \times 1.25 \mu\text{m}$.

To establish lasing in a random gain media, it is necessary to have a sufficient number of scattering particles so that multiple scattering increases the optical path length beyond the critical length. Figure 3.9 displays the electric field profile surrounding randomly distributed ensembles of 25 nm, 50 nm, and 100 nm diameter Al₂O₃ scattering cylinders suspended in methanol. Here, the scattering from multiple particles causes the radiation to be scattered throughout the particle ensemble.

3.3.3 *Spatial Distribution of Electric Field Surrounding Ag Nanoparticles*

A sharp contrast can be seen between the simulated EM field profiles from metallic nanoparticles and dielectric particles. This contrast arises from the SP excitation of the subwavelength sized metallic nanoparticle, which greatly alters the spatial distribution of EM fields near the particle surface. Figure 3.10 illustrates the time-averaged total electric field distribution surrounding 25 nm, 50 nm, and 100 nm Ag particles having a surface roughness of ~ 1 nm. The contribution of SP electric field localization is evident, as there is a localized region of high fields near the surface of each particle. For the particles with diameters of 25 nm, 50 nm, and 100 nm the magnitudes of the electric field enhancement near the surface at both $\lambda_{laser} = 564$ nm and $\lambda_{pump} = 532$ nm are calculated to be 21, 31, and 14 respectively. As can be seen in Figure 3.11, both λ_{laser} and λ_{pump} are enhanced to approximately the same extent in the same spatial region. Figure 3.11 illustrates the normalized peak intensity of the EM field as a function of the radial distance from the center of 25nm, 50 nm, and 100 nm diameter Ag particles. For both $\lambda_{laser} = 564$ nm and $\lambda_{pump} = 532$ nm, the intensity enhancement λ_{pump} occurs in a spatial region extending ~ 10 nm away from the surface of each particle. It should be noted that for $\lambda_{pump} = 532$ nm, this

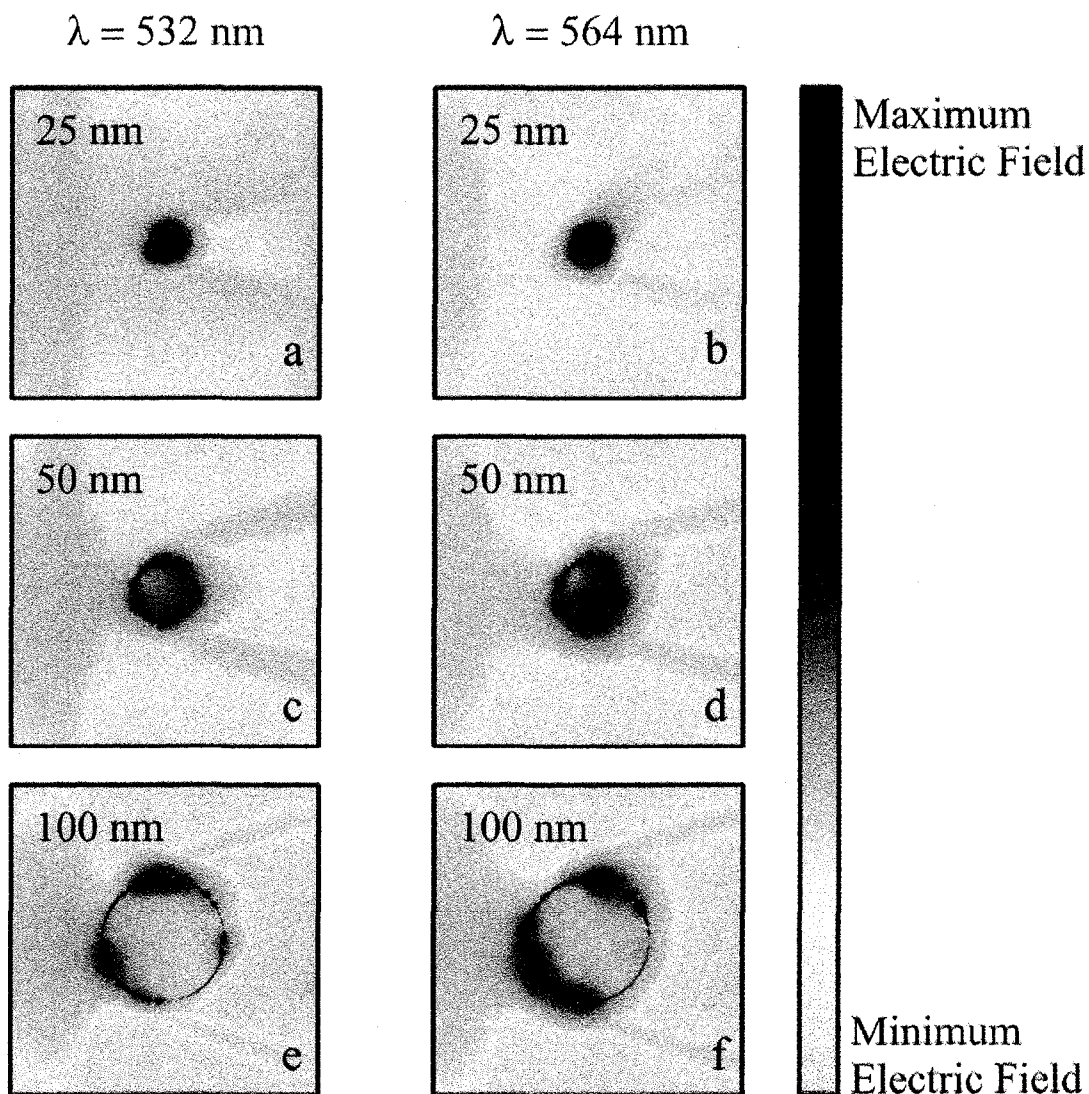


Figure 3.10 – Simulated average electric field distribution surrounding 25 nm (a, b), 50 nm (c, d) and 100 nm (e, f) diameter Ag particles suspended in methanol. The electric field is calculated for both $\lambda_{pump} = 532 \text{ nm}$ and $\lambda_{laser} = 564 \text{ nm}$ which are incident from the left side. Large electric field enhancement (~ 30) near the surface of each nanoparticle is evident at both wavelengths.

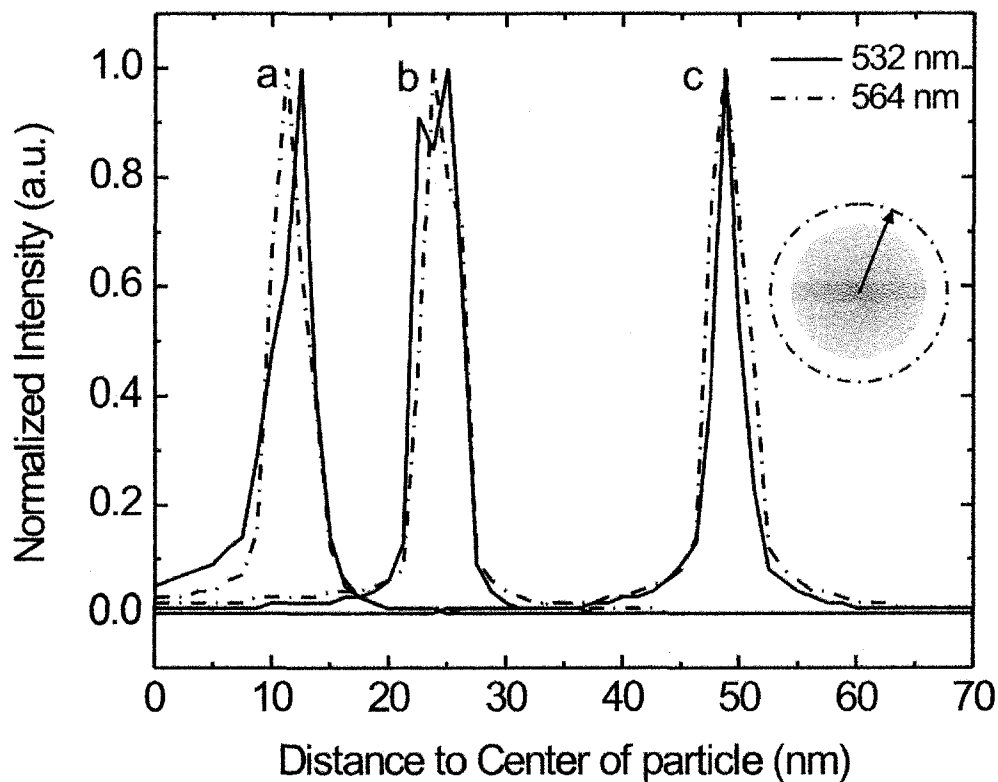


Figure 3.11 – Normalized peak intensity at $\lambda_{pump} = 532$ nm (solid line) and $\lambda_{laser} = 564$ nm (dashed-dotted line) as a function of the distance to the center of 25 nm (a), 50 nm (b), and 100 nm (c) Ag nanoparticles suspended in methanol. A near-field interaction region of large electromagnetic field enhancement is present within ~ 10 nm of the surface of each particle.

profile defines the near-field optical gain region. With such large intensities near the surface, the energy fluence near the surface is approximately an order of magnitude greater than in the far field. It is expected that because of this spatial overlap, a region of high optical gain will develop near the Ag particle surface. The localized high gain region will enhance the performance of a random laser constructed with Ag scattering particles when compared to one constructed with Al₂O₃ scattering particles.

The specific geometric shape of a silver nanoparticle determines the magnitude of the near-field electric field, the location of the peak SP resonance, and spectral width of the resonance [17]. With proper choice of the geometrical shape, localized electric field enhancements of up a factor of ~ 500 can be achieved for profiles with sharp corners [18]. Large enhancement can also be achieved for an incident wavelength at the peak of the SP resonance. Figure 3.12 displays the electric field profile surrounding Ag squares with 50 nm long sides and Ag triangles with 50 nm long bases pointing in the four cardinal directions. For the shapes shown in Figure 3.12 (a-j), the maximum field enhancement at $\lambda_{pump} = 532$ nm and $\lambda_{laser} = 564$ nm is ~ 38 .

In an ensemble of Ag nanoparticles, shown in Figure 3.13 (a-c), the scattered waves from individual Ag particles can coherently couple to SP waves in neighbouring Ag particles. Figure 3.14 depicts the electric field distribution for an ensemble consisting of 57% 50 nm diameter Ag and 43% 100 nm diameter Al₂O₃ nanoparticles. Regions of SP field enhancement are present between adjacent Ag nanoparticles and the scattered radiation penetrates deeper into the scattering media than for 50 nm Ag nanoparticles alone. Thus, a collection of both Ag and Al₂O₃ particles is likely to result in the use of a greater portion of the available gain volume in a random laser.

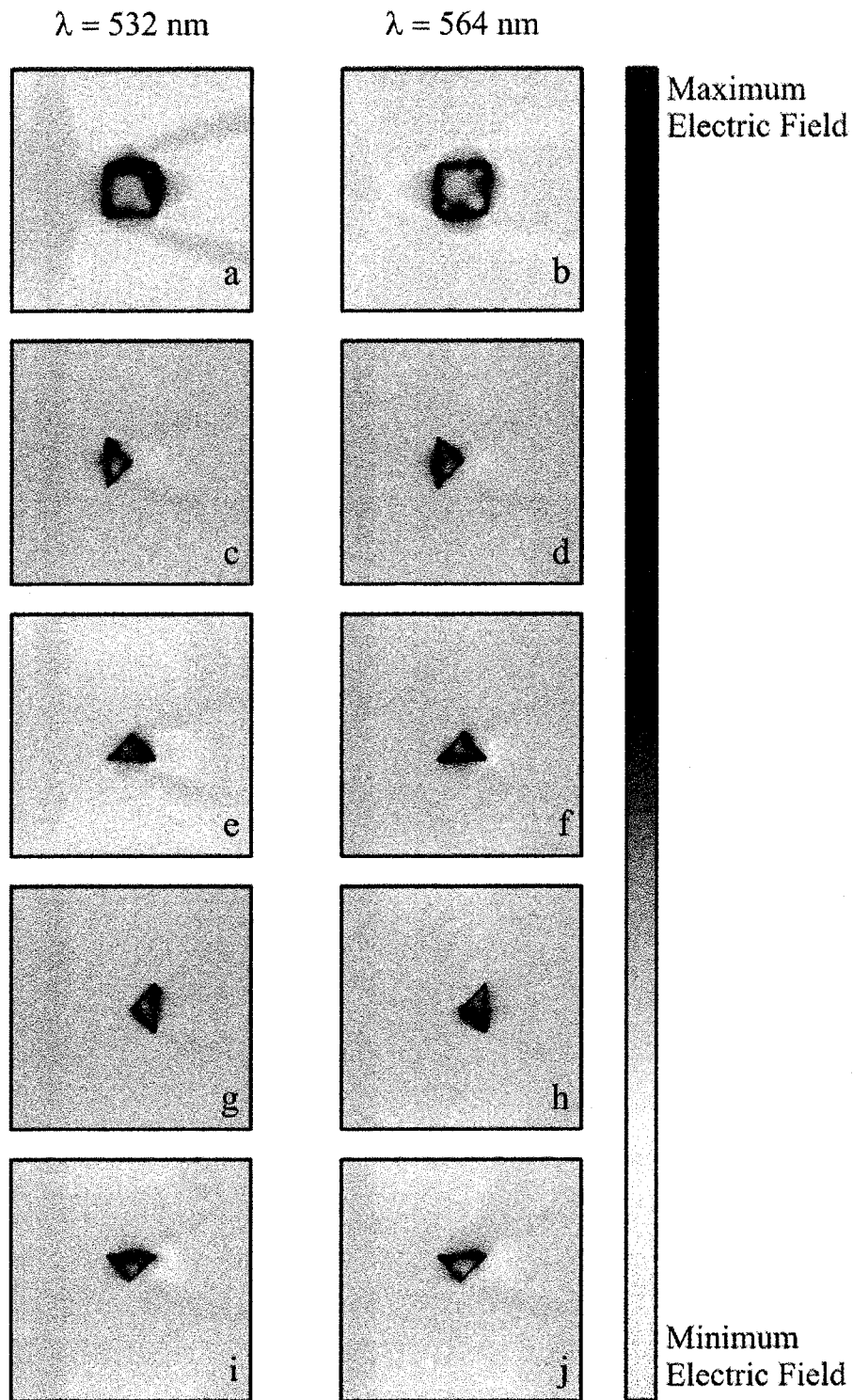


Figure 3.12 – Simulated average electric field distribution surrounding Ag squares having 50 nm long sides (a, b) and Ag triangles with 50 nm long bases (c-j) pointing in all cardinal directions. For the displayed particle shapes, the $\lambda_{pump} = 532$ nm and $\lambda_{laser} = 564$ nm radiation are incident from the left side.

$$\lambda = 532 \text{ nm}$$

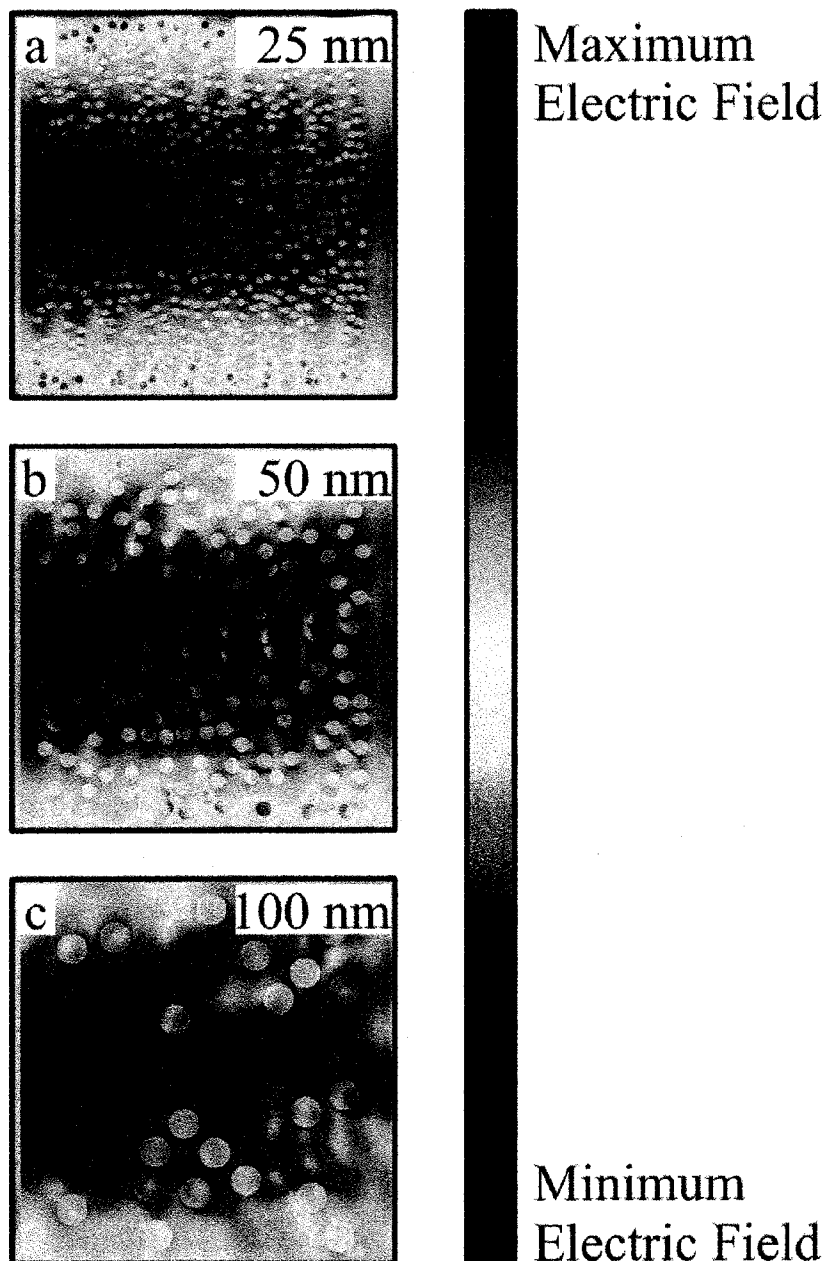


Figure 3.13 – Simulated average electric field distribution surrounding an ensemble of Ag nanoparticles with diameters of 25 nm (a), 50 nm (b), and 100 nm (c). The $\lambda_{\text{pump}} = 532 \text{ nm}$ incident (from the left side) radiation is scattered throughout the simulation space. Large electric field enhancement is evident at the surface of each particle and within regions between adjacent particles. Each image is $1.25 \mu\text{m} \times 1.25 \mu\text{m}$.

$$\lambda = 532 \text{ nm}$$

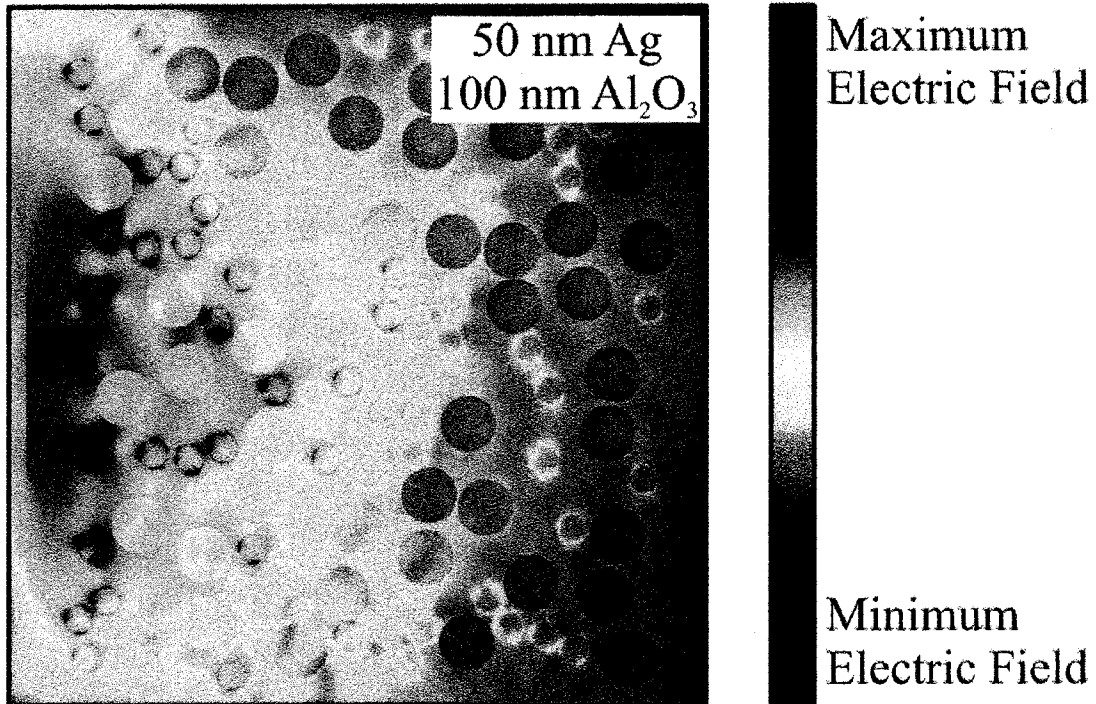


Figure 3.14 – Simulated average electric field distribution of an ensemble consisting of 57% 50 nm diameter Ag and 43% 100 nm diameter Al_2O_3 nanoparticles. The $\lambda_{\text{pump}} = 532 \text{ nm}$ radiation is incident from the left side. The image is $1.25 \mu\text{m} \times 1.25 \mu\text{m}$.

3.4 FDTD Gain Model Simulations

3.4.1 FDTD Simulation

Using the FDTD gain model outlined in section 3.2.7, the spatial and temporal distribution of the EM fields in both a resonant optical cavity and a random gain media are investigated. For the simulations discussed herein the material parameters were selected to approximate a laser dye [13]. The chosen material parameters were population level lifetimes of $\tau_{32} = 1 \times 10^{-13}$ s, $\tau_{21} = 1 \times 10^{-9}$ s, and $\tau_{10} = 1 \times 10^{-11}$ s. As the lifetime of level N_2 is more than two orders of magnitude greater than the lifetime of level N_1 , a population inversion will occur when level N_2 is pumped. The upper level N_3 also decays quickly enough such that the population in N_3 remains negligible. It is assumed that all atoms in the medium are initially in the ground state (N_0), with a number density of $5.5 \text{ mol}\cdot\text{m}^{-3}$, or $3.3 \times 10^{24} \text{ m}^{-3}$. Figure 3.15 illustrates the population of levels N_2 and N_1 at a pumping rate, $P_r = 1 \times 10^7 \text{ s}^{-1}$. Here, the population of N_2 asymptotically approaches a steady state value of $3.3 \times 10^{22} \text{ m}^{-3}$ within 5 ns.

3.4.2 Simulation of a Resonant Optical Cavity

To confirm that the optical gain model is capable of simulating laser operation, a simple laser system was investigated. This laser system consists of two $1 \text{ }\mu\text{m}$ thick silver mirrors separated by a gain medium as illustrated in Figure 3.16. In order to limit the computational resources required, the size of the geometry is limited to 500×500 grid points, with $\Delta s = 50 \text{ nm}$, and a cavity length of $20 \text{ }\mu\text{m}$. With these parameters, the time step, $\Delta t = 1 \times 10^{-16} \text{ s}$, making it possible to simulate the laser performance over hundreds of picoseconds. Here, both the peak gain wavelength and the peak emission wavelength

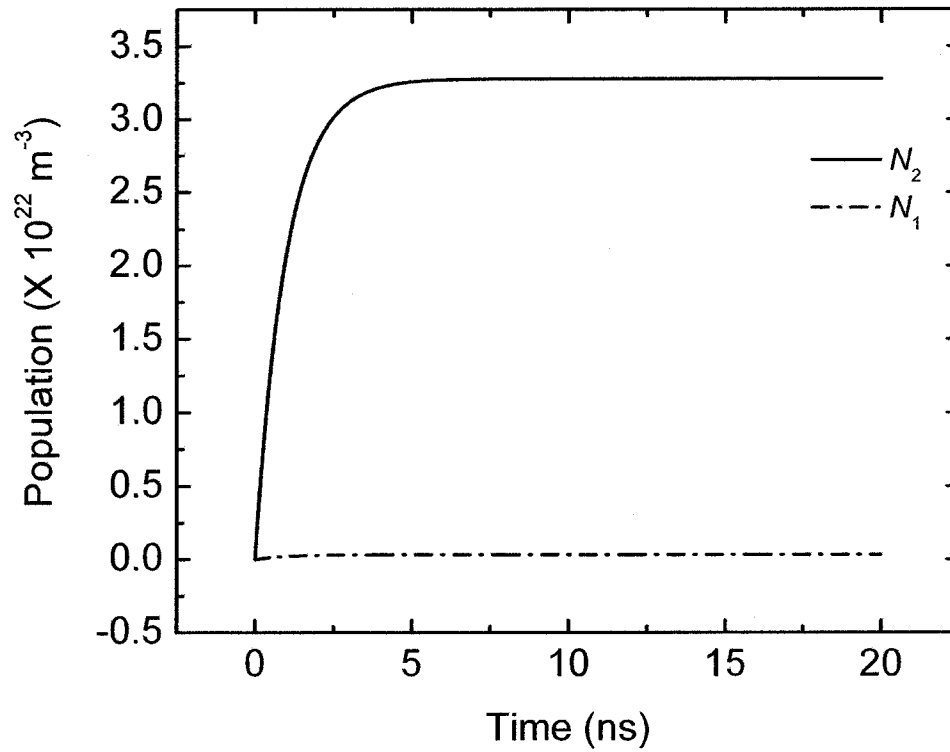


Figure 3.15 – Calculated atomic population levels for a four-level gain media (Levels N_0 and N_3 not shown) with a pumping rate of $1 \times 10^7 \text{ s}^{-1}$. The development of the population inversion for the gain media without a resonant cavity can be seen.

are centered at $\lambda_{laser} = 500$ nm, while the gain and emission bandwidth are chosen to be 60 nm. Figure 3.16 shows several images illustrating the modeling of this laser. Figure 3.16 (a) depicts the cavity geometry, colour coded according to the material at each grid point. Here, black represents free space, blue represents the gain material, and yellow represents the silver mirrors forming the resonant cavity. Figure 3.16 (b) illustrates the electric field magnitude of the pump beam at time, $t = 2$ ps. It is a continuous wave, Gaussian beam at $\lambda_{laser} = 500$ nm, with a focal spot size of 7.5 μm . Figure 3.16 (c) depicts the emitted electric field magnitude at $t = 2$ ps, illustrating the spontaneously emitted radiation due to the population of atoms at energy level N_2 . Here, the presence of what appears to be many point sources is due to the slight wavelength variation caused by the Lorentzian distribution of source wavelengths. The electric field at each grid point oscillates at a slightly different frequency, causing an interference pattern due to the superposition of fields. At $t = 80$ ps, the electric field magnitude is plotted in Figure 3.16 (d), which illustrates that the resonant cavity has preferentially selected radiation propagating along its optical axis, while the gain media has repeatedly amplified the emission.

It is illuminating to investigate the temporal development of the population inversion in the optical gain media for this simulated laser. Figure 3.17 depicts the population levels N_2 and N_1 as a function of t at the center of the optical resonator cavity. The material parameters of the gain material in this simulation are the same as for the gain material in section 3.4.1. Figure 3.17 illustrates that the population of level N_2 reaches a maximum of $4.8 \times 10^{21} \text{ m}^{-3}$ at $t = 140$ ps. The value of N_2 here is considerably smaller than the asymptotic maximum population of $3.3 \times 10^{22} \text{ m}^{-3}$ reached under steady

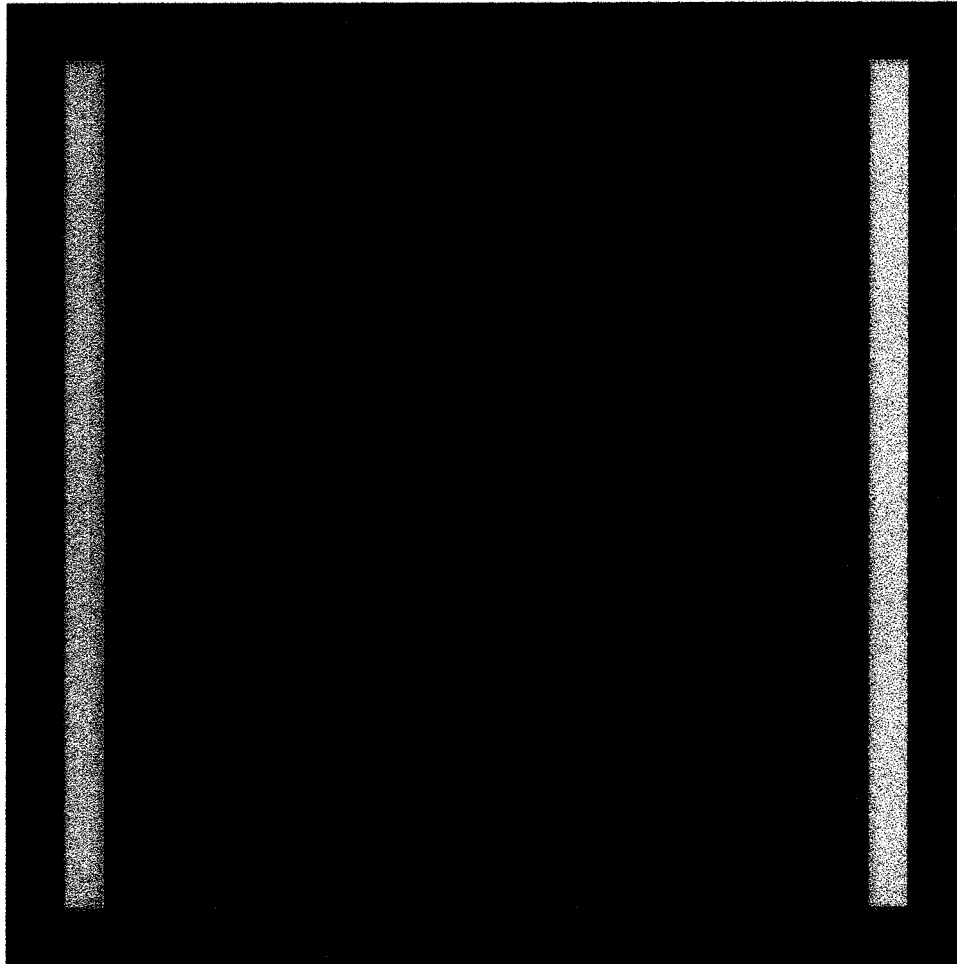


Figure 3.16 – Illustration of the $25\ \mu\text{m} \times 25\ \mu\text{m}$ simulated laser cavity. (a) The cavity geometry is colour coded according to the material at each grid point. Black represents free space, blue represents the gain material, and yellow represents the silver mirrors.

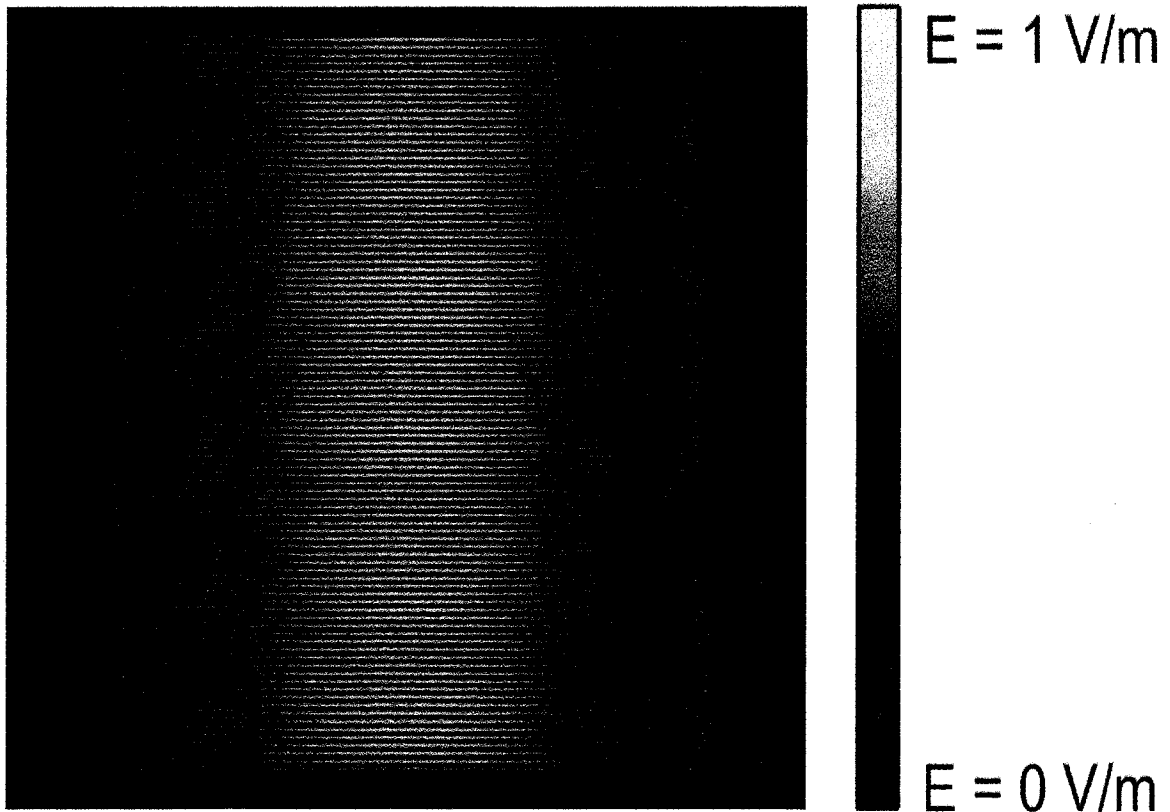


Figure 3.16 – (b) The electric field magnitude of the pump beam at time $t = 2$ ps. The pump beam is incident from the bottom at $\lambda = 500$ nm. The image size is $25 \mu\text{m} \times 25 \mu\text{m}$.

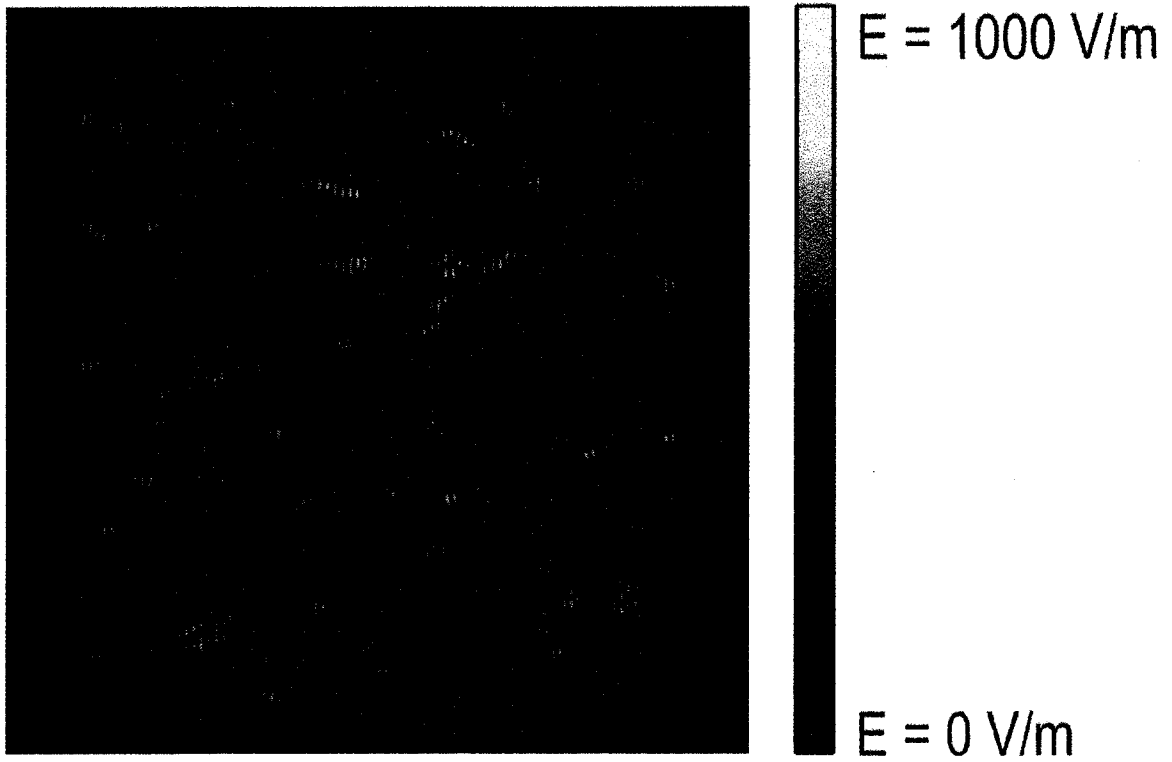


Figure 3.16 – (c) The spontaneously emitted electric field magnitude at $t = 2 \text{ ps}$. The image size is $25 \mu\text{m} \times 25 \mu\text{m}$.

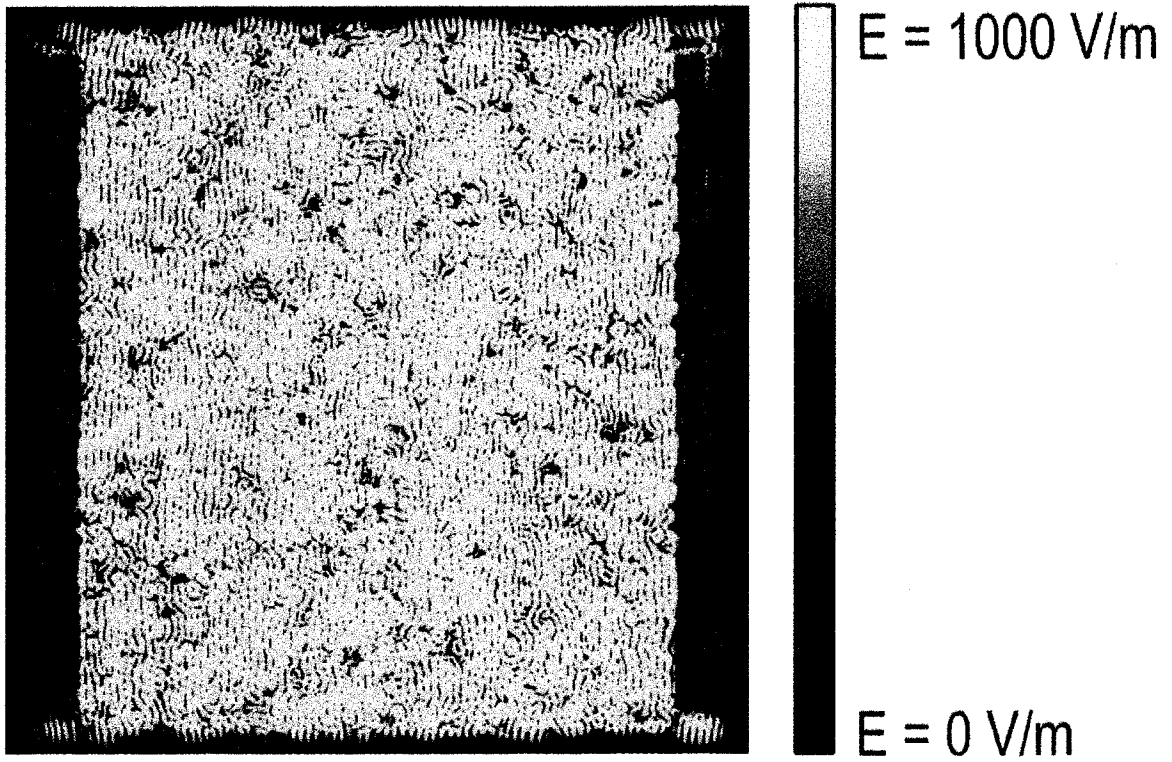


Figure 3.16 – (d) Electric field magnitude at $t = 80 \text{ ps}$ illustrating the amplification of radiation propagating along the optical axis of the resonator. The image size is $25 \mu\text{m} \times 25 \mu\text{m}$.

state conditions after 5 ns of excitation. As the intensity along the optical axis increases due to the combination of spontaneous emission and optical gain, the number of stimulated atomic transitions from N_2 to N_1 also increases accordingly. At $t = 137$ ps the combined rate of spontaneous and stimulated transitions from N_2 to N_1 is greater than the rate of spontaneous transitions from N_3 to N_2 , and the gain medium begins to saturate. In addition to the development of the population inversion in this optical gain media, it is also interesting to investigate the wavelength distribution of the spontaneous emission. Figure 3.18 illustrates the wavelength distribution of the spontaneous emission sources. The light gray lines in this figure depict the wavelength distribution of the radiation sources in the cavity, while the dashed-dotted line represents the theoretical distribution calculated according to equation 3.105. Here, it can be seen that there is a very close match between the expected and measured distributions.

Figure 3.19 presents a series of temporal snapshots of the spectral components that are present in the FDTD simulation of the emitted field. Each graph in the figure depicts the emitted radiation spectrum over a specific 10 ps long time period. Figure 3.19 (a) illustrates the spontaneous emission that occurs in the first 10 ps after the onset of pumping. This graph illustrates that the emission during this early time period is primarily broadband. As t advances to 40 ps, the spectrum becomes narrower, with individual spectral lines appearing in the output as in Figure 3.19 (d). The peak intensity also greatly increases by an order of magnitude from 1.3×10^8 to 2.0×10^9 as radiation propagates through the optical cavity. At $t = 100$ ps (Figure 3.19 (g)), a single, well-defined spectral peak at $\lambda = 514$ nm is present in the emission. This spectral peak indicates the onset of lasing in a single mode in the optical cavity. At $t = 150$ ps, (Figure

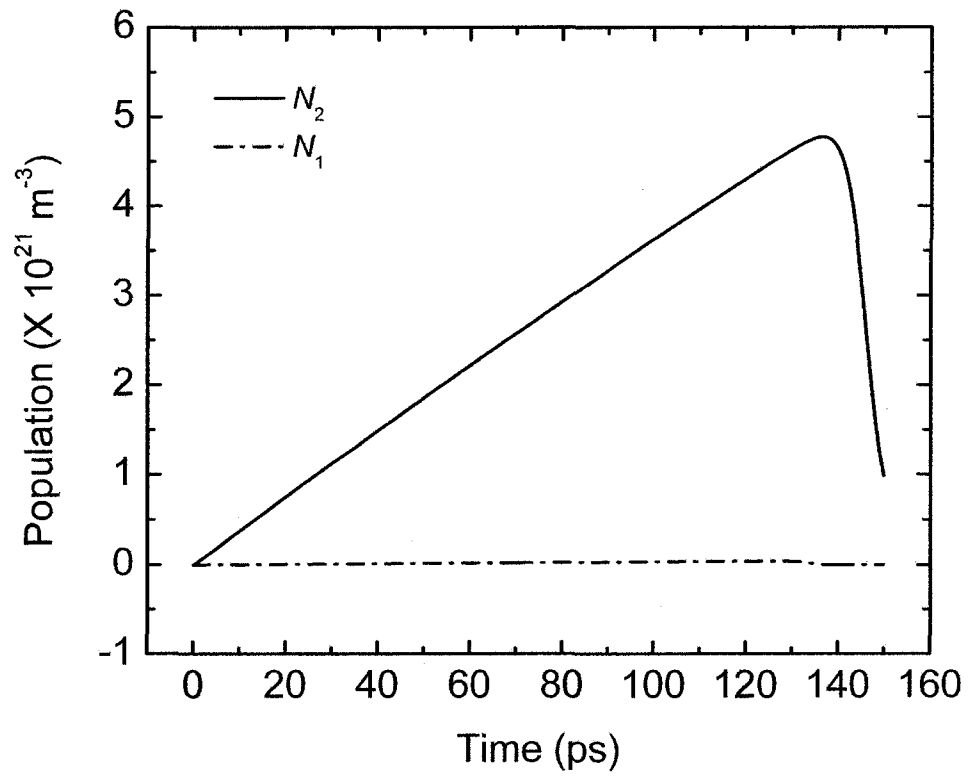


Figure 3.17 – Population levels N_2 and N_1 as calculated by the FDTD simulation as a function of t at the center of the optical resonator cavity shown in Figure 3.16.

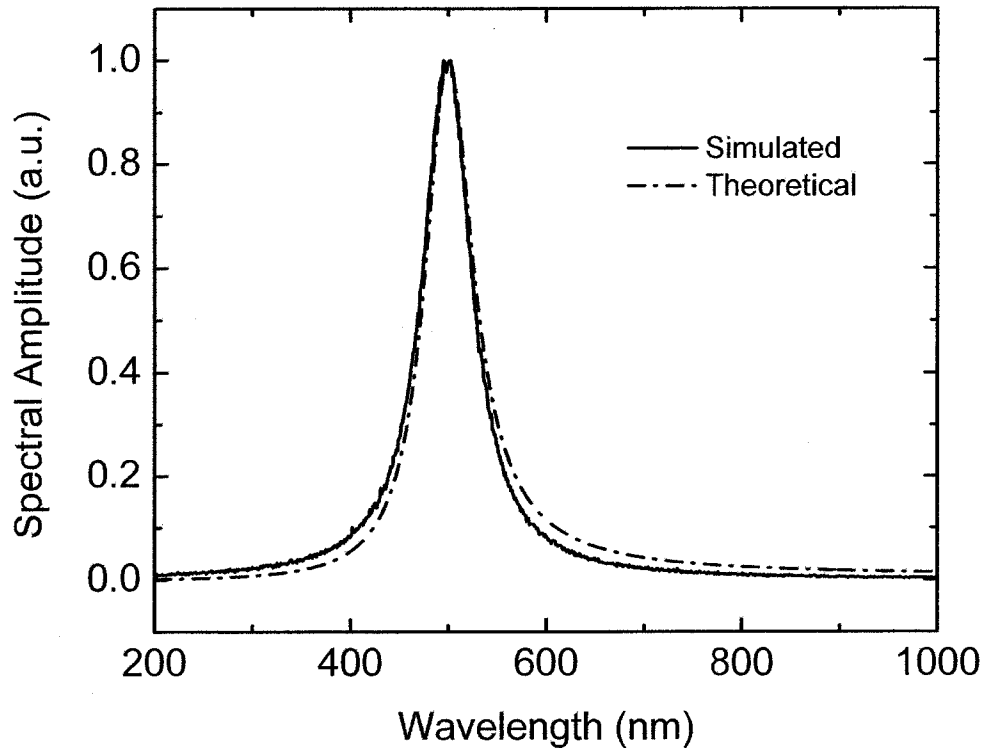


Figure 3.18 – The wavelength distribution of spontaneously emitted radiation for the FDTD simulation. The dashed-dotted line is the expected Lorentzian wavelength distribution with a bandwidth of 60 nm. The solid line is the actual distribution of radiation sources within the simulation space.

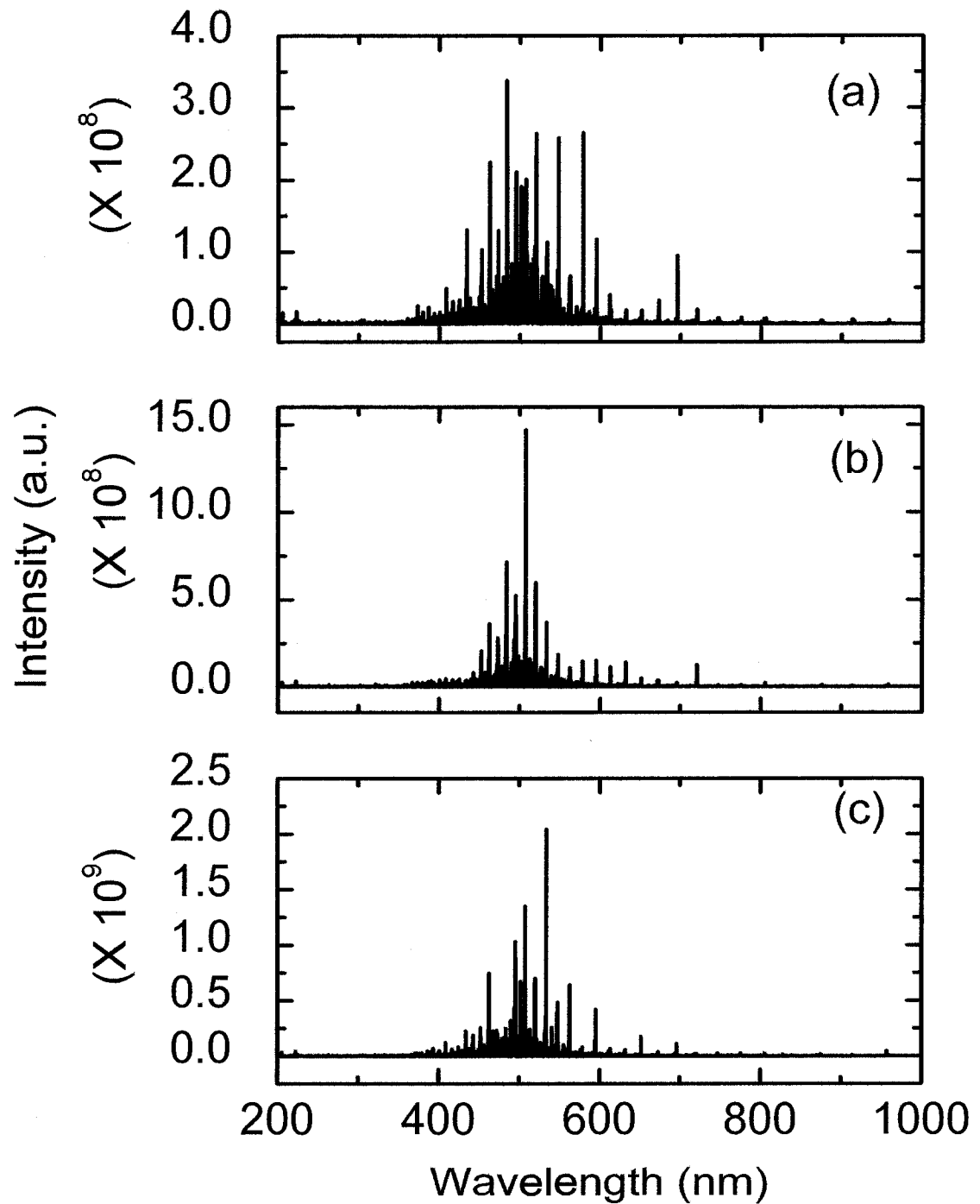


Figure 3.19 – The temporal evolution of the spectral components present in the FDTD simulation of the emitted field. Each graph in the figure represents the emitted radiation spectrum over a specific 10 ps long time period. (a) 0-10 ps (b) 10-20 ps (c) 20-30 ps

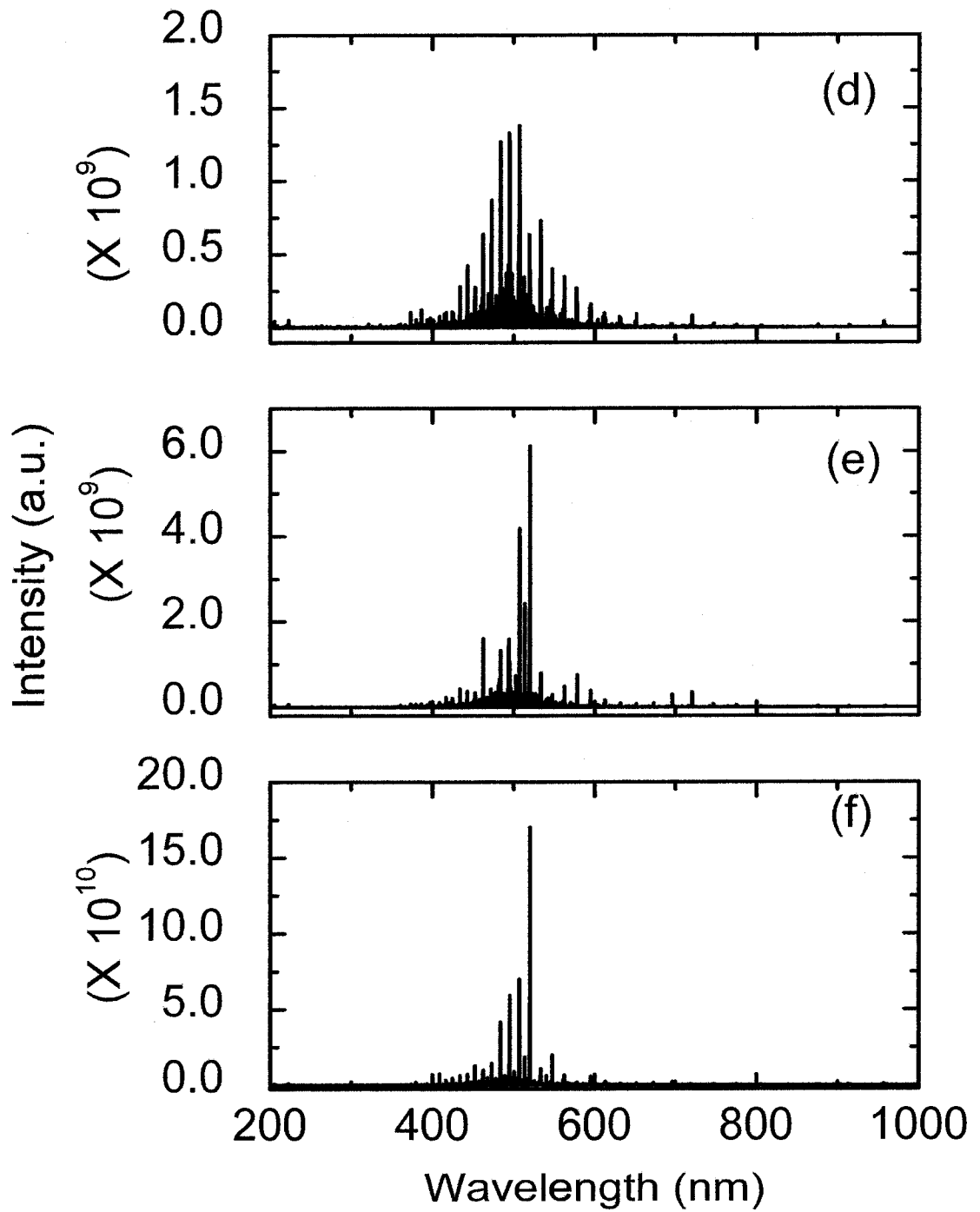


Figure 3.19 – (d) 30-40 ps (e) 50-60 ps (f) 70-80 ps

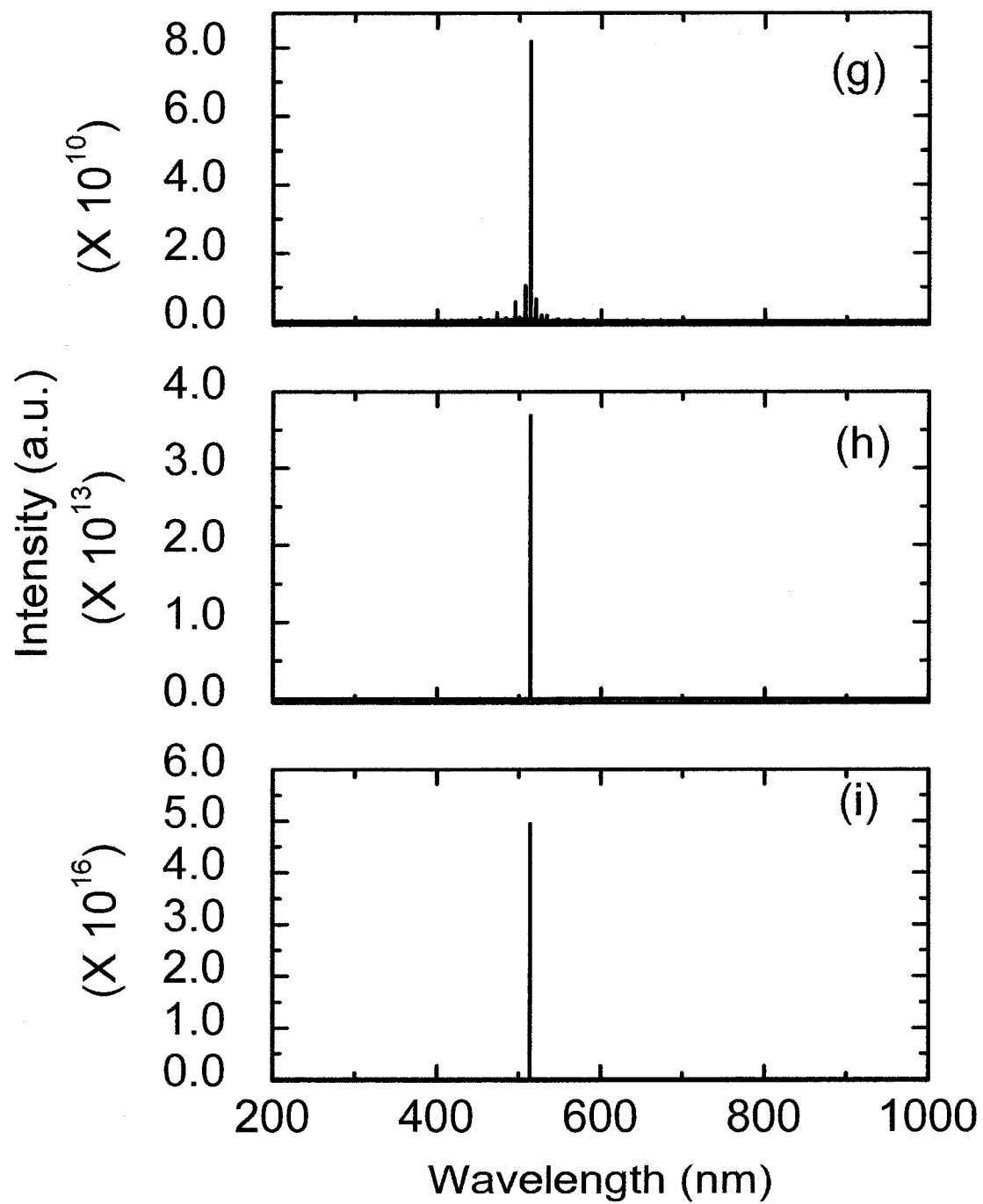


Figure 3.19 – (g) 90-100 ps (h) 110-120 ps (i) 140-150 ps.

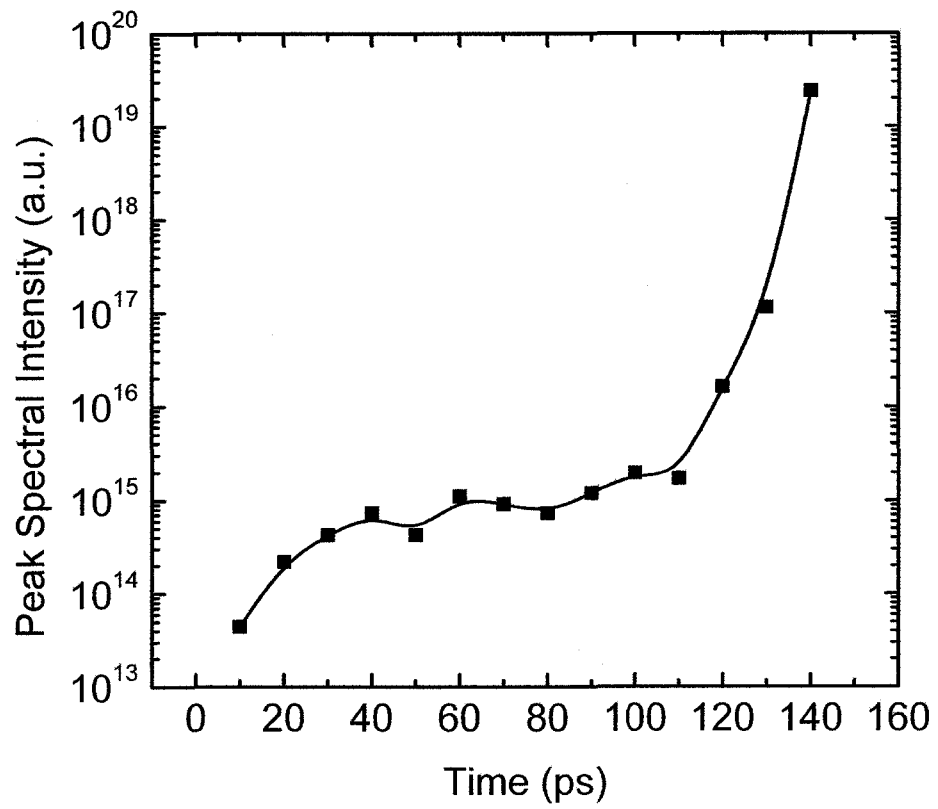


Figure 3.20 – Total spectral intensity as a function of time for the simulated optical resonator cavity.

3.19 (i)), the intensity increases by a factor of 2×10^6 and a single prominent spectral line is now apparent in the laser output. The peak spectral intensity in the simulated laser resonator cavity is depicted as a function of time in Figure 3.20.

3.4.3 *Simulation of a Random Gain Media*

While the simulated results of a simple optical cavity are interesting and useful to confirm the proper operation of the FDTD gain model, they are not strictly related to the operation of a random laser. In this section, the FDTD gain model is used to investigate the operation of an optical gain media with dispersed subwavelength sized Ag nanoparticles. There are several factors that must be controlled when investigating random laser operation with these small scattering centers. The primary issue is the computational resources required to simulate geometries where the scattering particles are only 50 nm in diameter, compared to the laser wavelength ($\lambda_{laser} = 500$ nm) in the FDTD simulation space. The small particle size requires the use of a spatial step $\Delta s = 5$ nm, which increases the memory requirements by a factor of 100 over the simulations discussed in 3.4.2. With a reduction in Δs by a factor of 10, Δt must also be reduced. In order to satisfy the stability criterion, Δt must be less than 8.3×10^{-18} s, and thus $\Delta t = 5 \times 10^{-18}$ s was chosen. Since this Δt is a factor of 20 smaller than the Δt used in section 3.4.2, the simulation must be run over a number of time steps larger by a factor of 20 in order to approach the same temporal development of the population inversion. In order to simulate a $25 \mu\text{m} \times 25 \mu\text{m}$ spatial region as in the resonator cavity, the memory requirement increases by a factor of 100, which increases the computational time for each time step by a factor of 100. As the number of required time steps required increases by

a factor of 20, the total computation time for the two-dimensional simulation increases as $O(n^3)$ where n is the number of time steps. In comparison with the resonator cavity simulation which required approximately a week of run time and ~ 1 GB of memory on a 2.2 GHz Pentium 4, the random laser simulation would now require more than 100 GB of RAM and 38 years of computational time, an unrealistic task on a standard personal computer. To reduce the simulation requirements, the spatial extent of the simulation was reduced to $5 \mu\text{m} \times 5 \mu\text{m}$, which with $\Delta x = 5 \text{ nm}$ fills a grid of 1000×1000 . This simulation can then be performed over the course of a few months through the use of simultaneous computation on 48 parallel MIPS R12000 Revision: 3.5 processors operating at 400 MHz provided by the Westgrid computational facility.

The random gain media was created by distributing 50 nm Ag scatterers at an area packing fraction of 0.21 as depicted in Figure 3.21 (a). Here, black represents free space, blue represents the gain material, and yellow represents the Ag nanoparticles. This geometry is highly scattering, as the average separation between neighbouring Ag particles is only 105 nm. In this simulation, λ_{pump} , λ_{laser} , and λ_{gain} are all set to 500 nm to create a test case, with the gain and emission bandwidth both equal to 60 nm. Figure 3.21 (b) illustrates the electric field magnitude of the pump beam at $t = 0.25 \text{ ps}$, which shows a highly concentrated spatial profile, with significant localization of the field increasing the amplitude near the surface of each Ag nanoparticle. Unlike the simple resonator cavity, the emission in this geometry is not distributed uniformly throughout the optical gain media. Figure 3.21 (c) depicts the electric field magnitude at $t = 0.25 \text{ ps}$ illustrating that spontaneous emission occurs primarily in the spatial region in the near field of each Ag nanoparticle. At this stage, radiation has begun to escape from the active gain region at

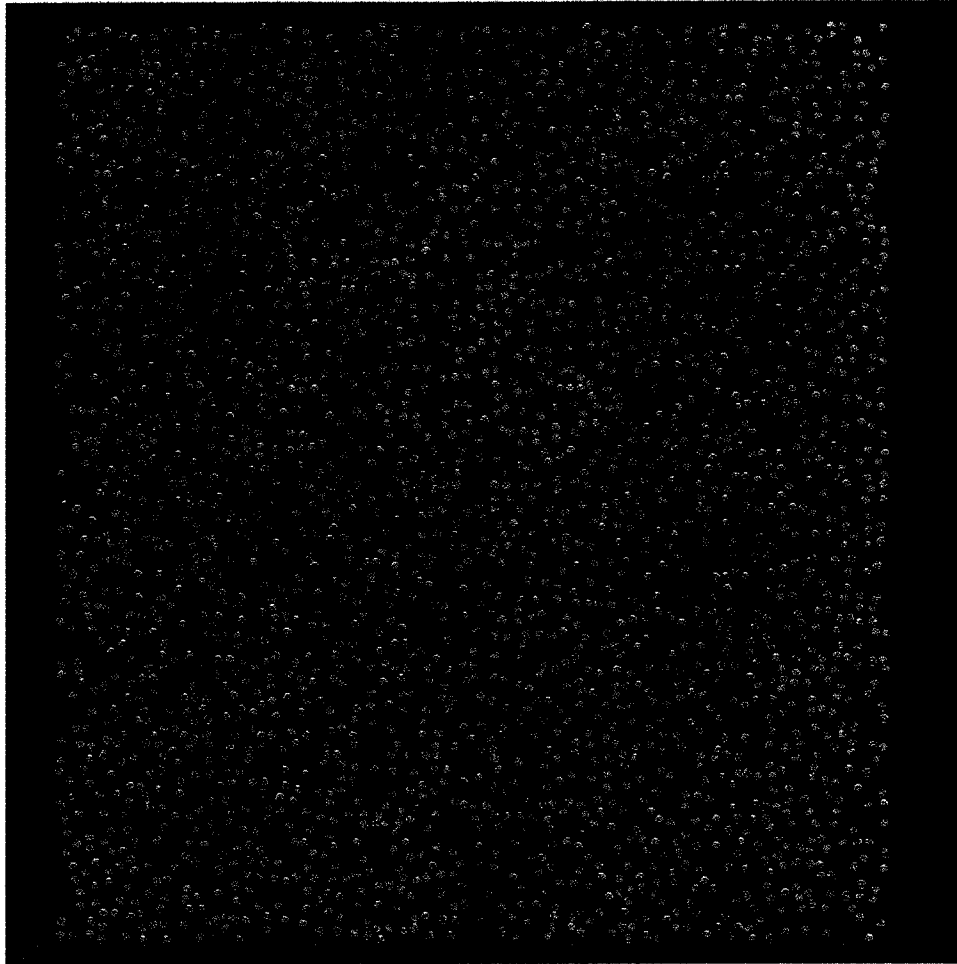


Figure 3.21 – Illustrations describing the operation of the simulated random laser. (a) The cavity geometry, which is $5\ \mu\text{m} \times 5\ \mu\text{m}$ and colour coded according to the material at each grid point. Black represents free space, blue represents the gain material, and yellow represents the silver mirrors.

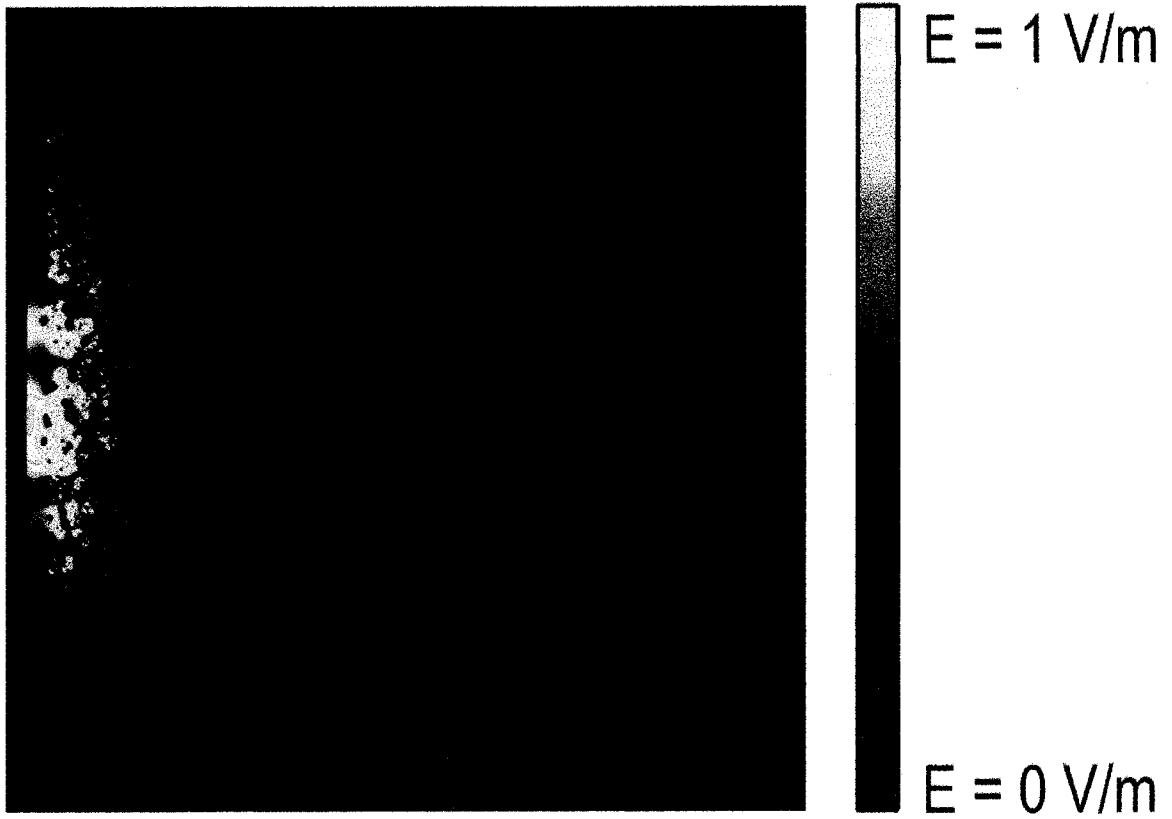


Figure 3.21 – (b) The electric field magnitude of the pump beam at time $t = 0.25 \text{ ps}$. The image size is $5 \mu\text{m} \times 5 \mu\text{m}$.

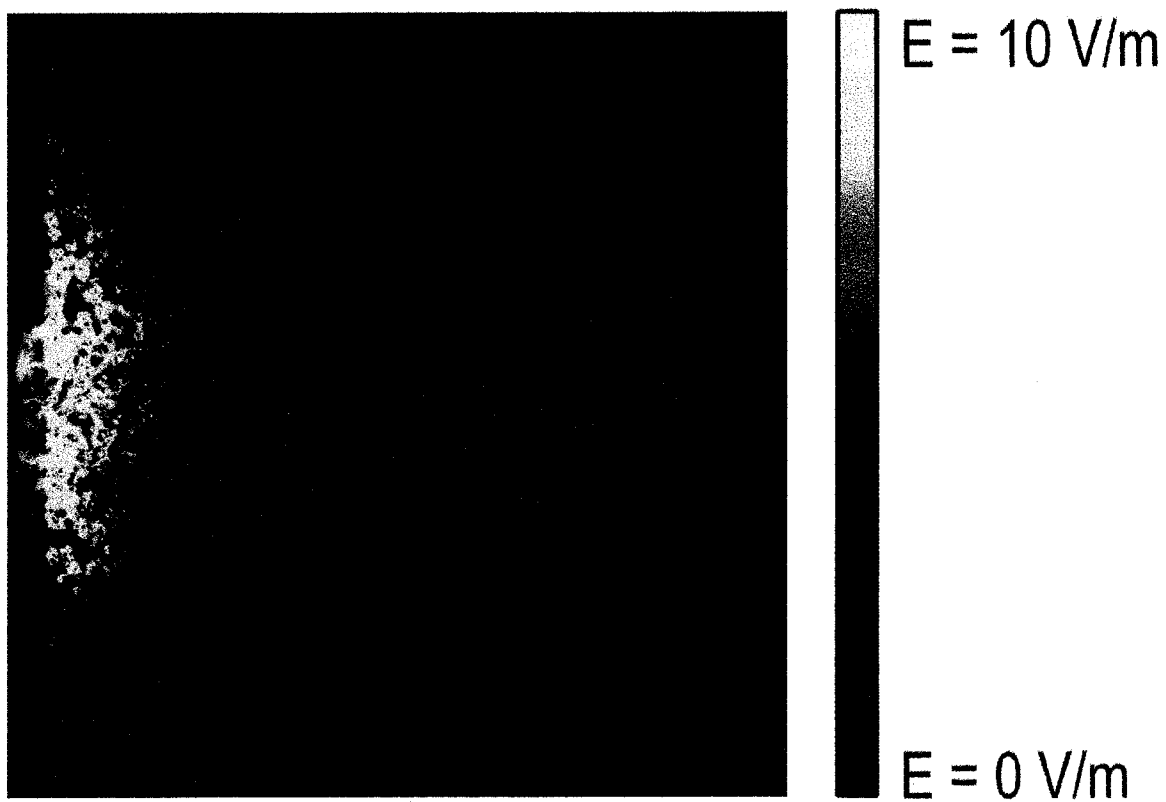


Figure 3.21 – (c) The spontaneously emitted electric field magnitude at $t = 0.25$ ps. The image size is $5 \mu\text{m} \times 5 \mu\text{m}$.

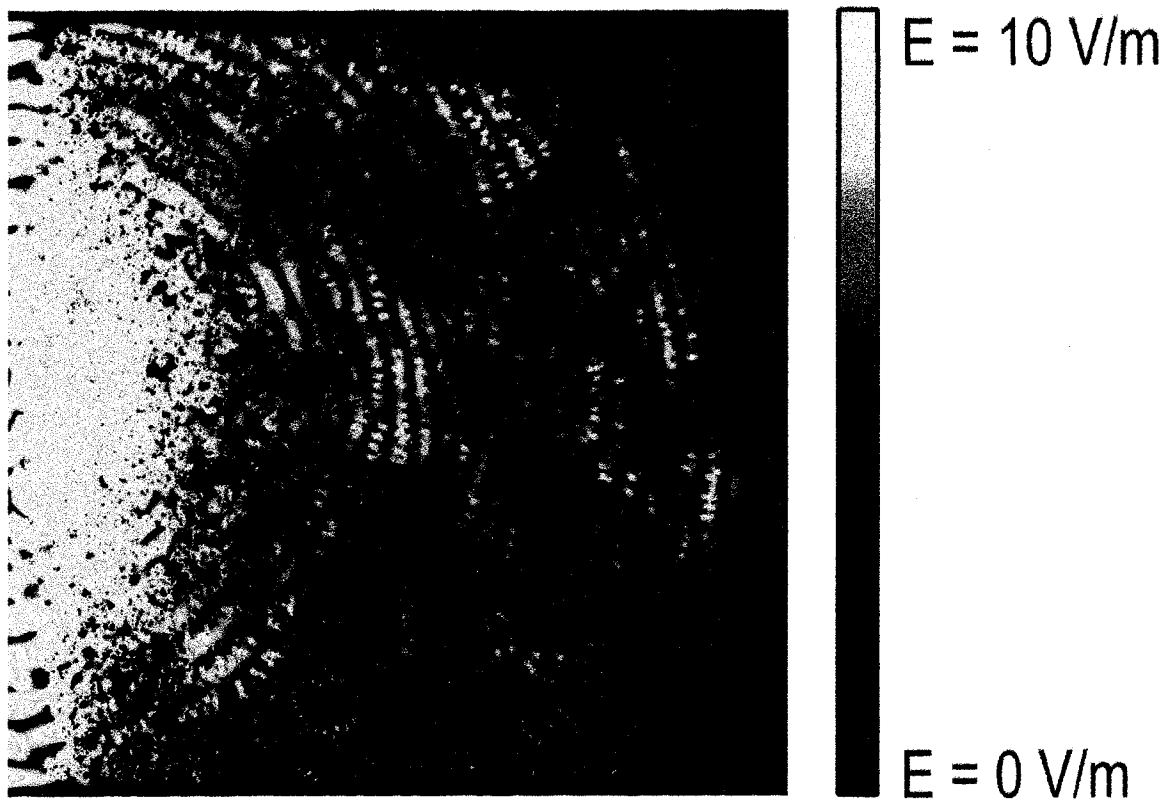


Figure 3.21 – (d) Electric field magnitude at $t = 15$ ps illustrating the intense amplification that occurs due to multiple scattering. The image size is $5 \mu\text{m} \times 5 \mu\text{m}$.

the surface of the random media. As the simulation time step progresses, each propagating wavefront is observed to scatter throughout the disordered gain media, with some wavefronts returning to the active region. Figure 3.21 (d) illustrates the electric field magnitude at $t = 15$ ps. Here, the emission has propagated from the intensely pumped active region in the vicinity of the excited surface throughout the bulk of the random media. The emitted radiation scatters through the simulation space and appears greatly amplified compared to the emission at $t = 0.25$ ps, indicating the onset of random laser emission from the sample.

Electric field enhancement near the surface of each Ag particle results in a factor of 20 increase in the energy fluence, which causes enhanced optical emission. Figure 3.22 depicts the temporal evolution of the spectral components that are present in the FDTD simulation of the emitted field. Each graph in the figure represents the emitted radiation spectrum over a specific 0.5 ps time period. Figure 3.23 (a) illustrates the broadband spontaneous emission that occurs in the first 0.5 ps after the onset of pumping. Such a lack of spectral narrowing is expected, as the emission during the first time slice has not experienced the multiple scattering required for optical feedback. As t advances to 10 ps (Figure 3.22 (f)), the spectrum becomes narrower, with individual spectral lines appearing in the output. There is an associated increase in the peak intensity by a factor of 250 as radiation is amplified through multiple scattering. At $t = 16$ ps (Figure 3.22 (i)), a single, well-defined spectral peak is present in the emission. This spectral peak indicates the onset of lasing in a single mode in the optical cavity. The peak emitted spectral intensity for the simulated random laser is depicted as a function of time in Figure 3.23. In this figure, the intensity can be seen to increase 400 times over the entire

simulated 16 ps interval. Unfortunately, the simulation would require more than a year of computational time to simulate the next several hundred picoseconds that would be required to determine if random lasing will occur in this specific geometry. The results of this simulation support the case for optical gain enhancement caused by surface plasmon resonance in silver nanoparticles.

In this chapter, the theoretical framework presented in this section provides the ability to develop models of any number of electromagnetic phenomena related to electromagnetic wave propagation through highly scattering media. The extension of this model to include the third dimension would greatly increase its predictive ability.

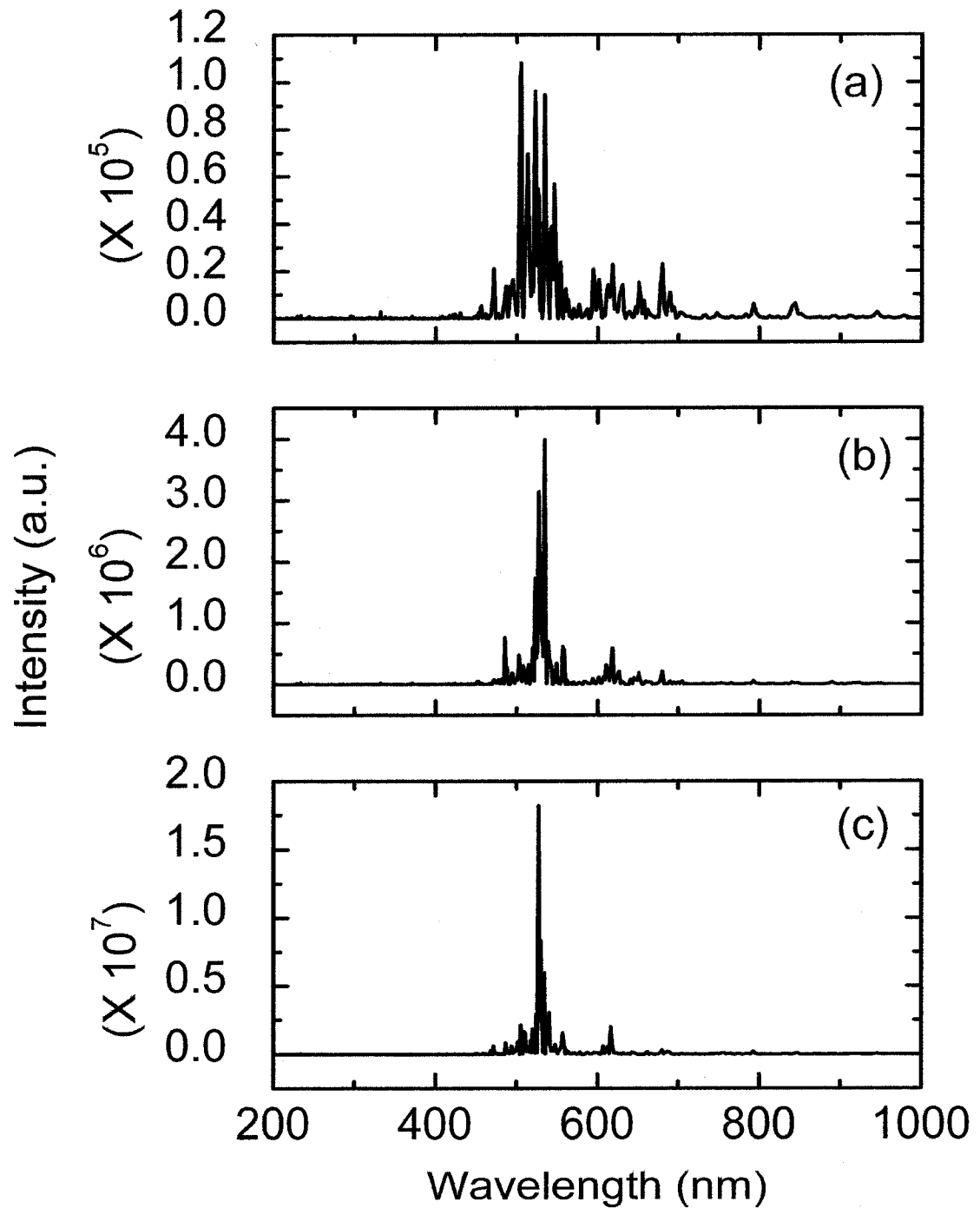


Figure 3.22 – The temporal evolution of the spectral components present in the FDTD simulation of the random laser. Each graph in the figure represents the emitted radiation spectrum over a specific 0.5 ps long time period. (a) 0-0.5 ps (b) 1.5-2.0 ps (c) 3.5-4.0 ps

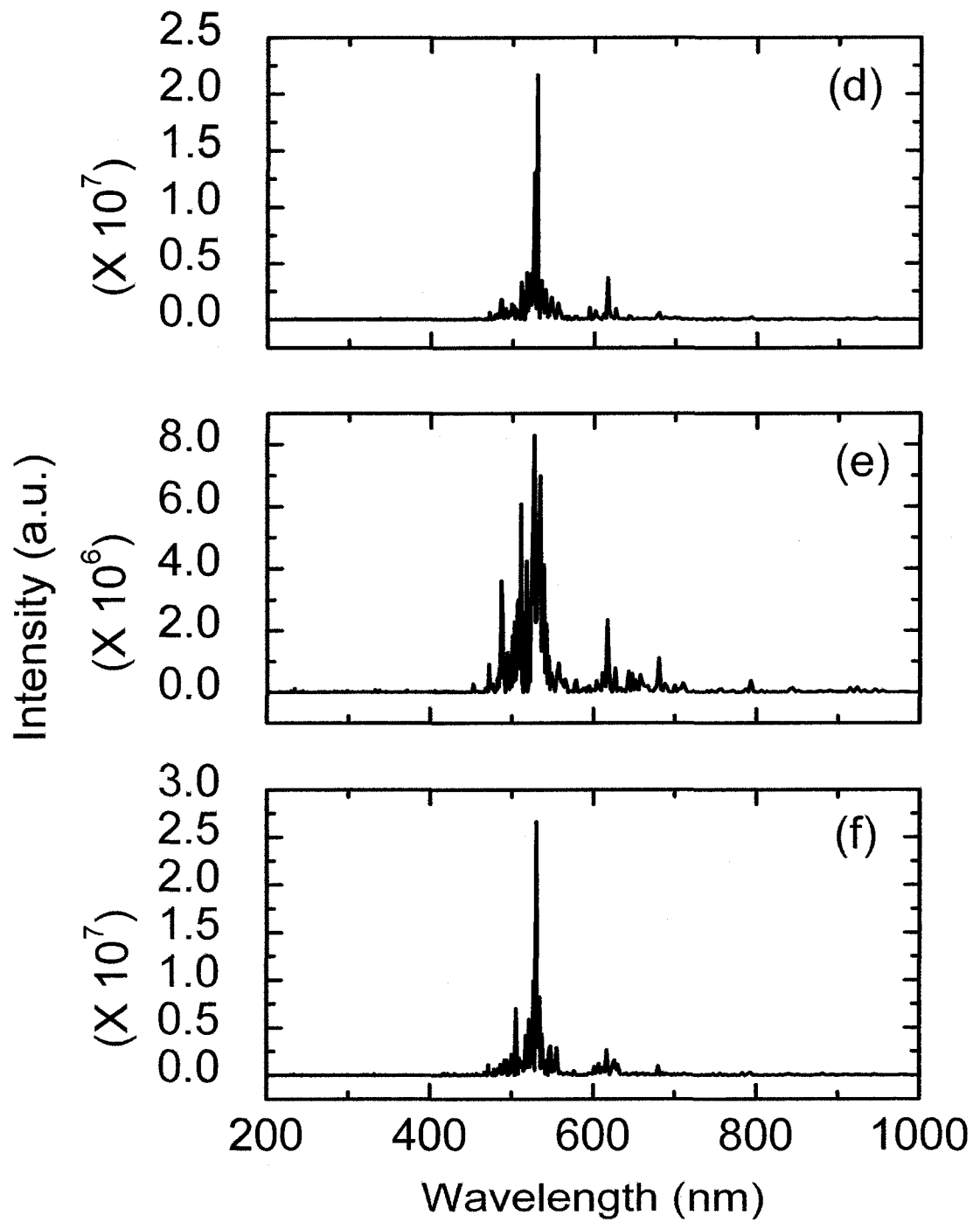


Figure 3.22 – (d) 5.5-6.0 ps (e) 7.5-8.0 ps (f) 9.5-10.0 ps

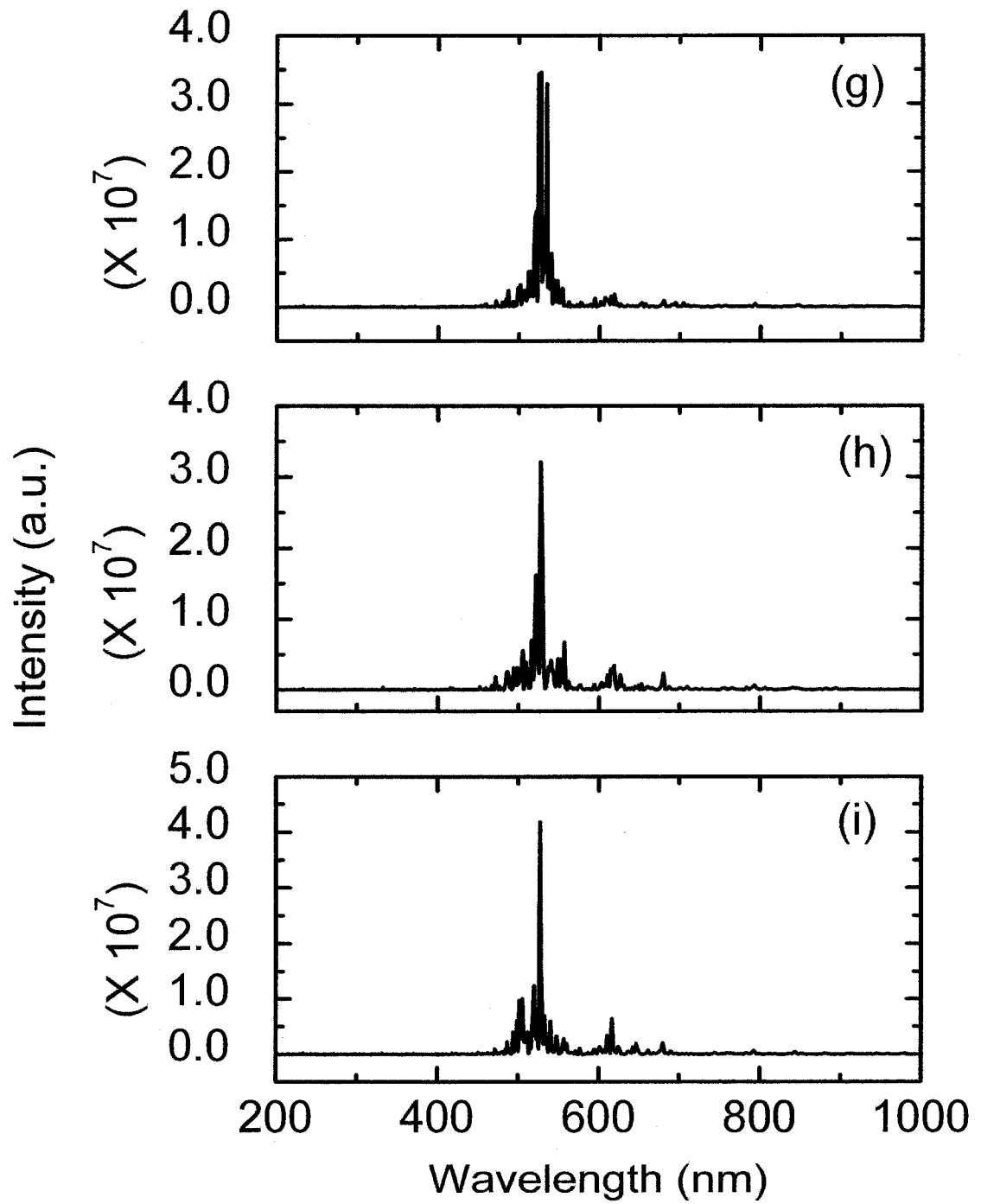


Figure 3.22 – (g) 11.5-12.0 ps (h) 13.5-14.0 ps (i) 15.5-16.0 ps.

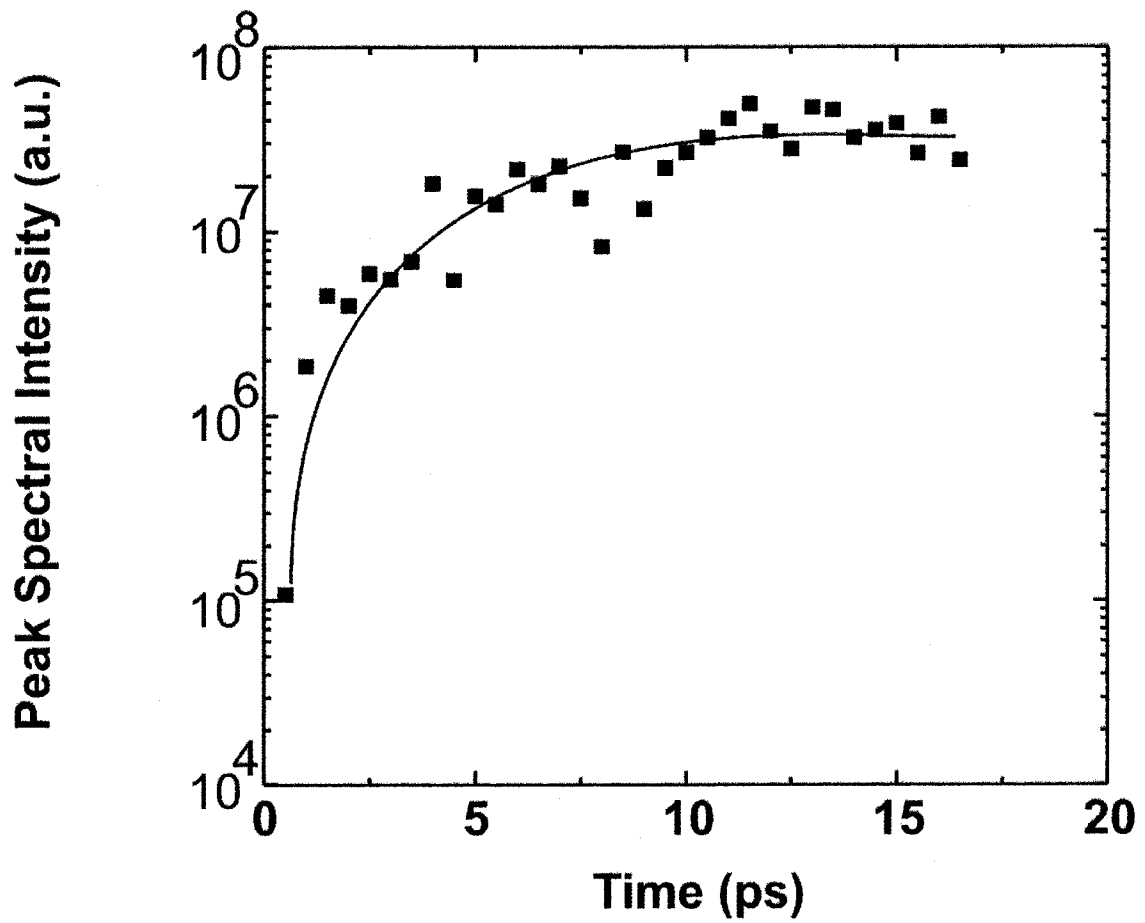


Figure 3.23 – Peak spectral intensity in the simulated random laser as a function of time.

3.5 References

- [1] S. Mujumdar, and H. Ramachandran, "Spectral features in emissions from random amplifying media," *Opt. Comm.*, **176**, 31 (2000).
- [2] D. S. Wiersma and A. Lagendijk, "Light diffusion with gain and random lasers," *Phys. Rev. E*, **54**, 4256-4265 (1996).
- [3] V. S. Letokhov, "Generation of light by a scattering medium with negative resonance absorption," *Sov. Phys. JETP*, **26**, 835 (1968).
- [4] K. S. Yee, "Numerical solution of initial boundary value problems involving Maxwell's equations in isotropic media," *IEEE Trans. Antennas Prop.*, **15**, 802-807 (1966).
- [5] A. Taflove, *Computational Electrodynamics* (Artech House, Boston, 1995).
- [6] V. P. Pasko, U. S. Inan, and T. F. Bell, "Spatial structure of sprites," *Geophys. Res. Lett.*, **25**, 2123-2126 (1998).
- [7] M. J. Weber, *CRC Handbook of Optical Materials*, (Boca Raton, CRC Press, 2003).
- [8] J. P. Berenger, "A perfectly matched layer for absorption of electromagnetic waves," *J. Comput. Phys.*, **114**, 185-200 (1994).
- [9] N. W. Ashcroft, and N. D. Mermin, *Solid State Physics*, (New York, Saunders College Publishing, 1976).
- [10] A. E. Dechant, and A. Y. Elezzabi, "Femtosecond optical pulse propagation in subwavelength metallic slits," *Appl. Phys. Lett.*, **84**, 4678-4680 (2004).

- [11] R. M. Joseph, and A. Taflove, "FDTD Maxwell's Equations Models for Nonlinear Electrodynamics and Optics," IEEE Trans. on Ant. and Prop., **45**, 364 (1997).
- [12] S. Nakamura, Y. Koyamada, N. Yoshida, N. Karasawa, H. Sone, M. Ohtani, Y. Mizuta, R. Morita, H. Shigekawa, and M. Yamashita, "Finite-Difference Time-Domain Calculation With All Parameters of Sellmeier's Fitting Equation for 12-fs Laser Pulse Propagation in a Silica Fiber," IEEE Phot. Tech. Lett., **14**, 480 (2002).
- [13] X. Jiang, and C. M. Soukoulis, "Time dependent theory for random lasers," Phys. Rev. Lett, **85**, 70-73 (2000).
- [14] A. E. Siegman, *Lasers*, (Mill Valley California, 1986)
- [15] S. A. Palkar, N. P. Ryde, M. R. Schure, N. Gupta, and J. B. Cole, "Finite difference time domain computation of light scattering by multiple colloidal particles," Langmuir, **14**, 3484-3492 (1998).
- [16] P. W. Barber, and S. C. Hill, *Light Scattering by Particles: Computational methods*, (Singapore, World Scientific Publishing, 1990).
- [17] J. J. Mock, M. Barbic, D. R. Smith, D. A. Schultz, and S. Schultz, "Shape effects in plasmon resonance of individual colloidal nanoparticles," J. Chem. Phys., **116**, 6755-6759 (2002).
- [18] M. Futumata, Y. Maruyama, M. Ishikawa, "Local electric field and scattering cross section of Ag nanoparticles under surface plasmon resonance by finite difference time domain method," J. Phys. Chem. B, **107**, 7607-7617 (2003).

Chapter 4 – Random Lasers from Scattering Particles Suspended in Laser Dye

4.1 Dye-Scatterer Based Random Lasers

When sufficient scattering and sufficient optical gain for random lasing is obtained through the suspension of many scattering particles in a laser dye, the overall optical system is called a dye-scatterer based random laser. In such a random gain media, the collection of scattering particles multiply scatters light within the active gain volume. In this chapter random lasers constructed from the suspension of dielectric and metallic scattering particles in a laser dye are investigated. Rhodamine 6G laser dye was chosen to create a random laser pumped by green laser light at $\lambda_{pump} = 532$ nm and achieve lasing in the visible spectrum at $\lambda_{laser} = 565$ nm.

4.1.1 Absorption Spectrum of Rhodamine 6G Laser Dye

Figure 4.1 depicts the measured absorption coefficient as a function of wavelength for the four-level Rhodamine 6G laser dye dissolved in methanol at a concentration of 10^{-3} mol/L. As illustrated in Figure 4.1, pump light at $\lambda_{pump} = 532$ nm from a frequency doubled Nd:YAG laser is absorbed within 40 μm of the surface, while emitted fluorescence at $\lambda_{laser} = 564$ nm traverses a much larger unpumped volume. Specifically, the absorption length at $\lambda = 532$ nm is 40 μm , while it is 1.6 mm at $\lambda = 564$ nm [1]. Thus, the characteristic length, L , as discussed in section 2.2.4, for a sample of Rhodamine 6G dye is 1.6 mm. In the dye, the light-induced conversion of fluorescent molecules into non-fluorescent forms is increased by excessive heating and pump fluence and is known as photobleaching [2, 3]. Photo-degradation of the laser dye places an upper limit on the amount of energy that can be extracted from the dye. For a liquid dye

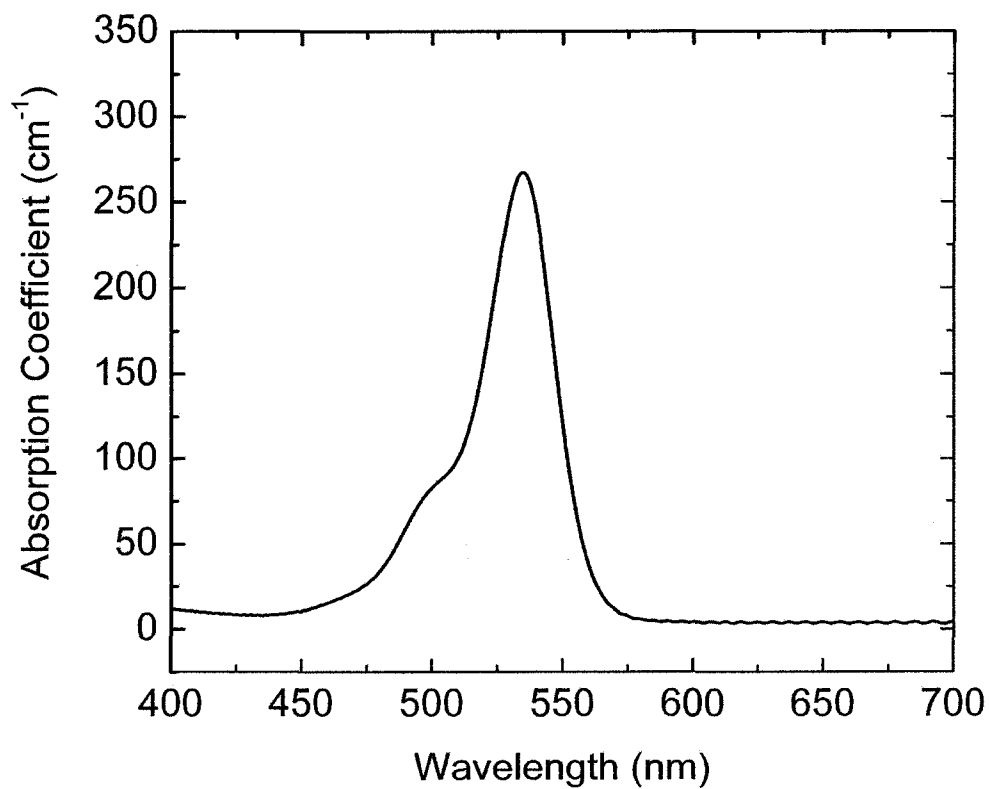


Figure 4.1 – The measured absorption coefficient as a function of wavelength for Rhodamine 6G dye dissolved in methanol at a concentration of 10^{-3} mol/L.

solution, this limitation is not severe, as there is a large supply of unbleached dye available in the optical cell.

4.1.2 Light Emission from Rhodamine 6G

Figure 4.2 illustrates the emission spectrum of 10^{-3} mol/L Rhodamine 6G dissolved in methanol over a range of input pump energy fluences from $F = 0.2$ mJ/cm² (Figure 4.2 (a)) to 10.9 mJ/cm² (Figure 4.2 (i)). At $F = 0.2$ mJ/cm² the broadband emission spectrum is typical for all liquid Rhodamine 6G dye solutions at this concentration, and is the result of fluorescence from spontaneous emission. As the input pump energy fluence is increased from $F = 0.2$ mJ/cm² to $F = 10.9$ mJ/cm², the peak output intensity increases by a factor of 70, while the FWHM linewidth of the emitted light decreases by a factor of 0.6 (Table 4.1). There is an additional shift in the peak emission wavelength as the input fluence increases from $F = 0.2$ mJ/cm² to 10.9 mJ/cm². The small decrease in the FWHM linewidth that occurs, as the input pump energy fluence increases, is the result of amplified spontaneous emission (ASE), which is a preferential amplification of the peak wavelength of emission. The reduction in the emitted FWHM linewidth from a random gain media must be greater than the linewidth decrease for the pure dye solution to demonstrate that random lasing has been achieved.

Table 4.1

Pump Fluence (mJ/cm ²)	Linewidth (nm)	Peak Wavelength (nm)
0.2	30	555
10.9	20	558

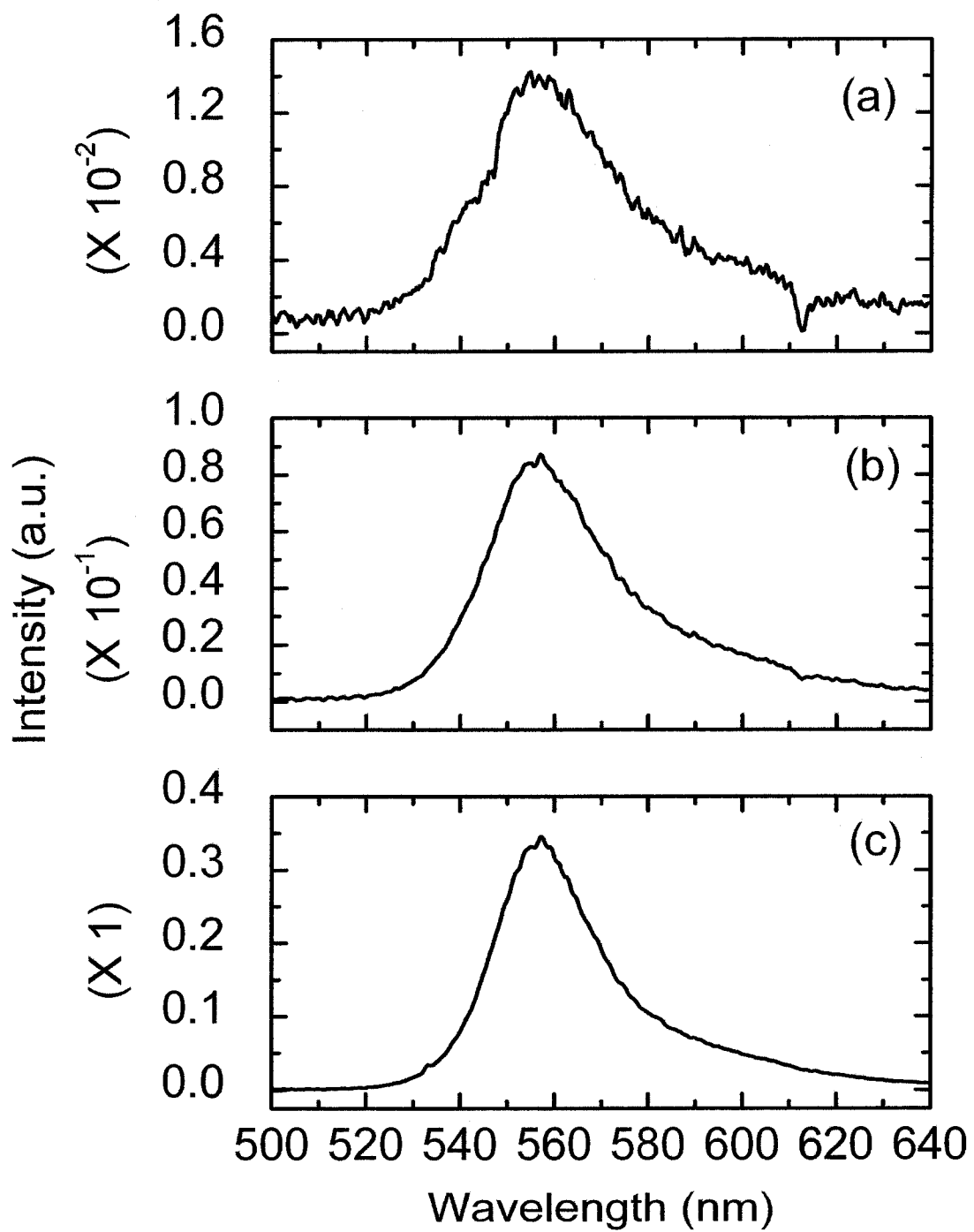


Figure 4.2 – The emission spectrum of 10^{-3} mol/L Rhodamine 6G dissolved in methanol at input pump energy fluences from $F = 0.2$ mJ/cm² to 10.9 mJ/cm². (a) $F = 0.2$ mJ/cm² (b) $F = 0.6$ mJ/cm² (c) $F = 1.7$ mJ/cm²

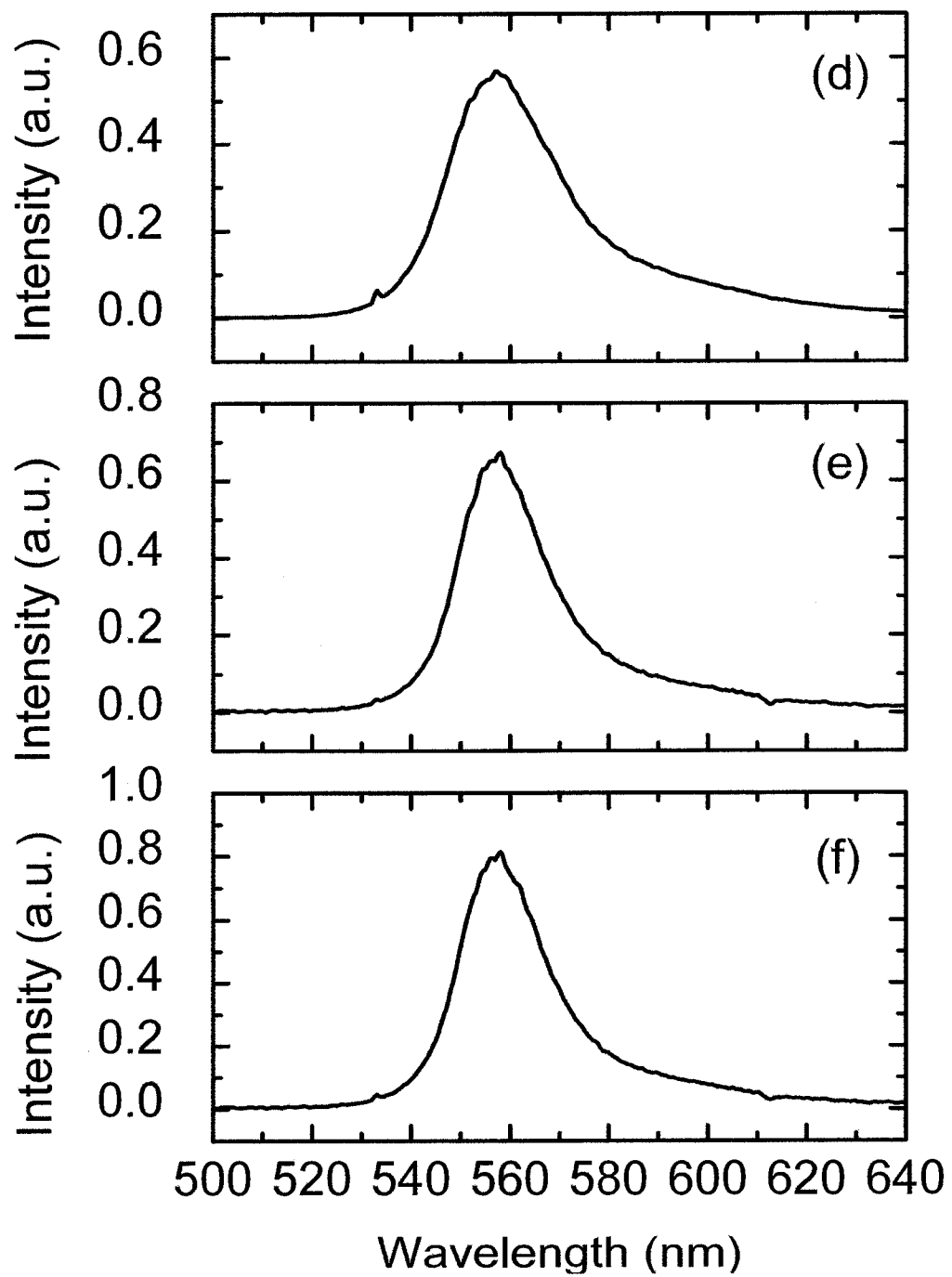


Figure 4.2 – (d) $F = 3.4 \text{ mJ/cm}^2$ (e) $F = 4.2 \text{ mJ/cm}^2$ (f) $F = 5.9 \text{ mJ/cm}^2$

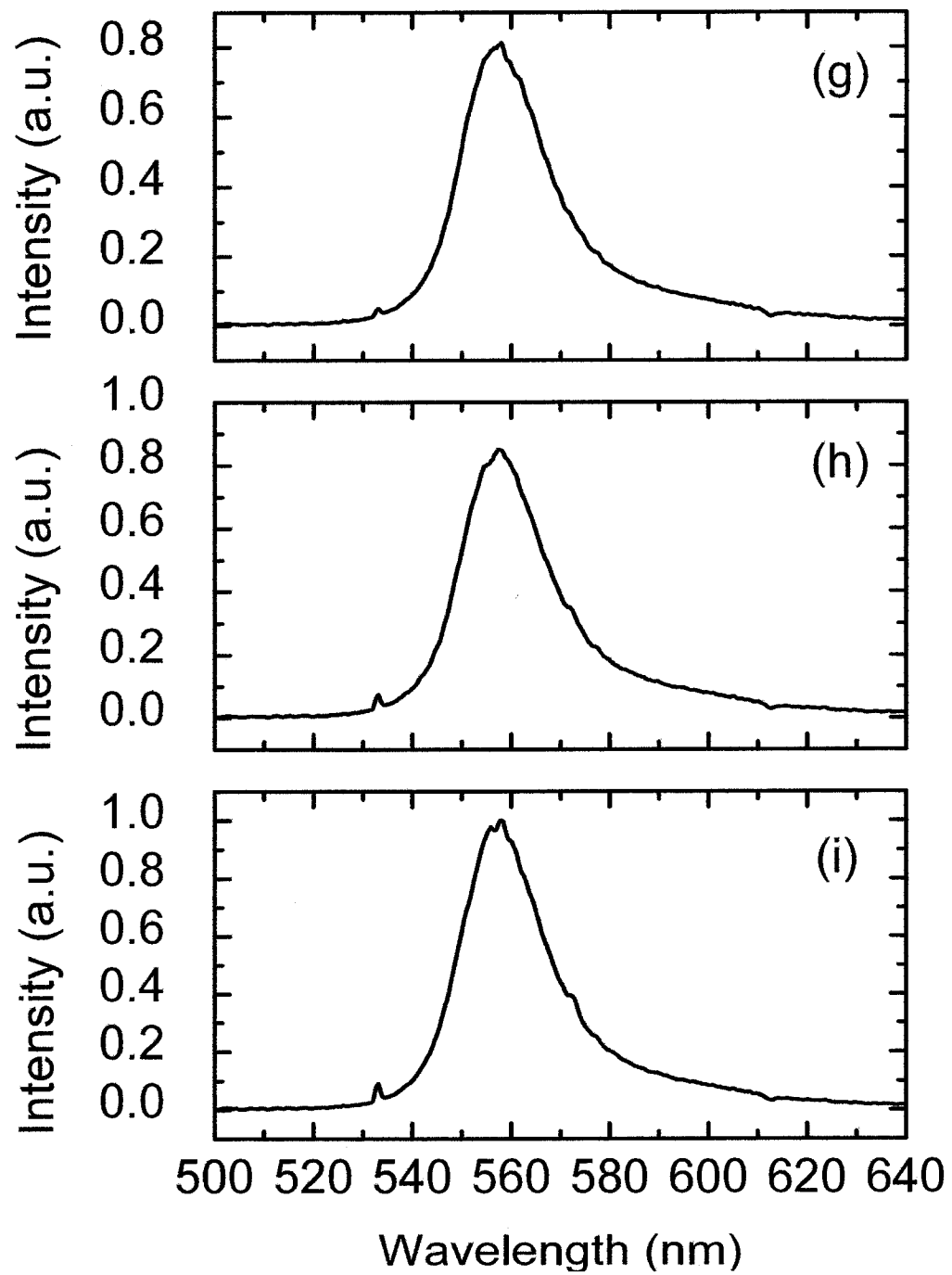


Figure 4.2 – (g) $F = 7.6 \text{ mJ/cm}^2$ (h) $F = 9.2 \text{ mJ/cm}^2$ (i) $F = 10.9 \text{ mJ/cm}^2$.

4.1.3 Dielectric Scattering Particles

In the experiments outlined herein, dye-scatterer based random lasers were constructed using dielectric scattering particles to create a performance baseline. Alumina (Al_2O_3) particles were chosen because their large refractive index contrast with methanol at the peak emission wavelength of Rhodamine 6G ($\lambda = 558 \text{ nm}$), makes them an effective scatterer of visible light ($n_{\text{Al}_2\text{O}_3} = 1.77$ vs. $n_{\text{meth}} = 1.33$). Subwavelength sized Al_2O_3 particles with a diameter of 100 nm were chosen to maximize the available active gain volume in the random gain media. As the Al_2O_3 particle is perfectly transparent in scattering calculations, the values of Q_{ext} and Q_{scat} are equal, while Q_{abs} is zero at all wavelengths. Figure 4.3 illustrates the theoretically calculated value of Q_{ext} as a function of wavelength for a 100 nm diameter Al_2O_3 particle suspended in methanol. Here, the curve depicts a monotonic decrease in Q_{ext} with increasing wavelength, and shows that 100 nm Al_2O_3 particles do not have a scattering resonance in the visible spectrum. Figure 4.4 depicts ℓ , calculated via equation 2.17, at $\lambda = 564 \text{ nm}$ for a 100 nm diameter Al_2O_3 sphere having $Q_{\text{ext}} = 0.031$, as a function of the concentration of Al_2O_3 particles in the dye solution. In the depicted concentration range, the scattering strength, L/ℓ , is in the modestly scattering regime ($10 \geq L/\ell \geq 1$), where scattering is neither wholly diffusive nor ballistic, for particle concentrations greater than 5 mg/mL. Figure 4.4 illustrates that precise control of the scattering strength of the random gain media is possible by varying the Al_2O_3 particle concentration. Though the scattering strength of the Al_2O_3 scatterer based random gain media can be adjusted throughout the weak and modestly scattering regimes, the active gain volume is significantly altered by doing so. As an example, the total volume fraction occupied by Al_2O_3 increases from $2 \times 10^{-2} \%$ to 2 % as

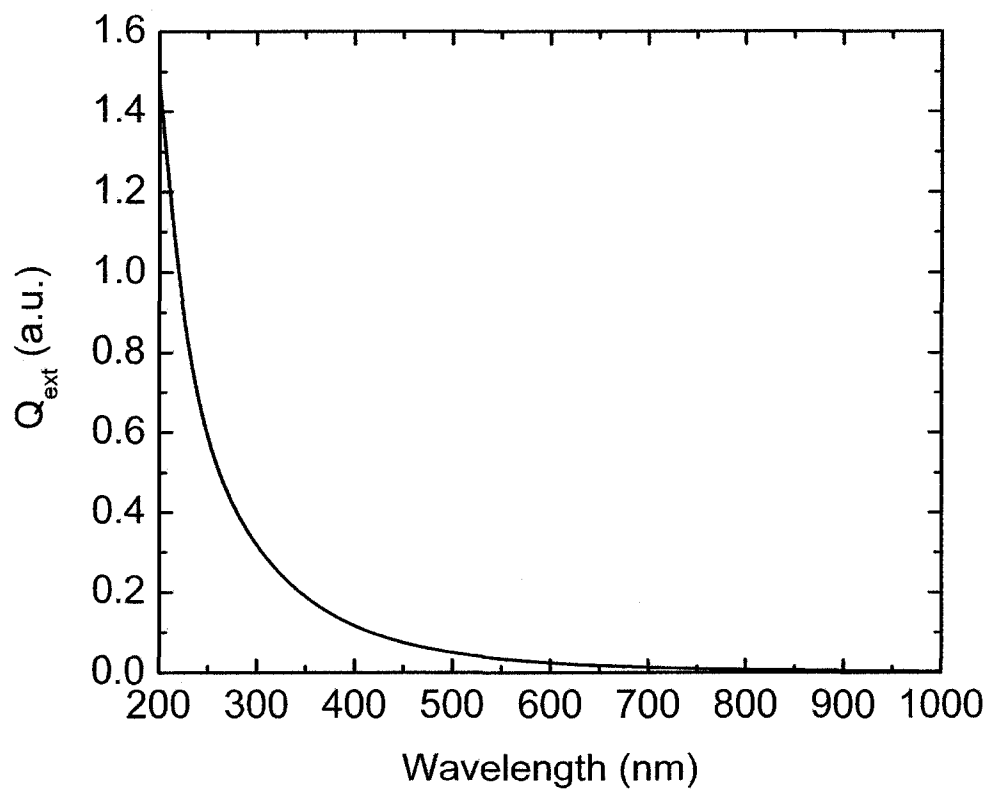


Figure 4.3 – The theoretically calculated value of Q_{ext} as a function of wavelength for a 100 nm diameter Al_2O_3 particle suspended in methanol.

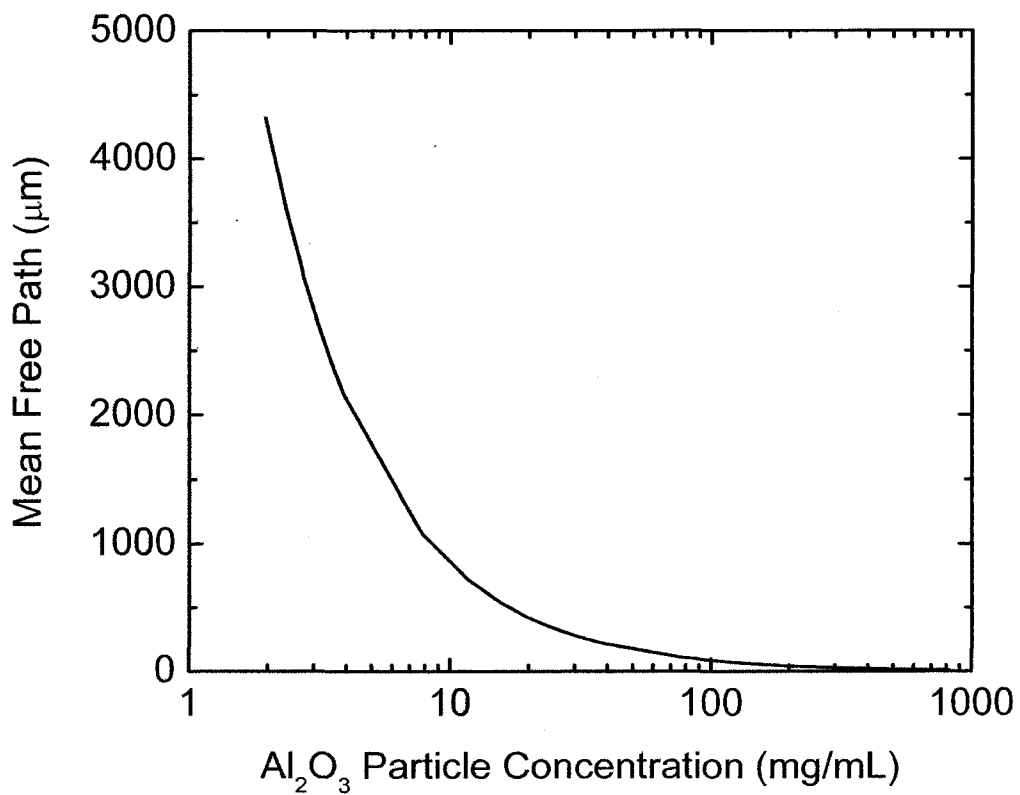


Figure 4.4 – The mean free path at $\lambda = 564$ nm for 100 nm diameter Al₂O₃ spheres suspended in methanol as a function of particle concentration.

ℓ is decreased from 10 mm to 100 μm . At the theoretical maximum volume packing fraction for spheres of 0.74 (2.9 g/mL for Al_2O_3), the minimum possible ℓ is 3 μm . Due to the $1/x$ dependence of ℓ on Al_2O_3 particle concentration, however, this minimum mean free path is reached with 3.6 times more Al_2O_3 than the 0.8 g/mL required for $\ell = 10 \mu\text{m}$. Thus there is a practical minimum ℓ of $\sim 11 \mu\text{m}$ at a volume packing fraction of 0.2. To further reduce ℓ it is necessary to select a scattering material that occupies less total volume for a given scattering cross-section.

4.1.4 Metallic Scattering Particles

Like sub-wavelength sized dielectric particles, sub-wavelength sized metallic particles are also capable of providing a strongly scattering environment for a random laser due to SP enhancement of the scattering cross-section. Silver particles are particularly attractive, as a fundamental factor influencing the operation of a plasmonically enhanced random laser is the location of the spectral peak of the SP resonance curve. Ideally, the SP resonance curve of the metal nanoparticles at both λ_{pump} and λ_{laser} will encompass the laser gain spectrum with minimum absorption. This can be achieved by tuning the SP resonance location and width by either altering the size of the nanoparticle or by choosing an appropriate metal. In Figure 4.5 (a), Q_{sca} and Q_{abs} are plotted as a function of a wavelength for a 55 nm diameter Ag nanoparticle. Both scattering and absorption efficiencies peak at the plasmon resonance peak of $\lambda = 411 \text{ nm}$. At the peak emission wavelength of Rhodamine 6G ($\lambda = 558 \text{ nm}$) Q_{sca} and Q_{abs} are both equal to 0.25, which is 5 % of the maximum SP enhanced value. Since the ratio $Q_{\text{sca}}/Q_{\text{abs}} = 1$, the local optical gain of a random laser must be high enough to overcome absorption. At a particle

diameter of 130 nm, as seen in Figure 4.5 (b), the Q_{sca} curve is much wider with a secondary maximum at $\lambda = 556$ nm. For this particle size, $Q_{sca}/Q_{abs} = 9.4$ at $\lambda = 558$ nm, which would greatly benefit the ratio of scattering to absorption in the gain media; however, the total volume occupied by the Ag particles increases by a factor of approximately 13 over that occupied by the 55 nm diameter Ag particles. This is expected to have a detrimental impact on the operation of the random laser due to a smaller active gain volume. Thus, the spectral mismatch between Ag nanoparticles and Rhodamine 6G laser dye can only be partially corrected through increasing the size of Ag nanoparticles. It would therefore be interesting to investigate the replacement of Ag scattering particles with either Cu or Au, which may support a better SP resonance match. Figure 4.5 (c) depicts Q_{sca} and Q_{abs} for 80 nm diameter Cu nanoparticles. For these Cu particles, Q_{sca} peaks at $\lambda = 594$ nm, and has a linewidth wide enough to include both the pump and emitted radiation in a Cu scatterer based random laser. This spectral peak at $\lambda = 580$ nm closely matches the peak gain for Rhodamine 6G ($\lambda = 559$ nm), which suggests on this basis alone that the use of Cu nanoparticles may be advantageous over Ag nanoparticles. However, as these Cu particles have $Q_{sca}/Q_{abs} = 0.4$, which would cause most of the incident light to be absorbed by Cu particles. Gold nanoparticles have similar issues as illustrated by Figure 4.5 (d), which depicts Q_{sca} and Q_{abs} for 80 nm diameter Au nanoparticles, which have the peak of the Q_{sca} curve at $\lambda = 566$ nm. If Au particles absorbed no light at $\lambda_{laser} = 564$ nm, they would likely be the ideal choice for a SP enhanced random laser. Absorption is high in these particles, however, as $Q_{sca}/Q_{abs} = 1.3$, requiring significant gain to overcome absorptive losses.

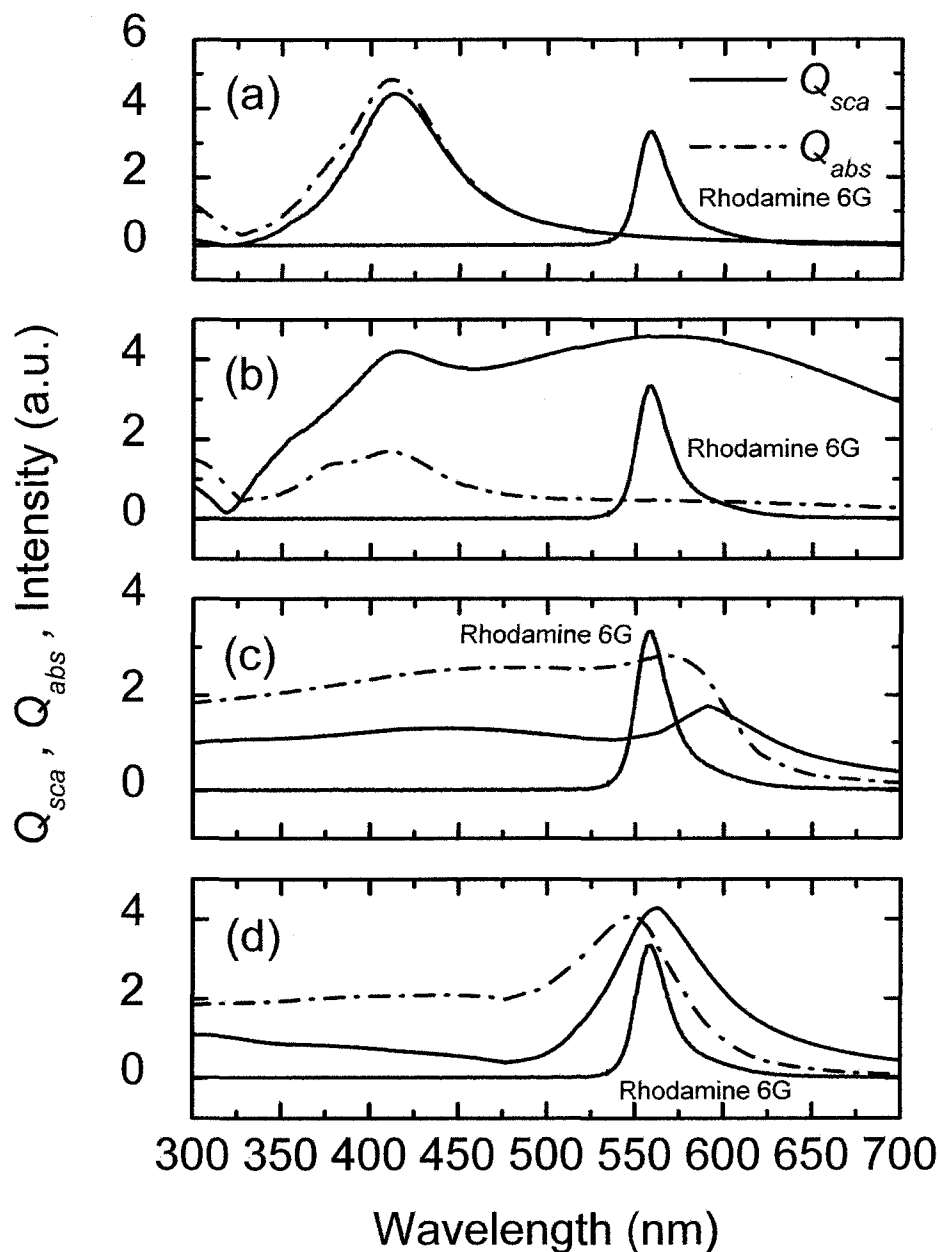


Figure 4.5 – (a) Scattering efficiency (Q_{sca}) (solid line) and absorption efficiency (Q_{abs}) (dashed-dotted line) for 55 nm diameter Ag nanoparticles. (b) Scattering efficiency (Q_{sca}) (solid line) and absorption efficiency (Q_{abs}) (dashed-dotted line) for 130 nm diameter Ag nanoparticles. (c) Scattering efficiency (Q_{sca}) (solid line) and absorption efficiency (Q_{abs}) (dashed-dotted line) for 80 nm diameter Cu nanoparticles. (d) Scattering efficiency (Q_{sca}) (solid line) and absorption efficiency (Q_{abs}) (dashed-dotted line) for 80 nm diameter Au nanoparticles. The normalized emission spectrum in each graph is for 10^{-3} mol/L Rhodamine 6G at a pump energy fluence of 10.9 mJ/cm², which has a peak wavelength of 559 nm.

The effective size of Ag particles suspended in methanol must be determined in order to construct a random laser with Ag particles as the scattering centers. To determine the dimensions of subwavelength size Ag nanoparticles, their characteristic optical extinction is measured with a spectrophotometer. As seen in Figure 4.6 (curve a), for Ag particles suspended in methanol at a concentration of 3 $\mu\text{g/mL}$ in an $L = 1$ cm long optical cell, the measured extinction peak is centred at 411 nm. Figure 4.6 (curve b) illustrates the theoretically calculated peak of the extinction curve for Ag particles with a known 55 nm diameter and known optical properties [4, 5]. An average nanoparticle size of 55 nm is deduced from the size dependence of the location of this SP resonance peak using Mie theory [4, 6]. Figure 4.7 (a) shows that these Ag particles are initially clumped together in micron sized bunches, which are too large for effective suspension in methanol. After the Ag particles are dispersed throughout the suspension by agitation in an ultrasonic bath for 30 minutes, they remain suspended for several hours. Figure 4.7 (b) is an SEM image of the Ag particles after ultrasonic dispersal, deposition on a glass substrate, and evaporation of the suspending methanol. The figure shows the roughly spherical shape of the nanoparticles their size, and their shape distribution.

55 nm diameter Ag nanoparticles display significantly different optical behaviour than 100 nm diameter Al_2O_3 particles. Figure 4.8 displays Q_{ext} (solid line), Q_{sca} (dashed-dotted line), and Q_{abs} (dotted line) from $\lambda = 200$ nm to 1000 nm for a 55 nm diameter spherical Ag nanoparticle, which has a refractive index of $0.26 + i3.68$ at $\lambda = 564$ nm. Each curve has a clear resonant peak at $\lambda = 411$ nm, which corresponds to the peak of the SP resonance curve for these particles. Because of the difference in Q_{sca} between 100 nm diameter Al_2O_3 particles and 55 nm diameter Ag particles, the concentration of sub-

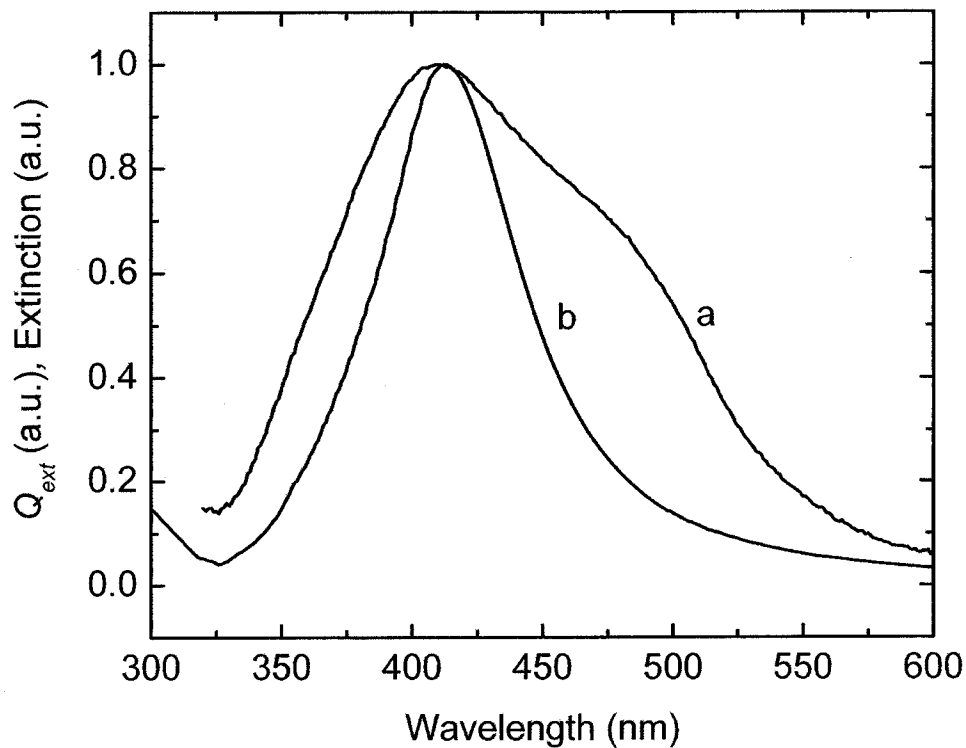


Figure 4.6 – (a) Measured optical extinction vs. wavelength for Ag nanoparticles suspended in methanol. (b) Q_{ext} calculated by Mie theory for a 55 nm diameter Ag nanosphere in methanol. Both measured and calculated extinctions peak at $\lambda = 411$ nm, and indicate the effective suspended particle size.

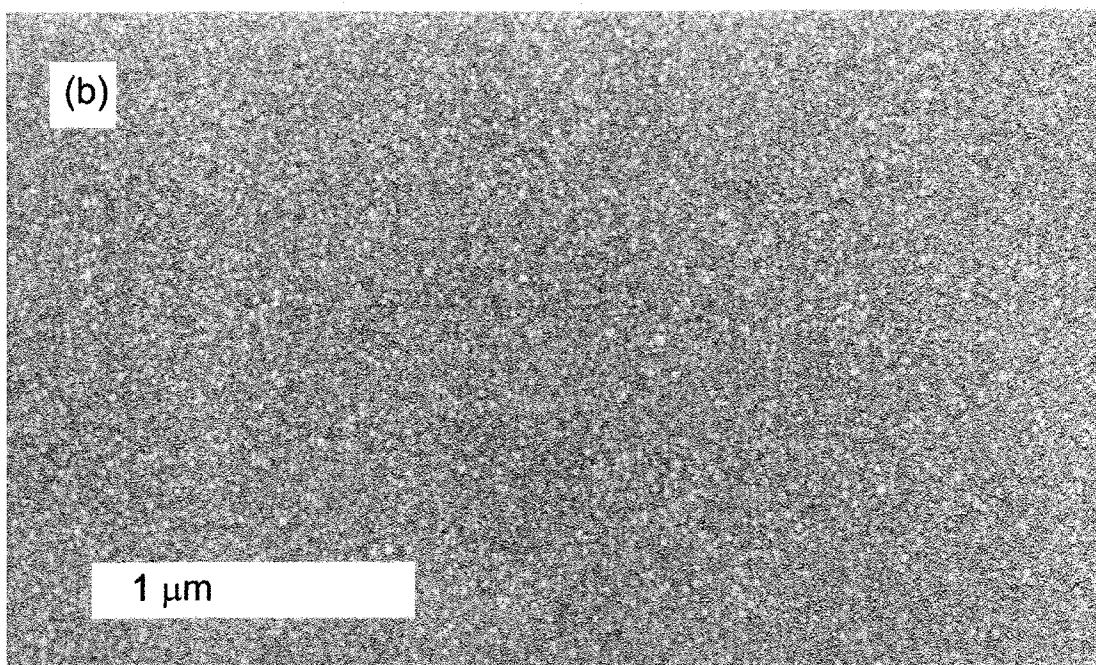
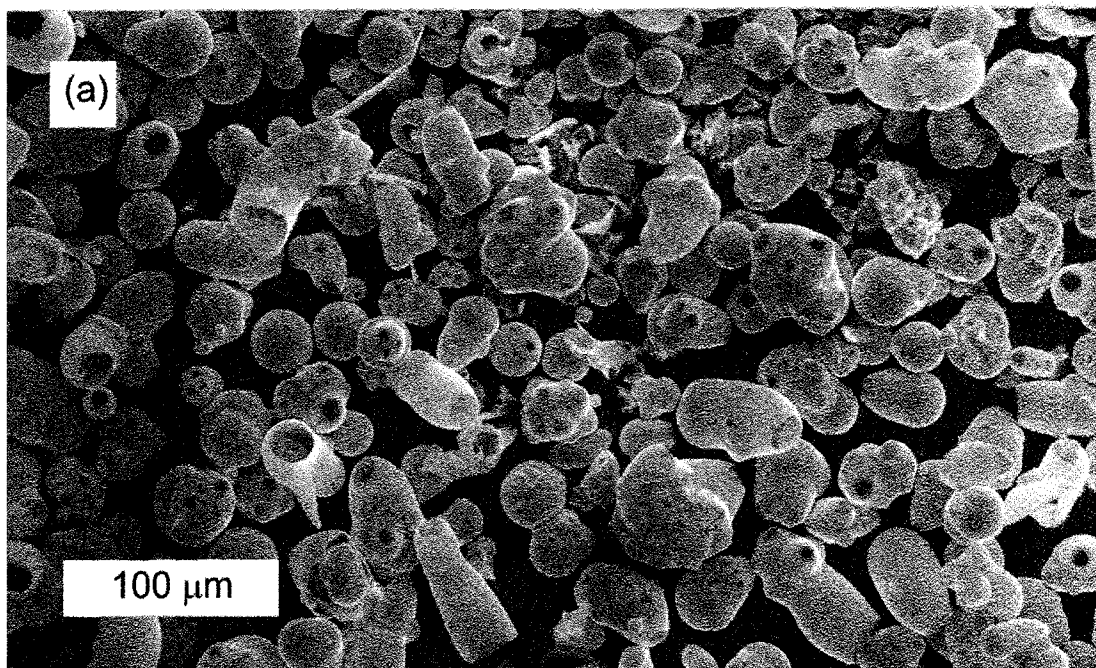


Figure 4.7 – (a) SEM Image of Ag particle microclusters before ultrasonic dispersal. (b) SEM image of Ag nanoparticles after dispersal.

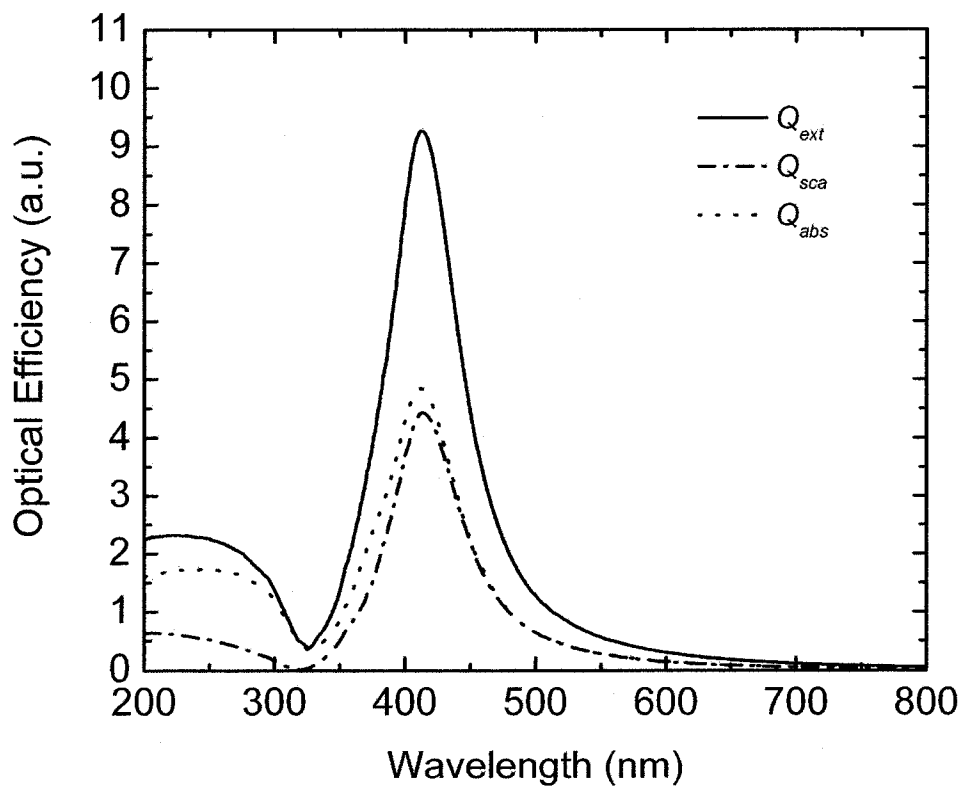


Figure 4.8 – Calculated values of (solid line) Q_{ext} , (dashed-dotted line) Q_{sca} , and (dotted line) Q_{abs} in the visible spectrum from $\lambda = 200$ nm to 1000 nm for a 55 nm diameter spherical Ag nanoparticle.

wavelength sized Ag particles required to achieve $\ell = 100 \mu\text{m}$ (17 mg/mL) is considerably less than that required for Al_3O_3 particles (90 mg/mL). Figure 4.9 illustrates this effect by graphing ℓ as a function of Ag particle concentration. Thus, at a given particle concentration, in the visible wavelength range, the value of ℓ achieved with the 55 nm diameter Ag scattering particles will be smaller than that achieved with Al_2O_3 scattering particles. A consequence of this is that the volume packing fraction required for Ag particles is significantly smaller than that for Al_2O_3 particles, as not only are fewer Ag particles required to reach a given ℓ , but each Ag particle occupies a volume that is six times smaller. Additionally, SP excitation enhances the pump radiation around the nanoparticle, leading to increased absorption by the dye. The emitted fluorescence is also localized within the same region, leading to enhanced amplification. Thus, weakly scattering random lasing is enhanced by this phenomenon even for cases where scattering events are unlikely ($L/\ell \ll 1$). SP resonance from metal nanoparticle scatterers provides a multiple scattering system that holds an edge over dielectric systems; an advantage that can be exploited to create a random laser with superior performance in terms of the minimum FWHM linewidth and the threshold energy fluence required to reach the minimum.

4.2 Dielectric Scatterer Based Random Laser Construction

A dielectric scatterer based random laser was constructed using the previously described 100 nm diameter Al_2O_3 scattering particles. These particles are suspended in a solution of 10^{-3} mol/L Rhodamine 6G laser dye dissolved in methanol, causing the normally clear, fluorescent orange laser dye solution to become milky white. To ensure that the Al_2O_3

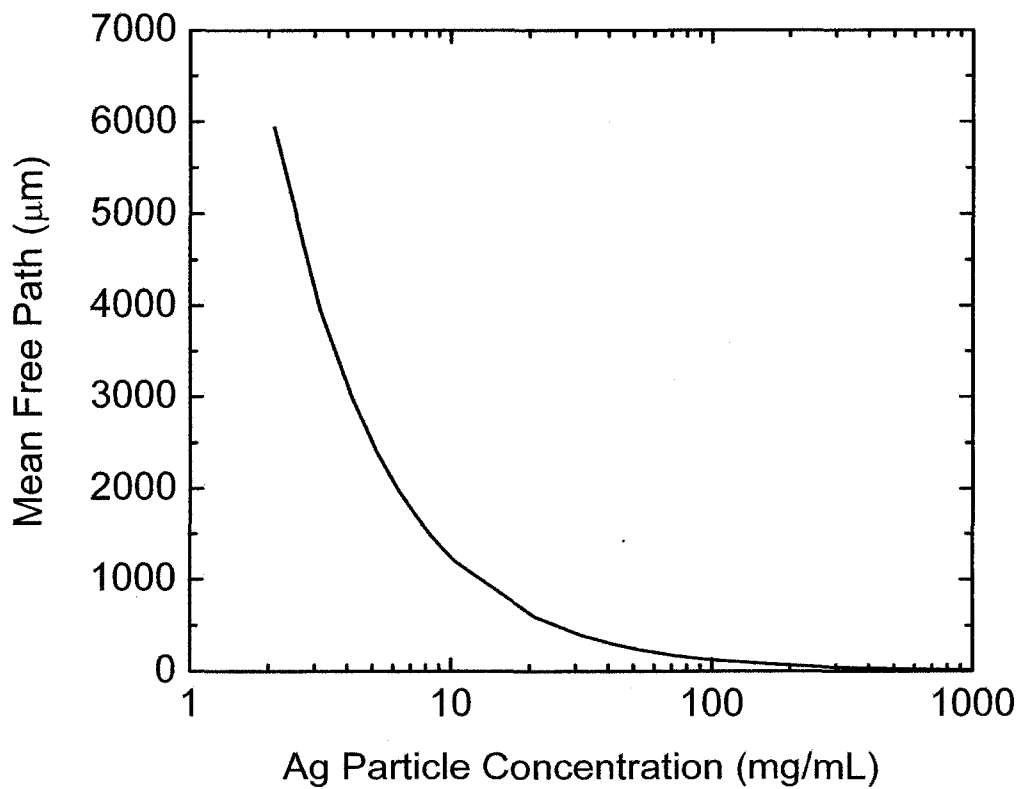


Figure 4.9 – The calculated value of the optical mean free path (ℓ) as a function of the concentration of 55 nm diameter Ag particles suspended in methanol.

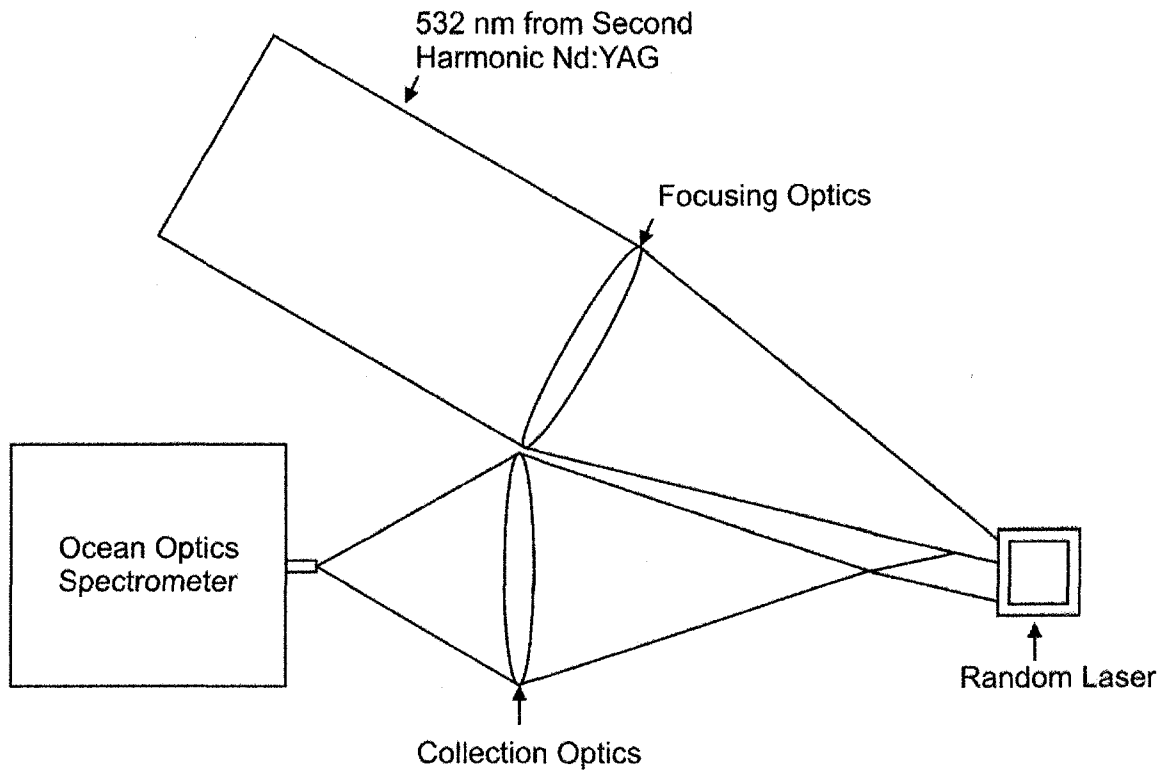


Figure 4.10 – The experimental setup used to collect random laser spectra. The pump laser is a green Nd:YAG second harmonic beam at $\lambda_{pump} = 532$ nm. The random laser is the suspended scattering particles in Rhodamine 6G laser dye. Emitted radiation is collected and analyzed by the Ocean Optic Spectrometer.

particles do not form clumps, the suspension is agitated in an ultrasonic bath for 30 minutes prior to measurements. An electric stirring device is employed to ensure that the particles remained uniformly suspended in a 1 cm thick glass optical cell. Figure 4.10 illustrates the position of pump and collection optics in the experimental setup. Optical pumping of the random gain media is performed by a frequency doubled Nd:YAG laser operating at $\lambda_{pump} = 532$ nm, having a pulse length of 10 ns, repetition rate of 10 Hz, and focal spot size of ~ 3 mm. Random gain media with Ag scatterers were created by varying the concentration of Ag particles from 21 mg/mL to 4 μ g/mL such that ℓ spans the weak to modest scattering regimes from $\ell = 78$ μ m to 43 cm [4]. The Ag particles are also agitated by an ultrasonic bath for 30 minutes to ensure that they remain suspended in the optical cell.

4.3 Spectral Features in Random Laser Emission

When scattering particles are added to a dye solution, their effects on the light emission are readily observed. Typically, a random laser will exhibit several characteristics indicating the transition from the spontaneous emission regime to the lasing regime, manifesting in a dramatic decrease in the FWHM emission linewidth beyond a threshold input pump energy fluence, and a sharp increase in the peak output intensity beyond the threshold energy fluence.

4.3.1 Spectral Features from Al_2O_3 Scatterer Based Random Lasers

The light emission from a random gain media with suspended Al_2O_3 scattering particles depends on the mean free path, the peak emission wavelength of the laser dye, and the

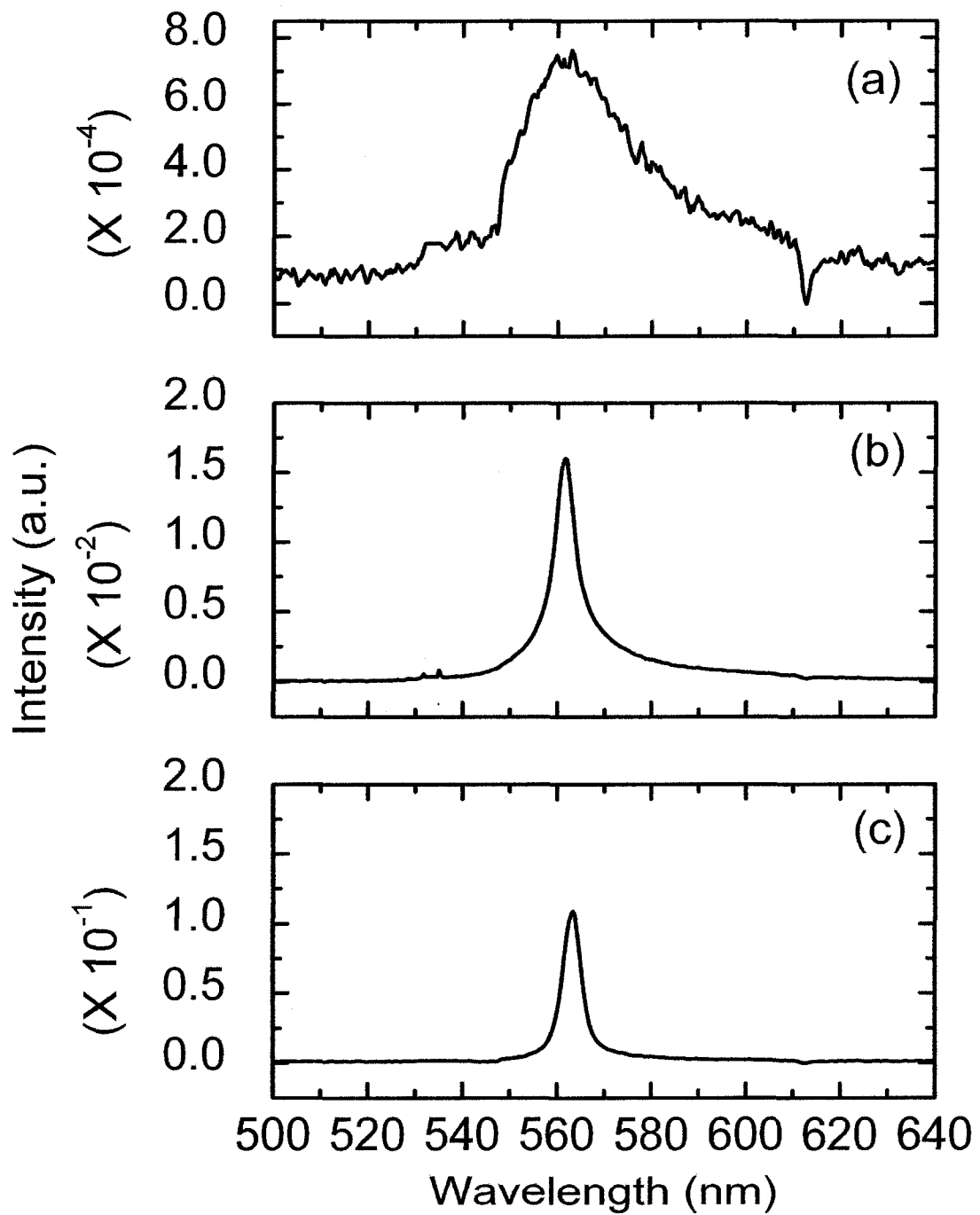


Figure 4.11 – The emission spectra for an Al_2O_3 scatterer based gain media having $\ell = 85 \mu\text{m}$ over input pump energy fluences from $F = 0.2 \text{ mJ/cm}^2$ to 10.9 mJ/cm^2 . (a) $F = 0.2 \text{ mJ/cm}^2$ (b) $F = 0.6 \text{ mJ/cm}^2$ (c) $F = 1.7 \text{ mJ/cm}^2$

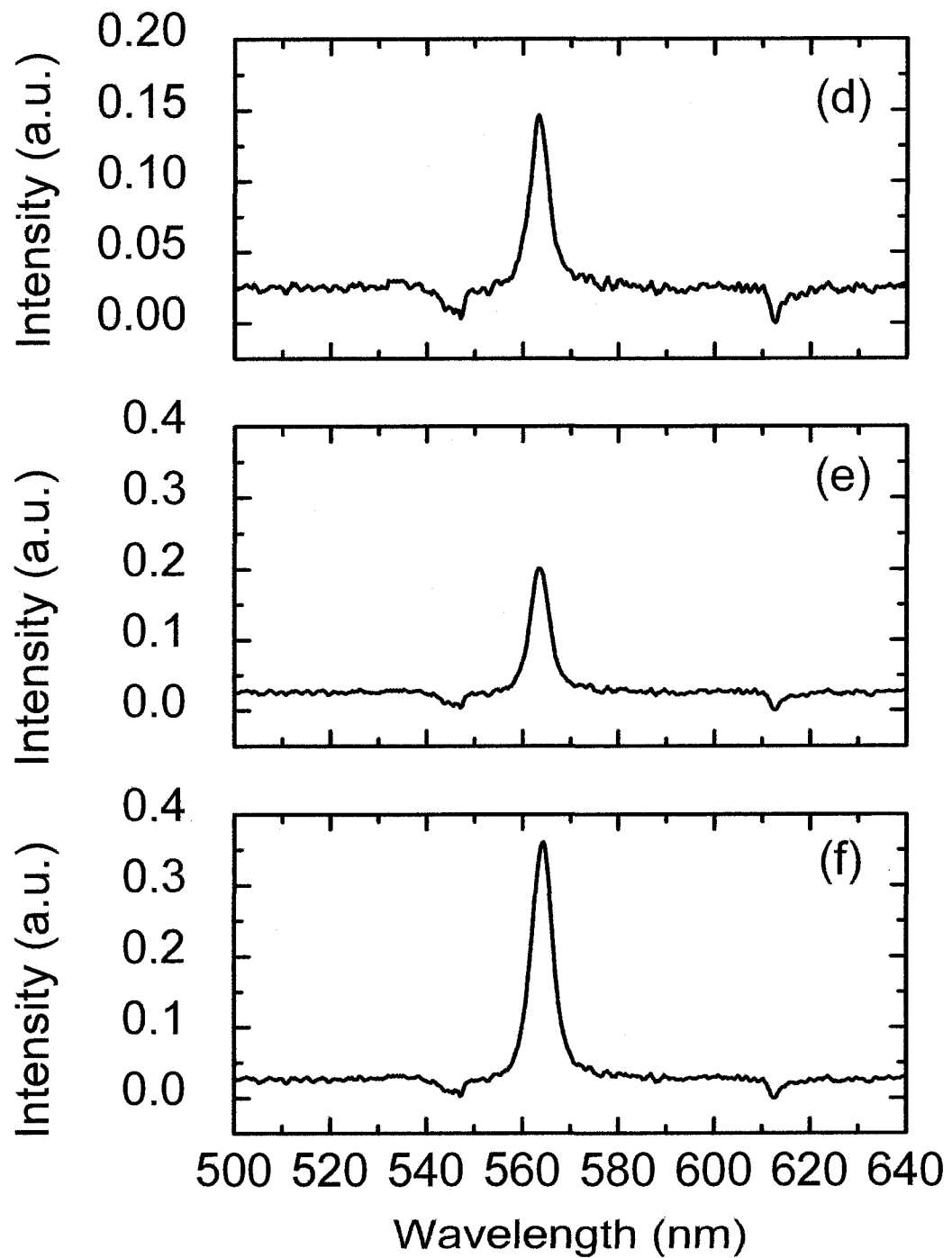


Figure 4.11 – (d) $F = 3.4 \text{ mJ/cm}^2$ (e) $F = 4.2 \text{ mJ/cm}^2$ (f) $F = 5.9 \text{ mJ/cm}^2$

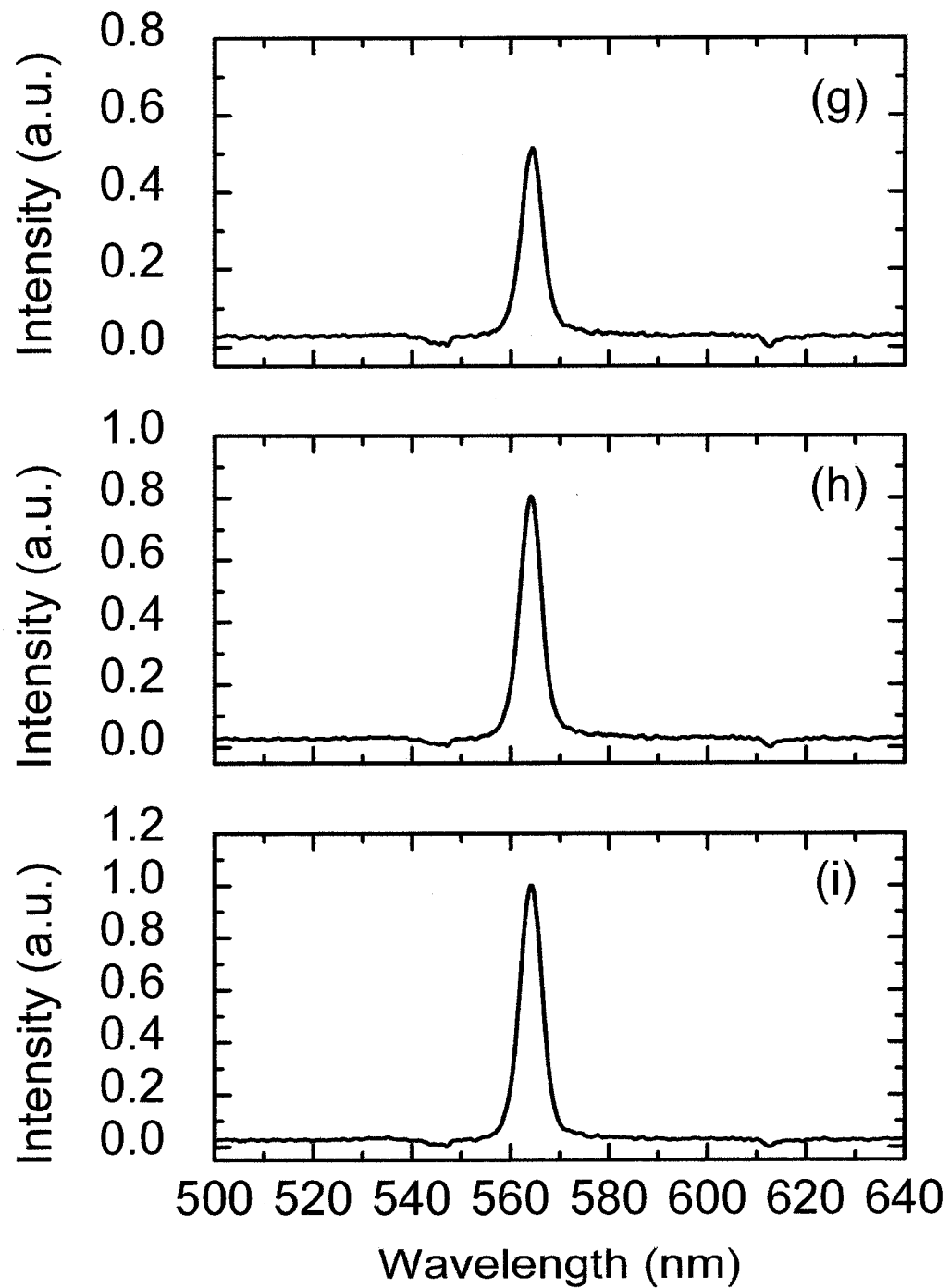


Figure 4.11 – (g) $F = 7.6 \text{ mJ}/\text{cm}^2$ (h) $F = 9.2 \text{ mJ}/\text{cm}^2$ (i) $F = 10.9 \text{ mJ}/\text{cm}^2$.

input pump energy fluence, F . Figure 4.11 (a - i) depicts the emission spectra for an Al_2O_3 scatterer based gain media having $\ell = 85 \mu\text{m}$, which is reached by adding 101 mg/mL of Ag nanoparticles to the dye solution. In this media, several scattering events are expected for each emitted and pump photon, as $L/\ell = 18.8$ places the random gain media into the strong scattering regime. Accordingly, the emitted light intensity distribution undergoes a dramatic change as the input pump energy fluence is increased from $F = 0.2 \text{ mJ/cm}^2$ to 10.9 mJ/cm^2 . For $F = 0.2 \text{ mJ/cm}^2$ broadband spontaneous emission is observed from the surface of the Al_2O_3 scatterer based random gain media. At an input pump energy fluence of $F = 0.6 \text{ mJ/cm}^2$ the FWHM emission linewidth drastically narrows to 6 nm (Table 4.2). This narrow linewidth, which does not occur for the pure Rhodamine 6G dye solution, is due to strong multiple scattering from within the random gain media. Spontaneous emission from the laser dye is amplified and scattered multiple times before exiting the optical cell. If the input pump energy fluence is further increased to $F = 10.9 \text{ mJ/cm}^2$ the FWHM emission linewidth remains constant with an increase in the peak emitted intensity by a factor of 1300 as shown in Figure 4.11 (i). This increase displays a nonlinear relationship with the input fluence, which is expected for a random laser system [7, 8].

Table 4.2

Pump Fluence (mJ/cm^2)	Linewidth (nm)	Peak Wavelength (nm)
0.2	30	563
0.6	6	565
10.9	5	565

As the concentration of Al_2O_3 particles in the random gain media decreases, there is an associated set of changes in the light emission intensity characteristics at a given

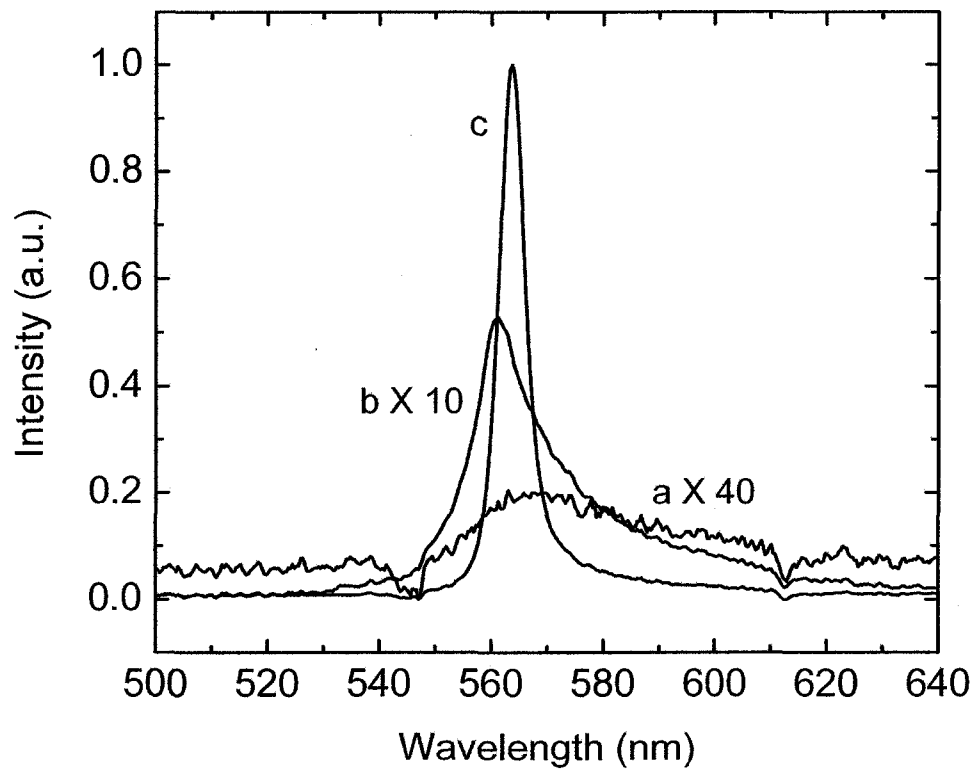


Figure 4.12 – Light emission spectra from Rhodamine 6G with Al_2O_3 nanoparticles at a mean free path $\ell = 340 \mu\text{m}$. (a) The broadband fluorescence spectrum (linewidth = 35 nm) from the sample pumped at $F = 0.6 \text{ mJ/cm}^2$. (b) The narrowband emission spectrum with linewidth = 5.5 nm pumped at $F = 4.2 \text{ mJ/cm}^2$. (c) The narrowband emission spectrum with linewidth = 5.5 nm pumped at $F = 10.9 \text{ mJ/cm}^2$.

pump energy fluence. For an Al_2O_3 particle concentration of 25 mg/mL, $\ell = 340 \mu\text{m}$, which lies within the modestly scattering regime ($L/\ell = 4.6$), ($10 \geq L/\ell \geq 1$), the emission spectrum has a characteristic functional dependence on the input pump energy fluence. The probability that any single photon is recurrently scattered in the active gain volume is thus less than for a random gain media with $\ell = 85 \mu\text{m}$. Figure 4.12 (a-c) illustrates the light emission spectra from the random gain media. At $F = 0.6 \text{ mJ/cm}^2$ (Figure 4.12 (curve a)), the emitted light displays the broadband characteristics of spontaneous emission from Rhodamine 6G (Table 4.3). As the pump fluence is increased above $F = 4 \text{ mJ/cm}^2$ to $F = 4.2 \text{ mJ/cm}^2$ (Figure 4.12 (curve b)) a dramatic decrease occurs in the FWHM emission linewidth, which is indicative of the onset of random lasing. This threshold pump fluence is greater than that for the $\ell = 85 \mu\text{m}$ random gain media ($F = 0.6 \text{ mJ/cm}^2$ vs. $F = 4 \text{ mJ/cm}^2$), because of the significantly smaller scattering strength for the $\ell = 340$ random gain media. There is still a transition, from the broadband emission (35 nm) below the input energy fluence threshold, to the narrowband emission (5.5 nm) of a random laser above the threshold. Such a narrow spectral emission line occurs because there is sufficient non-resonant optical feedback in the gain medium to provide the necessary amplification for a dielectric scatterer based random laser. As shown in Figure 4.12 (curve c), while the linewidth remains essentially constant there is a nonlinear increase in intensity by a factor of 1300 as the input pump energy fluence is increased from $F = 4 \text{ mJ/cm}^2$ to beyond the threshold value of $F = 10.9 \text{ mJ/cm}^2$.

Table 4.3

Pump Fluence (mJ/cm^2)	Linewidth (nm)	Peak Wavelength (nm)
0.2	35	563
0.6	5.5	564
10.9	5	564

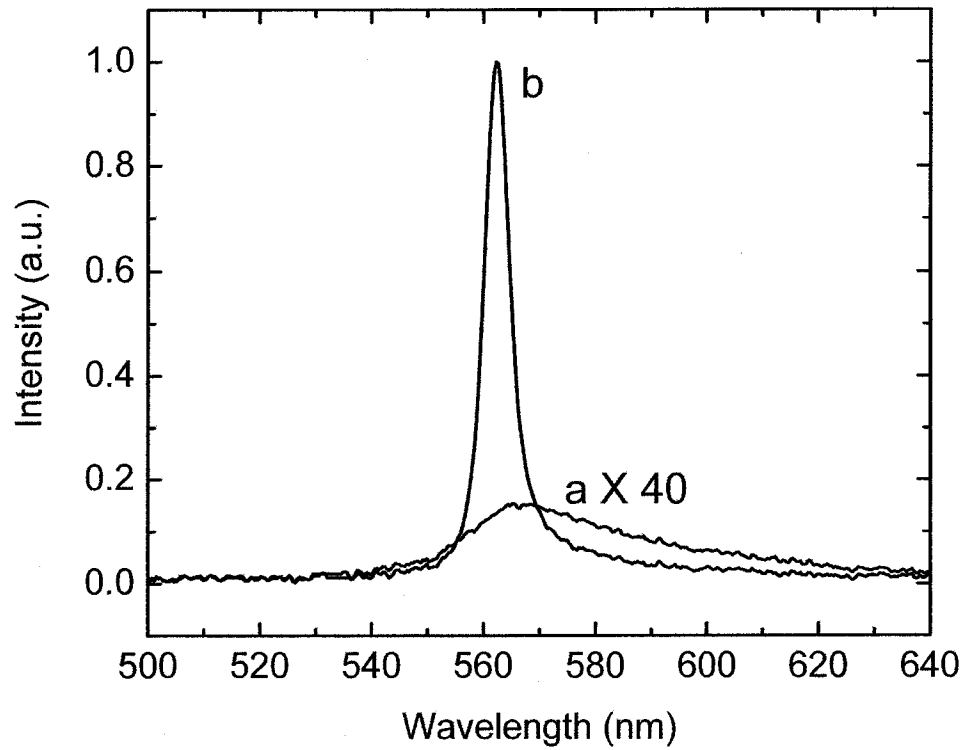


Figure 4.13 – Spectrum of light emission from Rhodamine 6G with Al_2O_3 nanoparticles at a mean free path $\ell = 680 \mu\text{m}$. (a) The broadband fluorescence spectrum (linewidth = 36 nm) from the sample pumped at $F = 0.4 \text{ mJ/cm}^2$. (b) The narrowband emission spectrum with linewidth = 5.7 nm pumped at $F = 10.9 \text{ mJ/cm}^2$.

As the concentration of Al_2O_3 particles is further decreased to 12.7 mg/mL, the operation of the random laser is affected in three major aspects. These are: an increase in the input pump energy fluence threshold; an increase in the final FWHM linewidth of the random laser emission; and a decrease in the peak intensity enhancement factor. Figure 4.13 illustrates these effects by depicting emission spectra for a random gain media with $\ell = 680 \mu\text{m}$ ($L/\ell = 2.3$) at pump fluences of $F = 0.4 \text{ mJ/cm}^2$ (Figure 4.13 (curve a)) and $F = 10.9 \text{ mJ/cm}^2$ (Figure 4.13 (curve b)). The scattering strength of this gain media places it near the edge of the modestly scattering regime. It is therefore expected that recurrent scattering of escaped light back to the active gain volume will occur, but with a smaller probability than for random gain media having $\ell = 85 \mu\text{m}$ or $\ell = 340 \mu\text{m}$. At $F = 0.4 \text{ mJ/cm}^2$ the spontaneous emission spectrum resembles the Rhodamine 6G spectrum (Table 4.4). As has been shown previously in Figures 4.11 and 4.12, this is typical of the random gain media pumped below its lasing threshold. For this random gain media, the dramatic FWHM linewidth narrowing that is characteristic of the onset of random laser emission occurs at a threshold pump energy fluence of $F = 4.2 \text{ mJ/cm}^2$. Here, the emission spectrum shows an intense, relatively narrow peak. The input pump fluence threshold is much greater than the $F = 0.6 \text{ mJ/cm}^2$ for the $\ell = 85 \mu\text{m}$ random laser, and approximately equal to the $F = 4 \text{ mJ/cm}^2$ required for the $\ell = 340 \mu\text{m}$ random laser. As the scattering strength of the random gain media is still within the modestly scattering regime, a constant linewidth for $F > 4 \text{ mJ/cm}^2$. The peak intensity enhancement factor of 850 for the emission between $F = 0.2 \text{ mJ/cm}^2$ and $F = 10.9 \text{ mJ/cm}^2$ is an additional indicator of non-resonant optical feedback.

Table 4.4

Pump Fluence (mJ/cm ²)	Linewidth (nm)	Peak Wavelength (nm)
0.4	36	563
4.2	6	564
10.9	5.7	564

As ℓ is increased beyond 1.6 mm, which is the absorption length at $\lambda = 564$ nm for 10^{-3} mol/L Rhodamine 6G, photon scattering events become less probable, and the random gain medium enters the weakly scattering regime where $L/\ell < 1$. In this scattering regime, a random laser requires significant input pump energy fluence to reach the lasing threshold [9]. Figure 4.14 (curves a - c) displays emission spectra for an Al₂O₃ scatterer based random gain medium in this weakly scattering regime with $\ell = 2700$ μm ($L/\ell = 0.6$). At a pump energy fluence of $F = 0.4$ mJ/cm² the spontaneous emission spectrum is broadband similar to all previously discussed Al₂O₃ scatterer based random gain media below threshold (Table 4.5). Unlike the Al₂O₃ scatterer based random lasers with shorter ℓ , this random gain media displays very different behaviour as a function of the input pump energy fluence. Figure 4.14 (curve b) displays the emission spectrum for the random gain medium at $F = 10.9$ mJ/cm². Here the emission spectrum has a well-defined peak with a relatively wide bandwidth. In this weak scattering regime, non-resonant optical feedback at $F = 10.9$ mJ/cm² is insufficient to develop the significant stimulated emission required to produce a narrow spectral emission line of ~ 5 nm. By further increasing F to 15.4 mJ/cm², as depicted in Figure 4.14 (curve c), the spectral emission line narrows to 6 nm, while the emission intensity doubles. Thus, unlike the Al₂O₃ scatterer based random lasers in the strong to modest scattering regimes, this laser does not demonstrate a plateau in the FWHM linewidth at large values of F .

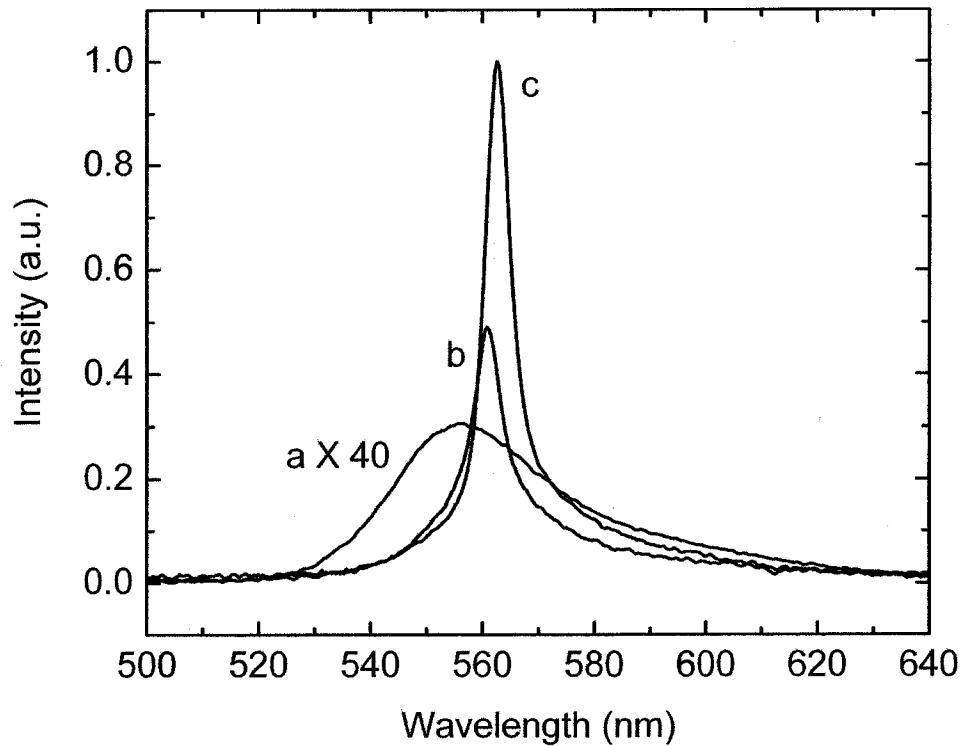


Figure 4.14 – Spectrum of light emission from Rhodamine 6G with Al_2O_3 nanoparticles at a mean free path $\ell = 2700 \mu\text{m}$. (a) The broadband fluorescence spectrum pumped at $F = 0.4 \text{ mJ/cm}^2$. (b) The emission spectrum at $F = 10.9 \text{ mJ/cm}^2$ which has a well-defined peak at 564 nm with a relatively wide linewidth of 8 nm . (c) The emission spectrum pumped at $F = 15.4 \text{ mJ/cm}^2$, where the spectral emission linewidth narrows to 6 nm and the emission intensity doubles.

Table 4.5

Pump Fluence (mJ/cm ²)	Linewidth (nm)	Peak Wavelength (nm)
0.4	35	558
10.9	8	564
15.4	6	564

4.3.2 Linewidth Variation for Al₂O₃ Scatterer Based Random Lasers

The variation of the FWHM linewidth of emitted light from an Al₂O₃ scatterer based random laser as a function of input pump fluence is a fundamental measurement that illustrates many aspects of random laser operation. Figure 4.15 (curves a-d) depicts the FWHM linewidth as a function of F , from 0.2 mJ/cm² to 15.4 mJ/cm², of random lasers with $\ell = 85 \mu\text{m}$ (■), 340 μm (●), 680 μm (▲), and 2700 μm (▼). This figure shows that the FWHM linewidth depends on the input pump energy fluence F , with significantly less dependence on ℓ . Each of the random lasers having $\ell < 1.6$ mm demonstrates approximately the same behaviour: a slow decrease in the FWHM linewidth at pump energy fluences less than the threshold. Above the threshold, the linewidth of each random laser drops to ~ 5 nm and remains constant as F increases. When ℓ is increased from 85 μm to 680 μm , the lasing threshold for collapse of the FWHM linewidth increases (Table 4.6). As there is strong scattering in these random lasers, with multiple scattering events for each emitted photon, isotropic, narrowband, laser-like light emission escapes from the surface of the random gain media. Unlike random lasers having $\ell = 85 \mu\text{m}$, 340 μm , or 680 μm , the $\ell = 2700 \mu\text{m}$ laser does not reach a FWHM linewidth plateau in the studied range of input pump energy fluences. Instead, the weakly scattering random gain media demonstrates a monotonic decrease in linewidth to ~ 8 nm at $F = 10.9$ mJ/cm², and a further slow decrease to 6 nm at $F = 15.4$ mJ/cm². This is due

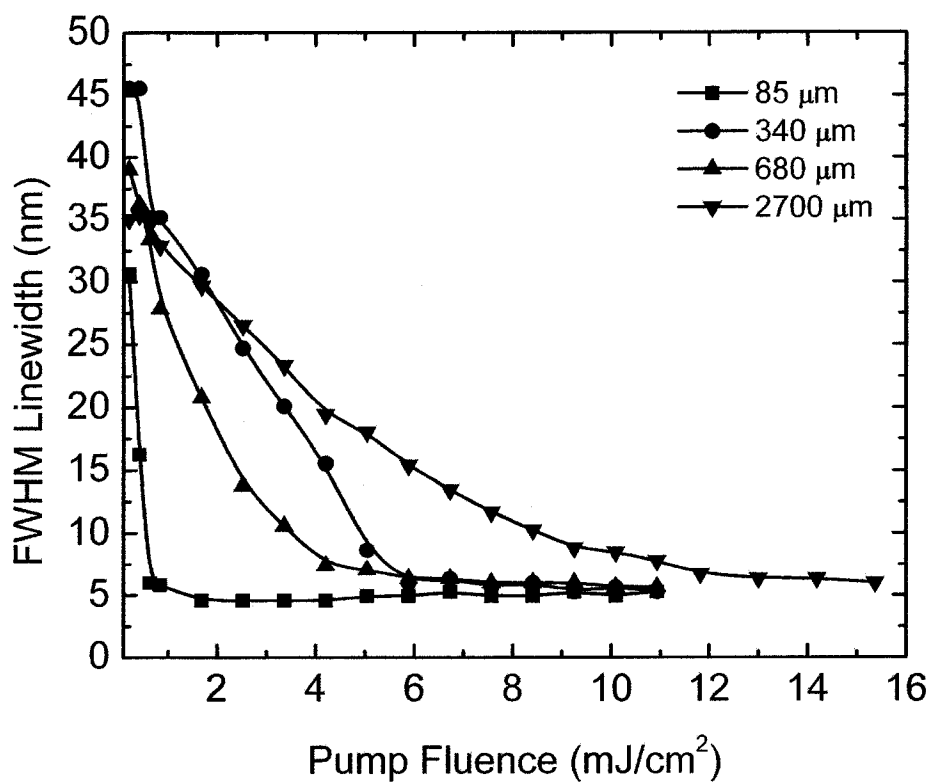


Figure 4.15 – FWHM linewidth variation of random lasers with $\ell = 85 \mu\text{m}$ (■), $340 \mu\text{m}$ (●), $680 \mu\text{m}$ (▲), and $2700 \mu\text{m}$ (▼), as a function of F from 0.2 mJ/cm^2 to 15.4 mJ/cm^2 .

to insufficient scattering to ensure that light escaping from the active gain volume is rescattered back into the active region.

Table 4.6

ℓ (μm)	Threshold Fluence (mJ/cm^2)	Minimum Linewidth (nm)
85	0.6	5
340	4	5
680	4.2	5.7
2700	N.A.	6

4.3.3 Intensity Variation for Al_2O_3 Scatterer Based Random Lasers

Figure 4.16 (curves a - d) depicts the relative peak intensity as a function of the input pump energy fluence of random lasers having $\ell = 85 \mu\text{m}$ (■), $340 \mu\text{m}$ (●), $680 \mu\text{m}$ (▲), and $2700 \mu\text{m}$ (▼). A general trend can be seen in the intensity curve, where the highly scattering random laser having $\ell = 85 \mu\text{m}$ shows a much greater increase in the peak emitted intensity over the same fluence range as each of the other random lasers. This trend is expected, as light in the random laser having $\ell = 85 \mu\text{m}$ experiences a factor of ~ 6 times greater scattering events than the random laser having $\ell = 340 \mu\text{m}$. For two random lasers in the modestly scattering regime, having $\ell = 340 \mu\text{m}$ and $680 \mu\text{m}$ respectively, the peak intensity reaches approximately the same relative intensity at $F = 10.9 \text{ mJ}/\text{cm}^2$, whereas for the random laser having $\ell = 2700 \mu\text{m}$, the intensity curve is approximately linear over much of the studied input energy fluence range.

4.4 Silver Scatterer Based Random Lasers

This section discusses the performance characteristics of random lasers based on nanometer sized Ag particles suspended in a solution of Rhodamine 6G laser dye. Compared to Al_2O_3 particles, an increase in scattering cross section accompanied by a

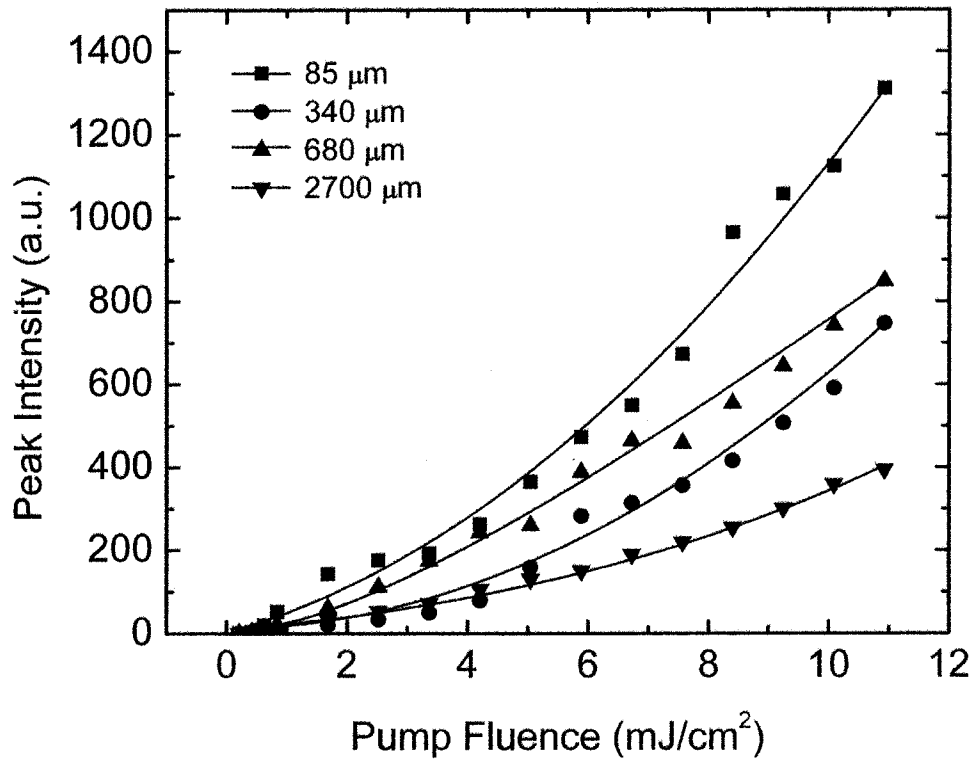


Figure 4.16 – Relative peak emitted intensity vs. input pump fluence F for Al_2O_3 scatterer based random lasers having $\ell = 85 \mu\text{m}$ (■), $\ell = 340 \mu\text{m}$ (●), $\ell = 680 \mu\text{m}$ (▲), and $\ell = 2700 \mu\text{m}$ (▼).

large gain volume, because of the small scatterer size and gain enhancement from SP excitation, enables a Ag scatterer based random laser to outperform an Al₂O₃ scatterer based random laser with the same ℓ . The Ag scatterer based random laser exhibits a narrower FWHM laser linewidth, and a lower pump energy fluence threshold than an Al₂O₃ scatterer based random laser.

4.4.1 Spectral features from Ag scatterer Based Random Lasers

A silver scatterer based random gain media with $\ell = 78 \mu\text{m}$, has a scattering strength, $L/\ell = 20.5$, which lies well within the strong scattering regime. Here, multiple scattering events are common, and emitted photons are scattered several times on average before exiting the gain media. Figure 4.17 (a - i) illustrates the emission spectrum for this random gain media. As the input pump energy fluence is increased from $F = 0.5 \text{ mJ/cm}^2$ (Figure 4.17 (a)) to $F = 24.6 \text{ mJ/cm}^2$ (Figure 4.17 (i)) the light emission undergoes changes similar to an Al₂O₃ scatterer based random laser. The broadband spontaneous emission from the Ag scatterer based random gain media can be seen at pump energy fluences below $F = 11 \text{ mJ/cm}^2$ (Figure 4.17 (a - e)). At $F = 13.2 \text{ mJ/cm}^2$ (Figure 4.17 (f)), the FWHM emission linewidth drastically narrows because of strong multiple scattering from the Ag particles in the random gain media (Table 4.7). In addition to this narrowing, the peak emission intensity also increases by a factor of 200 as the input energy fluence is increased from $F = 0.5 \text{ mJ/cm}^2$ (Figure 4.17 (a)) to 24.6 mJ/cm^2 (Figure 4.17 (i)). Above this value of F , the FWHM emission linewidth remains constant.

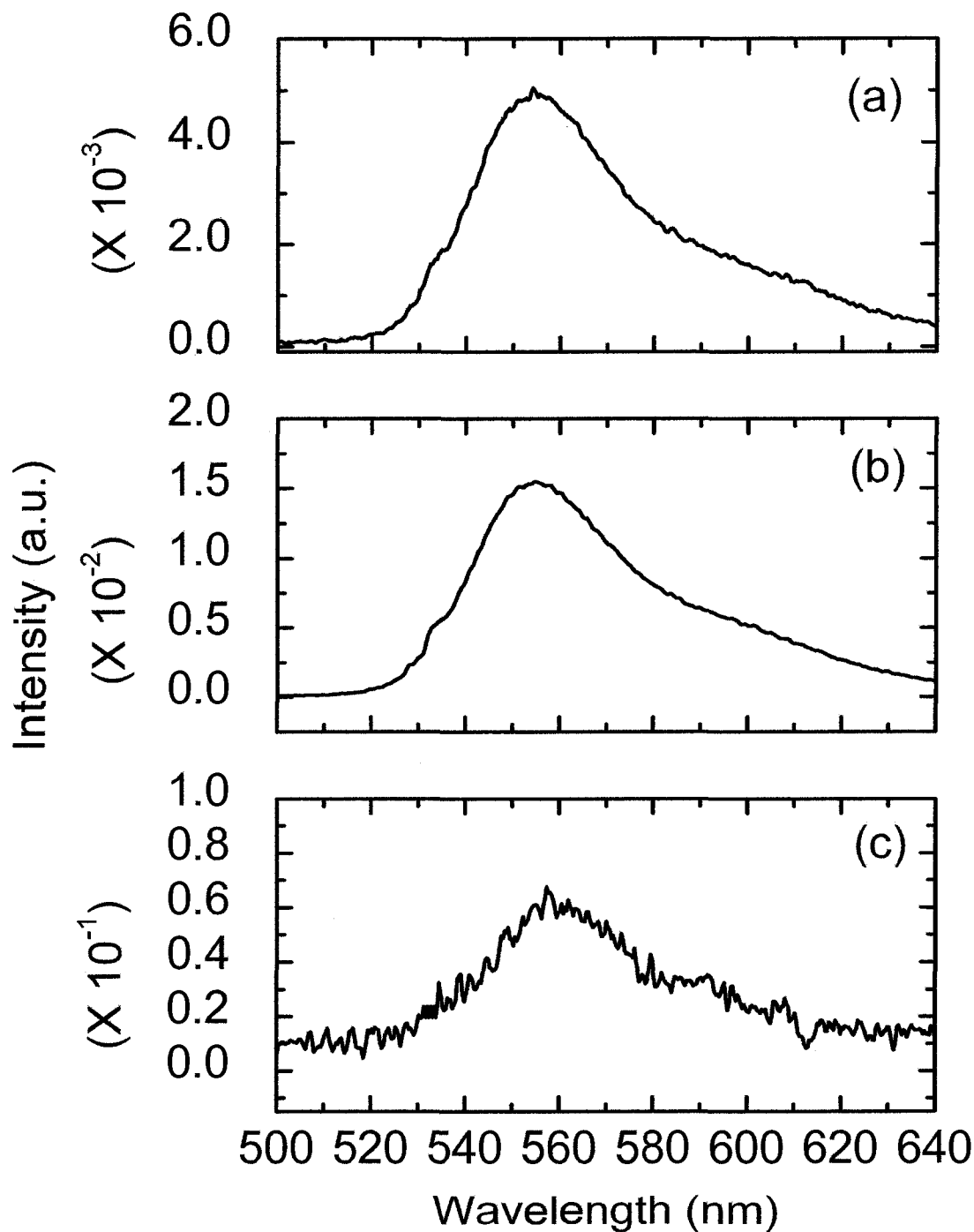


Figure 4.17 – The emission spectra for an Ag scatterer based gain media having $\ell = 78$ μm over input pump energy fluences from $F = 0.5$ mJ/cm^2 to 24.6 mJ/cm^2 . (a) $F = 0.5$ mJ/cm^2 (b) $F = 1.4$ mJ/cm^2 (c) $F = 3.8$ mJ/cm^2

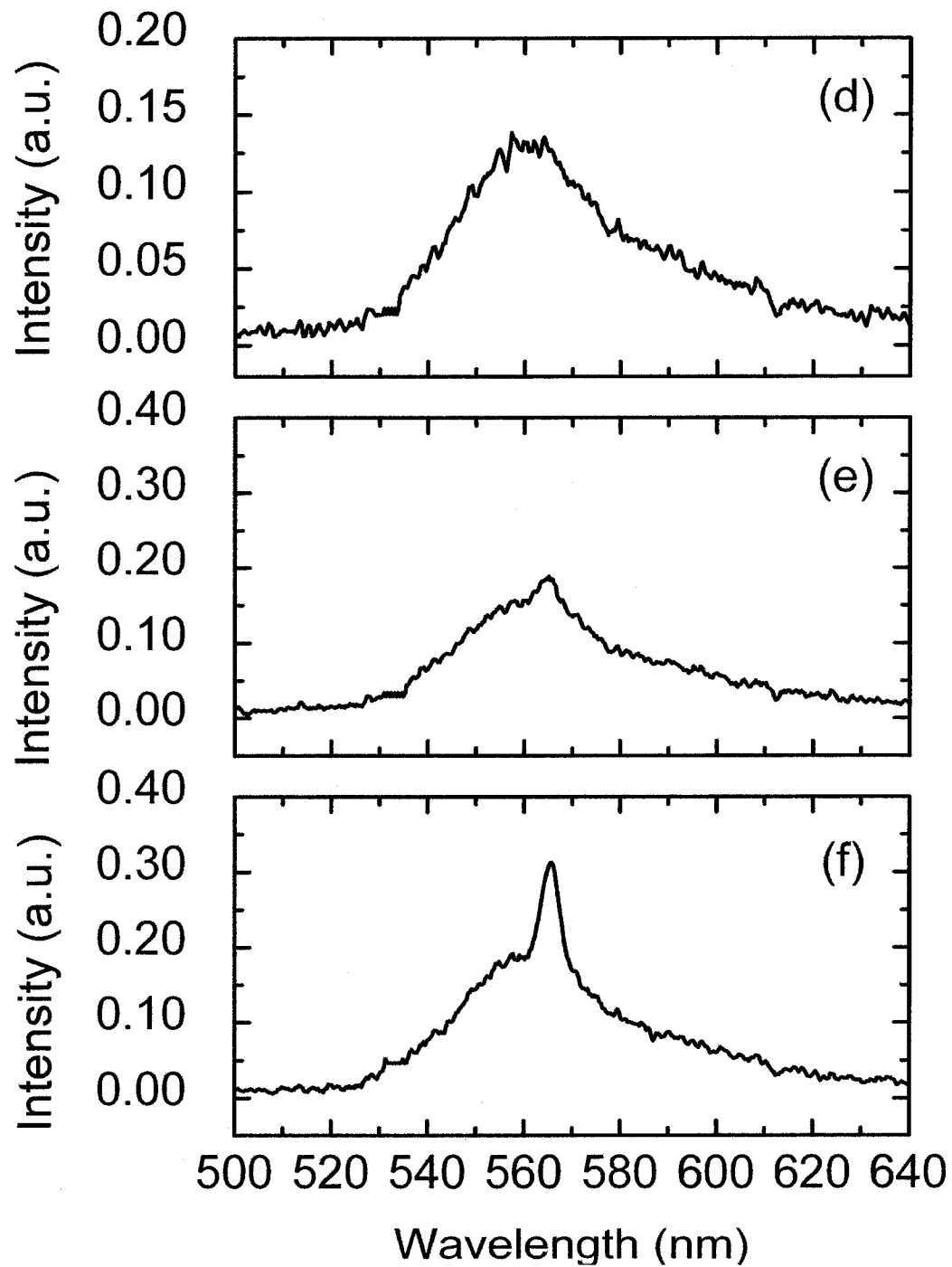


Figure 4.17 – (d) $F = 7.6 \text{ mJ/cm}^2$ (e) $F = 9.5 \text{ mJ/cm}^2$ (f) $F = 13.2 \text{ mJ/cm}^2$

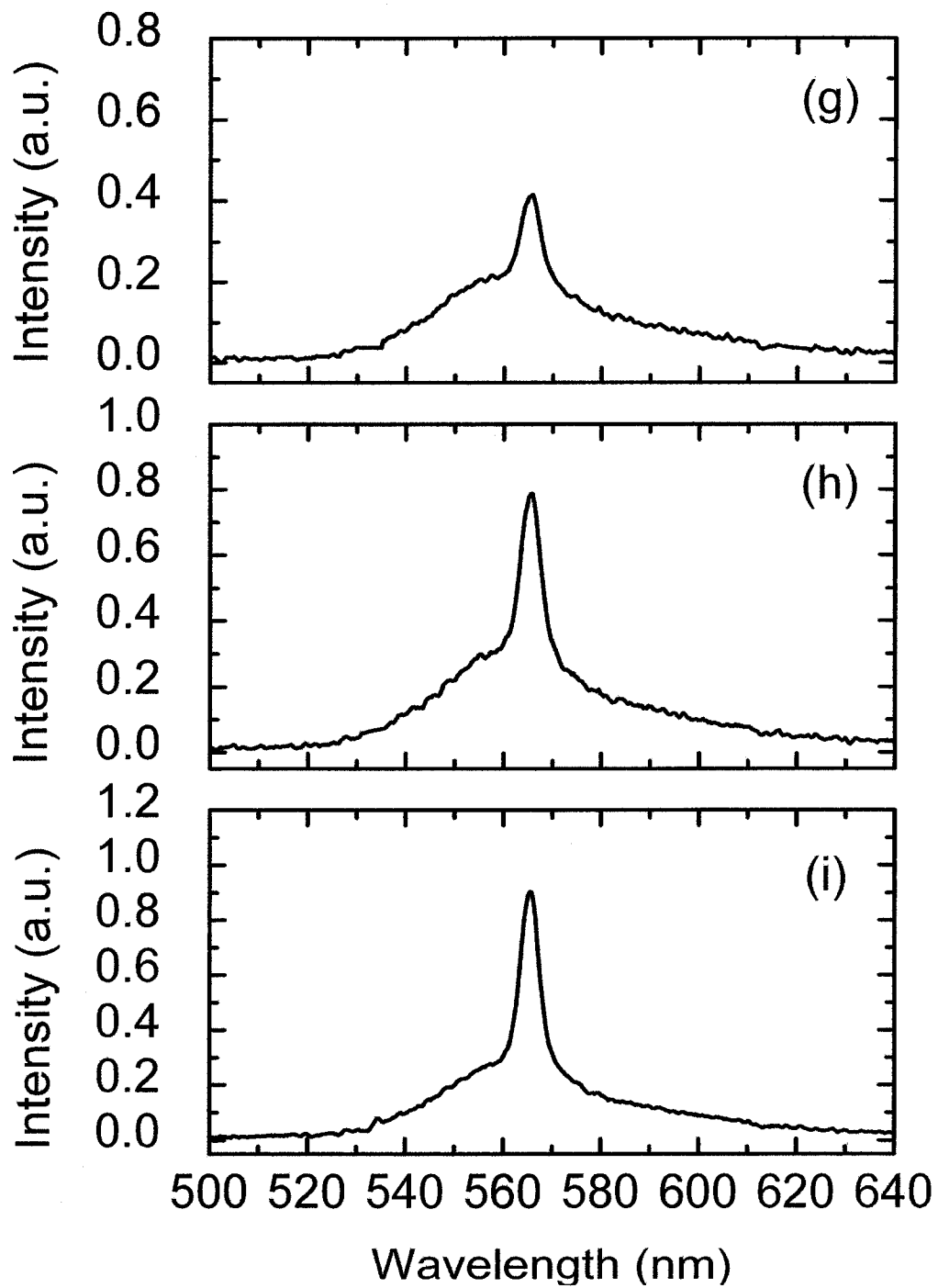


Figure 4.17 – (g) $F = 17.0 \text{ mJ/cm}^2$ (h) $F = 20.8 \text{ mJ/cm}^2$ (i) $F = 24.6 \text{ mJ/cm}^2$.

Table 4.7

Pump Fluence (mJ/cm ²)	Linewidth (nm)	Peak Wavelength (nm)
0.5	35	554
13.2	6.4	566
24.6	5.2	566

For a silver particle concentration of 4.7 mg/mL the mean free path is $\ell = 350$ μm , which is well within the modest scattering regime ($L/\ell = 4.7$). Figure 4.18 (curves a - c) and Table 4.8 respectively illustrate the emission spectra and laser characteristics measured from this random gain media. At $F = 0.95$ mJ/cm² the emission displays the standard broadband characteristics of Rhodamine 6G laser dye. As the pump fluence is increased to $F = 3.8$ mJ/cm² a sudden decrease in the emission linewidth indicates the onset of random lasing. This threshold pump fluence is smaller than for the Ag scatterer based random gain media with $\ell = 78$ μm ($F = 13.2$ mJ/cm²), which is attributed to less overall self-absorption caused by the smaller Ag particle concentration. The linewidth remains essentially constant, while the intensity increases fivefold as the input pump energy fluence is increased beyond the threshold to $F = 9.5$ mJ/cm².

Table 4.8

Pump Fluence (mJ/cm ²)	Linewidth (nm)	Peak Wavelength (nm)
0.95	35	555
3.8	4.5	563
9.5	4.2	564

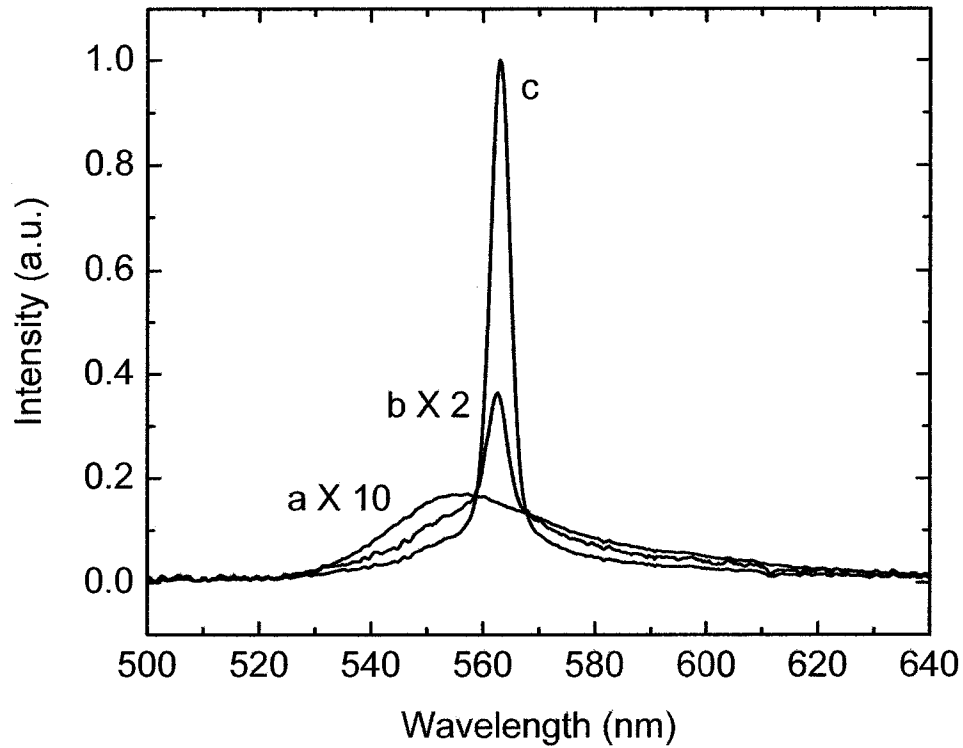


Figure 4.18 – Spectrum of light emission from Rhodamine 6G with suspended Ag nanoparticles at $\ell = 350 \mu\text{m}$. (a) The broadband fluorescence spectrum having a linewidth of 36 nm pumped at $F = 0.95 \text{ mJ/cm}^2$. (b) The narrowband emission spectrum at $F = 3.8 \text{ mJ/cm}^2$ which has a linewidth of 4.5 nm. (c) A 5-fold increase in emission intensity at $F = 9.5 \text{ mJ/cm}^2$ with the same 4.5 nm linewidth.

A random gain media with $\ell = 1.05$ mm ($L/\ell = 1.5$), falls very close to the edge of the modest scattering regime. Figure 4.19 (curves a - c) depicts the emission spectrum for this sample at $F = 0.5$ mJ/cm² (a), 3.8 mJ/cm² (b), and 24.6 mJ/cm² (c). At $F = 0.5$ mJ/cm² the spontaneous emission is typical of a random gain media below threshold as shown in Table 4.9. As F exceeds 3.8 mJ/cm² a threshold for lasing is reached as indicated by the bandwidth narrowing accompanied by intense light emission. As F is increased beyond 3.8 mJ/cm² to $F = 24.6$ mJ/cm² the linewidth further decreases, while the emitted intensity increases 30 times. The drastic narrowing, and 1900 fold intensity increase over the entire studied range of F are indicators of the effects of SP enhancement. It should be emphasized that, for $L/\ell \sim 1.5$, laser operation takes place in a regime where on average only a single scattering event occurs for each emitted photon. In this regime, non-resonant feedback must be accompanied by large optical gain to compensate for low scattering probabilities. The large optical gain must be provided by the SP enhancement near the surface of the Ag particles.

Table 4.9

Pump Fluence (mJ/cm ²)	Linewidth (nm)	Peak Wavelength (nm)
0.5	35	558
3.8	6.7	564
24.6	4.2	565

In a silver scatterer based random laser where ℓ is further increased to 3.2 mm, the scattering strength of $L/\ell = 0.5$, falls into the weakly scattering regime. Figure 4.20 (curves a - c) illustrates the emission spectra for this random gain media at $F = 0.95$ mJ/cm² (curve a), 3.8 mJ/cm² (curve b), and 9.5 mJ/cm² (curve c). At $F = 0.95$ mJ/cm² broadband spontaneous emission is observed. As indicated by intense light emission and bandwidth narrowing, a lasing threshold is reached when F exceeds 4.2 mJ/cm². Figure

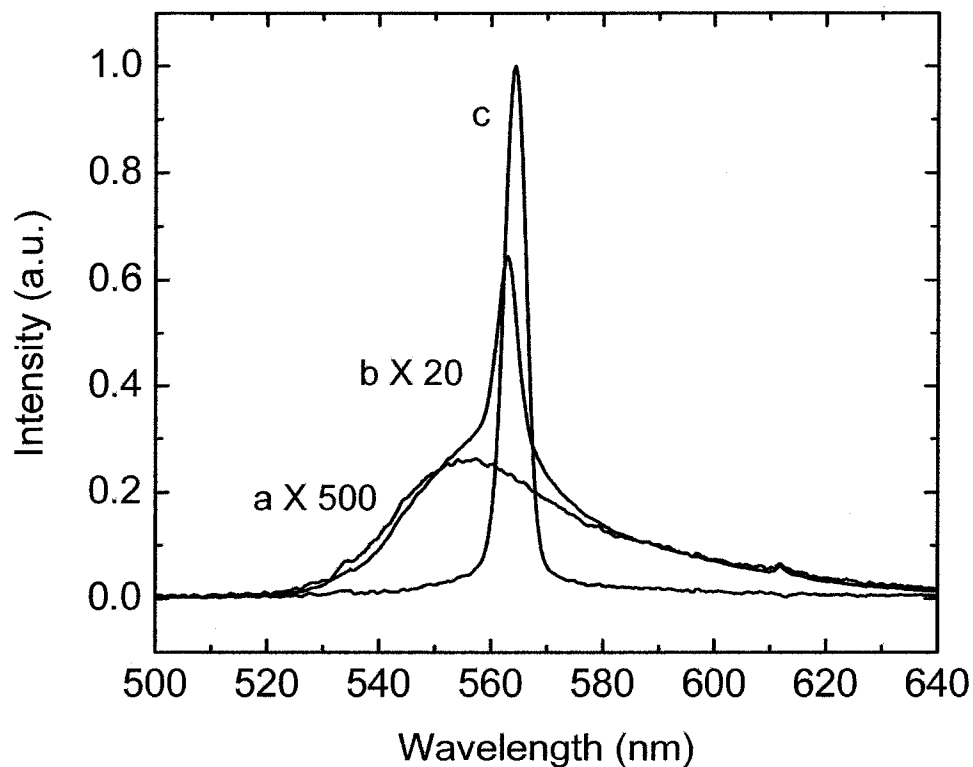


Figure 4.19 – Spectrum of light emission from Rhodamine 6G with suspended Ag nanoparticles at a mean free path $\ell = 1.05$ mm. (a) The broadband fluorescence spectrum (linewidth = 36 nm) pumped at $F = 0.5$ mJ/cm². (b) The narrowband emission spectrum at $F = 3.8$ mJ/cm² which has a linewidth of 6.7 nm. (c) A thirty fold increase in emission intensity at $F = 24.6$ mJ/cm² with a 4.2 nm emission linewidth.

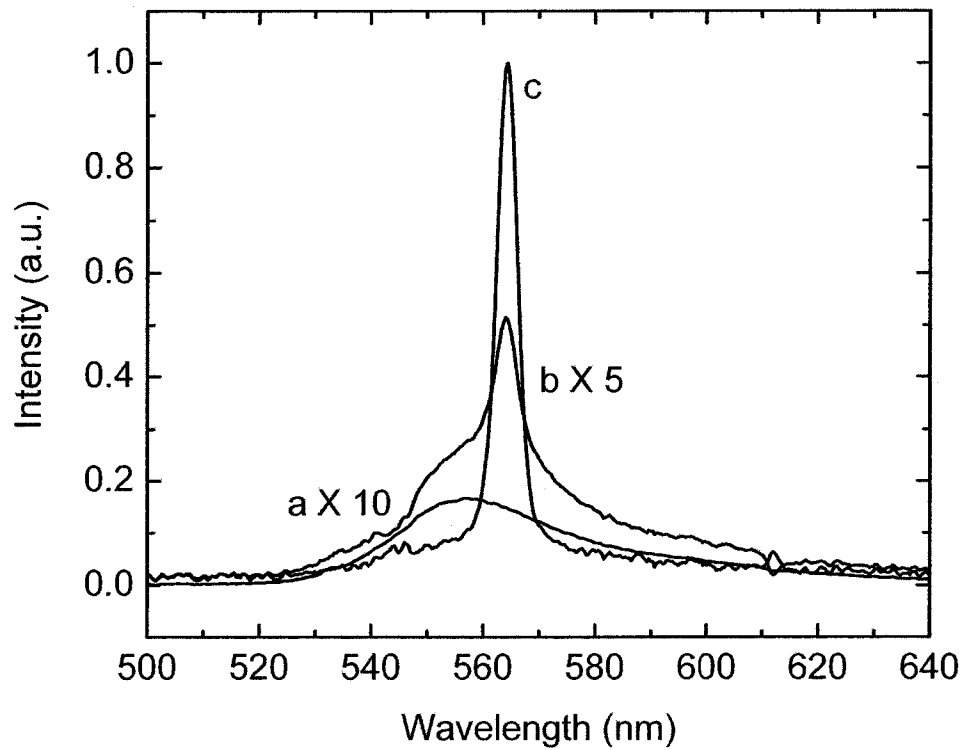


Figure 4.20 – Spectrum of light emission from Rhodamine 6G with Ag nanoparticles at a mean free path $\ell = 3200 \mu\text{m}$. (a) The broadband fluorescence spectrum (linewidth = 36 nm) pumped at $F = 0.95 \text{ mJ/cm}^2$. (b) The narrowband emission spectrum at $F = 3.8 \text{ mJ/cm}^2$. (c) An order of magnitude increase in the emission intensity at $F = 9.5 \text{ mJ/cm}^2$ with a bandwidth of 4.6 nm.

4.20 (curve c) illustrates that increasing F further to 9.5 mJ/cm^2 results in a spectral emission peak at 565 nm with a bandwidth of 4.6 nm . It should be noted that the threshold F required for $\ell = 3.2 \text{ mm}$ ($F = 4.2 \text{ mJ/cm}^2$) is greater than that required for $\ell = 1.05 \text{ mm}$ ($F = 3.8 \text{ mJ/cm}^2$) due to the decreased scattering in this sample. With increasing ℓ , scattering events are less probable, and the random gain medium enters the weakly scattering regime where $L/\ell < 1$. However, in contrast with the Al_2O_3 scatterer based random lasers having $\ell > 1.6 \text{ mm}$, the Ag scatterer based random gain media with $\ell = 3.2 \text{ mm}$ displays an abrupt lasing threshold and a linewidth plateau due to the effects of surface plasmon gain enhancement. Each scattering event in this Ag scatterer based random gain media is accompanied by a co-localized gain enhancement that compensates for low scattering probabilities to create the narrow spectral emission line. This is unlike the Al_2O_3 scatterer based random lasers that do not sustain laser-like emission at this ℓ and F . A summary of the emission characteristics is shown in Table 4.10.

Table 4.10

Pump Fluence (mJ/cm^2)	Linewidth (nm)	Peak Wavelength (nm)
0.95	36	558
5.7	4.6	564
9.5	4.6	565

4.4.2 Linewidth Variation in Ag Scatterer Based Random Lasers

The FWHM linewidth variation as a function of input pump fluence provides a basis for comparison of the performance of Ag scatterer based random lasers to that of Al_2O_3 scatterer based random lasers. Figure 4.21 illustrates the variation of the FWHM emission linewidth for Ag scatterer based random lasers having ℓ in the range of $\ell = 78 \text{ }\mu\text{m}$ to 43 mm . For comparison purposes, the FWHM linewidth from an Al_2O_3 scatterer based random laser having $\ell = 170 \text{ }\mu\text{m}$ is also shown. The SP enhancement of random

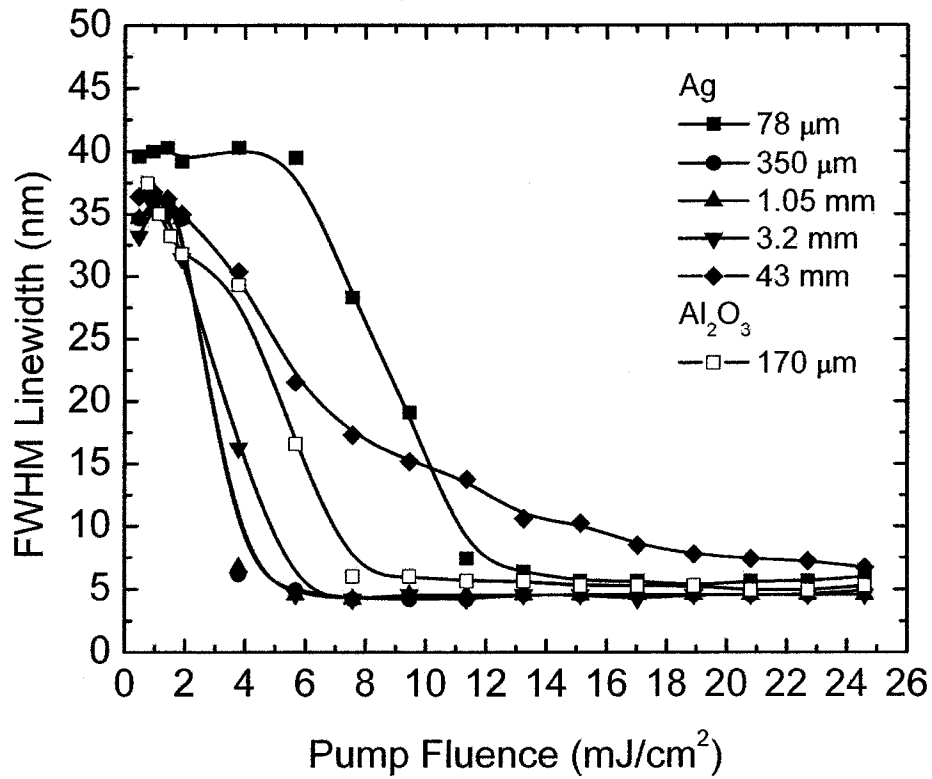


Figure 4.21 – Variation in emission linewidth as a function of input pump fluence F for Ag scatterer based random lasers having $\ell = 78 \mu\text{m}$ (■), $\ell = 350 \mu\text{m}$ (●), $\ell = 1.05 \text{ mm}$ (▲), $\ell = 3.2 \text{ mm}$ (downwards triangles), and $\ell = 43 \text{ mm}$ (◆). The Al_2O_3 scatterer based random laser having $\ell = 170 \mu\text{m}$ (□) is shown for comparison purposes. The effects of SP enhanced random lasing are evident, as the threshold energy fluence is $\sim 5 \text{ mJ/cm}^2$ at both $\ell = 3.2 \text{ mm}$ and $\ell = 350 \mu\text{m}$. Additionally, the Ag scatterer based random lasers with $\ell = 350 \mu\text{m}$, 1.05 mm , and 3.2 mm all have a smaller threshold fluence than the Al_2O_3 scatterer based random laser with $\ell = 170 \mu\text{m}$.

both $\ell = 1.05$ mm and 3.2 mm have a similar lasing threshold energy fluence and similar linewidth narrowing to an Al_2O_3 scatterer based random laser having $\ell = 170$ μm . This is due to the SP enhancement of local optical gain. SP enhancement allows weakly scattering Ag scatterer based random lasers to have superior performance compared to strongly scattering Al_2O_3 scatterer based random lasers. Interestingly, even at $\ell = 43$ mm, where an insignificant number of scattering events take place ($L/\ell \sim 0.04$), the Ag scatterer based random laser shows significant linewidth narrowing at $F = 24.6$ mJ/cm^2 to 6.7 nm. In this extremely weak scattering regime, the system has to be pumped with F a factor of 8 times larger than the minimum threshold F at smaller ℓ , to compensate for the lack of multiple scattering. A summary of the threshold fluences and minimum linewidths is contained in Table 4.11.

Table 4.11

Material	ℓ (μm)	Threshold Fluence (mJ/cm^2)	Minimum Linewidth (nm)
Ag	78	10.8	6
Ag	350	3	4.2
Ag	1050	3	4.2
Ag	3200	3.6	4.6
Ag	43×10^3	7.1	6.7
Al_2O_3	170	5.7	5.3

4.4.3 Intensity Variation in Ag Scatterer Based Random Lasers

In Figure 4.22, the relative peak intensity is displayed for Ag scatterer based random lasers with $\ell = 78$ μm (■), $\ell = 350$ μm (●), $\ell = 1.05$ mm (▲), $\ell = 3.2$ mm (▼), and $\ell = 43$ mm (◆) as a function of F . While the curves have similar trends, the maximum intensities reached by each laser at a given input energy fluence are very different. The random laser with the optimum scattering strength has a mean free path of 1.05 mm. The

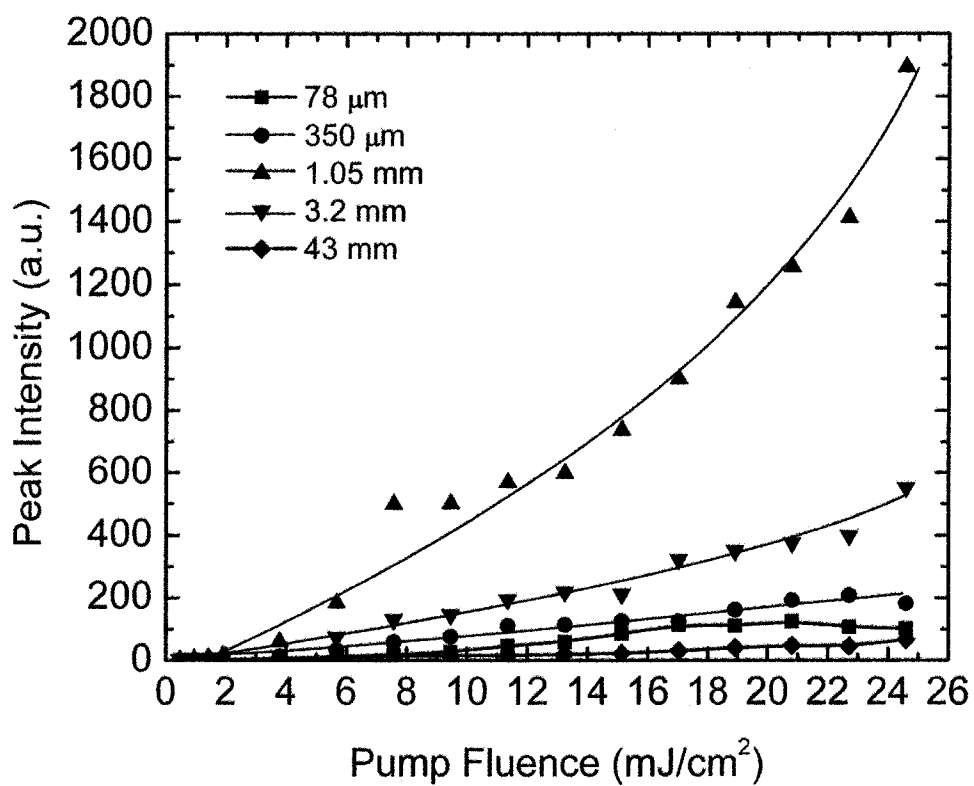


Figure 4.22 – Relative peak emitted intensity vs. input pump fluence F for Ag scatterer based random lasers having $\ell = 78 \mu\text{m}$ (■), $\ell = 350 \mu\text{m}$ (●), $\ell = 1.05 \text{ mm}$ (▲), $\ell = 3.2 \text{ mm}$ (▼), and $\ell = 43 \text{ mm}$ (◆).

general trend is that maximum intensity increases as ℓ increases until ℓ reaches 1.05 mm, whereupon it decreases with increasing ℓ . This trend arises from the absorption emitted photons by the Ag scattering particles, which overcomes the amplification as the particle concentration is increased.

4.4.4 *Input Pump Energy Fluence Threshold for Lasing*

A unique feature of the Ag scatterer based random laser is illustrated in figure 4.23. The dependence of the threshold F on scattering strength shows a clear minimum value. As L/ℓ increases from 3.7×10^{-3} to 1.5 the lasing threshold lowers, which is consistent with dielectric-scatterer based random lasers [10]. However, for $L/\ell \geq 1.5$, the energy fluence threshold begins to rise. For the highest concentration of silver nanoparticles (42 mg/mL) where $L/\ell = 41$, there is no indication of random lasing even for $F = 24.6 \text{ mJ/cm}^2$. Of greater interest is the range $14 > L/\ell > 0.5$, which includes the modest and weakly scattering regimes. A large linewidth narrowing is observed over this entire range. The lasing threshold drops from $F = 10.8 \text{ mJ/cm}^2$ at $L/\ell = 21$ to 3.0 mJ/cm^2 at $L/\ell = 1.5$, and then gradually rises as the scattering strength reduces. In the present Ag scatterer based random laser, the optimum scattering strength is observed to be $L/\ell = 1.5$ ($\ell = 1.05 \text{ mm}$), where the largest linewidth narrowing factor of 9.0 is obtained compared to 7.6 for the Al_2O_3 scatterer based random laser at $\ell = 170 \text{ }\mu\text{m}$. At high Ag particle concentrations, the probability that an emitted photon will be reabsorbed by a silver particle is greatly increased, and thus the overall intensity of emitted light decreases. At the critical concentration, the total absorption experienced by emitted photons overcomes

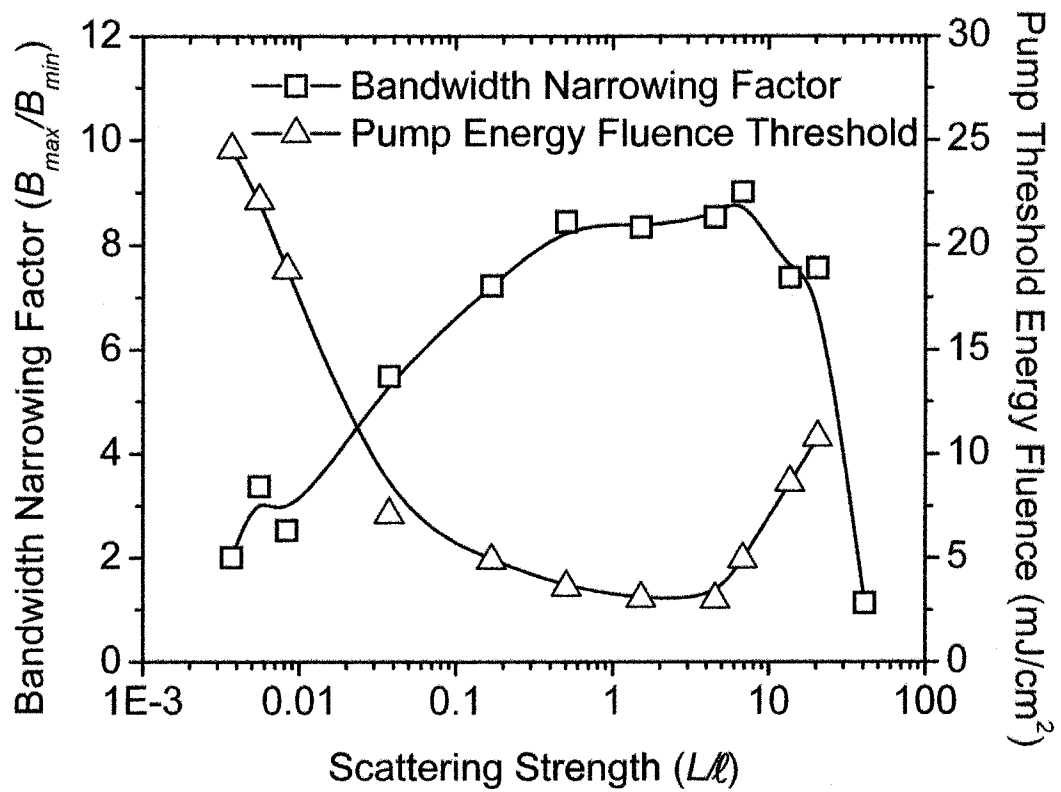


Figure 4.23 – Dependence of the input pump energy fluence threshold, F , (Δ) and the bandwidth narrowing factor (\square) on scattering strength, L/ℓ . Random lasing is observed over a wide optimal range of scattering strengths, centred at the crossover between the weak and modestly scattering regimes ($L/\ell = 1$).

the total enhanced gain provided by the additional Ag particles, and random lasing no longer occurs.

4.5 Hybrid Ag/Al₂O₃ Scatterer Based Random Lasers

When compared to a standard dielectric dye-scatterer based random laser, the Ag nanoparticle dye-scatterer based random laser demonstrates a reduced pump energy fluence threshold for strong stimulated emission, and a decreased linewidth at low scatterer concentrations. This performance is achieved by exploiting the unique scattering and field enhancement properties of Ag nanoparticles. A random laser created from the combination of metallic and dielectric particles can thus maximize the benefits of Ag particles by allowing the use of Ag concentrations below the absorption limit, while still enabling random lasing. Hence, a balance point between absorption and scattering from Ag nanospheres may be achieved. The following section reports on the investigation of the role of metal particles in the performance of a dye-scatterer random laser consisting of suspended Al₂O₃ scattering particles. To reduce the pump energy fluence threshold for lasing and increase the intensity of emitted light, the mean free path may be decreased by increasing the concentration of scattering centres; however, their physical size ultimately limits the available active gain volume. This effect occurs for both Ag and Al₂O₃ scatterers, with the significant absorption from Ag particles also playing a major role in the reduction of emitted light. In a hybrid random Ag/Al₂O₃ scatterer based random laser the Al₂O₃ particles dominate the performance. The inclusion of a small concentration of Ag nanoparticles provides electromagnetic field enhancement for both pumping and spontaneously emitted photons while not affecting the scattering

characteristics of the media. Alternatively, metal particles that do not significantly alter the scattering mean free path, and that have a small physical size, provide local optical gain enhancement. Several experiments were performed over a wide range of Ag and Al₂O₃ concentrations and various pump energy fluences, to determine the optimum parameters. For a dielectric scatterer based random laser having $\ell_{Al_2O_3} \ll L$, with a well-defined definite input pump energy fluence threshold, it was observed that the addition of a small amount ($\sim 2\%$) of Ag nanospheres resulted in a three-fold increase in the peak emission intensity. Such an enhancement was accompanied by a ~ 1 nm reduction of the minimum emission linewidth.

4.5.1 Hybrid Random Lasers

To determine the optimum concentration of Ag nanoparticles in a hybrid Ag/Al₂O₃ scatterer based random laser, 55 nm diameter Ag particles were suspended in a 10⁻³ mol/L solution of Rhodamine 6G dissolved in methanol. Regulated amounts of these particles were then transferred into an Al₂O₃ scatterer based random laser via a 2-20 μ L pipette, varying the final Ag nanoparticle concentration from 29 μ g/mL to 517 μ g/mL. At the peak random laser wavelength of $\lambda_{laser} = 564$ nm, each 100 nm diameter Al₂O₃ particle has a scattering cross-section of $\sigma_{sc} = 2.4 \times 10^{-16}$ m², while each 55 nm diameter Ag particle has a scattering cross-section of $\sigma_{sc} = 5.5 \times 10^{-16}$ m². Thus, while each Ag particle is approximately as likely to scatter light, the higher Al₂O₃ particle concentration ensures that scattering events from Al₂O₃ particles are more probable than those from Ag particles. With two scattering species in this random laser, the effective mean free path, ℓ_{eff} , is calculated from $1/\ell_{eff} = 1/\ell_{Ag} + 1/\ell_{Al_2O_3}$, where ℓ_{Ag} and $\ell_{Al_2O_3}$ are the mean free

path for each individual species. Figure 4.24 depicts ℓ_{eff} as a function of Ag particle concentration for Al₂O₃ scatterer based random lasers with $\ell_{Al_2O_3} = 340 \mu\text{m}$, $680 \mu\text{m}$, and $2700 \mu\text{m}$. As can be seen for the $\ell_{Al_2O_3} = 680 \mu\text{m}$ system, ℓ_{eff} decreases to $560 \mu\text{m}$ at the maximum Ag particle concentration of $517 \mu\text{g/mL}$. Since the change in ℓ_{eff} , $\Delta\ell_{eff}$, is not significant in this case, the primary optical effect of additional Ag particles is SP field enhancement of the local optical gain. While ℓ_{eff} does decrease with the addition of Ag nanoparticles, the change is substantial only for the Al₂O₃ scatterer based random laser with $\ell_{Al_2O_3} = 2700 \mu\text{m}$, where ℓ_{eff} is reduced to $1460 \mu\text{m}$. In this situation, the added Ag particles result in gain enhancement, scattering, and absorption in the random laser.

4.5.2 Spectral Behaviour of Hybrid Random Lasers

Figure 4.25 displays emission spectra at $F = 10.9 \text{ mJ/cm}^2$ for each of the hybrid Ag/Al₂O₃ random lasers with varying Ag particle concentrations. Figure 4.25 (a) depicts the emission spectra of a hybrid random laser at $\ell_{Al_2O_3} = 340 \mu\text{m}$ ($57 \mu\text{g/mL}$ of Ag particles). For relative comparison, the laser without Ag particles is also displayed on the same graph. In the hybrid random gain media, ℓ_{eff} is reduced by a mere $4 \mu\text{m}$ (from $340 \mu\text{m}$ to $336 \mu\text{m}$), indicating that scattering effects from Ag are minimal. While there is no change in the scattering, optical gain enhancement from the localized SP field causes the peak emitted intensity to be enhanced by a factor of ~ 3.1 at this very low Ag concentration. Accompanying this enhancement there is a 0.4 nm decrease in emission

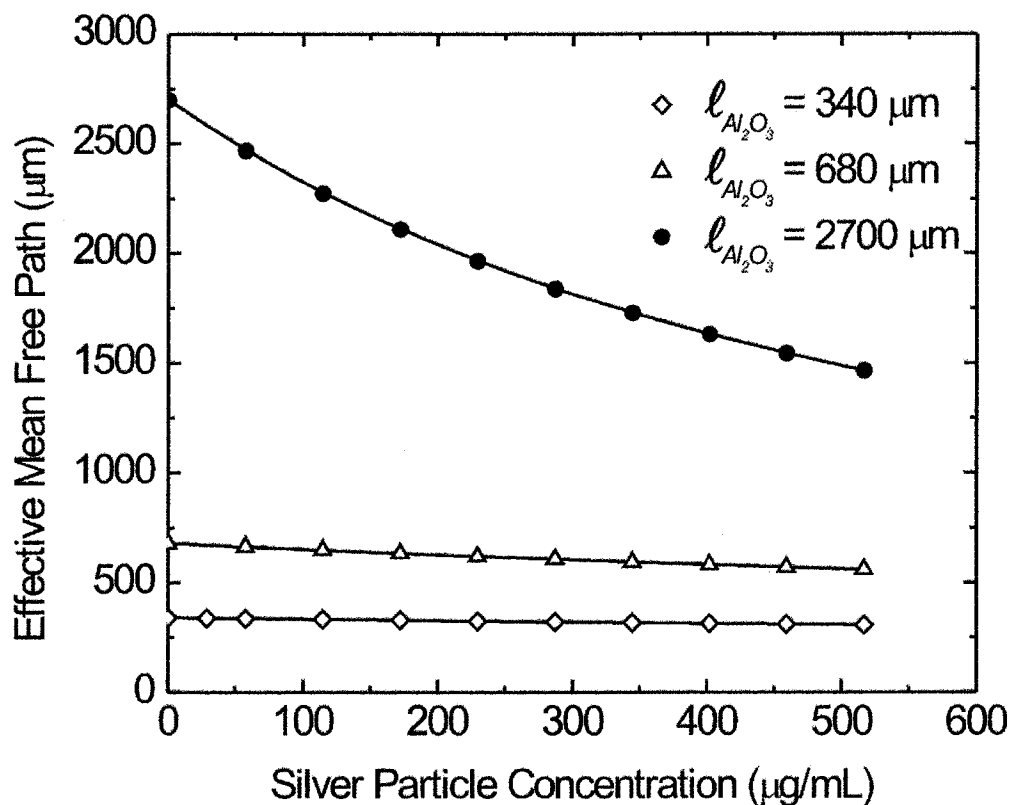


Figure 4.24 – Effective mean free path (ℓ_{eff}) vs. Ag particle concentration for hybrid Ag/Al₂O₃ scatterer based random lasers having $\ell_{Al_2O_3} = 340 \mu m$ (◇), $\ell_{Al_2O_3} = 680 \mu m$ (△) and $\ell_{Al_2O_3} = 2700 \mu m$ (●). There is little change in ℓ_{eff} for random lasers with $\ell_{Al_2O_3} = 340 \mu m$ and $\ell_{Al_2O_3} = 680 \mu m$, however, the random laser with $\ell_{Al_2O_3} = 2700 \mu m$ experiences significantly more scattering as Ag particles are added.

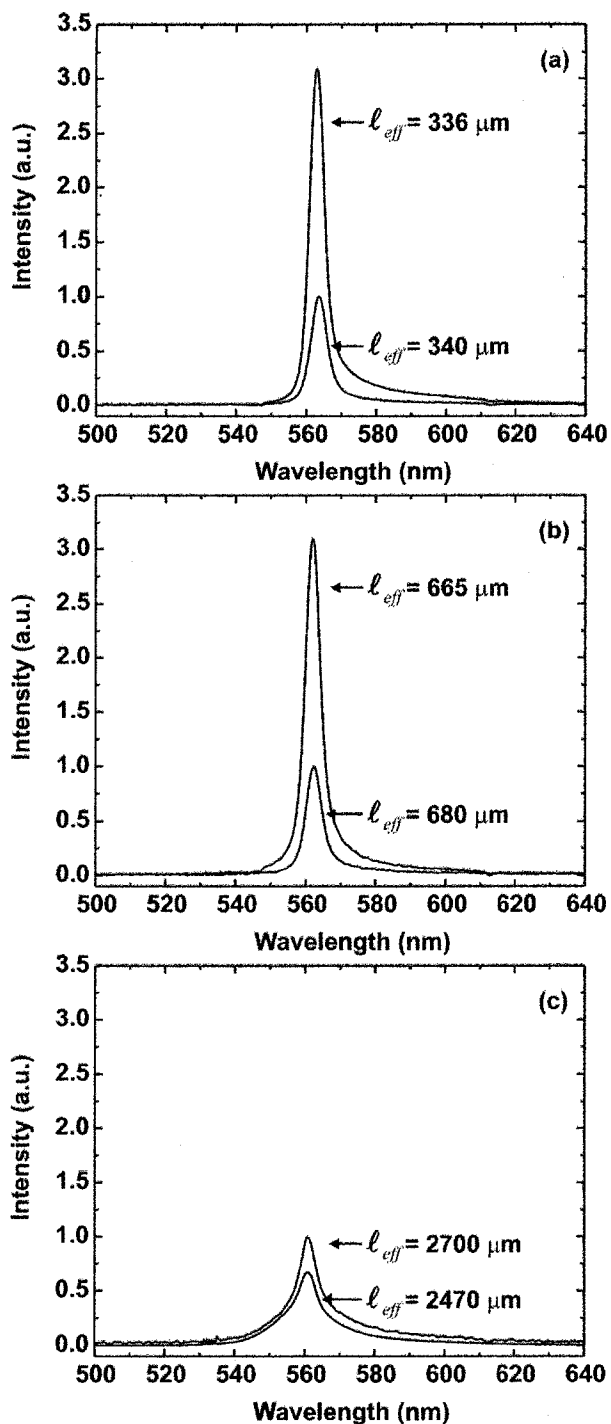


Figure 4.25 – Hybrid random laser spectra having $\ell_{Al_2O_3} = 340 \mu\text{m}$ (a), $\ell_{Al_2O_3} = 680 \mu\text{m}$ (b), and $\ell_{Al_2O_3} = 2700 \mu\text{m}$ (c). The spectra are depicted for cases without Ag particles, and at a Ag particle concentration of $57 \mu\text{g/mL}$. An intensity enhancement of ~ 3.1 is observed for random lasers with both $\ell_{Al_2O_3} = 340 \mu\text{m}$ and $\ell_{Al_2O_3} = 680 \mu\text{m}$. At $\ell_{Al_2O_3} = 2700 \mu\text{m}$ the peak emitted intensity is decreased by a factor of ~ 0.7 .

linewidth, from 5.3 nm (without Ag) to 4.9 nm (with Ag). Similarly, as shown in Figure 4.25 (b), an Al_2O_3 scatterer based random laser with $\ell_{\text{Al}_2\text{O}_3} = 680 \mu\text{m}$ has a peak output intensity enhancement of ~ 3.1 at the same Ag concentration. Clearly the likelihood of scattering events is not responsible for increased light output, as reducing ℓ_{eff} from 680 μm to 665 μm provided the same intensity enhancement. In contrast, as shown in Figure 4.25 (c), the addition of 57 $\mu\text{g}/\text{mL}$ of Ag to an Al_2O_3 scatterer based random laser ($\ell_{\text{Al}_2\text{O}_3} = 2700 \mu\text{m}$), reduces the emitted peak intensity by a factor of 0.7. For such a hybrid random laser, the decrease in the emitted intensity indicates that the relative concentration of Ag particles results in higher self-absorption. That is, the SP enhanced optical gain is overwhelmed by increased absorption by the Ag particles.

In each of the hybrid random lasers, the maximum Ag particle concentration studied was 517 $\mu\text{g}/\text{mL}$. At this concentration, the mean free path between Ag particles alone is 3.2 μm . From experiments described earlier, Ag scattering particles at this mean free path are expected to provide a lasing threshold of $F = 3.8 \text{ mJ}/\text{cm}^2$. The lasing threshold in the random gain media having $\ell_{\text{Al}_2\text{O}_3} = 2700 \mu\text{m}$ with 517 $\mu\text{g}/\text{mL}$ of Ag particles is slightly higher at 5 mJ/cm^2 . Clearly, there is another factor influencing the threshold in this hybrid random laser.

4.5.3 Linewidth Variation from Hybrid Random Lasers

The minimum FWHM emission linewidth as a function of Ag concentration is depicted in Figure 4.26 for hybrid random lasers having $\ell_{\text{Al}_2\text{O}_3} = 340 \mu\text{m}$, 680 μm , and 2700 μm .

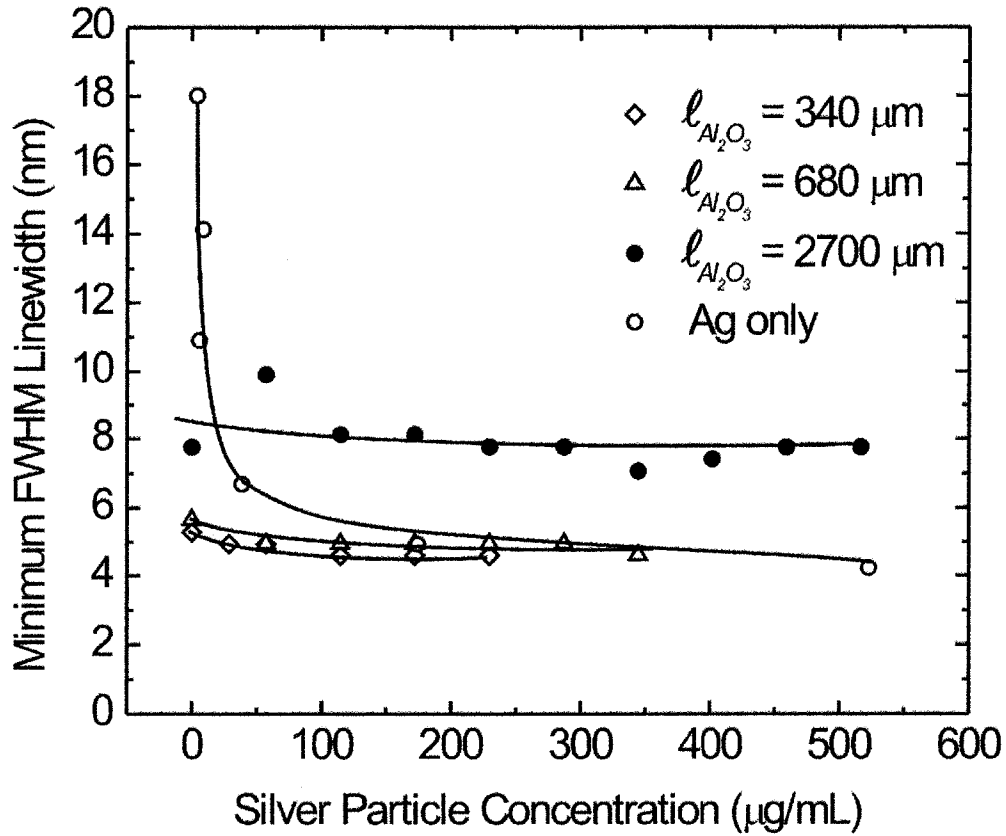


Figure 4.26 – Minimum FWHM emission linewidth vs. Ag particle concentration for hybrid Ag/Al₂O₃ scatterer based random lasers having $l_{Al_2O_3} = 340 \mu m$ (\diamond), $l_{Al_2O_3} = 680 \mu m$ (\triangle), and $l_{Al_2O_3} = 2700 \mu m$ (\bullet). The minimum FWHM emission linewidth for a silver scatterer based random laser (\circ) is depicted as a function of Ag particle concentration. A small decrease in linewidth with increasing Ag particle concentration can be seen for $l_{Al_2O_3} = 340 \mu m$, and $l_{Al_2O_3} = 680 \mu m$, while linewidth remains approximately constant for $l_{Al_2O_3} = 2700 \mu m$.

For Al_2O_3 scatterer based random lasers at $\ell_{\text{Al}_2\text{O}_3} = 340 \mu\text{m}$ and $\ell_{\text{Al}_2\text{O}_3} = 680 \mu\text{m}$, the linewidth decreases from 5.3 nm to 4.6 nm, and from 5.7 nm to 4.6 nm respectively. This decrease is attributed to the combination of increased scattering from Ag particles, and SP enhancement of the local optical gain. For a hybrid random laser having $\ell_{\text{Al}_2\text{O}_3} = 2700 \mu\text{m}$, however, the minimum linewidth remains constant at $\sim 8 \text{ nm}$.

4.5.4 Intensity Variation from Random Lasers

Figure 4.27 illustrates the peak emitted output intensity enhancement from a hybrid random laser as a function of various Ag particle concentrations. Here, the intensity enhancement factor is normalized to the peak intensity for each random laser when $\ell_{\text{eff}} = \ell_{\text{Al}_2\text{O}_3}$ (i.e. with no Ag particles). As shown, the hybrid random lasers with $\ell_{\text{Al}_2\text{O}_3} = 340 \mu\text{m}$ and $680 \mu\text{m}$ achieve a balance between SP gain enhancement and absorption producing maximal light output at a Ag particle concentration of $57 \mu\text{g/mL}$. Beyond this Ag concentration, the peak emitted intensity decreases because of interplay between optical absorption, scattering, and optical gain enhancement. However, the hybrid random laser with $\ell_{\text{Al}_2\text{O}_3} = 2700 \mu\text{m}$ displays a different general trend where the laser emission intensity decreases as the concentration of the Ag particles increases. Over this wide Ag particle concentration range, the laser is always operating in the weak scattering regime. Interestingly, even at the optimum concentration of the Ag particles of $57 \mu\text{g/mL}$, the emission intensity is reduced by 30%. The lack of sufficient scattering events clearly hinders the hybrid laser performance. At a silver particle concentration of $57 \mu\text{g/mL}$ random lasing is not expected at pump fluences less than 17 mJ/cm^2 . Thus, the

required optical feedback for random lasing is provided by Al_2O_3 particles for $\ell_{\text{Al}_2\text{O}_3} = 340 \text{ }\mu\text{m}$ and $680 \text{ }\mu\text{m}$, but is not present for $\ell_{\text{Al}_2\text{O}_3} = 2700 \text{ }\mu\text{m}$. The lack of intensity enhancement at a silver concentration of $517 \text{ }\mu\text{g/mL}$ can be attributed to a reduction in available optical gain caused by the presence of the two scattering species. At the highest Ag particle concentration of $517 \text{ }\mu\text{g/mL}$, the number density of Ag particles is $5.6 \times 10^{11} \text{ cm}^{-3}$. At $\ell_{\text{Al}_2\text{O}_3} = 2700 \text{ }\mu\text{m}$, the number density of Al_2O_3 particles is $1.2 \times 10^{12} \text{ cm}^{-3}$. This provides a 2:1 ratio of Al_2O_3 particles to Ag particles, so a photon scattered from a silver particle has a greater probability of subsequently scattering from an Al_2O_3 particle than it does from a second Ag particle. As an Al_2O_3 particle occupies 8 times the volume of an Ag particle, the overall system gain is reduced compared to the Ag scatterer based random laser reported previously [11]. Consequently, the input energy fluence threshold for random lasing is increased from $F = 3.8 \text{ mJ/cm}^2$ for Ag particles alone to $F = 5 \text{ mJ/cm}^2$ for the hybrid random laser.

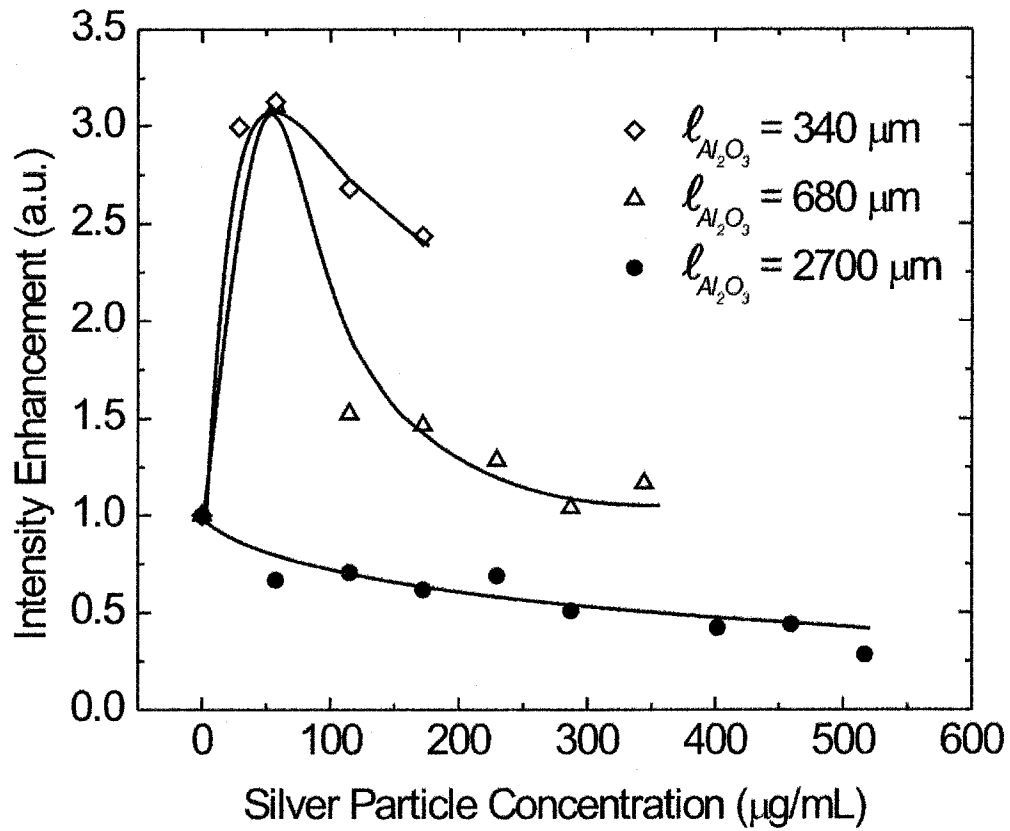


Figure 4.27 – Relative peak emitted intensity vs. Ag particle concentration for hybrid random lasers having $l_{Al_2O_3} = 340 \mu\text{m}$ (◇), $l_{Al_2O_3} = 680 \mu\text{m}$ (△), and $l_{Al_2O_3} = 2700 \mu\text{m}$ (●). The $l_{Al_2O_3} = 340$ and $l_{Al_2O_3} = 680 \mu\text{m}$ curves show that a maximum peak intensity enhancement factor of ~ 3.1 occurs at the optimum Ag particle concentration of $57 \mu\text{g/mL}$.

4.6 References

- [1] H. Du, R. A. Fuh, J. Li, A. Corkan, and J. S. Lindsey, "PhotochemCAD: A computer-aided design and research tool in photochemistry," *Photochemistry and Photobiology*, **68**, 141-142 (1998).
- [2] R. Zondervan, F. Kulzer, M. A. Kol'chenko, and M. Orrit, "Photobleaching of Rhodamine 6g in poly(vinyl alcohol) at the ensemble and single-molecule levels," *J. Phys. Chem. A*, **108**, 1657-1665 (2004).
- [3] R. Zondervan, F. Kulzer, S. B. Orlinskii, and M. Orrit, "Photoblinking of Rhodamine 6G in poly(vinyl alcohol): Radical dark state formed through the triplet," *J. Phys. Chem. A*, **107**, 6770-6776 (2003).
- [4] C. Bohren and D. Huffman, *Absorption and Scattering of Light by Small Particles* (Wiley, New York, 1983).
- [5] M. J. Weber, *CRC Handbook of Optical Materials*, (Boca Raton, CRC Press, 2003).
- [6] F. Mafune, H. Kohno, Y. Takeda, T. Kondow, and H. Sawabe, "Formation and size control of silver nanoparticles by laser ablation in aqueous solution," *J. Phys. Chem B*, **104**, 9111 (2000).
- [7] P. C. de Oliveira, J. A. McGreevy, and N. M. Lawandy, "External-feedback effects in high-gain scattering media," *Opt. Lett.*, **22**, 895-897 (1997).
- [8] H. Cao, "Lasing in random media," *Waves Random Media*, **13**, R1-R39 (2003).
- [9] B. R. Prasad, H. Ramachandran, A. K. Sood, C. K. Subramanian, N. Kumar, "Lasing in active, sub-mean-free path-sized systems with dense, random, weak scatterers," *Appl. Opt.*, **36**, 7718-7724 (1997).

- [10] A. L. Burin, H. Cao, and M. Ratner, "Understanding and control of random lasing," *Physica B*, **338**, 212 (2003).
- [11] G. D. Dice, S. Mujumdar, and A. Y. Elezzabi, "Plasmonically enhanced diffusive and subdiffusive metal nanoparticle-dye random laser," *Appl. Phys. Lett.*, **86**, 131105 (2005)

Chapter 5: Solid Random Laser

5.1 SU-8 Based Random Laser

There are several issues with the use of a liquid dye solution for the suspension of scattering particles. A liquid dye random laser is difficult to store, as the Rhodamine 6G is dissolved in methanol that evaporates and leaves behind a dried powdered dye. For long-term storage, the glass optical cell must also be protected from physical damage. As such, there are durability issues with a liquid based random laser. Additionally, as the Al_2O_3 and Ag scattering particles have densities greater than the methanol solvent, the particles eventually settle out of suspension. The random laser sample must be sufficiently agitated to maintain the suspended scattering particles. It is therefore desirable to develop a random laser that maintains the advantages of the suspended particles in a liquid dye construction, while removing the disadvantages of a liquid dye. The use of a solid to suspend scattering particles allows for the integration of a random laser into optical devices such as optical displays or identification tags.

5.2 Solid Suspension of Scattering Particles

It is a challenge to find a liquid solvent with a sufficient density to make silver particles with a density of $1.05 \times 10^4 \text{ kg/m}^3$ neutrally buoyant. In a solid state random laser, however, the silver particles will remain suspended indefinitely. Thus, a chemical is required that will dissolve the Rhodamine 6G, and that can be solidified. In optical terms, the solid must have a refractive index that allows for scattering from both dielectric and metallic particles.

Several solid-state random lasers have been constructed from the combination of an optically active solid material and scattering particles. These are typically formed from the dissolution of laser dye into a supporting solvent, which is then mixed with scattering particles and solidified. An example of this type of random laser is the mixture of 50 nm diameter SiO₂ nano-particles into a Rhodamine 6G doped poly-methyl methacrylate matrix [1]. A second example is the dissolution of Rhodamine 640 laser dye into a mixture of mono-methyl methacrylate and hydroxyethyl methacrylate, with the use of 250 nm diameter TiO₂ scattering particles [2].

A material that dissolves Rhodamine 6G and can be solidified is the photoresist SU-8, an EPON SU-8 epoxy based negative photoresist photosensitized with triaryl sulfonium salt [3] that can form layers tens of microns thick. SU-8 is dissolved in the organic solvent cyclopentanone, which also dissolves Rhodamine 6G. Thus, it is possible to dissolve the Rhodamine 6G in the cyclopentanone, add any required scattering particles, and then solidify the SU-8 through baking. The resulting mixture is then spuncoat onto a substrate to create a solid random gain media.

5.3 SU-8 Based Random Laser Construction

Random lasers with either Al₂O₃ or Ag scattering particles can be created with solid SU-8. The SU-8 2050 was obtained from Microchem as it will form a 30 μm thick layer. There is a very small amount of cyclopentanone solvent in SU-8 2050, greatly increasing the difficulty of dissolving the Rhodamine 6G laser dye. A laboratory vortex stirrer was used to disperse the dye throughout the SU-8, and complete dissolution of 4.2×10^{-3} mol/L of Rhodamine 6G in 10 mL of SU-8 occurred after approximately 24 hours.

5.3.1 Scattering Particles in SU-8

After complete dissolution, scattering particles are added to the SU-8. While the refractive index contrast between Al_2O_3 and SU-8 is small (see table 5.1) compared to the contrast with methanol, it is still large enough to cause scattering of light at the peak emission wavelength of $\lambda_{laser} = 564$ nm. In order to achieve a mean free path of $200 \mu\text{m}$ at $\lambda_{laser} = 564$ nm it is necessary to add 200 mg/mL of 100 nm diameter Al_2O_3 particles having $Q_{sca} = 6.92 \times 10^{-3}$. Vigorous agitation is required to suspend the Al_2O_3 particles as the final concentration has a volume packing fraction of approximately 5 %. The SP coupling into Ag particles is improved (as indicated by the value of Q_{sca} in Table 5.2) due to the higher refractive index of SU-8 compared to methanol as shown in Table 5.1.

Table 5.1

Material	Refractive Index
Al_2O_3	$n_{\text{Al}_2\text{O}_3} = 1.77$ [4]
SU-8	$n_{\text{SU-8}} = 1.59$ [5]
Methanol	$n_{\text{meth}} = 1.33$ [4]

Table 5.2

Material	Particle Diameter (nm)	Q_{sca} at $\lambda_{laser} = 564$ nm
Ag in methanol	55	0.233
Ag in SU-8	55	0.926

For 55 nm diameter Ag scattering particles having $Q_{sca} = 0.926$, the mean free path is set to $200 \mu\text{m}$ and $1000 \mu\text{m}$ by adding 2 mg/mL of Ag and $416 \mu\text{g/mL}$ respectively. These concentrations occupy volume packing fractions which are both a factor at least 250 times smaller than the packing fraction of Al_2O_3 as shown in Table 5.3. In order to properly disperse the scatterers, the Ag and Al_2O_3 particles are added to 1 mL of cyclopentanone and then placed in an ultrasonic bath for 30 minutes before the solvent is

added to the SU-8. Once these scattering particles have been thoroughly mixed with the SU-8, they are spun onto a glass substrate.

Table 5.3

Material	ℓ (μm)	Packing Fraction (%)
Ag	200	2×10^{-2}
Ag	1000	4×10^{-3}
Al_2O_3	200	5

5.3.2 Spincoating of SU-8 and Scattering Particles

Spincoating SU-8 to create a uniform film involves several procedural steps. The first step is cleaning the glass substrates in a piranha bath for 15 minutes. After cleaning, an adhesion promoting coating of Omnicoat XP (Microchem) is applied to the substrate. The spincoating procedure for the Omnicoat layer is: a 5 s ramp to a speed of 500 RPM for 5 seconds; a 10 s ramp to 3000 RMP for 30s; then a 20 s ramp to a complete stop. After the spin cycle, the substrate is baked at 200 °C for one minute to drive off any solvent. Once the pre-coat has been applied, SU-8 with embedded Al_2O_3 or Ag scattering particles is applied to the substrate. Approximately 5 mL of the SU-8 mixture is poured on the substrate to ensure a uniform coating. This mixture is then spun according to: a 5 s ramp to 500 RPM for 10 s; a 15 s ramp to 4000 RPM for 30 s; then a 20 s ramp to a complete stop. After a 5 minute waiting period to allow the escape of any air bubbles trapped in the SU-8, the polymer layer is soft-baked for three minutes at 65 °C, followed by a nine minute bake at 95 °C to drive off any remaining solvent. Following these baking steps, the solidified SU-8 has a thickness of approximately 20 μm .

5.3.3 Optical Arrangement

Optical pumping of the random gain media is performed by a frequency doubled Nd:YAG laser operating at $\lambda_{pump} = 532$ nm, having a pulse length of 10 ns, and repetition rate of 10 Hz. The light is coupled into the SU-8 as illustrated in Figure 5.1. Both circular and line excitation are investigated to determine the emission effects.

5.4 Rhodamine 6G and SU-8 based Random Lasers

Figure 5.2 depicts the measured absorption spectra for Rhodamine 6G dissolved in SU-8 at a concentration of 4.2×10^{-3} mol/L. The absorption peak for Rhodamine 6G dissolved in SU-8 at this concentration is shifted to $\lambda = 536$ nm compared to the peak absorption at $\lambda_{pump} = 532$ nm for Rhodamine 6G dissolved in methanol. The absorption coefficient of the dye as calculated from the spectrophotometer data depicted in Figure 5.2, shows that the absorption length is 9 μm at $\lambda_{pump} = 532$ nm, and 106 μm at $\lambda = 564$ nm. Since the thickness of the SU-8 layer is ~ 20 μm , the sample length, L , is chosen to be the thickness of the SU-8 layer. Unlike the liquid dye solutions, however, photodegradation of the Rhodamine 6G laser dye that has been dissolved in SU-8 is a serious issue. As the dye is locked in a single physical location, it is not replaced as bleaching occurs. This limits the maximum exposure time of the dye to approximately $1/5^{\text{th}}$ of a second for an input pulse with 9.6 mJ/cm^2 .

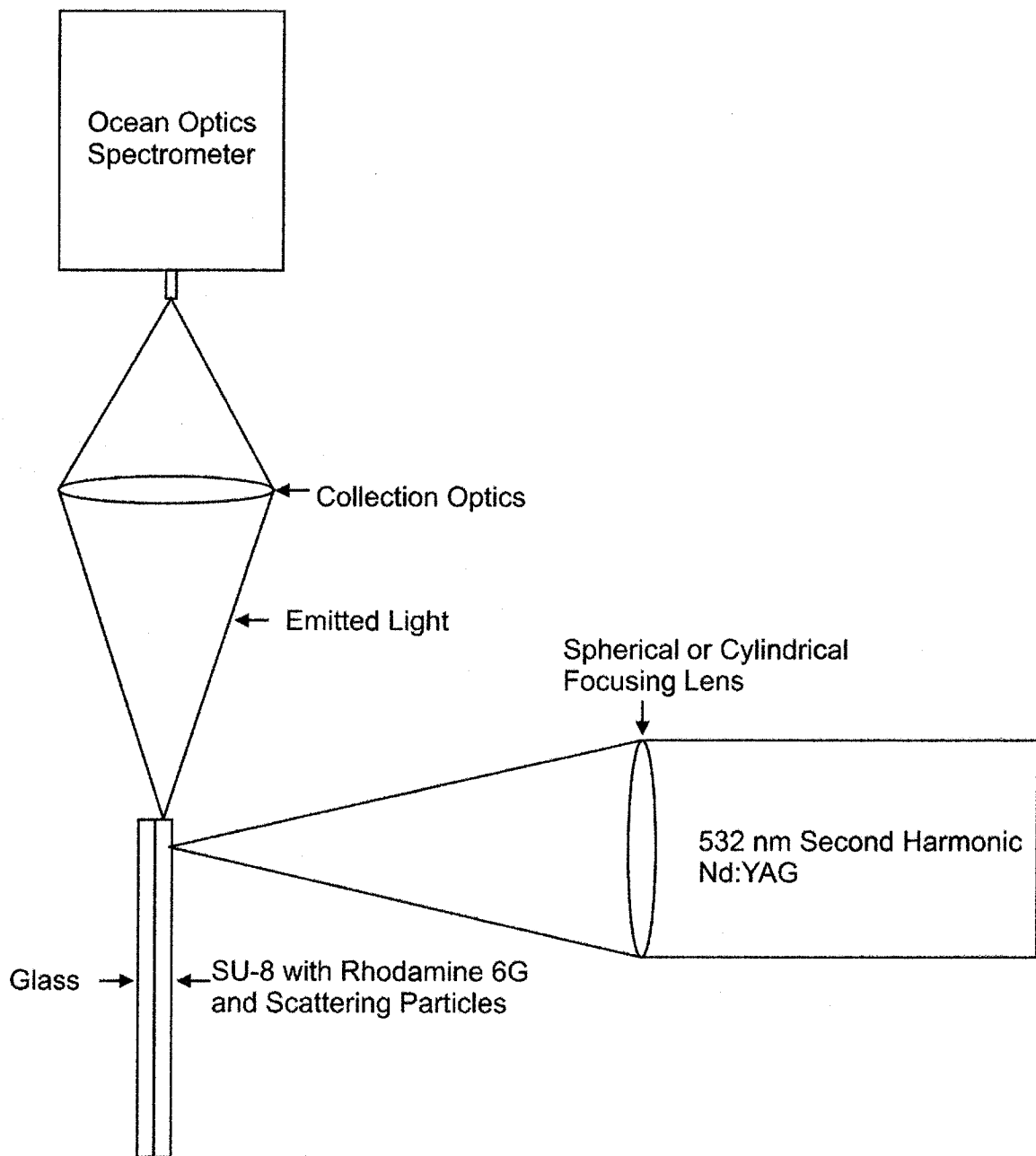


Figure 5.1 – Schematic depiction of the experimental apparatus for observation of random lasing using an SU-8 based scattering matrix. Pump light is coupled into the SU-8 + Rhodamine 6G layer. Edge emitted light is coupled into an Ocean Optics fiber spectrometer.

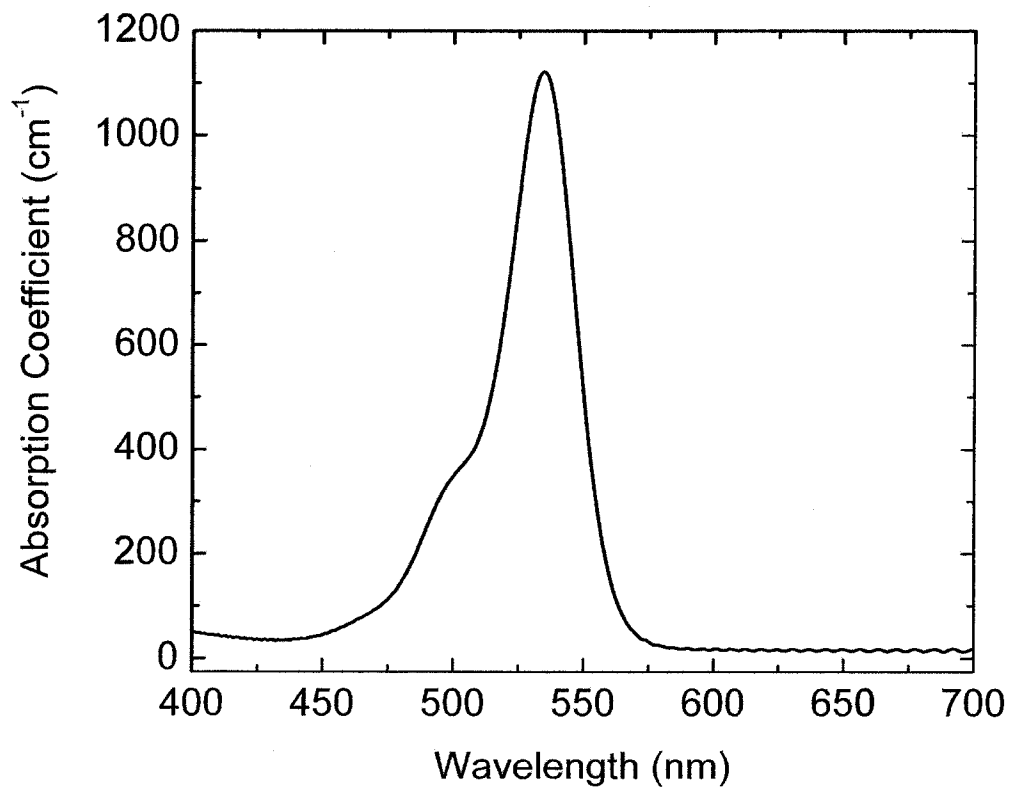


Figure 5.2 - The measured absorption coefficient as a function of wavelength for Rhodamine 6G dye dissolved in SU-8 at a concentration of 4.2×10^{-3} mol/L.

5.4.1 Light Emission from Rhodamine 6G dissolved in SU-8

Figure 5.3 depicts the emission spectrum of 4.2×10^{-3} mol/L Rhodamine 6G dissolved in SU-8 at $F = 7.6$ mJ/cm² (Figure 5.3 (curve a)) and $F = 114$ mJ/cm² (Figure 5.3 (curve b)). The pump fluences used in this study are higher than the range studied in chapter 4 ($F = 0.2$ mJ/cm² to 24.6 mJ/cm²). The broadband spontaneous emission spectrum at $F = 7.6$ mJ/cm² (Table 5.4) resembles the broadband emission spectrum of Rhodamine 6G dissolved in methanol (See section 4.4.1). When the input pump energy fluence is increased to $F = 114$ mJ/cm² there is a 1.9 times decrease in the FWHM linewidth. Additionally, the emission intensity increases by a factor of 9. This intensity increase will serve as the comparison point between the SU-8 based scattering gain media.

Table 5.4

Pump Fluence (mJ/cm ²)	Linewidth (nm)	Peak Wavelength (nm)	Intensity (a.u.)
7.6	35	570	55
114	18	570	470

5.4.2 Light Emission with Al₂O₃ Scattering Particles

In the outlined experiments, an SU-8 and Al₂O₃ scatterer based random laser was constructed from the mixture of 100 nm diameter Al₂O₃ particles in a solution of SU-8 and Rhodamine 6G laser dye. As with a liquid dye based random laser, dielectric scattering particles are used to create a comparative performance baseline. Figure 5.4 depicts the emission spectra for an Al₂O₃ scattering particle based SU-8 gain media having $\ell = 200$ μ m that is pumped at fluences of $F = 7.6$ mJ/cm² (Figure 5.4 (curve a)), 53 mJ/cm² (Figure 5.4 (curve b)), and 114 mJ/cm² (Figure 5.4 (curve c)). Since the mean free path is 10 times larger than the thickness of the SU-8 layer (ie. $L/\ell = 0.1$) for this

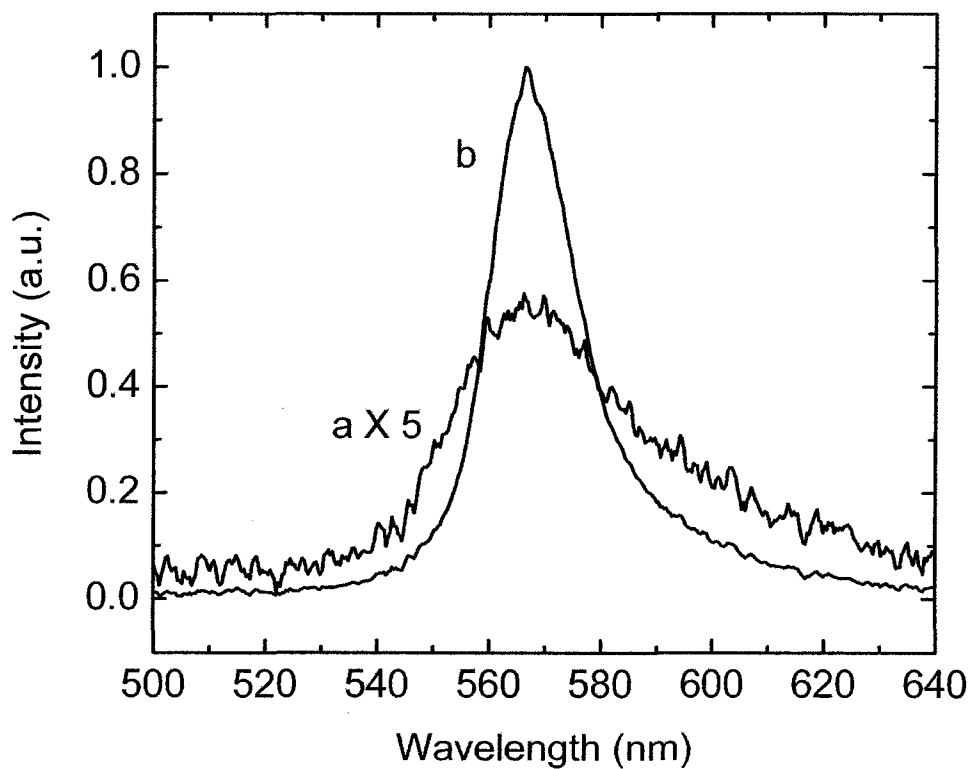


Figure 5.3 - Emission spectra from Rhodamine 6G dissolved in SU-8 at a concentration of 4.2×10^{-3} mol/L (a) The broadband fluorescence spectrum having a FWHM linewidth of 35 nm obtained from the sample when pumped at $F = 7.6$ mJ/cm². (b) The emission spectrum for the sample pumped at $F = 114$ mJ/cm², having a linewidth of 18.3 nm.

media. Multiple scattering must therefore occur along the direction parallel to the substrate surface to provide the feedback for random lasing. This directional scattering is aided by the waveguide effect confining emitted light between the glass substrate ($n_{\text{glass}} = 1.5$), the SU-8 ($n_{\text{SU-8}} = 1.59$), and the surrounding air. Along the plane parallel to the substrate, several scattering events are expected for each emitted and pump photon, as the active gain region is the size of the 1 mm diameter pump spot. At $F = 7.6 \text{ mJ/cm}^2$ the emission is broadband as shown in Table 5.5, similar to pure Rhodamine 6G in SU-8. Below the threshold fluence, there is insufficient optical gain to cause the characteristic line narrowing of random lasing. At $F = 53 \text{ mJ/cm}^2$ the FWHM linewidth narrows to 15 nm, indicating that the threshold energy fluence for lasing has been reached. Because of the thinness of the SU-8 layer this threshold value of F is greater than for an Al_2O_3 scatterer based liquid dye random laser having $\ell = 170 \text{ }\mu\text{m}$ (53 mJ/cm^2 for SU-8 vs. 7.6 mJ/cm^2 for the liquid). This is due to the fact that unlike the liquid dye, any emitted light that is scattered out of the SU-8 layer cannot return to the active gain region. As F is increased to 114 mJ/cm^2 the FWHM linewidth decreases to 6.7 nm. The maximum peak intensity is 5 times greater than from the pure Rhodamine 6G dye.

Table 5.5

Pump Fluence (mJ/cm^2)	Linewidth (nm)	Peak Wavelength (nm)	Intensity (a.u.)
7.6	32	574	76
53	15	568	524
114	6.7	567	2500

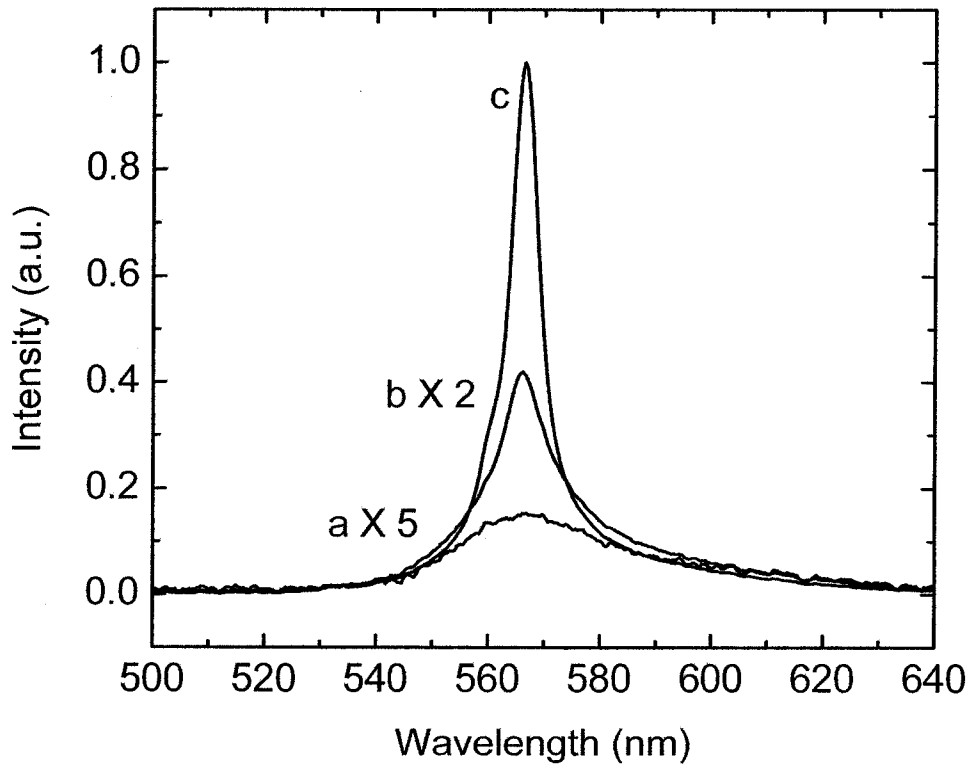


Figure 5.4 - Emission spectra from Rhodamine 6G dissolved in SU-8 with Al_2O_3 nanoparticles at $\ell = 200 \mu\text{m}$. (a) The broadband fluorescence spectrum having a FWHM linewidth of 32 nm obtained from the sample when pumped at $F = 7.6 \text{ mJ/cm}^2$. (b) The emission spectrum for the sample pumped at $F = 53 \text{ mJ/cm}^2$, having a linewidth of 15 nm. This spectrum indicates the onset of random lasing from the device. (c) The measured emission spectrum at $F = 114 \text{ mJ/cm}^2$, having a linewidth of 6.7 nm, indicating random lasing.

5.4.3 Light Emission with Ag Scattering Particles

In these experiments, two SU-8 based Ag scatterer random lasers were prepared from the addition of 55 nm diameter Ag particles to a solution of SU-8 and Rhodamine 6G laser dye. Similar to the liquid based Ag scatterer random lasers, the gain enhancement from SP coupling enables the Ag scatterer based random laser to outperform an Al₂O₃ scatterer based random laser at the same mean free path. The Ag scattering particle based SU-8 gain media exhibits a narrower FWHM linewidth, a lower input pump energy fluence threshold, and greater output intensity than the comparable Al₂O₃ scatterer based random laser.

A silver scatterer based random gain media with $\ell = 200 \mu\text{m}$, has a scattering strength of $L/\ell = 0.1$ across the thickness of the SU-8 layer, and thus multiple scattering events are only probable along the SU-8 waveguide layer. Since the edge emitted light is collected, scattering events along the waveguide are the primary source of any measured light. Figure 5.5 (curves a - c) illustrates the emission spectrum for this random gain media at $F = 15 \text{ mJ/cm}^2$ (curve a), 53 mJ/cm^2 (curve b), and 114 mJ/cm^2 (curve c). At $F = 15 \text{ mJ/cm}^2$ the broadband light is characteristic of spontaneous emission from the Ag scatterer based random gain media (see table 5.6). At $F = 53 \text{ mJ/cm}^2$ the FWHM linewidth has narrowed to 9.9 nm, indicative of the onset of random lasing. Like the Al₂O₃ scatterer based solid-state gain media, light is amplified as the spontaneous emission along the waveguide is scattered multiple times. For this random gain media, the threshold energy fluence for lasing is $\sim 38 \text{ mJ/cm}^2$, approximately 15 mJ/cm^2 less than the fluence required for lasing in the Al₂O₃ scatterer based random gain media. At $F = 114 \text{ mJ/cm}^2$ the FWHM emission is narrower (6 nm) than for the Al₂O₃ based gain

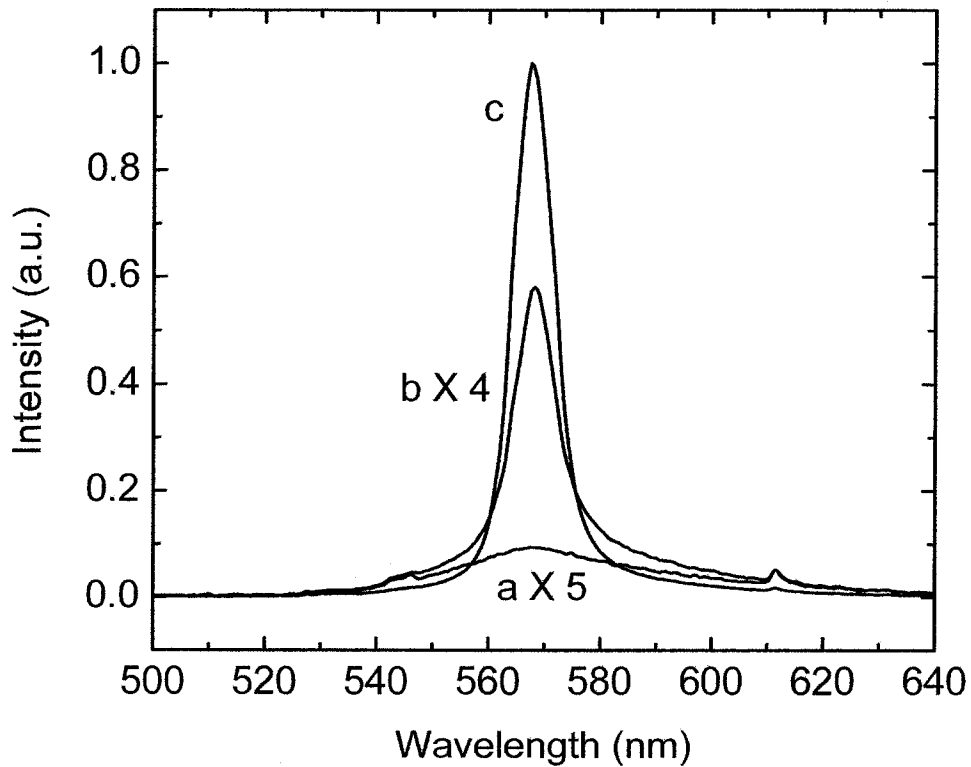


Figure 5.5 - Emission spectra from Rhodamine 6G dissolved in SU-8 with Ag nanoparticles at $\ell = 200 \mu\text{m}$. (a) The broadband fluorescence spectrum having a FWHM linewidth of 40 nm from the sample pumped at $F = 15 \text{ mJ/cm}^2$. (b) The emitted spectrum for the sample pumped at $F = 53 \text{ mJ/cm}^2$, having a linewidth of 9.9 nm. (c) The measured emission spectrum at $F = 114 \text{ mJ/cm}^2$, with a linewidth of 6 nm, indicating random lasing.

media previously studied (6.7 nm). Additionally, the peak intensity at $F = 114 \text{ mJ/cm}^2$ is 7 times greater than the emitted light from pure Rhodamine 6G, and 1.4 times greater than the emitted light from the Al_2O_3 scatterer in SU-8 based random gain media. Each of these three performance advantages of Ag scattering particles – the increased output power, the lower threshold fluence; and the narrower linewidth; – arise due to SP enhancement of optical gain in the immediate vicinity of the Ag particles.

Table 5.6

Pump Fluence (mJ/cm^2)	Linewidth (nm)	Peak Wavelength (nm)	Intensity (a.u.)
15	40	573	65
53	9.9	570	499
114	6.0	568	3400

A silver scatterer based random gain media having $\ell = 1000 \text{ }\mu\text{m}$ has a scattering strength of $L/\ell = 0.02$ across the SU-8 layer, and $L/\ell = 1$ along the actively pumped waveguide region. There is thus a high probability that emitted photons will escape the active gain volume, as the mean free path of scattering (1 mm) is equal to the pump spot diameter (1 mm). The fact that the mean free path is an order of magnitude greater than the absorption length (106 μm) means that photons which escape from the active gain volume are unlikely to return. Figure 5.6 (curves a - c) depicts the emission spectrum for this sample at $F = 7.6 \text{ mJ/cm}^2$ (curve a), $F = 53 \text{ mJ/cm}^2$ (curve b), and $F = 114 \text{ mJ/cm}^2$ (curve c). At $F = 7.6 \text{ mJ/cm}^2$ the spontaneous emission is typical of the SU-8 based random gain media below threshold (see table 5.7). However, at $F = 53 \text{ mJ/cm}^2$ the light emission remains broadband. For this random gain media, the threshold energy fluence is $F = 76 \text{ mJ/cm}^2$, which is considerably higher than the respective threshold fluences of 38 mJ/cm^2 and 53 mJ/cm^2 for the Ag and Al_2O_3 scatterer based solid-state

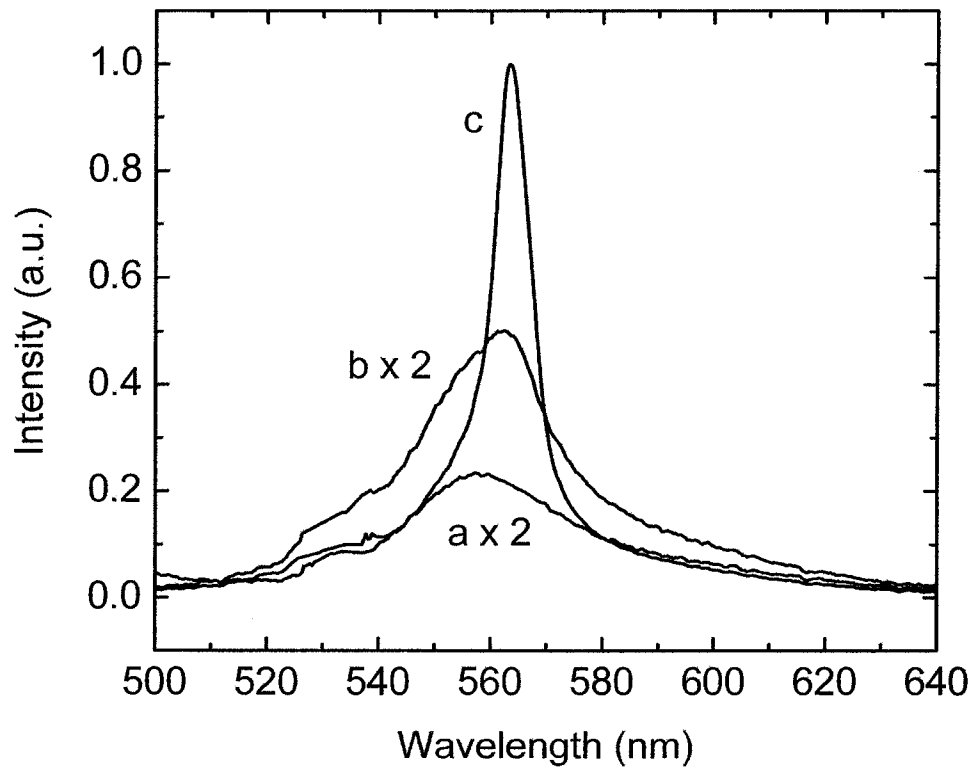


Figure 5.6 – Emission spectra from Rhodamine 6G dissolved in SU-8 with Ag nanoparticles at $\ell = 1000 \mu\text{m}$. (a) The broadband fluorescence spectrum having a FWHM linewidth of 36 nm from the sample pumped at $F = 7.6 \text{ mJ/cm}^2$. (b) The emitted spectrum for the sample pumped at $F = 53 \text{ mJ/cm}^2$, having a linewidth of 30 nm. This indicates that the random gain media is still below the lasing threshold. (c) The measured emission spectrum at $F = 114 \text{ mJ/cm}^2$, indicating random lasing with a linewidth of 8.8 nm.

random lasers having $\ell = 200 \mu\text{m}$. At $F = 114 \text{ mJ/cm}^2$ the FWHM linewidth has narrowed to 8.8 nm, indicating that the fluence is above the lasing threshold. For this weak scattering regime, the rarity of non-resonant optical feedback must be compensated for by large optical gain provided by co-localized SP gain enhancement.

Table 5.7

Pump Fluence (mJ/cm^2)	Linewidth (nm)	Peak Wavelength (nm)	Intensity (a.u.)
7.6	36	564	220
53	30	566	480
114	8.8	564	1900

5.4.4 Linewidth Variation for SU-8 Based Random Lasers

The variation of the FWHM linewidth of emitted light from the SU-8 solid-state random lasers as a function of F illustrates several interesting factors. Figure 5.7 (a - d) depicts the FWHM linewidth variation as a function of F from 7.6 mJ/cm^2 to 114 mJ/cm^2 for random lasers without any scatterers (\blacklozenge), with Al_2O_3 scatterers at $\ell = 200 \mu\text{m}$ (\blacksquare), and with Ag scatterers at $\ell = 200 \mu\text{m}$ (\bullet) and $1000 \mu\text{m}$ (\blacktriangle). This figure indicates that both the scatterer material and the mean free path control the lasing threshold. Above the lasing threshold, the minimum linewidth of the Al_2O_3 and Ag scatterer based random lasers having $\ell = 200 \mu\text{m}$ are approximately equal (see table 5.8). These two random lasers both demonstrate a definite linewidth plateau beyond the well-defined threshold F . As ℓ increases from $200 \mu\text{m}$ to $1000 \mu\text{m}$ for the Ag scatterer samples, the lasing threshold also increases. Even at $\ell = 1000 \mu\text{m}$ the Ag scatterer based random laser shows significant linewidth narrowing at $F = 114 \text{ mJ/cm}^2$. In this scattering regime, the system has to be pumped with F a factor of two times larger than the threshold F at $\ell = 200 \mu\text{m}$ to compensate for the lack of multiple scattering events. With multiple scattering

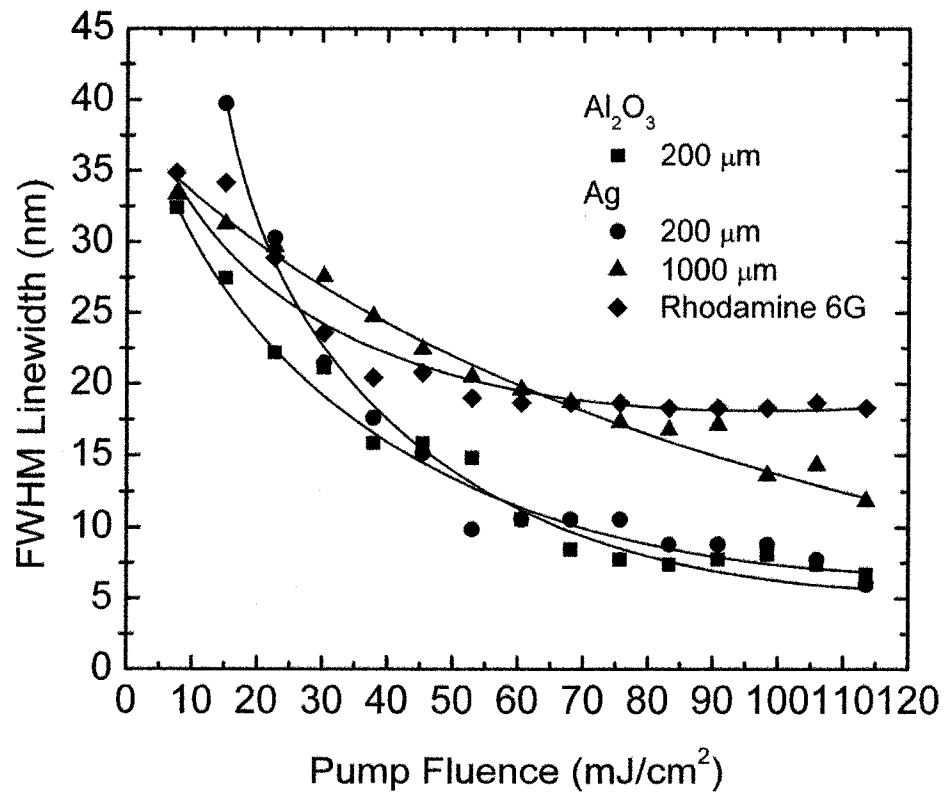


Figure 5.7 – The FWHM linewidth variation as a function of F from $F = 7.6 \text{ mJ/cm}^2$ to $F = 114 \text{ mJ/cm}^2$ for random gain media in SU-8 without any scatterers (\blacklozenge), with Al_2O_3 scatterers at $\ell = 200 \text{ }\mu\text{m}$ (\blacksquare), and with Ag scatterers at $\ell = 200 \text{ }\mu\text{m}$ (\bullet) and $1000 \text{ }\mu\text{m}$ (\blacktriangle).

events along the SU-8 waveguide layer, narrowband laser-like light emission escapes from the edge of the SU-8.

Table 5.8

Material	ℓ (μm)	Threshold Fluence (mJ/cm^2)	Minimum Linewidth (nm)
Al_2O_3	200	53	6.7
Ag	200	38	6.0
Ag	1000	76	12

5.4.5 Intensity Variation for Al_2O_3 Scatterer Based Random Lasers

Figure 5.8 (curves a - d) depicts the relative peak intensity variation as a function of F from $7.6 \text{ mJ}/\text{cm}^2$ to $114 \text{ mJ}/\text{cm}^2$ for random lasers without any scatterers (\blacklozenge), with Al_2O_3 scatterers at $\ell = 200 \mu\text{m}$ (\blacksquare), and with Ag scatterers at both $\ell = 200 \mu\text{m}$ (\bullet) and $1000 \mu\text{m}$ (\blacktriangle). This figure shows that both F and the dependence on L/ℓ of the effective cavity length traversed by emitted radiation determine the measured peak intensity. Both the Al_2O_3 and the Ag scatterer based random lasers emit have greater maximum emission intensities than the pure Rhodamine 6G dye (see Table 5.9), owing to strong scattering and SP gain enhancement for the Ag sample. Additionally, each of the random lasers having $\ell = 200 \mu\text{m}$ produces more output light above threshold than the Ag scatter based random laser having $\ell = 1000 \mu\text{m}$ as shown in Table 5.9.

Table 5.9

Material	ℓ (μm)	Peak Intensity (a.u.)
Pure Dye	N.A.	474
Al_2O_3	200	2500
Ag	200	3400
Ag	1000	1900

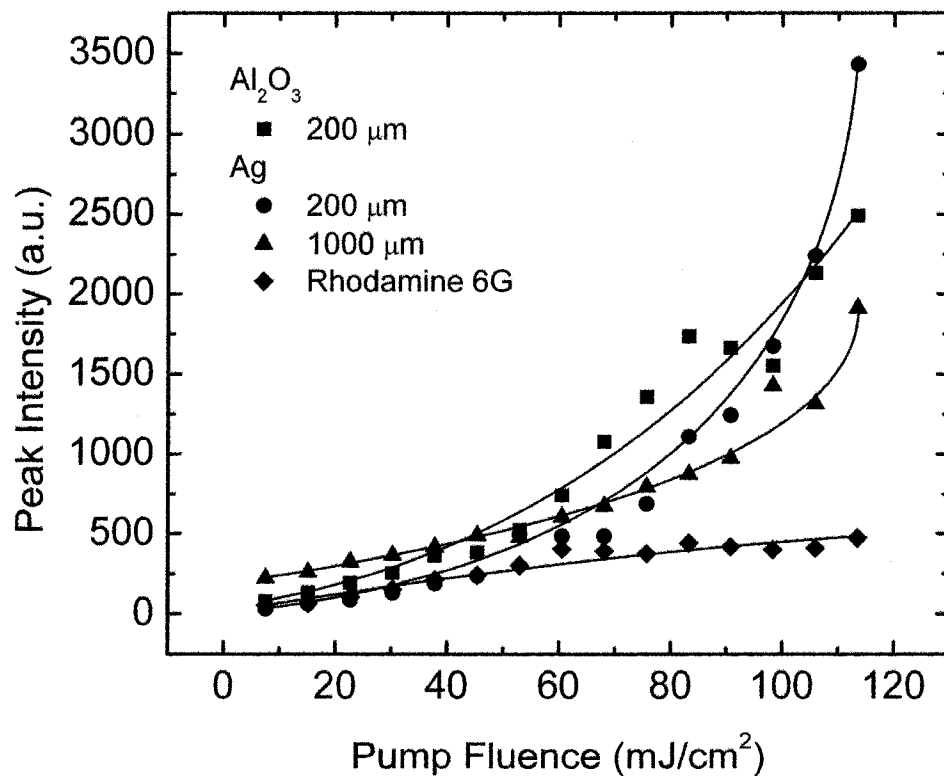


Figure 5.8 - The relative peak intensity variation as a function of F from 7.6 mJ/cm^2 to 114 mJ/cm^2 for random gain media in SU-8 without any scatterers (\blacklozenge), with Al_2O_3 scatterers at $\ell = 200 \text{ }\mu\text{m}$ (\blacksquare), and with Ag scatterers at both $\ell = 200 \text{ }\mu\text{m}$ (\bullet) and $1000 \text{ }\mu\text{m}$ (\blacktriangle).

5.5 Line Excitation of SU-8 Based Random Lasers

For an SU-8 based random gain media pumped at $\lambda_{pump} = 532$ nm, both the position of the pump spot, and its size control the output emission spectrum. When the optical focusing element is changed from a spherical lens to a cylindrical lens, the resultant line excitation preferentially pumps the dye along one direction. Hence, photons that propagate along an 8 mm long excitation line experiences a potentially greater optical path length than the maximum path length for a 1 mm diameter circular focal spot.

5.5.1 Line Excitation of Rhodamine 6G dissolved in SU-8

Figure 5.9 illustrates the emission spectrum at $F = 0.7$ mJ/cm² (curve a) and 11.1 mJ/cm² (curve b) of 4.2×10^{-3} mol/L Rhodamine 6G dissolved in SU-8 with an pump spot that is 1 mm wide and 8 mm long. At the lowest possible input fluence obtainable from the Nd:YAG laser system of $F = 0.7$ mJ/cm² the emission spectrum from the Rhodamine 6G has a FWHM linewidth less than what is expected for the spontaneous emission below the lasing threshold (see table 5.10). At $F = 11.1$ mJ/cm² the emission linewidth narrows slightly by 1.7 nm. Unlike a similar random gain media pumped with a circular focal spot, this device produces an extremely narrow spectrum at lower F . The narrow linewidth occurs at this F due to the formation of an optical resonator cavity. There is optical feedback in this system from the interface between the edge of the SU-8 and air, as the refractive index contrast between SU-8 ($n_{SU-8} = 1.59$) and air provides intensity feedback of 5.2 % at the edge of the waveguide.

Table 5.10

Pump Fluence (mJ/cm ²)	Linewidth (nm)	Peak Wavelength (nm)	Intensity (a.u.)
0.7	7	559	300
11.1	5.3	569	22000

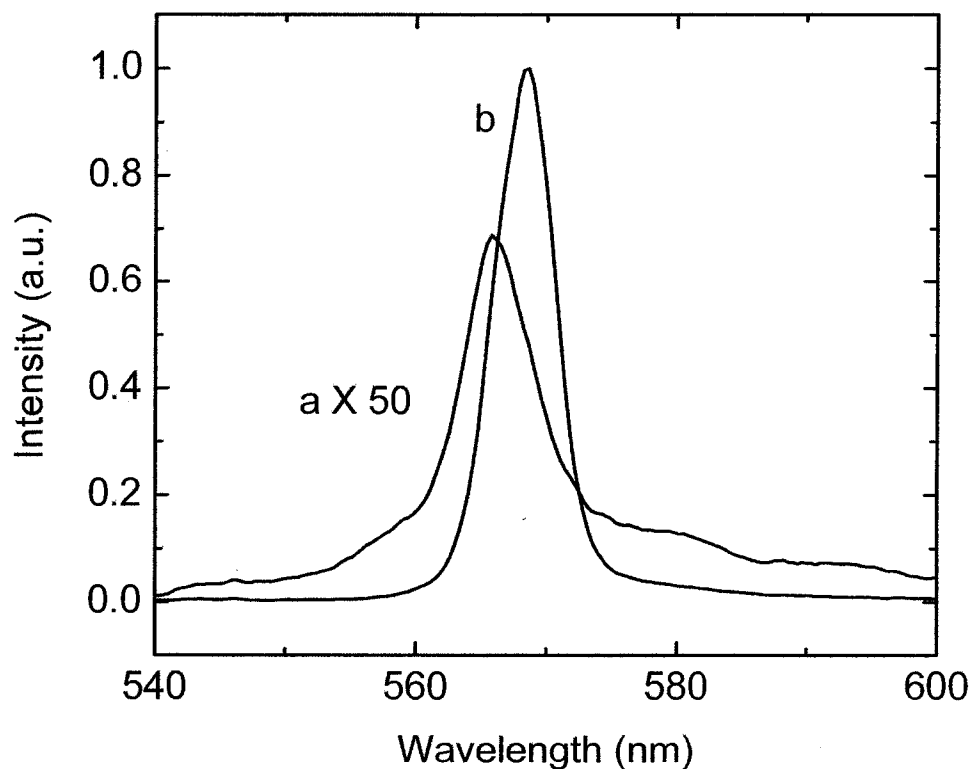


Figure 5.9 - Emission spectra from Rhodamine 6G dissolved in SU-8 at a concentration of 4.2×10^{-3} mol/L. A cylindrical lens focuses the pump spot to a line 1 mm wide and 8 mm long. (a) The narrowband spectrum having a FWHM linewidth of 7 nm obtained from the sample when pumped at $F = 0.7$ mJ/cm². (b) The emission spectrum for the sample pumped at $F = 11.1$ mJ/cm², having a linewidth of 5.3 nm.

5.5.2 Light Emission with Al_2O_3 Scattering Particles

An Al_2O_3 scatterer based solid state random gain media excited with a line source 8 mm long and 1 mm wide, was constructed with $\ell = 200 \mu\text{m}$. Figure 5.10 depicts the emission spectra for this device at $F = 0.7 \text{ mJ/cm}^2$ (curve a) and $F = 6.7 \text{ mJ/cm}^2$ (curve b). For this media, it is expected that multiple scattering events will occur as the scattering strength along the excitation line is $L/\ell = 40$. Strong scattering in the active region of the waveguide ensures that photons are scattered multiple times, creating a non-resonant optical cavity. Light traveling along the length of the excitation line is preferentially selected by collecting edge-emitted radiation. For $F = 0.7 \text{ mJ/cm}^2$ the emission is broadband with a FWHM linewidth typical of spontaneous emission (see table 5.11). This is much greater than the linewidth of the pure Rhodamine 6G based gain media at the same pump fluence. This difference potentially arises due to the resonant optical feedback from the interface between the edge of the SU-8 and the surrounding air. Assuming that the probability of a photon scattering within a single mean path approaches one, effectively no emitted photons will cross the 17 mm gap between the edge of the excited region and the outer edge of the SU-8. This is supported by visual observations indicating that the fluorescence of the dye does not extend to the far edge. The FWHM linewidth reaches a minimum at $F = 6.7 \text{ mJ/cm}^2$, which is much smaller than the lasing threshold of $F = 53 \text{ mJ/cm}^2$ for circular excitation.

Table 5.11

Pump Fluence (mJ/cm^2)	Linewidth (nm)	Peak Wavelength (nm)	Intensity (a.u.)
0.7	32	562	60
6.7	8	561	790

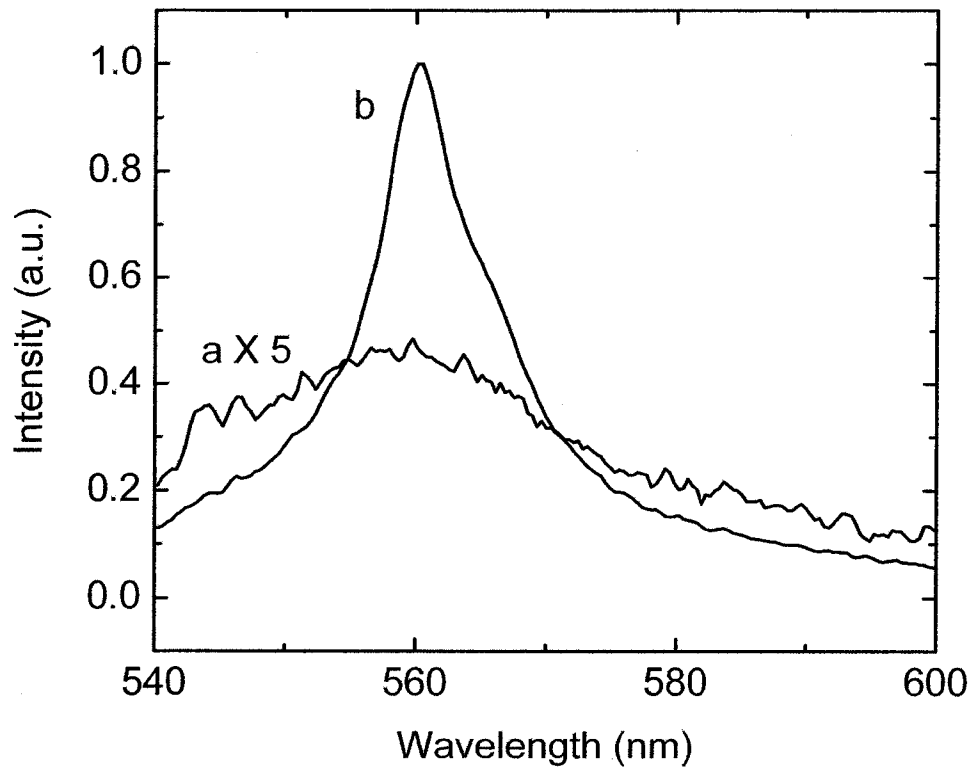


Figure 5.10 – The emission spectra from Rhodamine 6G dissolved in SU-8 with Al_2O_3 nanoparticles at $\ell = 200 \mu\text{m}$. (a) The broadband fluorescence spectrum having a FWHM linewidth of 32 nm obtained from the sample when pumped at $F = 0.7 \text{ mJ/cm}^2$. (b) The emission spectrum for the sample pumped at $F = 6.7 \text{ mJ/cm}^2$. The linewidth at this pump fluence is 8 nm.

5.5.3 Light Emission with Ag Scattering Particles

As in the circular excitation configuration, the gain enhancement from SP resonance enables the Ag scatterer based random laser to outperform an Al₂O₃ scatterer based random laser having the same mean free path. The Ag scatterer based solid state random lasers exhibit a narrower linewidth, a lower pump energy fluence threshold, and greater output intensity than the comparable Al₂O₃ scatterer based solid state random laser. For a silver scatterer based solid-state random gain media with $\ell = 200 \mu\text{m}$, the scattering strength is $L/\ell = 0.1$ across the thickness of the SU-8 layer. Figure 5.11 illustrates the emission spectrum for this random gain media at $F = 0.7 \text{ mJ/cm}^2$ (a) and $F = 11.1 \text{ mJ/cm}^2$ (b). At $F = 0.7 \text{ mJ/cm}^2$ the random gain media is above the threshold fluence with a FWHM emission linewidth is well below what is expected for spontaneous emission (see table 5.12). The emission linewidth for this device remains constant up to $F = 11.1 \text{ mJ/cm}^2$. Like the Al₂O₃ scatterer based random laser having $\ell = 200 \mu\text{m}$, it is unlikely that a photon will reflect off of the far edge of the SU-8 and return to the active gain region. Thus, this Ag scatterer based random gain media functions as a random laser under line excitation at energy fluences of at least 0.7 mJ/cm^2 . This performance is superior in both the required threshold input energy fluence, and the FWHM linewidth to the Al₂O₃ scatterer based random laser having $\ell = 200 \mu\text{m}$. The source of the enhanced performance is two-fold. First, to reach a mean free path of $200 \mu\text{m}$ using 55 nm diameter Ag particles requires an occupied volume packing fraction of only $2 \times 10^{-2} \%$, compared to the 5% required using 100 nm diameter Al₂O₃ particles. Secondly, the SP gain enhancement using Ag nanoparticles, described in Chapter 2.3.1, provides increased gain at each scattering event compared to the Al₂O₃ scattering events.

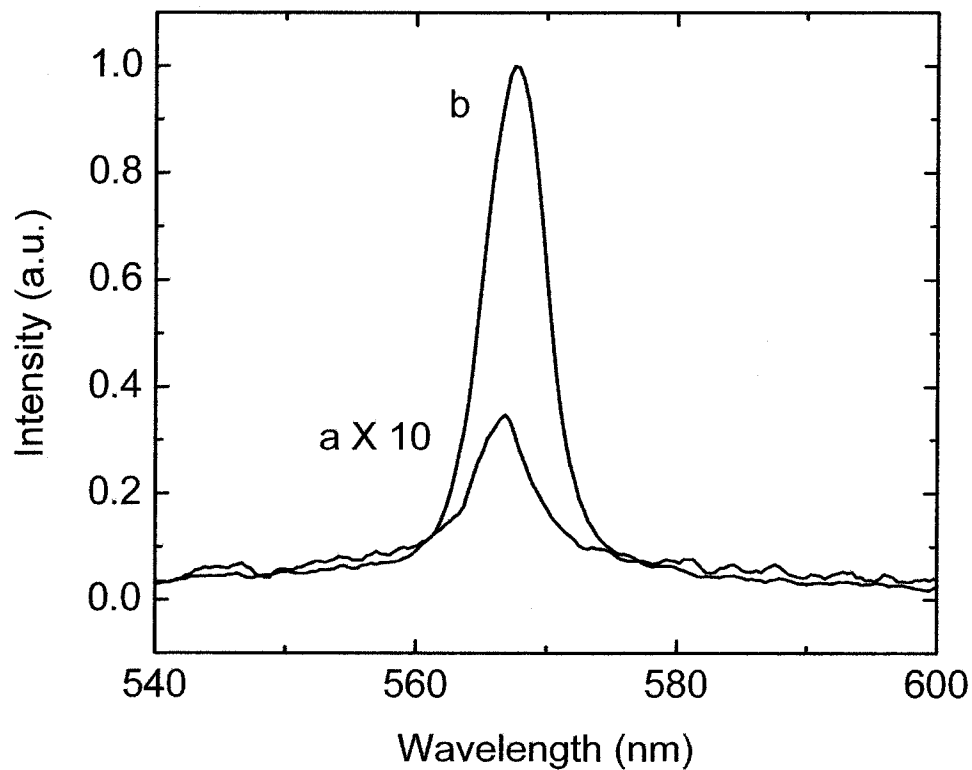


Figure 5.11 - Emission spectra obtained from Rhodamine 6G dissolved in SU-8 with Ag nanoparticles at $\ell = 200 \mu\text{m}$. (a) The narrowband emission spectrum with a FWHM linewidth of 6 nm from the sample pumped at $F = 0.7 \text{ mJ/cm}^2$. (b) The emission spectrum for the sample pumped at $F = 11.1 \text{ mJ/cm}^2$, having a linewidth of 6 nm. Random lasing occurs at all studied input fluences.

Table 5.12

Pump Fluence (mJ/cm ²)	Linewidth (nm)	Peak Wavelength (nm)	Intensity (a.u.)
0.7	6	569	130
11.1	6	568	3800

Figure 5.12 depicts the emission spectrum from a silver sample having $\ell = 1000 \mu\text{m}$ at $F = 0.7 \text{ mJ/cm}^2$ (curve a) and $F = 2.2 \text{ mJ/cm}^2$ (curve b). Figure 5.12 (curve a) clearly shows that the system is in the broadband spontaneous emission regime below the lasing threshold (see table 5.13). At $F = 2.2 \text{ mJ/cm}^2$ the emission spectrum drastically narrows, characteristic of random lasing. As expected, the threshold fluence of $\sim 2.2 \text{ mJ/cm}^2$ is higher than for an Ag scatterer based random gain media having $\ell = 200 \mu\text{m}$ due to the reduced scattering probability.

Table 5.13

Pump Fluence (mJ/cm ²)	Linewidth (nm)	Peak Wavelength (nm)	Intensity (a.u.)
0.7	32	564	75
2.2	6	564	3140

5.5.4 Lasing Energy Fluence Threshold for SU-8 Based Solid State Random Lasers

For each of the studied random lasers, as the length of the focal line is decreased from 8 mm to 1 mm, the input energy fluence threshold varies accordingly. Figure 5.13 charts the dependence between the threshold fluence and the length of the excitation line for random lasers with Al_2O_3 scatterers at $\ell = 200 \mu\text{m}$ (■), with Ag scatterers at both $\ell = 200 \mu\text{m}$ (●) and $1000 \mu\text{m}$ (▲), and without any scattering particles (◆). Here, each curve depicts the significant performance drop that results as the decrease in length of the pump line reduces the total delivered energy and the optical path length. The threshold fluence in this figure is defined as the energy at which the FWHM linewidth becomes less than 17 nm, approximately half of the 35 nm linewidth of spontaneous emission from pure

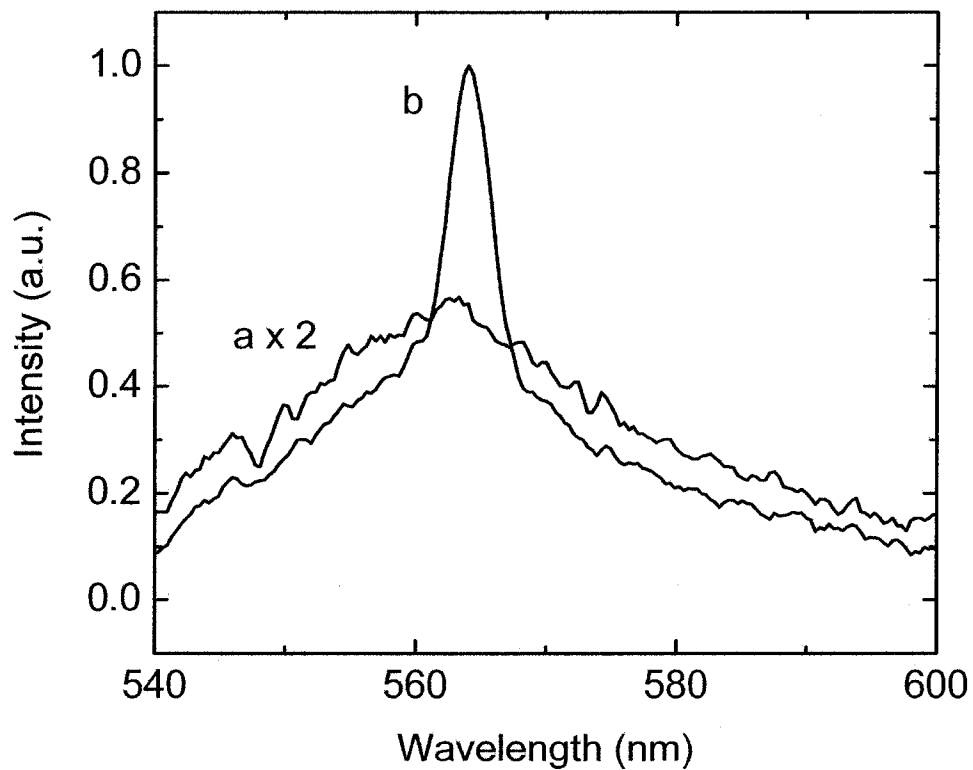


Figure 5.12 - Emission spectra from Rhodamine 6G dissolved in SU-8 with Ag nanoparticles at $\ell = 1000 \mu\text{m}$. (a) The broadband fluorescence spectrum having a FWHM linewidth of 32 nm from the sample pumped at $F = 0.7 \text{ mJ/cm}^2$. (b) The emitted spectrum for the sample pumped at $F = 2.2 \text{ mJ/cm}^2$, having a linewidth of 6 nm.

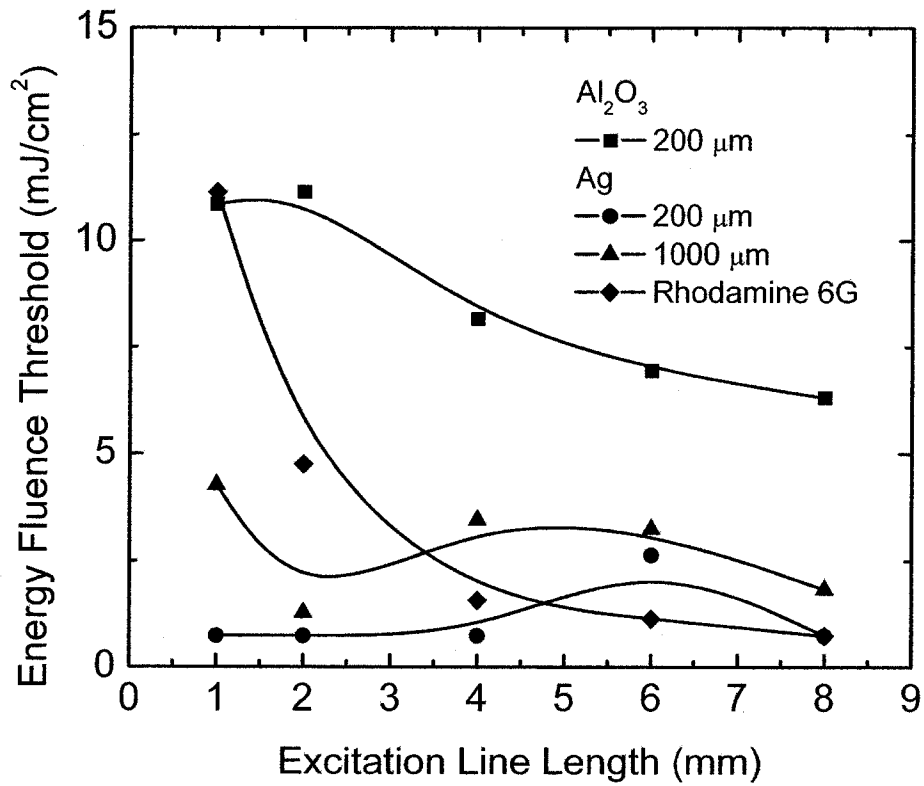


Figure 5.13 – Input pump energy fluence threshold graphed as a function of the length of the excitation line. The width of the excitation line is 1 mm in all cases. Each symbol represents a gain media with Al₂O₃ scatterers at $\ell = 200 \mu\text{m}$ (■), with Ag scatterers at both $\ell = 200 \mu\text{m}$ (●) and $1000 \mu\text{m}$ (▲), and without any scattering particles (◆).

Rhodamine 6G. As can be seen, both the threshold F and the minimum FWHM linewidth are highly dependent on the length of the pump line. For each random laser, the threshold fluence increases as the excitation length decreases. Additionally, the thresholds for both Ag scatterer based random lasers remain lower than the thresholds for the Al_2O_3 scatterer based random laser (see table 5.14). For the pure Rhodamine 6G dye, the threshold does not increase linearly with decreasing line length due to the presence of optical feedback at the edges of the SU-8 layer for this gain media.

Table 5.14

Material	ℓ (μm)	Line Fluence (mJ/cm^2)	Circular Fluence (mJ/cm^2)
Ag	200	0.74	2.6
Ag	1000	1.3	1.3
Al_2O_3	200	6.3	11.1

5.5.5 Intensity Variation for Al_2O_3 Scatterer Based Random Lasers

In addition to the dependence of the lasing threshold on the length of the pump line, the line length also determines the peak intensity reached by each random laser. Figure 5.14 depicts the relative peak intensity variation at $F = 11.1 \text{ mJ}/\text{cm}^2$ for random lasers with Al_2O_3 scatterers at $\ell = 200 \mu\text{m}$ (■), Ag scatterers at $\ell = 200 \mu\text{m}$ (●) and $1000 \mu\text{m}$ (▲), and for pure Rhodamine 6G dye (◆). The interesting feature depicted in the intensity plot is that while the peak intensities of the random lasers obey a linear relationship with the excitation line length, the intensity output of the conventional pure Rhodamine 6G laser increases rapidly at an excitation length between 4mm and 6 mm. The intensity dependence as a function of length illustrates the effect of scattering particles. Without scattering particles, the emitted light can be amplified over the entire length of the pump line. With scattering particles, the optical path length traveled is less dependent on the length of the pump line, and is instead a function of the mean free path between

scattering events. Thus, the feedback mechanism for the pure dye possibly displays an exponential dependence on length, while the ultimate dependence on the length of the excitation line for the random lasers with scattering particles is more linear. Additionally, the greater intensity at $F = 11.1 \text{ mJ/cm}^2$ for the Ag scatterer based random lasers compared to the Al_2O_3 based gain media illustrates the effect of SP gain enhancement (see table 5.15).

Table 5.15

Material	ℓ (μm)	Peak Intensity (a.u.)
Pure Dye	N.A.	22000
Al_2O_3	200	790
Ag	200	3800
Ag	1000	3100

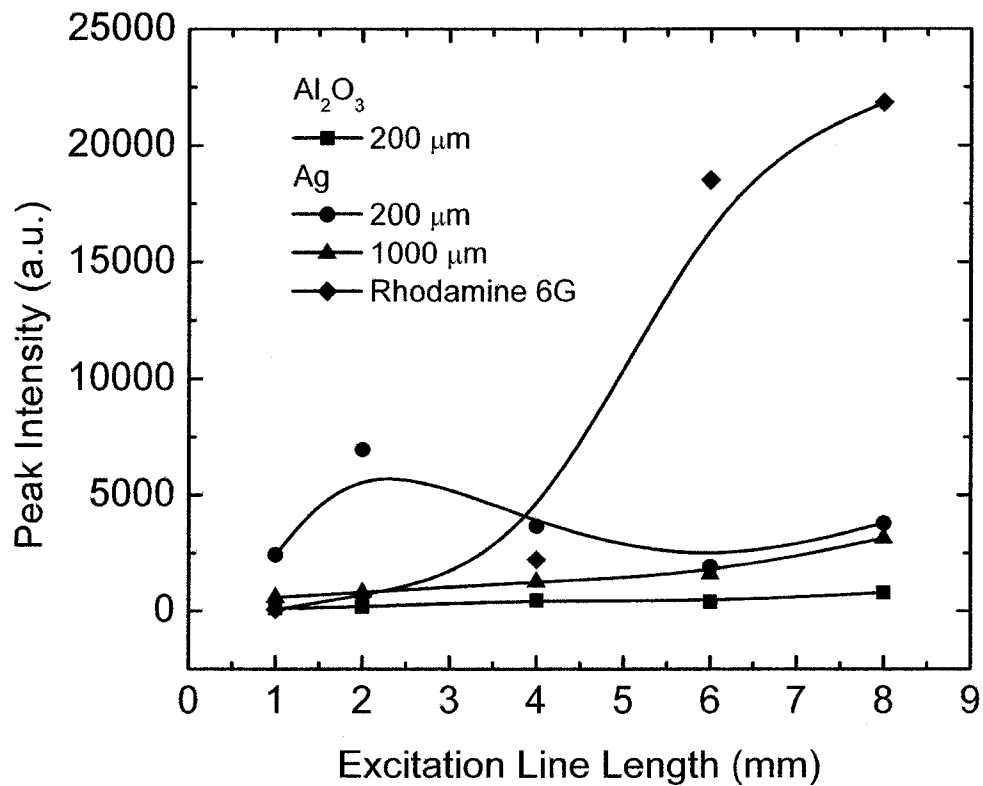


Figure 5.14 – Peak output intensity as a function of the length of the excitation line. The width of the excitation line is 1 mm in all cases. Each symbol represents a gain media with Al₂O₃ scatterers at $\ell = 200 \mu\text{m}$ (■), with Ag scatterers at both $\ell = 200 \mu\text{m}$ (●) and $1000 \mu\text{m}$ (▲), and without any scattering particles (◆).

5.6 References

- [1] H. Watanabe, Y. Oki, M. Maeda, T. Omatsu, "Waveguide dye laser including a SiO₂ nanoparticle dispersed random scattering active layer," *Appl. Phys. Lett.*, **86**, 151123 (2005).
- [2] R. M. Balachandran, D. P. Pacheco, and N. M. Lawandy, "Laser action in polymeric gain media containing scattering particles," *Appl. Opt.*, **35**, 640-643 (1996).
- [3] K. Y. Lee, N. LaBianca, S. A. Rishton, S. Zolgharnain, J. D. Gelorme, J. Shaw, and T. H. P. Chang, "Micromachining applications of a high-resolution ultrathick photoresist," *J. Vac. Sci. Technol. B*, **13**, 3012-3016 (1995).
- [4] M. J. Weber, *CRC Handbook of Optical Materials*, (Boca Raton, CRC Press, (2003).
- [5] MicroChem Inc., Private Communication.

Chapter 6: Conclusions

6.1 Conclusion

This thesis presents the results of experimental and theoretical investigation of the effects of surface plasmon resonance on random laser systems. A discussion of the techniques required for numerical modeling of random laser systems is included. The theoretical simulations involve the inclusion of numerical methods into the FDTD algorithm to account for dispersive metals and dielectrics, as well as optical gain materials. The results of this simulation support the case for optical gain enhancement caused by surface plasmon resonance in silver nanoparticles.

In the experimental sections of the thesis, random lasers have been constructed by the addition of 100 nm diameter alumina and 55 nm diameter silver scattering spheroids to a solution of high gain Rhodamine 6G laser dye dissolved in methanol. The use of silver scattering particles reduces the minimum spectral emission linewidth to ~ 4 nm from the ~ 6 nm obtained for Al_2O_3 scatterers. The input energy fluence threshold for lasing is comparable or lower in the Ag scatterer based random gain media even when the mean free path is greater. A threshold lasing fluence of 3.8 mJ/cm^2 was measured for a silver scatterer based random gain media having a mean free path of $3200 \mu\text{m}$, while the threshold was 4 mJ/cm^2 for an alumina scatterer based random laser having a mean free path of $340 \mu\text{m}$. For the sub-wavelength diameter silver particles, the electromagnetic field near the particle surface is resonantly enhanced due to the excitation of particle surface plasmons. This field enhancement causes an increase in the optical gain surrounding each silver particle, and leads to the observed significant improvement of random laser operation.

A hybrid random laser was constructed using both alumina and silver scattering particles to investigate the role of surface plasmon enhancement of optical gain. Here, the silver particles are utilized for their surface plasmon enhancement characteristics, while the alumina particles provide non-resonant feedback through multiple scattering. Due to local electromagnetic field enhancement from surface plasmon coupling into Ag the silver nanoparticles, the addition of Ag nanoparticles to an Al₂O₃ scatterer based random laser results in an increase in the peak intensity of emitted radiation accompanied by narrower linewidth. The result is a three-fold enhancement of the emitted intensity from the hybrid random laser. It is interesting that the required Ag concentration is small compared to the concentration of Al₂O₃ particles needed to achieve random lasing, indicating the utility of providing metal particles in a random laser to assist development of applications such as nano sized random lasers. The experimental results illustrate that a balance must be maintained between the large absorption arising from the metal particles and optical gain.

In addition to random lasers constructed from the suspension of dielectric and metallic scattering particles in liquid laser dyes, several solid state random laser devices were developed. These devices involved the suspension of 55 nm diameter Ag and 100 nm diameter Al₂O₃ scattering particles in the thick negative photoresist SU-8. Rhodamine 6G laser dye was dissolved into the SU-8 to provide optical gain. The mixture was deposited on a glass substrate to create a solid-state random lasing device. Experimental emission spectra obtained from the solid state random gain media indicated that linear excitation of the silver scattering particle layer lowers the threshold energy fluence for lasing by a factor of up to 54 times compared to circular excitation of the

same sample. The threshold is also lowered fivefold compared to an Ag scatterer based random laser suspended in a liquid dye. The formation of a conventional laser resonator cavity is enabled through line excitation in a pure Rhodamine 6G sample, but does not appear with a circular focal spot.

6.2 Future Possibilities

The surface plasmon enhanced random lasers outlined in this work provide a basis for future experimental work on improving the performance of random lasers. Further experimental work is likely to proceed in this area through the use of both silver nanoparticles of alternative sizes, as well as scattering particles formed from metals such as copper or gold.

The theoretical framework presented in this thesis provides the ability to develop models of any number of electromagnetic phenomena related to electromagnetic wave propagation through highly scattering media. The extension of this model to include the third dimension would greatly increase its predictive ability.

The ability to enhance random laser operation through the use of nanometer sized metallic scattering particles has the potential to improve the utility of random lasers for applications in the field of microlasers and microscopic light sources. Further, the ease of fabrication of nanoscopic metal particles compared to dielectric particles make them excellent candidates for use in such applications.

Appendix A: Finite-Difference Time-Domain Software Source Code

The following is the complete source code for the software suite developed for the simulation of random laser systems.

```

/*****
//File main.h
//Contains material constants and other controlling parameters
/*****
#ifdef MAIN_H
#define MAIN_H

#include "util.h"
#include <limits.h>

#define PARALLELIZE //defined to set the program to compile for a multi-threaded using
OPENMP
const int NUM_THREADS = 32;//The number of threads that the code should run in
//Some basic constants for the program. Needs to eventually go into a
//data file with a reader to load it.
//This is a two-dimensional code. Z direction is assumed to be infinitely the same
const double cnaught = 3e8;//The speed of light in free space (m/s)
const double enaught = 8.85e-12;//The permittivity free space (F/m)
const double pi = 3.14159265359;//Pi
const double munaught = 4*pi*1e-7;//The permeability of free space (H/m)
const double hbar = 6.63e-34/(2*pi);//The reduced Planck's constant
const double e_charge = 1.6e-19;//The charge on an electron (Coulombs)
const double e_mass = 9.11e-31;//The mass of an electron (kg)

const double grid_size = 50e-9;//feature_size/10 in m; The size of the simulation grid
const double delta_time = 1e-16;//grid_size/(2*cnaught) in s; The simulation time step
const int time_steps = 2000000;//The number of time steps that the simulation will
undergo

const int x_size = 500;//The width of the simulation space in grid spaces
const int y_size = 500;//The height of the simulation space in grid spaces
const int PML_width = 20;// The width of the perfectly matched layer boundary condition
//empirically, 10 works, but 20 seems to
work better
const int PML_cond = 100000;//conductivity of the outside layer of the PML
//outside layer - 1000 for THz,
100000 for optical

//Source Constants

const bool random_sources = true;//Create a set of point sources with a wavelengths
randomly distributed along
//a Lorentzian curve
const bool line_source = true;//Whether to use a radiation source distributed along a
line at y_source
const bool single_cycle = false;//THz pulse derivative of modified Gaussian - true is THz
experiment (Currently deprecated)
const bool gaussian = true; //Gaussian beam profile
const double beam_FWHM = 150*grid_size;//The intensity FWHM of the source beam
const bool pulsed = false;//True to create a pulsed source
const double pulse_FWHM = 8e-15; //The intensity FWHM duration of the pulsed source
const double pulse_start = 6*pulse_FWHM; //Time at which the pulse will be at its
maximum value
const double wavelength = 500e-9;//The central wavelength of the source.
const double max_field = 1;//The maximum field amplitude of the sources

//Geometry Constants

const int file_spacing = 5000;//spacing between output files
const int check_space = 5000;//number of timesteps to complete before creating a
checkpoint
const bool reload = true;//start from the last known good checkpoint

```

```

//geom.bmp is now loaded automatically, and must be built beforehand with the geometry
builder
//const bool load_geometry = true;
const bool text_output = true; //output text files instead of picture files

const int source_x = x_size/2; //horizontal centre of the beam
const int source_y = 25; //vertical position of the beam. must be > PML_width

//Integration Line Constants
const int first_line_y = source_y+PML_width; //Position of the first line to integrate
field strength over
const int second_line_y = y_size-2*PML_width; //Position of the second line to integrate
field strength over

/**/ Parameters for random medium (deprecated)
const int radius = 10; //Grid quanta, not physical size
const int num_cylinders = 100; //748;*/

const double output_circle_radius = 25; //The radius of the circle along which data will
be output for scattering calculations

//const double epsilon_medium = 1;
//const double epsilon_material = 2.25; //3.08424;

//parameters for Laser Gain
//Pumping rate
//const double pump_rate = 1e7;
//Centre frequency of gain spectrum
const double omega_a = 2*pi*cnaught/wavelength; //5.6e14;
//Level lifetimes
const double tau_32 = 1e-13; //Level lifetimes
const double tau_21 = 1e-9;
const double tau_10 = 1e-11;
//Starting Electron densities
/*const double N0_start = 3.2779e+024;
const double N1_start = 3.2778e+020;
const double N2_start = 3.2778e+022;
const double N3_start = 3.2779e+018;*/
const double N0_start = 5.5*6.02e23;
const double N1_start = 0;
const double N2_start = 0;
const double N3_start = 0;
//mean time between dephasing events
const double T2 = 2.18e-14;
//FWHM linewidth of atomic transition
const double delta_omega_a = 1/tau_21 + 2/T2;
//Real decay rate of second level
const double gamma_r = 1/tau_21;
//Classical decay rate of second level
const double gamma_c =
e_charge*e_charge*omega_a*omega_a/(e_mass*6*pi*enaught*cnaught*cnaught*cnaught);

//Lorentzian Lineshape stuff.
const double freqnaught = cnaught/500e-9; //The central frequency of the Lorentzian
const double delta_freq = cnaught/470e-9 - cnaught/530e-9; //The bandwidth of the
Lorentzian distribution of sources
const int source_spacing = 10; //No longer needed. Originally the average spacing between
randomly distributed sources

//Constants determining what material inhabits each grid square
enum {FREE_SPACE, DISPERSIONLESS_GLASS, ALUMINA, CHROMIUM, SILVER, GAIN,
num_material_types};

#endif

//*****
//File bitmap.h
//Constants for the bitmap I/O routines
//*****
#endif BITMAP_H

```

```

#define BITMAP_H

#include "material.h"
//Implements a bitmap reader and writer for output of data and input of geometry
information
//Also implements the text file output for data so that it can be moved out of the FDTD
section

//#undef BYTE

#define Bitmap_File_Header BITMAPFILEHEADER
#define Bitmap_Info_Header BITMAPINFOHEADER

class bitmap
{
public:
    //Output a colormapped bitmap with a maximum value of max
    //and using the data stored in field_data
    static void write(char * filename, double ** field_data, double max);
    //Output a graphical representation of the simulation geometry
    static void output_geometry(char * filename, material *** media_data);
    //Read in a graphical representation of the simulation geometry
    static void read_geometry(char * filename, int ** media_data);
};

#endif

//*****
//File geometry.cpp
//Contains constants for I?O of geometry files under *NIX
//Operating systems
//*****

#ifndef BITMAP_H
#define BITMAP_H

#include "material.h"

class geometry
{
public:
    //Output a text based geometry file
    static void output_geometry(char * filename, material *** media_data);
    //Read a text based geometry file
    static void read_geometry(char * filename, int ** media_data);
};

#endif

//*****
//File material.h
//Defines the material parameters for a specific type of material
//*****
#ifndef MATERIAL_H
#define MATERIAL_H

#include "main.h"

class material
{
public:
    //Default material is uninitialized space
    material();

    //Set the material constants for this particular material
    //double permittivity is the relative permittivity
    //double permeability is the relative permeability
    //double conductivity is the electrical conductivity of the material
    //double mag_cond is the magnetic conductivity of the material

```

```

//double B1, double B2, double B3, double reson_1, double reson_2, double reson_3
//Sellmeier coefficients for the material if it is a dispersive dielectric
//B1, B2, B3 are the fitting coefficients
//reson_1, reson_2, reson_3 are the resonant wavelengths
//double freq_plasma is the plasma frequency of the metal for the Drude model
//double freq_scatter is the scattering frequency of the metal
//bool dispersive controls whether the material is dispersive
//bool metallic controls whether the material is metallic
//bool gain controls whether the the material is a gain media
//All metals and gain material must also be set to dispersive
void set_material(double permittivity, double permeability, double conductivity,
double mag_cond, double B1, double B2, double B3, double reson_1, double
reson_2,
double reson_3, double freq_plasma, double freq_scatter, bool dispersive,
bool metallic, bool gain);

//The next four terms are the FDTD algorithm coefficients Cn, Dn
inline double H_Hcoeff()//1
{
return H_Hcoeff_var;
}
inline double H_Ecoeff()//(delta_time/(munaught*grid_size))
{
return H_Ecoeff_var;
}
inline double E_Ecoeff()//prefactor_a
{
return E_Ecoeff_var;
}
inline double E_Hcoeff()//prefactor_b
{
return E_Hcoeff_var;
}
//Return the relative permittivity
inline double get_permittivity()
{
return epsilon;
}
//Return the relative permeability
inline double get_permeability()
{
return mu;
}
inline bool is_dispersive()
{
return dispersion;
}
inline bool is_metal()
{
return metal;
}
inline bool is_gain()
{
return gain;
}
inline double get_x1()
{
return x1;
}
inline double get_x2()
{
return x2;
}
inline double get_x3()
{
return x3;
}
inline double get_y1()
{
return y1;
}
}

```

```

inline double get_y2()
{
    return y2;
}
inline double get_y3()
{
    return y3;
}
inline double get_z1()
{
    return z1;
}
inline double get_z2()
{
    return z2;
}
inline double get_z3()
{
    return z3;
}
inline double get_m1()
{
    return m1;
}
inline double get_m2()
{
    return m2;
}
inline double get_m3()
{
    return m3;
}
inline double get_m4()
{
    return m4;
}
inline double get_q1()
{
    return q1;
}
inline double get_q2()
{
    return q2;
}
inline double get_q3()
{
    return q3;
}
/* inline double get_a1()
{
    return a1;
}*/
inline double get_d1()
{
    return d1;
}
inline double get_c2()
{
    return c2;
}
inline double get_d2()
{
    return d2;
}
inline double get_b3()
{
    return b3;
}
inline double get_c3()
{
    return c3;
}

```

```

    }
    /* inline double get_a4()
    {
        return a4;
    }*/
    inline double get_b4()
    {
        return b4;
    }
    /* inline double get_e1()
    {
        return e1;
    }*/
    inline double get_h1()
    {
        return h1;
    }
    inline double get_g2()
    {
        return g2;
    }
    inline double get_h2()
    {
        return h2;
    }
    inline double get_i2()
    {
        return i2;
    }
    inline double get_f3()
    {
        return f3;
    }
    inline double get_g3()
    {
        return g3;
    }
    inline double get_i3()
    {
        return i3;
    }
    /* inline double get_e4()
    {
        return e4;
    }*/
    inline double get_f4()
    {
        return f4;
    }
}

private:
//Relative permittivity, relative permeability, electric conductivity, magnetic
conductivity
double epsilon, mu, e_cond, h_cond;
//Whether the material is dispersive
bool dispersion;
//Whether the material is a metal
bool metal;
//Whether the material is a gain media
bool gain;
//The FDTD coefficients.
double H_Hcoeff_var, H_Ecoeff_var, E_Ecoeff_var, E_Hcoeff_var;

//Sellmeier dispersion coefficients
double omegal, omega2, omega3;//Resonant frequencies
double w1, w2, w3;//Fitting coefficients
double x1, x2, x3, y1, y2, y3, z1, z2, z3;//Constants

//Drude Model Coefficients
double m1, m2, m3, m4;//Material dependent constants
double plasma_freq, scatter_freq;//Plasma frequency and scattering frequency

```

```

//Gain Model Coefficients
double q1, q2, q3;//Material dependent constants
double d1, c2, d2, b3, c3, b4, h1, g2, h2, i2, f3, g3, i3, f4;

};

#endif

/*****
//File two_dim.h
//Stores the electromagnetic field data for the simulation space
/*****
#ifndef TWO_DIM_H
#define TWO_DIM_H

#include "main.h"
#include "material.h"
#include <stdio.h>

class two_dim
{
public:
    two_dim();
    ~two_dim();
    void TE_solve();//Solve a TE problem. Currently not functional for multithreaded
applications
    void TM_solve();//Solve a TM problem. Necessary to excite surface plasmons

private:

    double ** Ez, ** Ezx, ** Ezy;//Electric field in the z direction, and PML
components
    double ** Ez_prev, ** Ez_prev_prev;//Electric field from the previous, and
previous previous time steps
    double ** Ex;//Electric field in the x direction
    double ** Ex_prev;//Previous time steps electric field in the x direction
    double ** Ey;//Electric field in the y direction
    double ** Ey_prev;//Previous time steps electric field in the y direction
    double ** Et;//The total EM field for TM mode

    //Displacements for dispersion
    //Displacement in the x direction, and previous two time step values
    double ** Dx, ** Dx_prev, ** Dx_prev_prev;
    //Displacement in the x direction, and previous two time step values
    double ** Dy, ** Dy_prev, ** Dy_prev_prev;
    //Displacement in the x direction, and previous two time step values
    double ** Dz, ** Dz_prev, ** Dz_prev_prev;

    //Magnetic fields in the x, y, and z directions, as well as the total magnetic
field for TE mode
    double ** Hx, ** Hy, ** Hz, ** Ht;
    //Magnetic field components for TM mode PML
    double ** Hzx, ** Hzy;

//Pump Beam for TM
//Identical to previous constants except that it represents an isolated simulations space
    double ** Hzp, ** Hzxp, ** Hzyp;
    double ** Exp, ** Eyp;
    double ** Ex_prevp, ** Ey_prevp;
    double ** Etp;
    double ** Dxp, ** Dyp;
    double ** Dx_prevp, ** Dy_prevp;
    double ** Dx_prev_prevp, ** Dy_prev_prevp;

//Random sources
    int num_sources;//The number of sources in the simulation space
    double ** source_wavelength;//An array containing the wavelength of each source at
each grid point

```

```

//Polarizations for dispersion model (TE mode)
double ** P1_prev, ** P2_prev, ** P3_prev;
double ** P1_prev_prev, ** P2_prev_prev, ** P3_prev_prev;

//Polarizations for dispersion model (TM mode)
double ** P1X_prev, ** P2X_prev, ** P3X_prev;
double ** P1X_prev_prev, ** P2X_prev_prev, ** P3X_prev_prev;
double ** P1Y_prev, ** P2Y_prev, ** P3Y_prev;
double ** P1Y_prev_prev, ** P2Y_prev_prev, ** P3Y_prev_prev;

//Polarization for laser gain model
double ** Pgain;
double ** Pgain_prev;
double ** Pgainx, ** Pgainy;
double ** Pgain_prevx, ** Pgain_prevy;
//Population Levels for Laser Gain
double ** N3, ** N2, ** N1, ** N0;
double ** N3_prev, ** N2_prev, ** N1_prev, ** N0_prev;
double ** pump_rate;//The current pumping rate at each grid point

material * the_materials;//The different materials that can be used
material *** media;//Array of pointers to each material

//The electric conductivity of the PML layer as a function of distance into the
layer
double Econd(int position);
//The magnetic conductivity of the PML layer as a function of distance into the
layer
double Hcond(int position);

//TE Mode radiation source terms
double source_Hx(double x, double y, double time_step);
double source_Ez(double x, double y, double time_step);

//TM Mode radiation source terms
double source_Ex(double x, double y, double time_step);
double source_Hz(double x, double y, double time_step);
double * THz_pulse_scaling;//deprecated
int THz_pulse_length;//deprecated

//The FDTD coefficients that are used in the PML region
double H_Hcoeffs[PML_width], H_Ecoeffs[PML_width], E_Hcoeffs[PML_width],
E_Ecoeffs[PML_width];
//Obtain the refractive index of the underlying material at a specific location
double ref_index(int x, int y);

void new_cylinder(int centre_x, int centre_y, int radius);
//Places a circle of arbitrary material centred at a specified point with a
specific radius

bool can_fit(int centre_x, int centre_y, int radius);
//Checks to see if the circle defined by the coordinates overlaps with any other
circles
//If so, it returns false

//Data outputting procedures

//Output a file containing raw binary data of the specified field quantity
void write_data(FILE * textfile, double ** field_data);
//Read in a file containing raw binary data to field_data
void read_data(FILE * textfile, double ** field_data);
//Write an ASCII representation of the field_data
void write_data_text(FILE * outfile, double ** field_data);
//Write an ASCII representation of the field_data
void read_data_text(FILE * infile, double ** field_data);

//Calculate the total intensity along a specified line for a specified field
double integrate(int line_y, double ** field_data);
//write a data file containing the field values at each
//point around a circle at the specified radius at each time step

```

```

        void output_circle(FILE * outfile, double ** field_data, int n);
        //Initialize the circular output file
        void output_circle_start(FILE * outfile);
};

#endif

//*****
//File util.h
//General utility files
//Defines initialization routines for the RNG
//*****
#ifndef UTIL_H
#define UTIL_H

#include <time.h>

//Produces a random number that is greater than or equal to lower, and less than higher
int get_rand(int lower, int higher);
double get_rand(double lower, double higher);

double real_rand();

//Initialize the RNG
void start_rand();

typedef unsigned long uint32;
//The seed value for the RNG uses this type.

#endif

//*****
//File main.cpp
//Start the program
//*****

#include <math.h>
#include <iostream>
#include <stdio.h>

#include "main.h"
#include "two_dim.h"
#include "util.h"

int main(int argc, char * argv)
{
    start_rand();//Seeds the random number generator

    two_dim solver;

    solver.TM_solve();//TM is needed to excite plasmons
    //solver.TE_solve();//TE won't excite plasmons
    return 0;
}

//*****
//File bitmap.cpp
//Geometry and output file manipulation procedures
//*****
#include "bitmap.h"
#include <windows.h>
#include <stdio.h>
#include "main.h"
#include <math.h>

void bitmap::write(char * filename, double ** field_data, double max)
//Write a bitmap using max as the max field value

```

```

{
    Bitmap_Info_Header bih;
    Bitmap_File_Header bfh;
    char BMP_filename[512];
    FILE BMP_file;

    //Constants to set the bitmap parameters
    bfh.bfType = 19778;
    bfh.bfReserved1 = 0;
    bfh.bfReserved2 = 0;
    bfh.bfOffBits = sizeof(bfh) + sizeof(bih);
    bfh.bfSize = bfh.bfOffBits + x_size*y_size*3;

    bih.biSize = sizeof(bih);
    bih.biWidth = x_size;
    bih.biHeight = y_size;
    bih.biPlanes = 1;
    bih.biBitCount = 24;
    bih.biCompression = BI_RGB;
    bih.biSizeImage = x_size*y_size*3;
    bih.biXPelsPerMeter = bih.biYPelsPerMeter = 0;
    bih.biClrUsed = 0;
    bih.biClrImportant = 0;

    sprintf(BMP_filename, "%s.bmp", filename);
    BMP_file = fopen(BMP_filename, "wb");

    fwrite(&bfh, sizeof(bfh), 1, BMP_file);
    fwrite(&bih, sizeof(bih), 1, BMP_file);

    double min = -max;

    for (int j = 0; j < y_size; j++)
    {
        for (int i = 0; i < x_size; i++)
        {
            unsigned char bgr[3];
            int colorRange = (5*256);
            double percent = ( fabs(min) + field_data[i][j] ) / ( fabs(max) +
fabs(min) );
            int color = (int)(percent*colorRange);
//The potential colormaps
/*
- color : ( color <= 5*256/2 ? 0 : ( color < 9*256/2 ? color - 7*256/2 : 255 ) ) );
: ( color <= 5*256/2 ? 0 : ( color < 7*256/2 ? color-5*256/2 :
( color < 9*256/2 ? 255 : 255 ) ) );
: ( color <= 5*256/2 ? 5*256/2 - color : ( color < 7*256/2 ? 0 :
( color < 9*256/2 ? 0 : color-9*256/2 ) ) );*/
            bgr[0] = color <= 128 ? 255 : ( color <= 3*256/2 ? 3*256/2
: ( color <= 5*256/2 ? 5*256/2 - color : ( color < 7*256/2 ? 0 :
color-9*256/2 ) ) );
            bgr[1] = color <= 128 ? 255 : ( color <= 3*256/2 ? 3*256/2
- color : ( color <= 5*256/2 ? 0 : ( color < 7*256/2 ? 0
: ( color < 9*256/2 ? color - 7*256/2 : 255 ) ) );
            bgr[2] = color <= 128 ? 128-color : ( color <= 3*256/2 ? 0
: ( color <= 5*256/2 ? 0 : ( color < 7*256/2 ? color-5*256/2 :
( color < 9*256/2 ? 255 : 255 ) ) );
            fwrite(bgr, sizeof(unsigned char), 3, BMP_file);
        }
    }
//Take care of the misaligned bits
    if( i % 4 != 0 )
    {
        unsigned char space = 0;
        int n = 0;
        for( n=0; n<i%4 ; n ++ )
            fwrite(&space, sizeof(unsigned char), 1, BMP_file);
    }
}

```

```

    }
}

fclose(BMP_file);
}

//Output what the geometry file looks like
void bitmap::output_geometry(char * filename, material *** media_data)
{
    Bitmap_Info_Header bih;
    Bitmap_File_Header bfh;
    char textfilename[512], BMP_filename[512];
    FILE * BMP_file;

    bfh.bfType = 19778;
    bfh.bfReserved1 = 0;
    bfh.bfReserved2 = 0;
    bfh.bfOffBits = sizeof(bfh) + sizeof(bih);
    bfh.bfSize = bfh.bfOffBits + x_size*y_size*3;

    bih.biSize = sizeof(bih);
    bih.biWidth = x_size;
    bih.biHeight = y_size;
    bih.biPlanes = 1;
    bih.biBitCount = 24;
    bih.biCompression = BI_RGB;
    bih.biSizeImage = x_size*y_size*3;
    bih.biXPelsPerMeter = bih.biYPelsPerMeter = 0;
    bih.biClrUsed = 0;
    bih.biClrImportant = 0;

    sprintf(BMP_filename, "%s.bmp", filename);

    BMP_file = fopen(BMP_filename, "wb");

    int i,j;
    fwrite(&bfh, sizeof(bfh), 1, BMP_file);
    fwrite(&bih, sizeof(bih), 1, BMP_file);

    for (j = 0; j < y_size; j++)
    {
        for (i = 0; i < x_size; i++)
        {
            unsigned char bgr[3];
            int colorRange = (5*256);

            bgr[0] = 0;
            bgr[1] = 0;
            bgr[2] = 0;

/*
            if (media_data[i][j].get_permittivity() == epsilon_material)
            {
                bgr[0] = 0;
                bgr[1] = 255;
                bgr[2] = 0;
            }*/
            //Check if it is dispersive
            if (media_data[i][j]->is_dispersive())
            {
                bgr[0] = 0;
                bgr[1] = 0;
                bgr[2] = 255;
            }
            //Check if it is a metal
            if (media_data[i][j]->is_metal())
            {
                bgr[0] = 0;
                bgr[1] = 255;
                bgr[2] = 255;
            }
            //Check if it is a gain material

```

```

        if (media_data[i][j]->is_gain())
        {
            bgr[0] = 255;
            bgr[1] = 0;
            bgr[2] = 0;
        }
        //Put a green line where the source is
        if (j == source_y)
        {
            bgr[0] = 0;
            bgr[1] = 255;
            bgr[2] = 0;
        }
        //Make the PML region white
        if (i < PML_width || j < PML_width || i >= x_size-PML_width || j >=
y_size-PML_width)
        {
            bgr[0] = 255;
            bgr[1] = 255;
            bgr[2] = 255;
        }

        fwrite(bgr,sizeof(unsigned char),3,BMP_file);
    }

    if( i % 4 != 0)
    {
        unsigned char space = 0;
        int n = 0;
        for( n=0; n<i%4 ; n ++ )
            fwrite(&space,sizeof(unsigned char),1,BMP_file);
    }

    fclose(BMP_file);
}
//Here is where material parameters are set from data read from the geometry file.
void bitmap::read_geometry(char * filename, int ** media_data)
{
    Bitmap_Info_Header bih;
    Bitmap_File_Header bfh;
    char BMP_filename[512];
    FILE * BMP_file;

    sprintf(BMP_filename, "%s.bmp", filename);
    BMP_file = fopen(BMP_filename, "rb");

    fread(&bfh,sizeof(bfh),1,BMP_file);
    fread(&bih,sizeof(bih),1,BMP_file);

    for (int j = 0; j < y_size; j++)
    {
        for (int i = 0; i < x_size; i++)
        {
            unsigned char bgr[3];
            fread(bgr,sizeof(unsigned char),3,BMP_file);

            if (bgr[0] == 0 && bgr[1] == 0 && bgr[2] == 0) //(blue && green &&
red) yellow=green + red
            {
                //Free Space
                media_data[i][j] = FREE_SPACE;
            }
            else if (bgr[0] == 0 && bgr[1] == 255 && bgr[2] == 255)
            {
                //Silver
                media_data[i][j] = SILVER;
            }
            else if (bgr[0] == 0 && bgr[1] == 255 && bgr[2] == 0)
            {
                //Dispersionless Glass

```

```

        media_data[i][j] = DISPERSIONLESS_GLASS;
    }
    else if (bgr[0] == 255 && bgr[1] == 0 && bgr[2] == 0)
    {
//Gain material
        media_data[i][j] = GAIN;
    }
    else
    {
//Free Space
        media_data[i][j] = FREE_SPACE;
//The media is the external medium here
    }
    if( i % 4 != 0)
    {
        unsigned char space = 0;
        int n = 0;
        for( n=0; n<i%4 ; n ++ )
            fread(&space,sizeof(unsigned char),1,BMP_file);
    }
    fclose(BMP_file);
}

//*****
//File geometry.cpp
//geometry.h and geometry.cpp are used for operation under *NIX
//instead of bitmap.h and bitmap.cpp
//*****

#include "geometry.h"
#include "main.h"
#include <stdio.h>
#include <stdlib.h>

//Output an ASCII text file representation of the simulation geometry
void geometry::output_geometry(char * filename, material *** media_data)
{
    char BMP_filename[512];
    FILE * BMP_file;

    sprintf(BMP_filename, "%s.txt", filename);

    BMP_file = fopen(BMP_filename, "wt");

    int i,j;

    for (j = 0; j < y_size; j++)
    {
        for (i = 0; i < x_size; i++)
        {
//select what character to output according to what material is present
            int temp = FREE_SPACE;
            if (media_data[i][j]->is_metal())
            {
                temp = SILVER;
            }
            else if (media_data[i][j]->is_gain())
            {
                temp = GAIN;
            }
            else
            {
                temp = FREE_SPACE;
            }
            fprintf(BMP_file, "%d ", temp);
        }
    }
}

```

```

        fprintf(BMP_file, "\n");
    }
    fclose(BMP_file);
}
//material parameters are set here according to the geometry file.
void geometry::read_geometry(char * filename, int ** media_data)
{
    char BMP_filename[512];
    FILE * BMP_file;

    sprintf(BMP_filename, "%s.txt", filename);
    BMP_file = fopen(BMP_filename, "r");

    for (int j = 0; j < y_size; j++)
    {
        for (int i = 0; i < x_size; i++)
        {
            int type = FREE_SPACE;

            fscanf(BMP_file, "%d", &type);
            //          (temp, 2, BMP_file);

            //metallic materials are also dispersive
            if (type == FREE_SPACE)
            {
                //Free Space
                media_data[i][j] = FREE_SPACE;
            }
            else if (type == SILVER)
            {
                //Silver
                media_data[i][j] = SILVER;
            }
            else if (type == DISPERSIONLESS_GLASS)
            {
                //Dispersionless Glass
                media_data[i][j] = DISPERSIONLESS_GLASS;
            }
            else if (type == GAIN)
            {
                //Gain material
                media_data[i][j] = GAIN;
            }
            else
            {
                //Free Space
                media_data[i][j] = FREE_SPACE;
            }
            //The media is the external medium here
        }
    }

    fclose(BMP_file);
}

//*****
//File material.cpp
//*****
#include "material.h"
#include "main.h"

//Code to handle the various materials

material::material()
{
}

//Set the material parameters
void material::set_material(double permittivity, double permeability, double
conductivity,

```

```

double mag_cond, double B1, double B2, double B3, double reson_1, double reson_2,
double reson_3, double freq_plasma, double freq_scatter, bool dispersive, bool
metallic, bool isgain)
{
    epsilon = permittivity;
    mu = permeability;
    e_cond = conductivity;
    h_cond = mag_cond;
    dispersion = dispersive;
    metal = metallic;
    gain = isgain;

    omega1 = reson_1 == 0 ? 0:2*pi*cnaught/reson_1;
    omega2 = reson_2 == 0 ? 0:2*pi*cnaught/reson_2;
    omega3 = reson_3 == 0 ? 0:2*pi*cnaught/reson_3;
    w1 = B1;
    w2 = B2;
    w3 = B3;
    plasma_freq = freq_plasma;
    scatter_freq = freq_scatter;

    //Calculate the FDTD coefficients
    H_Hcoeff_var = (1-
h_cond*delta_time/(2*mu*munaught))/(1+h_cond*delta_time/(2*mu*munaught));
    H_Ecoeff_var =
(delta_time/(mu*munaught*grid_size))/(1+h_cond*delta_time/(2*mu*munaught));
    E_Ecoeff_var = (1-
e_cond*delta_time/(2*epsilon*enaught))/(1+e_cond*delta_time/(2*epsilon*enaught));
    E_Hcoeff_var =
(delta_time/(epsilon*enaught*grid_size))/(1+e_cond*delta_time/(2*epsilon*enaught));

    //Calculate the constants to be used for the polarization dependent dispersion
    x1 = 2 + omega1*omega1*delta_time*delta_time*(1+w1);
    x2 = 2 + omega2*omega2*delta_time*delta_time*(1+w2);
    x3 = 2 + omega3*omega3*delta_time*delta_time*(1+w3);
    y1 = omega1*omega1*w1*delta_time*delta_time;
    y2 = omega2*omega2*w2*delta_time*delta_time;
    y3 = omega3*omega3*w3*delta_time*delta_time;
    z1 = -2 - omega1*omega1*delta_time*delta_time*(1+w1);
    z2 = -2 - omega2*omega2*delta_time*delta_time*(1+w2);
    z3 = -2 - omega3*omega3*delta_time*delta_time*(1+w3);

    //Calculate Drude Model Constants
    m1 = 2 + scatter_freq*delta_time;
    m2 = 2 - scatter_freq*delta_time;
    m3 = plasma_freq*plasma_freq*enaught*delta_time*delta_time
        - scatter_freq*enaught*epsilon*delta_time + 2*enaught*epsilon;
    m4 = plasma_freq*plasma_freq*enaught*delta_time*delta_time
        + scatter_freq*enaught*epsilon*delta_time + 2*enaught*epsilon;

    //Calculate constants to be used for the gain model
    q1 = -2 + delta_time*delta_omega_a - delta_time*delta_time*omega_a*omega_a;
    q2 = 2*delta_time*delta_time * gamma_r * e_charge*e_charge/(gamma_c*e_mass);
    q3 = 2 + delta_time*delta_omega_a + delta_time*delta_time*omega_a*omega_a;

    //
    a1 = -delta_time*pump_rate*tau_32;
    d1 = tau_32 + delta_time;
    c2 = hbar*omega_a*tau_32*tau_21 + delta_time*hbar*omega_a*tau_32;
    d2 = -delta_time*hbar*omega_a*tau_21;
    b3 = hbar*omega_a*tau_21*tau_10 + delta_time*hbar*omega_a*tau_21;
    c3 = -delta_time*hbar*omega_a*tau_10;
    //
    a4 = tau_10 + delta_time*pump_rate*tau_10;
    b4 = -delta_time;

    //
    e1 = delta_time*pump_rate*tau_32;
    h1 = tau_32 - delta_time;
    g2 = hbar*omega_a*tau_32*tau_21 - delta_time*hbar*omega_a*tau_32;
    h2 = delta_time*hbar*omega_a*tau_21;
    i2 = tau_32*tau_21;
    f3 = hbar*omega_a*tau_21*tau_10 - delta_time*hbar*omega_a*tau_21;
    g3 = delta_time*hbar*omega_a*tau_10;

```

```

        i3 = tau_21*tau_10;
//      e4 = tau_10 - delta_time*pump_rate*tau_10;
        f4 = delta_time;
    }

//*****
//File two_dim.cpp
//The bulk of the solver code
//*****

#include "two_dim.h"
#include "main.h"
#include <math.h>
#include <stdio.h>
#include <iostream>
#include "geometry.h"

#ifdef PARALLELIZE
#include <omp.h>
#endif

//Returns the value of the Lorentzian distribution at the frequency mu
double lorentzian(double mu);
//returns the distance between (x,y) and (centre)x, centre_y)
double position(double x, double y, int centre_x, int centre_y);

two_dim::two_dim()
{
}

two_dim::~two_dim()
{
}

//Solve it in TE mode
//Not set up for parallel operation hence the #if 0
void two_dim::TE_solve()
{
    #if 0//This prevents the following codee block from being compiled
        FILE * ezdatafile;
        char * filename;
        double P1, P2, P3;

        filename = new char[200];

        printf("Initializing Media Array.\n");
//Set the FDTD coefficients for the PML
        for (int p = 0; p < PML_width; p++)
        {
            H_Hcoeffs[p] = exp(-Hcond(p)*delta_time/munaught);
            E_Ecoeffs[p] = exp(-Econd(p)*delta_time/enaught);
            H_Ecoeffs[p] = (1-exp(-Hcond(p)*delta_time/munaught))/Hcond(p)/grid_size;
            E_Hcoeffs[p] = (1-exp(-Econd(p)*delta_time/enaught))/Econd(p)/grid_size;
        }

//Prevent a divide by zero error
        H_Ecoeffs[0] = delta_time/munaught/grid_size;

//Allocate memory for each array
        media = new material * [x_size];
        for (int x = 0; x < x_size; x++)
        {
            media[x] = new material [y_size];
        }

//Set the geometry using the old style memory sucking method
        for (x = 0; x < x_size; x++)
        {
            for (int y = 0; y < y_size; y++)
            {

```

```

//Free Space
media[x][y]-
>set_material(1,1,0,0,0,0,0,0,0,0,0,0,0,0,0,0,false,false,false);
}

printf("Starting Geometry Generation.\n");
//Geometry generation routines that have now been outsourced to a separate program
for clarity
if (!load_geometry)
{
    if (central_cylinder)
    {
        new_cylinder(x_size/2, y_size/2, radius);
    }
    else
    {
        int count = num_cylinders;
        int keep_going = 2000;
        int temp_x, temp_y;

        while (count > 0 && keep_going > 0)
        {
            temp_x = get_rand(PML_width+radius, x_size-PML_width-
radius);
            temp_y = get_rand(2*PML_width+source_y+2*radius, y_size-
4*PML_width);

            if (can_fit(temp_x, temp_y, radius))
            {
                new_cylinder(temp_x, temp_y, radius);
                count--;
            }
            else
            {
                keep_going--;
            }
        }
    }
}
else
{
    //bitmap::read_geometry("./data/geom", media);
}

//bitmap::output_geometry("./data/geomout", media);
//More memory allocation and initialization
printf("Finished Geometry Generation.\n");
int final_n = 0;
int begin_n = 0;

printf("Allocated memory.\n");
printf("Initializing Field Arrays.\n");

Ez = new double *[x_size];
Ezx = new double *[x_size];
Ezy = new double *[x_size];

Ez_prev = new double *[x_size];

Dz = new double *[x_size];
Dz_prev = new double *[x_size];
Dz_prev_prev = new double *[x_size];
Hx = new double *[x_size];
Hy = new double *[x_size];
Ht = new double *[x_size];

P1_prev = new double * [x_size];
P2_prev = new double * [x_size];
P3_prev = new double * [x_size];

P1_prev_prev = new double * [x_size];

```

```

P2_prev_prev = new double * [x_size];
P3_prev_prev = new double * [x_size];

Pgain = new double *[x_size];

Pgain_prev = new double *[x_size];

N0 = new double *[x_size];
N1 = new double *[x_size];
N2 = new double *[x_size];
N3 = new double *[x_size];

N0_prev = new double *[x_size];
N1_prev = new double *[x_size];
N2_prev = new double *[x_size];
N3_prev = new double *[x_size];

pump_rate = new double *[x_size];

for (x = 0; x < x_size; x++)
{
    Ez[x] = new double [y_size];
    Ezx[x] = new double [y_size];
    Ezy[x] = new double [y_size];

    Ez_prev[x] = new double [y_size];

    Dz[x] = new double [y_size];
    Dz_prev[x] = new double [y_size];
    Dz_prev_prev[x] = new double [y_size];

    Hx[x] = new double [y_size];
    Hy[x] = new double [y_size];
    Ht[x] = new double [y_size];

    P1_prev[x] = new double [y_size];
    P2_prev[x] = new double [y_size];
    P3_prev[x] = new double [y_size];

    P1_prev_prev[x] = new double [y_size];
    P2_prev_prev[x] = new double [y_size];
    P3_prev_prev[x] = new double [y_size];

    Pgain[x] = new double [y_size];

    Pgain_prev[x] = new double [y_size];

    N0[x] = new double [y_size];
    N1[x] = new double [y_size];
    N2[x] = new double [y_size];
    N3[x] = new double [y_size];

    N0_prev[x] = new double [y_size];
    N1_prev[x] = new double [y_size];
    N2_prev[x] = new double [y_size];
    N3_prev[x] = new double [y_size];

    pump_rate[x] = new double [y_size];
}

printf("Allocated Field Memory.\n");
printf("Initializing Field Components\n");

for (x = 0; x < x_size; x++)
{
    for (int y = 0; y < y_size; y++)
    {
        Ez[x][y] = 0;
        Ezx[x][y] = 0;
        Ezy[x][y] = 0;
    }
}

```

```

        Ez_prev[x][y] = 0;

        Dz[x][y] = 0;
        Dz_prev[x][y] = 0;
        Dz_prev_prev[x][y] = 0;

        Hx[x][y] = 0;
        Hy[x][y] = 0;
        Ht[x][y] = 0;

        P1_prev[x][y] = 0;
        P2_prev[x][y] = 0;
        P3_prev[x][y] = 0;

        P1_prev_prev[x][y] = 0;
        P2_prev_prev[x][y] = 0;
        P3_prev_prev[x][y] = 0;

        Pgain[x][y] = 0;

        Pgain_prev[x][y] = 0;

        N0[x][y] = N0_start;
        N1[x][y] = N1_start;
        N2[x][y] = N2_start;
        N3[x][y] = N3_start;

        N0_prev[x][y] = N0_start;
        N1_prev[x][y] = N1_start;
        N2_prev[x][y] = N2_start;
        N3_prev[x][y] = N3_start;

        pump_rate[x][y] = 0;
    }
}
printf("Field Components Initialized\n");
printf("Beginning FDTD Computations.\n");

FILE * temp_outfile;
temp_outfile = fopen("./data/output_circle_points.txt", "w+");
output_circle_start(temp_outfile);
fclose(temp_outfile);

FILE * fieldoutput, * point_output, * integrate_output, * vector_output, *
vector_output_end, * circle_output;

//Various output files
fieldoutput = fopen("./data/output_count.txt", "w+");
vector_output = fopen("./data/output_field.txt", "w+");
point_output = fopen("./data/output_point.txt", "w+");
// integrate_output = fopen("./data/output_line.txt", "w+");
// vector_output_start = fopen("./data/output_vector_start.txt", "w+");
// vector_output_end = fopen("./data/output_vector_end.txt", "w+");
circle_output = fopen("./data/output_circle.txt", "w+");

for (int n = 0; n < time_steps; n++)
{
    printf("Done %f %s\n", (double)(100*n)/time_steps, "%");

    output_circle(circle_output, Ez, n);

//    fprintf(vector_output_start, "%e ", n*delta_time);
//    fprintf(vector_output_end, "%e ", n*delta_time);
/*    for (int temp_y = 0; temp_y < y_size; temp_y++)
    {
        fprintf(vector_output_start, "%e ", Ez[x_size/2][temp_y]);
//        fprintf(vector_output_end, "%e ", Ez[x][second_line_y]);
    }
    fprintf(vector_output_start, "\n");*/
/*    fprintf(vector_output_end, "\n");*/

```

```

/*      double tot_Ez_start, tot_Hx_start, tot_Hy_start,
        tot_Ez_end, tot_Hx_end, tot_Hy_end;

        tot_Ez_start = integrate(first_line_y, Ez);
        tot_Hx_start = integrate(first_line_y, Hx);
        tot_Hy_start = integrate(first_line_y, Hy);
        tot_Ez_end = integrate(second_line_y, Ez);
        tot_Hx_end = integrate(second_line_y, Hx);
        tot_Hy_end = integrate(second_line_y, Hy);

        fprintf(integrate_output, "%e %e %e %e %e %e %e\n", n*delta_time,
tot_Ez_start,
                tot_Hx_start, tot_Hy_start, tot_Ez_end, tot_Hx_end, tot_Hy_end);

        fprintf(fieldoutput, "%e %e %e %e %e %e
%e\n", n*delta_time, Ez[x_size/2][first_line_y],
                Hx[x_size/2][first_line_y], Hy[x_size/2][first_line_y],
                Ez[x_size/2][second_line_y], Hx[x_size/2][second_line_y],
                Hy[x_size/2][second_line_y]);*/
        int tempnum = y_size/10;

        //output electric field at regular intervalled points along the centre of
the geometry
        fprintf(vector_output, "%e %e %e %e %e %e %e %e %e %e
%e\n", n*delta_time, Ez[x_size/2][tempnum],
                Ez[x_size/2][tempnum*2], Ez[x_size/2][tempnum*3],
                Ez[x_size/2][tempnum*4], Ez[x_size/2][tempnum*5],
                Ez[x_size/2][tempnum*6], Ez[x_size/2][tempnum*7],
                Ez[x_size/2][tempnum*8], Ez[x_size/2][tempnum*9],
                Ez[x_size/2][tempnum*10]);

        //Gain model output
        fprintf(fieldoutput, "%e %e %e %e %e %e %e
%e\n", n*delta_time, Ez[x_size/2][y_size/2],
                N0[x_size/2][y_size/2], N1[x_size/2][y_size/2], N2[x_size/2][y_size/2],
                N3[x_size/2][y_size/2], Pgain[x_size/2][y_size/2], Dz[x_size/2][y_size/2]);

        //More gain model output
        fprintf(point_output, "%e %e %e\n", n*delta_time, Ez[x_size/2][y_size/2],
pump_rate[x_size/2][y_size/2]);

        if (n % file_spacing == 0)
        {
                //output pictures or raw data files
                sprintf(filename, "./data/%6.0d_data", n);
/*      if (bitmap_output)
                {
                        bitmap::write(filename, Ez, max_field);
                }*/
                if (text_output)
                {
                        write_data(filename, Ez);
                }
        }

        //Step through each grid point
        for (int x = 0; x < x_size; x++)
        {
                //printf("%f\n", x);
                for (int y = 0; y < y_size; y++)
                {
                        //Check to see if we are in a boundary
                        //if so, use the PML
                        if (x < PML_width || y < PML_width || x >= x_size-PML_width
|| y >= y_size-PML_width)
                        {
                                double H_Hcoeff_Y, H_Ecoeff_Y, H_Hcoeff_X,
H_Ecoeff_X,

```

```

E_Ecoeff_X, E_Hcoeff_X, E_Ecoeff_Y,
E_Hcoeff_Y;
//There are 4 edges and 8 corners
//The default coefficients for any surface that doesn't show up in the rest of the
//overlapping regions

H_Hcoeff_X = media[x][y]->H_Hcoeff();
H_Ecoeff_X = media[x][y]->H_Ecoeff();
E_Hcoeff_X = media[x][y]->E_Hcoeff();
E_Ecoeff_X = media[x][y]->E_Ecoeff();

H_Hcoeff_Y = H_Hcoeff_X;
H_Ecoeff_Y = H_Ecoeff_X;
E_Hcoeff_Y = E_Hcoeff_X;
E_Ecoeff_Y = E_Ecoeff_X;

int temp = 0;
if (x < PML_width)
{
    //In the left edge
    temp = PML_width - x - 1;
    H_Hcoeff_Y = H_Hcoeffs[temp];
    H_Ecoeff_Y = H_Ecoeffs[temp];
    E_Hcoeff_X = E_Hcoeffs[temp];
    E_Ecoeff_X = E_Ecoeffs[temp];
}
if (y < PML_width)
{
    //In the bottom edge
    temp = PML_width - y - 1;
    H_Hcoeff_X = H_Hcoeffs[temp];
    H_Ecoeff_X = H_Ecoeffs[temp];
    E_Hcoeff_Y = E_Hcoeffs[temp];
    E_Ecoeff_Y = E_Ecoeffs[temp];
}
if (x >= x_size-PML_width)
{
    //In the right edge
    temp = x - x_size + PML_width;
    H_Hcoeff_Y = H_Hcoeffs[temp];
    H_Ecoeff_Y = H_Ecoeffs[temp];
    E_Hcoeff_X = E_Hcoeffs[temp];
    E_Ecoeff_X = E_Ecoeffs[temp];
}
if (y >= y_size-PML_width)
{
    //In the top edge
    temp = y - y_size + PML_width;
    H_Hcoeff_X = H_Hcoeffs[temp];
    H_Ecoeff_X = H_Ecoeffs[temp];
    E_Hcoeff_Y = E_Hcoeffs[temp];
    E_Ecoeff_Y = E_Ecoeffs[temp];
}

//The FDTD equations for the PML are below
double temp_Ez;

temp_Ez = y == y_size-1 ? 0.0:Ez[x][y+1];
Hx[x][y] = H_Hcoeff_X*Hx[x][y]
    + H_Ecoeff_X * (Ez[x][y] - temp_Ez);
temp_Ez = x == x_size-1 ? 0.0:Ez[x+1][y];
Hy[x][y] = H_Hcoeff_Y*Hy[x][y]
    + H_Ecoeff_Y * (temp_Ez - Ez[x][y]);

//Electric field calculations

double temp_Hx, temp_Hy;

temp_Hy = x == 0 ? 0.0:Hy[x-1][y];
temp_Hx = y == 0 ? 0.0:Hx[x][y-1];

```



```

energy = media[x][y]-
>get_permittivity()*enaught*Ez[x][y]*Ez[x][y]/2
+ media[x][y]-
>get_permeability()*munaught*(Hx[x][y]*Hx[x][y] + Hy[x][y]*Hy[x][y])/2;

double B04 = 1;
pump_rate[x][y] =

energy/(hbar*omega_a)*B04;

//Calculate the gain model constants
a1 = -
a4 = tau_10 +
e1 =
e4 = tau_10 -

q1 = media[x][y]->get_q1();
q2 = media[x][y]->get_q2();
q3 = media[x][y]->get_q3();

// a1 = media[x][y]->get_a1();
// d1 = media[x][y]->get_d1();
// c2 = media[x][y]->get_c2();
// d2 = media[x][y]->get_d2();
// b3 = media[x][y]->get_b3();
// c3 = media[x][y]->get_c3();
// a4 = media[x][y]->get_a4();
// b4 = media[x][y]->get_b4();

// e1 = media[x][y]->get_e1();
// h1 = media[x][y]->get_h1();
// g2 = media[x][y]->get_g2();
// h2 = media[x][y]->get_h2();
// i2 = media[x][y]->get_i2();
// f3 = media[x][y]->get_f3();
// g3 = media[x][y]->get_g3();
// i3 = media[x][y]->get_i3();
// e4 = media[x][y]->get_e4();
// f4 = media[x][y]->get_f4();

temp_N0 = N0[x][y];
temp_N1 = N1[x][y];
temp_N2 = N2[x][y];
temp_N3 = N3[x][y];
temp_Pgain = Pgain[x][y];

//Calculate the polarization
Pgain[x][y] = (4*Pgain[x][y] +
q1*Pgain_prev[x][y] + q2*(N1[x][y] - N2[x][y])*Ez[x][y]) / q3;

//Calculate the electric field due to
te polarization and the displacement
Ez[x][y] = (1.0/enaught)*(Dz[x][y] -
Pgain[x][y]);

//Update the population levels
* h1; K1 = N0_prev[x][y] * e1 + N3_prev[x][y]
* h2 + Ez[x][y]*(Pgain[x][y] - Pgain_prev[x][y])*i2; K2 = N2_prev[x][y] * g2 + N3_prev[x][y]
N2_prev[x][y] * g3 + Ez[x][y]*(Pgain[x][y] - Pgain_prev[x][y])*i3; K3 = N1_prev[x][y] * f3 +
N1_prev[x][y] * f4; K4 = N0_prev[x][y] * e4 +

```



```

P2 = -c2*(-a3+c3)/denominator*K1-
(a1*a3-c1*c3)/denominator*K2+c2*(a1-c1)/denominator*K3;
P3 = -c3*(c2-
a2)/denominator*K1+c3*(a1-c1)/denominator*K2-(a1*a2-c1*c2)/denominator*K3;

//Determine the electric field
Ez[x][y] = (1.0/enaught)*(Dz[x][y] -

P1 - P2 - P3);
}
else
{
//it is not a dispersive material, and the
normal FDTD update equations apply
/*
if (x == x_size/2 && y == y_size/2)
int temp = 0;*/
E_Ecoeff_Z = media[x][y]->E_Ecoeff();
E_Hcoeff_Z = media[x][y]->E_Hcoeff();
P1 = 0;
P2 = 0;
P3 = 0;
Ez[x][y] = E_Ecoeff_Z*Ez[x][y]
+ E_Hcoeff_Z*(Hy[x][y] - Hy[x-1][y]
+ Hx[x][y-1] - Hx[x][y] +
Hxinc);
}
//Store the previous time steps information
Ez_prev[x][y] = temp_Ez;
Dz_prev_prev[x][y] = Dz_prev[x][y];
Dz_prev[x][y] = Dz[x][y];

N0_prev[x][y] = temp_N0;
N1_prev[x][y] = temp_N1;
N2_prev[x][y] = temp_N2;
N3_prev[x][y] = temp_N3;
Pgain_prev[x][y] = temp_Pgain;

P1_prev_prev[x][y] = P1_prev[x][y];
P2_prev_prev[x][y] = P2_prev[x][y];
P3_prev_prev[x][y] = P3_prev[x][y];

P1_prev[x][y] = P1;
P2_prev[x][y] = P2;
P3_prev[x][y] = P3;
} //end of FDTD calcs
Ht[x][y] = sqrt(Hx[x][y]*Hx[x][y] + Hy[x][y]*Hy[x][y]);
} //end of y
} //end of x
}

/*
fclose(fieldoutput);
fclose(integrate_output);
fclose(vector_output_start);
fclose(vector_output_end);
fclose(circle_output);*/
#endif
}

//Returns the distance between (x,y) and (centre_x,centre_y)
double position(double x, double y, int centre_x, int centre_y)
{
return sqrt((x-centre_x)*(x-centre_x) + (y-centre_y)*(y-centre_y));
}

//Returns the electric conductivity inside of the PML layer at position
double two_dim::Econd(int position)
{
return PML_cond*((double)(position+0.5)/(double)PML_width);
}

//Returns the magnetic conductivity inside of the PML layer at position

```

```

double two_dim::Hcond(int position)
{
    return (PML_cond*munaught/enaught)*((double)position/(double)PML_width);
}

//TE Mode
//returns the magnetic field in the x direction at the specified location
//for the source
double two_dim::source_Hx(double x, double y, double time_step)
{
    //wz is the beam waist at the specified location
    //wo is the beam waist
    //Zo is the Rayleigh range
    //Hfield is the return value
    //scaling is the Gaussian scaling factor
    //wave is the oscillating carrier
    //x_offset is the x shift
    //y_offset is the y shift
    double wz, wo, Zo, Hfield, scaling, wave, x_offset, y_offset;
    //pulse_scaling is the time scaling of the field
    //time_factor is the scaling factor for the pulse length
    //time_offset is the shift compared to the pulse centre
    double pulse_scaling, time_factor, time_offset;

    //calculate the beam waist
    wo = beam_FWHM;
    //get the rayleigh range
    Zo = pi * ref_index((int)x, (int)y)*wo*wo/wavelength;

    //Find the x and y shifts
    x_offset = (x-source_x)*grid_size;
    y_offset = (y-source_y)*grid_size;

    //determine the beam diameter at the current location
    wz = wo * sqrt(1 + (y_offset*y_offset/(Zo*Zo)));

    //calculate the Gaussian distribution of the beam
    scaling = wo/wz * exp(- (x_offset*x_offset)/(wz*wz));

    //Time scale the pulse to get the proper FWHM
    time_factor = 2*log(sqrt(2.0)+1)/pulse_FWHM;
    //Calculate the time shift from the pulse centre for scaling purposes
    time_offset = time_step*delta_time-pulse_start;
    //Calculate the relative amplitude at the current time for the time pulse
    pulse_scaling = 2/(exp(time_offset*time_factor) + exp(-time_offset*time_factor));

    //Create the carrier wave
    wave = cos(- 2*pi*cnaught/wavelength*delta_time*time_step);

    //Check to see if the source is supposed to be pulsed or Gaussian
    pulse_scaling = pulsed ? pulse_scaling:1.0;
    scaling = gaussian ? scaling:1.0;

    //Calculate the actual Hfield at this location and time step
    Hfield = max_field*pulse_scaling*scaling*wave*sqrt(enaught/munaught);
    return Hfield;
}

//TE Mode
double two_dim::source_Ez(double x, double y, double time_step)
{
    //wz is the beam waist at the specified location
    //wo is the beam waist
    //Zo is the Rayleigh range
    //Efield is the return value
    //scaling is the Gaussian scaling factor
    //wave is the oscillating carrier
    //x_offset is the x shift
    //y_offset is the y shift
    double wz, wo, Zo, Efield, scaling, wave, x_offset, y_offset;
    //pulse_scaling is the time scaling of the field

```

```

//time_factor is the scaling factor for the pulse length
//time_offset is the shift compared to the pulse centre
double pulse_scaling, time_factor, time_offset;

//calculate the beam waist and Rayleigh range
wo = beam_FWHM;
Zo = pi * ref_index((int)x, (int)y)*wo*wo/wavelength;

//Find the x and y shifts
x_offset = (x-source_x)*grid_size;
y_offset = (y-source_y)*grid_size;

//determine the beam diameter at the current location
wz = wo * sqrt(1 + (y_offset*y_offset/(Zo*Zo)));

//calculate the Gaussian spatial distribution of the beam
scaling = wo/wz * exp(- (x_offset*x_offset)/(wz*wz));

//Time scale the pulse to get the proper FWHM
time_factor = 2*log(sqrt(2.0)+1)/pulse_FWHM;
//Calculate the time shift from the pulse centre for scaling purposes
time_offset = time_step*delta_time-pulse_start;
//Calculate the relative amplitude at the current time for the time pulse
pulse_scaling = 2/(exp(time_offset*time_factor) + exp(-time_offset*time_factor));

//The carrier is shifted back by a half time and space step for this wave to
create
//a uni-directional beam
wave = cos(-pi/wavelength*grid_size -
2*pi*cnaught/wavelength*delta_time*(time_step-0.5));

pulse_scaling = pulsed ? pulse_scaling:1.0;
scaling = gaussian ? scaling:1.0;

Efield = max_field*pulse_scaling*scaling*wave;
return Efield;
}

//TM Mode
//Source terms for the TM mode.
double two_dim::source_Hz(double x, double y, double time_step)
{
//wz is the beam waist at the specified location
//wo is the beam waist
//Zo is the Rayleigh range
//Hfield is the return value
//scaling is the Gaussian scaling factor
//wave is the oscillating carrier
//x_offset is the x shift
//y_offset is the y shift
double wz, wo, Zo, Hfield, scaling, wave, x_offset, y_offset;
//pulse_scaling is the time scaling of the field
//time_factor is the scaling factor for the pulse length
//time_offset is the shift compared to the pulse centre
double pulse_scaling, time_factor, time_offset;

//calculate the beam waist and Rayleigh range
wo = beam_FWHM;
Zo = pi * ref_index((int)x, (int)y)*wo*wo/wavelength;

//Find the x and y shifts
x_offset = (x-source_x)*grid_size;
y_offset = (y-source_y)*grid_size;

//determine the beam diameter at the current location
wz = wo * sqrt(1 + (y_offset*y_offset/(Zo*Zo)));

//calculate the Gaussian spatial distribution of the beam
scaling = wo/wz * exp(- (x_offset*x_offset)/(wz*wz));

//Time scale the pulse to get the proper FWHM

```

```

time_factor = 2*log(sqrt(2.0)+1)/pulse_FWHM;
//Calculate the time shift from the pulse centre for scaling purposes
time_offset = time_step*delta_time-pulse_start;
//Calculate the relative amplitude at the current time for the time pulse
pulse_scaling = 2/(exp(time_offset*time_factor) + exp(-time_offset*time_factor));

//The carrier wave for the source
wave = cos(2*pi*cnaught/wavelength*delta_time*time_step);

//Modulate the waveform
pulse_scaling = pulsed ? pulse_scaling:1.0;
scaling = gaussian ? scaling:1.0;
//Magnetic fields need to be scaled properly to the electric fields
Hfield = max_field*pulse_scaling*scaling*wave*sqrt(enaught/munaught);

//Approximate a single-cycle THz pulse
if (single_cycle)
{
    double sigma = beam_FWHM / (2*sqrt(2*log(2.0)));
    double pulse_sigma = pulse_FWHM / (2*sqrt(2*log(2.0)));
    double scaling_factor = 2*exp(-0.5);
    double offset = grid_size * sqrt((x - source_x) * (x - source_x));
    Hfield = sqrt(enaught/munaught)*exp(-0.5*offset*offset/sigma/sigma);
    Hfield*=-2/scaling_factor*(time_offset)/pulse_sigma*exp(-
(time_offset)*(time_offset)
    / (2*pulse_sigma*pulse_sigma));
    //The recovery of the pulse is smaller than the initial spike
    if (Hfield < 0)
    {
        scaling = 0.688;
    }
    else
    {
        scaling = 1.0;
    }
    return -Hfield*scaling;
}
return Hfield;
}

//TM Mode
//The electric field for TM mode solution sources
double two_dim::source_Ex(double x, double y, double time_step)
{
    //wz is the beam waist at the specified location
    //wo is the beam waist
    //Zo is the Rayleigh range
    //Efield is the return value
    //scaling is the Gaussian scaling factor
    //wave is the oscillating carrier
    //x_offset is the x shift
    //y_offset is the y shift
    double wz, wo, Zo, Efield, scaling, wave, x_offset, y_offset;
    //pulse_scaling is the time scaling of the field
    //time_factor is the scaling factor for the pulse length
    //time_offset is the shift compared to the pulse centre
    double pulse_scaling, time_factor,time_offset;

    //calculate the beam waist and Rayleigh range
    wo = beam_FWHM;
    Zo = pi * ref_index((int)x,(int)y)*wo*wo/wavelength;

    //Calculate x and y shifts
    x_offset = (x-source_x)*grid_size;
    y_offset = (y-source_y)*grid_size;

    //determine the beam diameter at the current location
    wz = wo * sqrt(1 + (y_offset*y_offset/(Zo*Zo)));

    //calculate the amplitude of the beam at this specific location
    scaling = wo/wz * exp(- (x_offset*x_offset)/(wz*wz));
}

```

```

//Time scale the pulse to get the proper FWHM
time_factor = 2*log(sqrt(2.0)+1)/pulse_FWHM;
//Calculate the time shift from the pulse centre for scaling purposes
time_offset = time_step*delta_time-pulse_start;
//Calculate the relative amplitude at the current time for the time pulse
pulse_scaling = 2/(exp(time_offset*time_factor) + exp(-time_offset*time_factor));

//One half space and time step in front of the Hz field
wave = cos(-pi/wavelength*grid_size +
2*pi*cnaught/wavelength*delta_time*(time_step+0.5));

//Amplitude modulation
pulse_scaling = pulsed ? pulse_scaling:1.0;
scaling = gaussian ? scaling:1.0;
Efield = max_field*pulse_scaling*scaling*wave;

//Approximate a single-cycle THz pulse
if (single_cycle)
{
    double sigma = beam_FWHM / (2*sqrt(2*log(2.0)));
    double pulse_sigma = pulse_FWHM/(2*sqrt(2*log(2.0)));
    double scaling_factor = 2*exp(-0.5);
    double offset = grid_size * sqrt((x - source_x)*(x - source_x));
    Efield = exp(-0.5*offset*offset/sigma/sigma);

    Efield *= -
2/scaling_factor*(time_offset+0.5*grid_size/cnaught)/pulse_sigma
    * exp( -
(time_offset+0.5*grid_size/cnaught)*(time_offset+0.5*grid_size/cnaught)
/(2*pulse_sigma*pulse_sigma));
    if (Efield < 0)
    {
        scaling = 0.688;
    }
    else
    {
        scaling = 1.0;
    }
    return Efield*scaling;
}
return -Efield;
}

//Return the refractive index of the material at (x,y)
double two_dim::ref_index(int x, int y)
{
    return sqrt(media[x][y]->get_permittivity());
}

//Write a raw binary data file of field_data
void two_dim::write_data(FILE * textfile, double ** field_data)
{
    for (int i = 0; i < x_size; i++)
    {
        for (int j = 0; j < y_size; j++)
        {
            fwrite(&field_data[i][j],sizeof(field_data[i][j]),1,textfile);
        }
    }
}

//Read a raw binary data file into field_data
void two_dim::read_data(FILE * textfile, double ** field_data)
{
    for (int i = 0; i < x_size; i++)
    {
        for (int j = 0; j < y_size; j++)
        {
            fread(&field_data[i][j],sizeof(field_data[i][j]),1,textfile);
        }
    }
}

```

```

    }
}

//Write an ASCII representation of field_data
void two_dim::write_data_text(FILE * outfile, double ** field_data)
{
    for (int i = 0; i < x_size; i++)
    {
        for (int j = 0; j < y_size; j++)
        {
            fprintf(outfile, "%e ", field_data[i][j]);
        }
        fprintf(outfile, "\n");
    }
}

//Read an ASCII file into field_data
void two_dim::read_data_text(FILE * infile, double ** field_data)
{
    for (int i = 0; i < x_size; i++)
    {
        for (int j = 0; j < y_size; j++)
        {
            fscanf(infile, "%e", &field_data[i][j]);
        }
    }
}

//Solve the geometry in TM mode
//Works on parallel processors
void two_dim::TM_solve()
{
    char * filename;
    //Temporary storage for polarization for dispersion model
    double P1X, P1Y, P2X, P2Y, P3X, P3Y;

    filename = new char[200];

    printf("Initializing Media Array.\n");

    //Set up the FDTD coefficients for the PML region
    for (int p = 0; p < PML_width; p++)
    {
        H_Hcoeffs[p] = exp(-Hcond(p)*delta_time/munaught);
        E_Ecoeffs[p] = exp(-Econd(p)*delta_time/enaught);
        H_Ecoeffs[p] = (1-exp(-Hcond(p)*delta_time/munaught))/Hcond(p)/grid_size;
        E_Hcoeffs[p] = (1-exp(-Econd(p)*delta_time/enaught))/Econd(p)/grid_size;
    }

    //Prevent a divide by zero error
    H_Ecoeffs[0] = delta_time/munaught/grid_size;
    //new memory saving material selection
    the_materials = new material[num_material_types];
    //Free Space
    the_materials[FREE_SPACE].set_material(1,1,0,0,0,0,0,0,0,0,0,0,false,false,false);
    //Dispersionless Glass
    the_materials[DISPERSIONLESS_GLASS].set_material(2.25,1,0,0,0,0,0,0,0,0,0,0,false,
false,false);
    //Sapphire/Alumina
    the_materials[ALUMINA].set_material(2.25,1,0,0,1.5039759,0.55069141,6.59273791,7.4
0288E-08,1.21653E-07,2.00722E-05,0,0,true,false,false);
    //Chromium
    the_materials[CHROMIUM].set_material(1,1,0,0,0,0,0,0,0,0,7.0405e15,7.3222e13,true,
true,false);
    //Silver
    the_materials[SILVER].set_material(1,1,0,0,0,0,0,0,0,0,5.66e15,6.301e13,true,true,
false);
    //Gain
    the_materials[GAIN].set_material(1,1,0,0,0,0,0,0,0,0,0,0,true,false,true);
}

```

```

int x = 0; //Do I ever hate VC++6.0

//Initialize all of the variables that need to be initialized
media = new material ** [x_size];
for (x = 0; x < x_size; x++)
{
    media[x] = new material * [y_size];
    for (int y = 0; y < y_size; y++)
    {
        media[x][y] = NULL;
    }
}

for (x = 0; x < x_size; x++)
{
    for (int y = 0; y < y_size; y++)
    {
        media[x][y] = &the_materials[FREE_SPACE];
    }
}

int ** media_type;
media_type = new int * [x_size];

for (x = 0; x < x_size; x++)
{
    media_type[x] = new int [y_size];
    for (int y = 0; y < y_size; y++)
    {
        media_type[x][y] = 0;
    }
}

//Read in the geometry file *NIX based
geometry::read_geometry("../data/geom", media_type);

//Set the pointers to each material type
for (x = 0; x < x_size; x++)
{
    for (int y = 0; y < y_size; y++)
    {
        media[x][y] = &the_materials[media_type[x][y]];
    }
}

//Get rid of the memory spent on the now useless media_type array
for (x = 0; x < x_size; x++)
{
    delete [] media_type[x];
}
delete [] media_type;
media_type = NULL;

//Output the geometry so that it can be checked
geometry::output_geometry("../data/geomout", media);

//Continue allocating memory and initializing variables
printf("Allocated memory.\n");
printf("Initializing Field Arrays.\n");
Ex = new double *[x_size];
Ey = new double *[x_size];
Et = new double *[x_size];

Ex_prev = new double *[x_size];
Ey_prev = new double *[x_size];

Dx = new double *[x_size];
Dx_prev = new double *[x_size];
Dx_prev_prev = new double *[x_size];
Dy = new double *[x_size];
Dy_prev = new double *[x_size];

```

```

Dy_prev_prev = new double *[x_size];

Hz = new double *[x_size];
Hxz = new double *[x_size];
Hzy = new double *[x_size];

/*
P1X_prev = new double * [x_size];
P1Y_prev = new double * [x_size];
P2X_prev = new double * [x_size];
P2Y_prev = new double * [x_size];
P3X_prev = new double * [x_size];
P3Y_prev = new double * [x_size];

P1X_prev_prev = new double * [x_size];
P1Y_prev_prev = new double * [x_size];
P2X_prev_prev = new double * [x_size];
P2Y_prev_prev = new double * [x_size];
P3X_prev_prev = new double * [x_size];
P3Y_prev_prev = new double * [x_size];*/

Pgainx = new double *[x_size];
Pgainy = new double *[x_size];

Pgain_prevx = new double *[x_size];
Pgain_prevy = new double *[x_size];

N0 = new double *[x_size];
N1 = new double *[x_size];
N2 = new double *[x_size];
N3 = new double *[x_size];

N0_prev = new double *[x_size];
N1_prev = new double *[x_size];
N2_prev = new double *[x_size];
N3_prev = new double *[x_size];

pump_rate = new double *[x_size];

Hzp = new double *[x_size];
Hzxp = new double *[x_size];
Hzyp = new double *[x_size];
Exp = new double *[x_size];
Eyp = new double *[x_size];
Ex_prevp = new double *[x_size];
Ey_prevp = new double *[x_size];
Etp = new double *[x_size];
Dxp = new double *[x_size];
Dyp = new double *[x_size];
Dx_prevp = new double *[x_size];
Dy_prevp = new double *[x_size];
Dx_prev_prevp = new double *[x_size];
Dy_prev_prevp = new double *[x_size];

for (x = 0; x < x_size; x++)
{
    Ex[x] = new double [y_size];
    Ex_prev[x] = new double [y_size];
    Ey[x] = new double [y_size];
    Ey_prev[x] = new double [y_size];

    Et[x] = new double [y_size];

    Dx[x] = new double [y_size];
    Dx_prev[x] = new double [y_size];
    Dx_prev_prev[x] = new double [y_size];
    Dy[x] = new double [y_size];
    Dy_prev[x] = new double [y_size];
    Dy_prev_prev[x] = new double [y_size];

    Hz[x] = new double [y_size];
    Hxz[x] = new double [y_size];

```

```

Hzy[x] = new double [y_size];

/*
P1X_prev[x] = new double [y_size];
P1Y_prev[x] = new double [y_size];
P2X_prev[x] = new double [y_size];
P2Y_prev[x] = new double [y_size];
P3X_prev[x] = new double [y_size];
P3Y_prev[x] = new double [y_size];

P1X_prev_prev[x] = new double [y_size];
P1Y_prev_prev[x] = new double [y_size];
P2X_prev_prev[x] = new double [y_size];
P2Y_prev_prev[x] = new double [y_size];
P3X_prev_prev[x] = new double [y_size];
P3Y_prev_prev[x] = new double [y_size];*/

Pgainx[x] = new double [y_size];
Pgainy[x] = new double [y_size];

Pgain_prevx[x] = new double [y_size];
Pgain_prevy[x] = new double [y_size];

N0[x] = new double [y_size];
N1[x] = new double [y_size];
N2[x] = new double [y_size];
N3[x] = new double [y_size];

N0_prev[x] = new double [y_size];
N1_prev[x] = new double [y_size];
N2_prev[x] = new double [y_size];
N3_prev[x] = new double [y_size];

pump_rate[x] = new double [y_size];

Hzp[x] = new double [y_size];
Hzxp[x] = new double [y_size];
Hzyp[x] = new double [y_size];
Exp[x] = new double [y_size];
Eyp[x] = new double [y_size];
Ex_prevp[x] = new double [y_size];
Ey_prevp[x] = new double [y_size];
Etp[x] = new double [y_size];
Dxp[x] = new double [y_size];
Dyp[x] = new double [y_size];
Dx_prevp[x] = new double [y_size];
Dy_prevp[x] = new double [y_size];
Dx_prev_prevp[x] = new double [y_size];
Dy_prev_prevp[x] = new double [y_size];
}

printf("Allocated Field Memory.\n");
printf("Initializing Field Components\n");

for (x = 0; x < x_size; x++)
{
    for (int y = 0; y < y_size; y++)
    {
        Ex[x][y] = 0;
        Ey[x][y] = 0;
        Et[x][y] = 0;

        Ex_prev[x][y] = 0;
        Ey_prev[x][y] = 0;

        Dx[x][y] = 0;
        Dx_prev[x][y] = 0;
        Dx_prev_prev[x][y] = 0;
        Dy[x][y] = 0;
        Dy_prev[x][y] = 0;
        Dy_prev_prev[x][y] = 0;
    }
}

```

```

        Hz[x][y] = 0;
        Hzx[x][y] = 0;
        Hzy[x][y] = 0;

/*
        P1X_prev[x][y] = 0;
        P1Y_prev[x][y] = 0;
        P2X_prev[x][y] = 0;
        P2Y_prev[x][y] = 0;
        P3X_prev[x][y] = 0;
        P3Y_prev[x][y] = 0;

        P1X_prev_prev[x][y] = 0;
        P1X_prev_prev[x][y] = 0;
        P2X_prev_prev[x][y] = 0;
        P2Y_prev_prev[x][y] = 0;
        P3X_prev_prev[x][y] = 0;
        P3Y_prev_prev[x][y] = 0;*/

        Pgainx[x][y] = 0;
        Pgainy[x][y] = 0;

        Pgain_prevx[x][y] = 0;
        Pgain_prevy[x][y] = 0;

        N0[x][y] = N0_start;
        N1[x][y] = N1_start;
        N2[x][y] = N2_start;
        N3[x][y] = N3_start;

        N0_prev[x][y] = N0_start;
        N1_prev[x][y] = N1_start;
        N2_prev[x][y] = N2_start;
        N3_prev[x][y] = N3_start;

        pump_rate[x][y] = 0;

        Hzp[x][y] = 0;
        Hzxp[x][y] = 0;
        Hzyp[x][y] = 0;
        Exp[x][y] = 0;
        Eyp[x][y] = 0;
        Ex_prevp[x][y] = 0;
        Ey_prevp[x][y] = 0;
        Etp[x][y] = 0;
        Dxp[x][y] = 0;
        Dyp[x][y] = 0;
        Dx_prevp[x][y] = 0;
        Dy_prevp[x][y] = 0;
        Dx_prev_prevp[x][y] = 0;
        Dy_prev_prevp[x][y] = 0;
    }

    //Every grid point gets a random laser source
    num_sources = x_size*y_size;///(source_spacing*source_spacing);

    source_wavelength = new double * [x_size];

    for (x = 0; x < x_size; x++)
    {
        source_wavelength[x] = new double [y_size];
    }
    for (x = 0; x < x_size; x++)
    {
        for (int y = 0; y < y_size; y++)
        {
            source_wavelength[x][y] = -1;//Negative numbers means that no
source is in this location
        }
    }
}

```

```

if (!reload)//Start a fresh simulation
{
    //Create the random distribution of random laser sources
    for (x = PML_width; x < x_size-PML_width; x++)
    {
        for (int y = PML_width; y < y_size-PML_width; y++)
        {
            if (media[x][y]->is_gain())
            {
                double value, mu, temp;
                do
                {
                    mu = get_rand(cnaught/1000e-9,cnaught/200e-
9);
                    value = real_rand();
                    temp = lorentzian(mu);
                } while (value > temp);

                double lambda = cnaught/mu;

                source_wavelength[x][y] = lambda;
            }
            if (source_wavelength[x][y] < 0)
            {
                Et[x][y] = 0;
            }
            else
            {
                Et[x][y] = 1;
            }
        }
    }
    //Create files containing the source wavelength distribution
    sprintf(filename, "./data/source_locations_check.txt");
    FILE * outfile;
    outfile = fopen(filename, "wb");
    write_data(outfile, Et);
    fclose(outfile);

    sprintf(filename, "./data/wavelength_data.txt");
    outfile = fopen(filename, "w+");
    write_data_text(outfile, source_wavelength);
    fclose(outfile);

    sprintf(filename, "./check/wavelength_data.txt");
    outfile = fopen(filename, "wb");
    write_data(outfile, source_wavelength);
    fclose(outfile);
}
else//Reloading from a checkpointed state
{
    FILE * wavelength_file;
    wavelength_file = fopen("./check/wavelength_data.txt", "rb");
    read_data(wavelength_file, source_wavelength);

    for (x = 0; x < x_size; x++)
    {
        for (int y = 0; y < y_size; y++)
        {
            if (source_wavelength[x][y] < 0)
            {
                Et[x][y] = 0;
            }
            else
            {
                Et[x][y] = 1;
            }
        }
    }
    fclose(wavelength_file);
}

```

```

        sprintf(filename, "./check/source_locations.txt");
        FILE * outfile;
        outfile = fopen(filename, "w+");
        write_data_text(outfile, Et);
        fclose(outfile);

        sprintf(filename, "./check/wavelength_data_check.txt");
        outfile = fopen(filename, "wb");
        write_data(outfile, source_wavelength);
        fclose(outfile);
    }

    printf("Field Components Initialized\n");

    printf("Beginning FDTD Computations.\n");

    //Files for various data output tasks
    FILE * fieldoutput, * point_output, * vector_output;
    /*fieldoutput = fopen("./data/output_point.txt", "w+");
    integrate_output = fopen("./data/output_line.txt", "w+");*/
    fieldoutput = fopen("./data/output_count.txt", "a");
    vector_output = fopen("./data/output_field.txt", "a");
    point_output = fopen("./data/output_point.txt", "a");

#ifdef PARALLELIZE
    #if defined (_OPENMP)
    //    printf("Threads are defined\n");
    omp_set_num_threads(NUM_THREADS);
    #endif
#endif

    int start_n = 0;
    if (!reload)
    {
        start_n = 0;
    }
    else//Reload from the last check point
    {
        //Read in all of the data
        //the order of these reads from the raw binary data file must be completed
        //by a machine using the same bit order, word size, and the order must not
be changed
        //or the results will be meaningless
        FILE * check_data_file, * check_data;

        check_data_file = fopen("./check/check_data.txt", "r");
        fscanf(check_data_file, "%d", &start_n);

        fclose(check_data_file);

        check_data = fopen("./check/check_fields.txt", "rb");

        read_data(check_data, Ex);
        read_data(check_data, Ey);
        read_data(check_data, Et);

        read_data(check_data, Ex_prev);
        read_data(check_data, Ey_prev);

        read_data(check_data, Dx);
        read_data(check_data, Dx_prev);
        read_data(check_data, Dx_prev_prev);
        read_data(check_data, Dy);
        read_data(check_data, Dy_prev);
        read_data(check_data, Dy_prev_prev);

        read_data(check_data, Hz);
        read_data(check_data, Hzx);
        read_data(check_data, Hzy);

        read_data(check_data, Pgainx);
        read_data(check_data, Pgainy);

```

```

read_data(check_data, Pgain_prevx);
read_data(check_data, Pgain_prevy);

read_data(check_data, N0);
read_data(check_data, N1);
read_data(check_data, N2);
read_data(check_data, N3);

read_data(check_data, N0_prev);
read_data(check_data, N1_prev);
read_data(check_data, N2_prev);
read_data(check_data, N3_prev);

read_data(check_data, pump_rate);

read_data(check_data, Hzp);
read_data(check_data, Hzxp);
read_data(check_data, Hzyp);
read_data(check_data, Exp);
read_data(check_data, Eyp);
read_data(check_data, Ex_prevp);
read_data(check_data, Ey_prevp);
read_data(check_data, Etp);
read_data(check_data, Dxp);
read_data(check_data, Dyp);
read_data(check_data, Dx_prevp);
read_data(check_data, Dy_prevp);
read_data(check_data, Dx_prev_prevp);
read_data(check_data, Dy_prev_prevp);

fclose(check_data);
}

int check_set = 0; //select which of the two checkpoints to save

for (int n = start_n; n < time_steps; n++)
{
printf("Done %f %s\n", (double)(100*n)/time_steps, "%");
if (n % check_space == 0) //Saving the current checkpoint state
{
FILE * check_data, * check_data_file;
//Select the correct checkpoint file to save
if (check_set == 1)
{
check_set = 0;
check_data_file = fopen("./check/check_data_1.txt", "w+");
check_data = fopen("./check/check_fields_1.txt", "wb");
}
else
{
check_set = 1;
check_data_file = fopen("./check/check_data_0.txt", "w+");
check_data = fopen("./check/check_fields_0.txt", "wb");
}

fprintf(check_data_file, "%d\n", n);
fclose(check_data_file);
//Save the checkpoint. Do not change the order here without changing the order of
reading

write_data(check_data, Ex);
write_data(check_data, Ey);
write_data(check_data, Et);

write_data(check_data, Ex_prev);
write_data(check_data, Ey_prev);

write_data(check_data, Dx);
write_data(check_data, Dx_prev);
write_data(check_data, Dx_prev_prev);
write_data(check_data, Dy);
}
}

```

```

        write_data(check_data, Dy_prev);
        write_data(check_data, Dy_prev_prev);

        write_data(check_data, Hz);
        write_data(check_data, Hzx);
        write_data(check_data, Hzy);

        write_data(check_data, Pgainx);
        write_data(check_data, Pgainy);

        write_data(check_data, Pgain_prevx);
        write_data(check_data, Pgain_prevy);

        write_data(check_data, N0);
        write_data(check_data, N1);
        write_data(check_data, N2);
        write_data(check_data, N3);

        write_data(check_data, N0_prev);
        write_data(check_data, N1_prev);
        write_data(check_data, N2_prev);
        write_data(check_data, N3_prev);

        write_data(check_data, pump_rate);

        write_data(check_data, Hzp);
        write_data(check_data, Hzxp);
        write_data(check_data, Hzyp);
        write_data(check_data, Exp);
        write_data(check_data, Eyp);
        write_data(check_data, Ex_prevp);
        write_data(check_data, Ey_prevp);
        write_data(check_data, Etp);
        write_data(check_data, Dxp);
        write_data(check_data, Dyp);
        write_data(check_data, Dx_prevp);
        write_data(check_data, Dy_prevp);
        write_data(check_data, Dx_prev_prevp);
        write_data(check_data, Dy_prev_prevp);

        fclose(check_data);
    }
//
// double tot_Ex_start, tot_Ey_start, tot_Et_start, tot_Hz_start,
//      tot_Ex_end, tot_Ey_end, tot_Et_end, tot_Hz_end;
/*
tot_Ex_start = integrate(first_line_y, Ex);
tot_Ey_start = integrate(first_line_y, Ey);
tot_Et_start = integrate(first_line_y, Et);
tot_Hz_start = integrate(first_line_y, Hz);
tot_Ex_end = integrate(second_line_y, Ex);
tot_Ey_end = integrate(second_line_y, Ey);
tot_Et_end = integrate(second_line_y, Et);
tot_Hz_end = integrate(second_line_y, Hz);*/
/*
fprintf(integrate_output, "%e %e %e %e %e %e %e %e %e %e\n", n*delta_time,
tot_Ex_start,
        tot_Ey_start, tot_Et_start, tot_Hz_start, tot_Ex_end, tot_Ey_end,
        tot_Et_end, tot_Hz_end);

fprintf(fieldoutput, "%e %e %e %e %e %e
%e\n", n*delta_time, Ex[x_size/2][first_line_y],
        Ey[x_size/2][first_line_y], Hz[x_size/2][first_line_y],
        Ex[x_size/2][second_line_y], Ey[x_size/2][second_line_y],
        Hz[x_size/2][second_line_y]);*/
int tempnum = y_size/10;
//Output the magnetic fields at 10 points along the centre of the simulation space
fprintf(vector_output, "%e %e %e %e %e %e %e %e %e %e %e\n", n*delta_time,
        Hz[x_size/2][tempnum], Hz[x_size/2][tempnum*2],
        Hz[x_size/2][tempnum*3], Hz[x_size/2][tempnum*4],
        Hz[x_size/2][tempnum*5], Hz[x_size/2][tempnum*6],
        Hz[x_size/2][tempnum*7], Hz[x_size/2][tempnum*8],

```

```

        Hz[x_size/2][tempnum*9], Hz[x_size/2][tempnum*10]);

//Output gain model information at the centre of the geometry
        fprintf(fieldoutput, "%e %e %e %e %e %e %e %e %e %e\n", n*delta_time, Et[x_size/2][y_size/2],

                N0[x_size/2][y_size/2], N1[x_size/2][y_size/2], N2[x_size/2][y_size/2],

                N3[x_size/2][y_size/2], Pgainx[x_size/2][y_size/2], Pgainy[x_size/2][y_size/2]);

//Output field quantities at the centre of the geometry
        fprintf(point_output, "%e %e %e %e %e %e %e %e %e %e\n", n*delta_time, Et[x_size/2][y_size/2],

                Ex[x_size/2][y_size/2], Ey[x_size/2][y_size/2],

                Hz[x_size/2][y_size/2], pump_rate[x_size/2][y_size/2]);

        //Check if it's time to write an output file
        if (n % file_spacing == 0)
        {
                if (text_output)
                {
                        FILE * outfile;
                        sprintf(filename, "./data/%6.0d_data_pump.txt", n);
                        outfile = fopen(filename, "wb");
                        write_data(outfile, Etp);
                        fclose(outfile);
                        sprintf(filename, "./data/%6.0d_data.txt", n);
                        outfile = fopen(filename, "wb");
                        write_data(outfile, Et);
                        fclose(outfile);
                }
        }

//The program option to allow the OPENMP compiler to handle multiple threads.
#ifdef PARALLELIZE
#pragma omp parallel for default(none) shared(n) private(P1X, P2X, P3X, P1Y, P2Y, P3Y)
#endif

//Beginning of E_FIELD_SECTION
//Includes only code that calculates the electric fields
for (int x = 0; x < x_size; x++)
{
        for (int y = 0; y < y_size; y++)
        {
                //Check to see if we are in a boundary
                if (x < PML_width || y < PML_width || x >= x_size-PML_width
|| y >= y_size-PML_width)
                {
                        double E_Ecoeff_X, E_Hcoeff_X, E_Ecoeff_Y,
E_Hcoeff_Y;
//There are 4 edges and 8 corners
//The default coefficients for any surface that doesn't show up in the rest of the
//overlapping regions

                        E_Hcoeff_X = media[x][y]->E_Hcoeff();
                        E_Ecoeff_X = media[x][y]->E_Ecoeff();

                        E_Hcoeff_Y = E_Hcoeff_X;
                        E_Ecoeff_Y = E_Ecoeff_X;

//Set the FDTD coefficients for the PML region
int temp = 0;
if (x < PML_width)
{
                //In the left edge
                temp = PML_width - x - 1;
                E_Hcoeff_Y = E_Hcoeffs[temp];
                E_Ecoeff_Y = E_Ecoeffs[temp];
}
if (y < PML_width)
{
                //In the bottom edge
                temp = PML_width - y - 1;
                E_Hcoeff_X = E_Hcoeffs[temp];
}
}
}
}

```

```

        E_Ecoeff_X = E_Ecoeffs[temp];
    }
    if (x >= x_size-PML_width)
    {
        //In the right edge
        temp = x - x_size + PML_width;
        E_Hcoeff_Y = E_Hcoeffs[temp];
        E_Ecoeff_Y = E_Ecoeffs[temp];
    }
    if (y >= y_size-PML_width)
    {
        //In the top edge
        temp = y - y_size + PML_width;
        E_Hcoeff_X = E_Hcoeffs[temp];
        E_Ecoeff_X = E_Ecoeffs[temp];
    }
}

//EM field calculations

//The FDTD equations for the PML are below
double temp_Hz;

temp_Hz = y == y_size-1 ? 0.0:Hz[x][y+1];
Ex[x][y] = E_Ecoeff_X*Ex[x][y]
           - E_Hcoeff_X * (Hz[x][y] - temp_Hz);

temp_Hz = x == x_size-1 ? 0.0:Hz[x+1][y];
Ey[x][y] = E_Ecoeff_Y*Ey[x][y]
           - E_Hcoeff_Y * (temp_Hz - Hz[x][y]);

//Beginning of code block to handle pumping
temp_Hz = y == y_size-1 ? 0.0:Hzp[x][y+1];
Exp[x][y] = E_Ecoeff_X*Exp[x][y]
            - E_Hcoeff_X * (Hzp[x][y] - temp_Hz);

temp_Hz = x == x_size-1 ? 0.0:Hzp[x+1][y];
Eyp[x][y] = E_Ecoeff_Y*Eyp[x][y]
            - E_Hcoeff_Y * (temp_Hz - Hzp[x][y]);

//End of first pump block
}
else//We are not in a boundary, so calculate a normal FDTD
timestep
{
    double E_Ecoeff, E_Hcoeff;
    //Temporary storage for the original values before

    //for this time step
    double temp_Ex = Ex[x][y];
    double temp_Ey = Ey[x][y];
    double temp_Exp = Exp[x][y];
    double temp_Eyp = Eyp[x][y];
    double temp_N0, temp_N1, temp_N2, temp_N3,

temp_Pgainx, temp_Pgainy;

    //The incident fields from the source
    double Hzinc = 0.0;
    double Hzincp = 0.0;

    double denominator = 0.0;
    double a1, a2, a3, c1, c2, c3, g1, g2, g3;
    double K1X, K2X, K3X;
    double K1Y, K2Y, K3Y;
    double m1, m2, m3, m4;
    a1 = 0;
    a2 = 0;
    a3 = 0;
    c1 = 0;
    c2 = 0;
    c3 = 0;
}

```

```

g1 = 0;
g2 = 0;
g3 = 0;
m1 = 0;
m2 = 0;
m3 = 0;
m4 = 0;
Hzinc = 0.0;
Hzincp = 0.0;

//Get the source field if this coordinate is on the
source line
if (y == source_y)
{
    Hzincp = source_Hz(x,y,n);
}

//Calculate the displacement via the update
equations for both the fluorescence
//and pump field
Dxp[x][y] = Dxp[x][y] +
delta_time/grid_size*(Hzp[x][y+1] - Hzp[x][y] - Hzincp);
Dx[x][y] = Dx[x][y] +
delta_time/grid_size*(Hz[x][y+1] - Hz[x][y] - Hzinc);

Dyp[x][y] = Dyp[x][y] +
delta_time/grid_size*(Hzp[x][y] - Hzp[x+1][y]);
Dy[x][y] = Dy[x][y] +
delta_time/grid_size*(Hz[x][y] - Hz[x+1][y]);

//Check if the material is dispersive
if (media[x][y]->is_dispersive())
{
    //Check if it is a gain material
    if (media[x][y]->is_gain())
    {
        //Constants for the gain model
        double a1, d1, c2, d2, b3, c3, a4,
b4, e1, h1, g2, h2, i2, f3, g3, i3, e4, f4;

        double K1, K2, K3, K4;//, K5;
        double q1, q2, q3;
        double energy = 0.0;//related to the
intensity of the the EM field at this point

        //Get a relative amount of atoms that
are pumped to the highest energy level
        //according to the intensity of the
pump field
        energy = media[x][y]-
>get_permittivity()*enaught*(Exp[x][y]*Exp[x][y] + Eyp[x][y]*Eyp[x][y])/2
+ media[x][y]-
>get_permeability()*munaught*(Hzp[x][y]*Hzp[x][y])/2;

        double B04 = 1;
        pump_rate[x][y] =
energy/(hbar*omega_a)*B04;//Approximate the pump rate

        //Calculate the constatsns that are
dependent on the pump rate
        a1 = -
delta_time*pump_rate[x][y]*tau_32;
        a4 = tau_10 +
delta_time*pump_rate[x][y]*tau_10;

        e1 =
delta_time*pump_rate[x][y]*tau_32;
        e4 = tau_10 -
delta_time*pump_rate[x][y]*tau_10;

        //Obtain the material constants for
this gain media

```

```

q1 = media[x][y]->get_q1();
q2 = media[x][y]->get_q2();
q3 = media[x][y]->get_q3();

//
a1 = media[x][y]->get_a1();
d1 = media[x][y]->get_d1();
c2 = media[x][y]->get_c2();
d2 = media[x][y]->get_d2();
b3 = media[x][y]->get_b3();
c3 = media[x][y]->get_c3();
//
a4 = media[x][y]->get_a4();
b4 = media[x][y]->get_b4();

//
e1 = media[x][y]->get_e1();
h1 = media[x][y]->get_h1();
g2 = media[x][y]->get_g2();
h2 = media[x][y]->get_h2();
i2 = media[x][y]->get_i2();
f3 = media[x][y]->get_f3();
g3 = media[x][y]->get_g3();
i3 = media[x][y]->get_i3();
e4 = media[x][y]->get_e4();
f4 = media[x][y]->get_f4();

//Save the current values
temp_N0 = N0[x][y];
temp_N1 = N1[x][y];
temp_N2 = N2[x][y];
temp_N3 = N3[x][y];
temp_Pgainx = Pgainx[x][y];
temp_Pgainy = Pgainy[x][y];

//Calculate the new polarization
Pgainx[x][y] = (4*Pgainx[x][y] +
q1*Pgain_prevx[x][y] + q2*(N1[x][y] - N2[x][y])*Ex[x][y]) / q3;
Pgainy[x][y] = (4*Pgainy[x][y] +
q1*Pgain_prevy[x][y] + q2*(N1[x][y] - N2[x][y])*Ey[x][y]) / q3;

//Determine the electric field using
the displacement and the polarization
Pgainx[x][y];
Pgainy[x][y];
Ex[x][y] = (1.0/enaught)*(Dx[x][y] -
Ey[x][y] = (1.0/enaught)*(Dy[x][y] -

//Calculate the new population levels
K1 = N0_prev[x][y] * e1 + N3_prev[x][y]
* h1;
K2 = N2_prev[x][y] * g2 + N3_prev[x][y]
* h2 + Ex[x][y]*(Pgainx[x][y] - Pgain_prevx[x][y])*i2 + Ey[x][y]*(Pgainy[x][y] -
Pgain_prevy[x][y])*i2;
K3 = N1_prev[x][y] * f3 +
N2_prev[x][y] * g3 + Ex[x][y]*(Pgainx[x][y] - Pgain_prevx[x][y])*i3 +
Ey[x][y]*(Pgainy[x][y] - Pgain_prevy[x][y])*i3;
K4 = N0_prev[x][y] * e4 +
N1_prev[x][y] * f4;

N0[x][y] = b4*d2*c3/(a1*b4*d2*c3-
a4*b3*d1*c2)*K1-b4*d1*c3/(a1*b4*d2*c3-a4*b3*d1*c2)*K2+b4*d1*c2/(a1*b4*d2*c3-
a4*b3*d1*c2)*K3-b3*d1*c2/(a1*b4*d2*c3-a4*b3*d1*c2)*K4;
N1[x][y] = -a4*d2*c3/(a1*b4*d2*c3-
a4*b3*d1*c2)*K1+a4*d1*c3/(a1*b4*d2*c3-a4*b3*d1*c2)*K2-a4*d1*c2/(a1*b4*d2*c3-
a4*b3*d1*c2)*K3+a1*d2*c3/(a1*b4*d2*c3-a4*b3*d1*c2)*K4;
N2[x][y] = a4*d2*b3/(a1*b4*d2*c3-
a4*b3*d1*c2)*K1-a4*d1*b3/(a1*b4*d2*c3-a4*b3*d1*c2)*K2+a1*d2*b4/(a1*b4*d2*c3-
a4*b3*d1*c2)*K3-a1*d2*b3/(a1*b4*d2*c3-a4*b3*d1*c2)*K4;
N3[x][y] = -a4*c2*b3/(a1*b4*d2*c3-
a4*b3*d1*c2)*K1+a1*c3*b4/(a1*b4*d2*c3-a4*b3*d1*c2)*K2-a1*c2*b4/(a1*b4*d2*c3-
a4*b3*d1*c2)*K3+a1*c2*b3/(a1*b4*d2*c3-a4*b3*d1*c2)*K4;

//Clamp the population levels

```

```

if (N0[x][y] < 0)
{
    N0[x][y] = 0;
}
if (N1[x][y] < 0)
{
    N1[x][y] = 0;
}
if (N2[x][y] < 0)
{
    N2[x][y] = 0;
}
if (N3[x][y] < 0)
{
    N3[x][y] = 0;
}

//Begin pump section to calculat the pump field without the influence of the gain
material

E_Ecoeff = media[x][y]->E_Ecoeff();
E_Hcoeff = media[x][y]->E_Hcoeff();
Exp[x][y] = E_Ecoeff*Exp[x][y]
            + E_Hcoeff*(Hzp[x][y+1] -
Hzp[x][y] - Hzincp);

Eyp[x][y] = E_Ecoeff*Eyp[x][y]
            + E_Hcoeff*(Hzp[x][y] -
Hzp[x+1][y]);
//End pump section

}
//Check if it's a metal
else if (media[x][y]->is_metal())
{
    //Get the material constants
    m1 = media[x][y]->get_m1();
    m2 = media[x][y]->get_m2();
    m3 = media[x][y]->get_m3();
    m4 = media[x][y]->get_m4();

    //Calculate the electric field from
    Ex[x][y] = (m1*Dx[x][y] -
                + 4*enaught*media[x][y]-
                - m3*Ex_prev[x][y]) / m4;
    Ey[x][y] = (m1*Dy[x][y] -
                + 4*enaught*media[x][y]-
                - m3*Ey_prev[x][y]) / m4;
    Exp[x][y] = (m1*Dxp[x][y] -
                + 4*enaught*media[x][y]-
                - m3*Exp_prevp[x][y]) / m4;
    Eyp[x][y] = (m1*Dyp[x][y] -
                + 4*enaught*media[x][y]-
                - m3*Eyp_prevp[x][y]) / m4;
}
else
{
    //If dispersive, but not a metal or
gain media, then it's a dispersive dielectric

```

```

the Sellmeier equation

//get the constants for the ADE for
a1 = media[x][y]->get_x1();
a2 = media[x][y]->get_x2();
a3 = media[x][y]->get_x3();
c1 = media[x][y]->get_y1();
c2 = media[x][y]->get_y2();
c3 = media[x][y]->get_y3();
g1 = media[x][y]->get_z1();
g2 = media[x][y]->get_z2();
g3 = media[x][y]->get_z3();

denominator = -a1*a2*a3 + a1*c2*c3 +
c2*c1*a3 - 2*c2*c1*c3 + c3*c1*a2;

//Calculate the polarizations
K1X = c1*(Dx[x][y] +
+ 4*P1X_prev[x][y] +
g1*P1X_prev_prev[x][y]);
K2X = c2*(Dx[x][y] +
+ 4*P2X_prev[x][y] +
g2*P2X_prev_prev[x][y]);
K3X = c3*(Dx[x][y] +
+ 4*P3X_prev[x][y] +
g3*P3X_prev_prev[x][y]);
K1Y = c1*(Dy[x][y] +
+ 4*P1Y_prev[x][y] +
g1*P1Y_prev_prev[x][y]);
K2Y = c2*(Dy[x][y] +
+ 4*P2Y_prev[x][y] +
g2*P2Y_prev_prev[x][y]);
K3Y = c3*(Dy[x][y] +
+ 4*P3Y_prev[x][y] +
g3*P3Y_prev_prev[x][y]);

P1X = (-a2*a3+c2*c3)/denominator*K1X-
c1*(-a3+c3)/denominator*K2X-c1*(c2-a2)/denominator*K3X;
P2X = -c2*(-a3+c3)/denominator*K1X-
(a1*a3-c1*c3)/denominator*K2X+c2*(a1-c1)/denominator*K3X;
P3X = -c3*(c2-
a2)/denominator*K1X+c3*(a1-c1)/denominator*K2X-(a1*a2-c1*c2)/denominator*K3X;
P1Y = (-a2*a3+c2*c3)/denominator*K1Y-
c1*(-a3+c3)/denominator*K2Y-c1*(c2-a2)/denominator*K3Y;
P2Y = -c2*(-a3+c3)/denominator*K1Y-
(a1*a3-c1*c3)/denominator*K2Y+c2*(a1-c1)/denominator*K3Y;
P3Y = -c3*(c2-
a2)/denominator*K1Y+c3*(a1-c1)/denominator*K2Y-(a1*a2-c1*c2)/denominator*K3Y;

//Determine the electric fields
Ex[x][y] = (1.0/enaught)*(Dx[x][y] -
P1X - P2X - P3X);
Ey[x][y] = (1.0/enaught)*(Dy[x][y] -
P1Y - P2Y - P3Y);
}
else
{

```

```

normal FDTD update equations apply

//It's not a dispersive material, and the
E_Ecoeff = media[x][y]->E_Ecoeff();
E_Hcoeff = media[x][y]->E_Hcoeff();
P1X = 0;
P2X = 0;
P3X = 0;
P1Y = 0;
P2Y = 0;
P3Y = 0;

Ex[x][y] = E_Ecoeff*Ex[x][y]
          + E_Hcoeff*(Hz[x][y+1] - Hz[x][y] -
Hzinc);

Ey[x][y] = E_Ecoeff*Ey[x][y]
          + E_Hcoeff*(Hz[x][y] - Hz[x+1][y]);

//Begin pump section
Exp[x][y] = E_Ecoeff*Exp[x][y]
          + E_Hcoeff*(Hzp[x][y+1] - Hzp[x][y] -
Hzincp);

Eyp[x][y] = E_Ecoeff*Eyp[x][y]
          + E_Hcoeff*(Hzp[x][y] - Hzp[x+1][y]);

//End pump section
}
//Store the previous time step's values
N0_prev[x][y] = temp_N0;
N1_prev[x][y] = temp_N1;
N2_prev[x][y] = temp_N2;
N3_prev[x][y] = temp_N3;

Pgain_prevx[x][y] = temp_Pgainx;
Pgain_prevy[x][y] = temp_Pgainy;

Ex_prev[x][y] = temp_Ex;
Ey_prev[x][y] = temp_Ey;

Ex_prevp[x][y] = temp_Exp;
Ey_prevp[x][y] = temp_Eyp;

Dx_prev_prev[x][y] = Dx_prev[x][y];
Dx_prev[x][y] = Dx[x][y];
Dy_prev_prev[x][y] = Dy_prev[x][y];
Dy_prev[x][y] = Dy[x][y];

Dx_prev_prevp[x][y] = Dx_prevp[x][y];
Dx_prevp[x][y] = Dxp[x][y];
Dy_prev_prevp[x][y] = Dy_prevp[x][y];
Dy_prevp[x][y] = Dyp[x][y];

/*
P1X_prev_prev[x][y] = P1X_prev[x][y];
P2X_prev_prev[x][y] = P2X_prev[x][y];
P3X_prev_prev[x][y] = P3X_prev[x][y];

P1X_prev[x][y] = P1X;
P2X_prev[x][y] = P2X;
P3X_prev[x][y] = P3X;

P1Y_prev_prev[x][y] = P1Y_prev[x][y];
P2Y_prev_prev[x][y] = P2Y_prev[x][y];
P3Y_prev_prev[x][y] = P3Y_prev[x][y];

P1Y_prev[x][y] = P1Y;
P2Y_prev[x][y] = P2Y;
P3Y_prev[x][y] = P3Y;*/
} //end of FDTD calcs
//Calculate the magnitude of the electric field
Et[x][y] = sqrt(Ex[x][y]*Ex[x][y] + Ey[x][y]*Ey[x][y]);
Etp[x][y] = sqrt(Exp[x][y]*Exp[x][y] +
Eyp[x][y]*Eyp[x][y]);

```

```

        } //end of y
    } //end of x
//End of E_FIELD_SECTION

    //Beginning of M_FIELD_SECTION
    //Only includes sections of the FDTD model that modify the magnetic field
#ifdef PARALLELIZE
#pragma omp parallel for default(none) shared(n) //private(P1X, P2X, P3X, P1Y, P2Y, P3Y)
#endif
    for (int x = 0; x < x_size; x++)
    {
        for (int y = 0; y < y_size; y++)
        {
            //Check to see if we are in a boundary
            if (x < PML_width || y < PML_width || x >= x_size-PML_width
|| y >= y_size-PML_width)
            {
                double H_Hcoeff_Y, H_Ecoeff_Y, H_Hcoeff_X,
H_Ecoeff_X;
                //There are 4 edges and 8 corners
                //The default coefficients for any surface that doesn't show up in the rest of the
                //overlapping regions

                H_Hcoeff_X = media[x][y]->H_Hcoeff();
                H_Ecoeff_X = media[x][y]->H_Ecoeff();

                H_Hcoeff_Y = H_Hcoeff_X;
                H_Ecoeff_Y = H_Ecoeff_X;

                int temp = 0;
                if (x < PML_width)
                {
                    //In the left edge
                    temp = PML_width - x - 1;
                    H_Hcoeff_X = H_Hcoeffs[temp];
                    H_Ecoeff_X = H_Ecoeffs[temp];
                }
                if (y < PML_width)
                {
                    //In the bottom edge
                    temp = PML_width - y - 1;
                    H_Hcoeff_Y = H_Hcoeffs[temp];
                    H_Ecoeff_Y = H_Ecoeffs[temp];
                }
                if (x >= x_size-PML_width)
                {
                    //In the right edge
                    temp = x - x_size + PML_width;
                    H_Hcoeff_X = H_Hcoeffs[temp];
                    H_Ecoeff_X = H_Ecoeffs[temp];
                }
                if (y >= y_size-PML_width)
                {
                    //In the top edge
                    temp = y - y_size + PML_width;
                    H_Hcoeff_Y = H_Hcoeffs[temp];
                    H_Ecoeff_Y = H_Ecoeffs[temp];
                }
            }

            //EM field calculations

            //The FDTD equations for the PML are below
            double temp_Ex, temp_Ey;

            temp_Ey = x == 0 ? 0.0: Ey[x-1][y];
            temp_Ex = y == 0 ? 0.0: Ex[x][y-1];

            Hzx[x][y] = H_Hcoeff_X*Hzx[x][y]
                - H_Ecoeff_X * (Ey[x][y] - temp_Ey);

            Hzy[x][y] = H_Hcoeff_Y*Hzy[x][y]
                - H_Ecoeff_Y * (temp_Ex - Ex[x][y]);

            //This code brings the tangential fields into the normal field area

```

```

//This works because the values here will only be accessed by the
//code for the non-PML region at the boundary
//interface between the two regions, and by the PML code
//at the same boundary interface with the interior area
    Hz[x][y] = Hzx[x][y] + Hzy[x][y];

//Beginning of code block to handle pumping
    temp_Ey = x == 0 ? 0.0:Eyp[x-1][y];
    temp_Ex = y == 0 ? 0.0:Exp[x][y-1];

    Hzxp[x][y] = H_Hcoeff_X*Hzxp[x][y]
        - H_Ecoeff_X * (Eyp[x][y] - temp_Ey);

    Hzyp[x][y] = H_Hcoeff_Y*Hzyp[x][y]
        - H_Ecoeff_Y * (temp_Ex - Exp[x][y]);

    Hzp[x][y] = Hzxp[x][y] + Hzyp[x][y];

//End of first pump block
}
else//We are not in a boundary so now calculate the
magnetic field
{
    double H_Hcoeff, H_Ecoeff;

    double Exincp = 0.0;
    double Exinc = 0.0;

    //Check if we are at a source line and get the
source field
    if (y == source_y)
    {
        Exincp = source_Ex(x,y,n);
    }

    //Add in a field term that corresponds to the random
sources
    double Exdrop = 0;
    if (media[x][y]->is_gain() && random_sources &&
source_wavelength[x][y] >=0)
    {
        Exdrop =
4/sqrt(2.0)*sqrt((hbar*omega_a*N2[x][y]*grid_size)/(pi*tau_21))
        *cos(2*pi*cnaught/source_wavelength[x][y]*delta_time*n);
    }

    H_Hcoeff = media[x][y]->H_Hcoeff();
    H_Ecoeff = media[x][y]->H_Ecoeff();

    //Calculate the new magnetic field
    Hz[x][y] = H_Hcoeff*Hz[x][y]
        + H_Ecoeff*(Ex[x][y] - Ex[x][y-1] - Ey[x][y]
+ Ey[x-1][y] - Exinc - Exdrop);

    Hzp[x][y] = H_Hcoeff*Hzp[x][y]
        + H_Ecoeff*(Exp[x][y] - Exp[x][y-1] -
Eyp[x][y] + Eyp[x-1][y] - Exincp);
    }//end of FDTD calcs
    }//end of y
    }//end of x
    //End of M_FIELD_SECTION
}
fclose(fieldoutput);
}

//Add up the specified field_data over the specified y coordinate
double two_dim::integrate(int line_y, double ** field_data)
{
    double cur_total = 0.0;
    for (int i = 0; i < x_size; i++)

```

```

        {
            cur_total += field_data[i][line_y];
        }

    return cur_total;
}

//Output a file that lists the coordinates of each point in the output_circle file
void two_dim::output_circle_start(FILE * outfile)
{
    int angle;

    for (angle = 0; angle <= 180; angle += 1)
    {
        int i1 = (int)(-output_circle_radius * sin(angle*pi/180));
        int j1 = (int)(output_circle_radius * cos(angle*pi/180));
        int i2 = -i1;
        int j2 = j1;

        i1 += x_size/2;
        i2 += x_size/2;
        j1 += y_size/2;
        j2 += y_size/2;

        fprintf(outfile, "%d %d\n%d %d\n", i1, j1, i2, j2);
    }
}

//Output field values at points around a 180 degree semicircle at a specified radius
void two_dim::output_circle(FILE * outfile, double ** field_data, int n)
{
    fprintf(outfile, "%e ", n*delta_time);
    int angle;

    for (angle = 0; angle <= 180; angle += 1)
    {
        int i1 = (int)(-output_circle_radius * sin(angle*pi/180));
        int j1 = (int)(output_circle_radius * cos(angle*pi/180));
        int i2 = -i1;
        int j2 = j1;

        i1 += x_size/2;
        i2 += x_size/2;
        j1 += y_size/2;
        j2 += y_size/2;

        fprintf(outfile, "%e ", field_data[i1][j1]);
        fprintf(outfile, "%e ", field_data[i2][j2]);
    }
    fprintf(outfile, "\n");
}

double lorentzian(double mu)
//The lorentzian lineshape function
{
    double temp;
    temp = delta_freq*delta_freq/(4*((mu-freqnaught)*(mu-freqnaught) +
(delta_freq/2)*(delta_freq/2)));
    return temp;
}

//*****
//File util.cpp
//*****

//Random number generation procedures

#include "util.h"
#include "mtrand.h"

```

```

MTRand rand_gen;
//Create an instance of the Mersenne Twister random number generator using
//the library version

double real_rand();
//Return a random double in the range 0.0 <= x < 1.0

void start_rand()
{
    int ran_seed;//The seed value for the RNG.

    ran_seed = time(NULL); //Get a seed value.
    rand_gen.seed(ran_seed);//Seed the generator.
}

int get_rand(int lower, int higher)
//Returns a random integer in the range lower <= x < higher.
{
    int num;
    num = (int)((higher-lower)*real_rand() + lower);
    return num;
}

double get_rand(double lower, double higher)
//Returns a random integer in the range lower <= x < higher.
{
    double num;
    num = (double)((higher-lower)*real_rand() + lower);
    return num;
}

double real_rand()
//Returns a random double in the range 0.0 <= x < 1.0
{
    double L2D = (1.0/4294967296.0);
    double d;
    d = rand_gen();
    return d * L2D;
}

```